Modeling and Simulation in Science,
Engineering and Technology

Livio Gibelli
Nicola Bellomo
Editors

Crowd Dynamics, Volume 1

Theory, Models, and Safety Problems

Birkhäuser

Modeling and Simulation in Science, Engineering and Technology

Series editors

Editorial Advisory Board

More information about this series at http://www.springer.com/series/4960

Livio Gibelli • Nicola Bellomo
Editors

Crowd Dynamics, Volume 1

Theory, Models, and Safety Problems

Birkhäuser

Editors
Livio Gibelli
School of Engineering
University of Edinburgh
Edinburgh, UK

Nicola Bellomo
Department of Mathematical Sciences
Politecnico di Torino
Torino, Italy

ISSN 2164-3679 ISSN 2164-3725 (electronic)
Modeling and Simulation in Science, Engineering and Technology
ISBN 978-3-030-05128-0 ISBN 978-3-030-05129-7 (eBook)
https://doi.org/10.1007/978-3-030-05129-7

Library of Congress Control Number: 2018967310

Mathematics Subject Classification (2019): SCM, SCM13090, SCM14068, SCP19090, SCP33000

This book is published under the imprint Birkhäuser, www.birkhauser-science.com by the registered company Springer Nature Switzerland AG.
The registered company address is: Gewerbestrasse 11, 6330 Cham, Switzerland

Preface

The study of human crowds is a challenging interdisciplinary research field which requires contributions from different disciplines, including technology (to detect the main features of the crowd), mathematics (to derive models), and computational science (to simulate the crowd dynamics).

Contributions from psychology are also needed to model the dynamics of emotional behaviors which can modify the pedestrians' walking strategy and from neurology to deeply understand the collective learning dynamics of people that face crisis situations.

Accordingly, the modeling and simulation of human crowds needs a synergetic interaction between the so-called hard and soft sciences.

The realistic modeling and simulation of crowd behavior would lead to enormous benefits for society. Crowd dynamics models may support crisis managers who need to deal with extreme situations where decision-making needs to be taken in a very short time. A typical example is the rapid evacuation from complex venues induced by fires or other types of incidents. In these situations, the stress induced by the perception of danger can lead to behaviors that jeopardize the safety of walkers.

Recent events have also highlighted the importance of modeling the possible subgroup behavior within crowds such as groups of activists who fight one against the other in a public demonstration.

Besides these extreme cases, the optimization of pedestrian flow can reduce the time spent in nonproductive activities, ergo reducing the cost of transportation and consequently pollution.

The application of crowd dynamics models to realistic flow conditions poses formidable analytical and computational challenges. Just to cite a few examples, the qualitative analysis of solutions should account for nonlocal interactions of pedestrians among themselves and with walls; and the presence of stress conditions leads to models with nonlinear parameters that depend on local flow conditions, hence on the dependent variables.

These difficulties offer a very interesting research perspective to applied mathematicians.

A key problem in crowd dynamics modeling worth pointing out is the selection of the modeling scale. As it is known, three different scales can be adopted: namely, the microscopic, mesoscopic, and macroscopic, which lead to individual-based, kinetic, and hydrodynamic models. Different mathematical structures correspond to each scale.

In particular, *individual-based models* consist in large systems of ordinary differential equations which describe the dynamics of walkers represented by their individual position and velocity; *kinetic models* are in the form of integrodifferential equations which give the space and time evolution of a probability distribution function over the individual microscopic state of each walker, namely, its position and velocity; and *hydrodynamic models* are balance equations of mass and/or momentum, where the dependent variables are the local density and the local mean velocity, and the independent variables are the time and position.

As critically discussed in Chap. 1, rather than opening a dispute on the selection of the most appropriate modeling scale, we believe that a unified vision should be adopted which leads to models developed at each scale based on the same rationale.

The chapters of this edited book have been written by recognized experts in the field and provide a general overview of different aspects of modeling and simulation of human crowds. The first chapter, authored by the editors, provides a detailed presentation and critical analysis of the different contributions. The focus is on the conceptual framework underlying the derivation of models and their applications to safety problems. Some perspectives toward analytic problems are also brought to the attention of the interested reader.

Hopefully, this book will contribute to the future research activity in the field of crowd dynamics. We do not claim that all relevant topics have been treated, and, indeed, many major scientific contributions are certainly still to come. This volume should be viewed as the first of a sequence of volumes to be periodically published with the aim of continuously updating the state of the art.

Torino, Italy — Nicola Bellomo
Edinburgh, UK — Livio Gibelli
September 2018

Contents

Contributors

Boris Andreianov LMPT, CNRS UMR 7350, Université de Tours, Tours, France

Rafael Bailo Department of Mathematics, Imperial College London, London, UK

Nicola Bellomo Department of Mathematical Sciences, Politecnico di Torino, Torino, Italy

Raul Borsche TU Kaiserslautern, Kaiserslautern, Germany

José A. Carrillo Department of Mathematics, Imperial College London, London, UK

Mohcine Chraibi Institute of Advanced Simulation, Forschungszentrum Jülich GmbH, Jülich, Germany

Matteo Colangeli Università degli Studi dell'Aquila, LAquila, Italy

Pierre Degond Department of Mathematics, Imperial College London, London, UK

Carlotta Donadello Laboratoire de Mathématiques CNRS UMR 6623, Université Bourgogne Franche-Comté, Besançon, France

Livio Gibelli School of Engineering, University of Edinburgh, Edinburgh, UK

Max Kinateder Department of Psychological and Brain Sciences, Dartmouth College, Hanover, NH, USA

Axel Klar TU Kaiserslautern, Kaiserslautern, Germany

Adrian Muntean Karlstad University, Karlstad, Sweden

Daniel Nilsson Department of Civil and Natural Resources Engineering, University of Canterbury, New Zealand

Benedetto Piccoli Department of Mathematical Sciences, Rutgers University – Camden, Camden, NJ, USA

Ulrich Razafison Laboratoire de Mathématiques CNRS UMR 6623, Université Bourgogne Franche-Comté, Besançon, France

Omar Richardson Karlstad University, Karlstad, Sweden

Enrico Ronchi Department of Fire Safety Engineering, Lund University, Lund, Sweden

Massimiliano Daniele Rosini Department of Mathematics and Computer Science, University of Ferrara, Ferrara, Italy

Francesco Rossi Department of Mathematics "Tullio Levi–Civita", University of Padova, Padova, Italy

Andreas Schadschneider Institut für Theoretische Physik, Universität zu Köln, Köln, Germany

Florian Schneider TU Kaiserslautern, Kaiserslautern, Germany

Armin Seyfried Institute of Advanced Simulation, Forschungszentrum Jülich GmbH, Jülich, Germany

Thi Kim Thoa Thieu Gran Sasso Science Institute, LAquila, Italy

Antoine Tordeux School of Mechanical Engineering and Safety Engineering, University of Wuppertal, Wuppertal, Germany

William H. Warren Department of Cognitive, Linguistic & Psychological Sciences, Brown University, Providence, RI, USA

Trenton D. Wirth Department of Cognitive, Linguistic & Psychological Sciences, Brown University, Providence, RI, USA

Jun Zhang State Key Laboratory of Fire Science, University of Science and Technology of China, Hefei, China

Behavioral Human Crowds

Nicola Bellomo and Livio Gibelli

Abstract This chapter provides an introduction to the contents of Bellomo and Gibelli (Crowd dynamics, volume 1 – theory, models, and safety problems. Modeling and simulation in science, engineering, and technology. Birkhäuser, New York, 2018) and a general critical analysis on crowd modeling. The presentation is organized in three parts: firstly, a general framework and rationale toward the modeling and simulations of human crowds are proposed; subsequently the contents of Chaps. 2, 3, 4, 5, 6, 7, 8 and 9 are summarized by referring to the existing literature; finally, by taking advantage of the contents of the whole book, some speculations are proposed on possible research perspectives. Five key problems are presented, and hints are given to tackle them within a multiscale vision which appears to be the most looking forward idea to be pursued in research projects.

1 Plan of the Chapter

As mentioned in the Preface, the study of human crowds is a challenging interdisciplinary research field which requires the contributions from different disciplines. These range from technology, which is needed to detect the main features of crowds, to mathematics and computational science, which allow one to derive models of crowds and to simulate their dynamics, respectively. Psychology is also needed to understand the dynamics of emotional behaviors of crowds which in turn modify the pedestrians' walking strategy.

Mathematical models can be used to support crisis managers in extreme situations where the safety conditions might be threatened and decision-making needs

N. Bellomo
Department of Mathematical Sciences, Politecnico of Torino, Torino, Italy
e-mail: nicola.bellomo@polito.it

L. Gibelli (✉)
School of Engineering, University of Edinburgh, Edinburgh, UK
e-mail: livio.gibelli@ed.ac.uk

L. Gibelli, N. Bellomo (eds.), *Crowd Dynamics, Volume 1*, Modeling and Simulation in Science, Engineering and Technology,
https://doi.org/10.1007/978-3-030-05129-7_1

to be taken in a very short time. An example is the sudden and rapid evacuation from complex venues which might be induced by incidents. In this case, the stress induced by the perception of danger may lead to certain behaviors that jeopardize the safety of pedestrians. Extreme situations also appear when the crowd includes groups of activists that confront with each other [29]. In all these applications, the pedestrian's dynamics is strongly influenced by social interactions [1, 25, 32] which contribute to spread out the social behaviors over the crowd.

It is plain that the benefits of the realistic modeling and simulation of crowds are important also in the case of pedestrians' flows with limited presence of stress. In fact, the optimization of pedestrian flow can reduce the time spent in nonproductive activities, ergo reducing the cost of transportation and consequently pollution.

Mathematicians have been attracted by the analytic and computational difficulties generated by the complexity features which are typical of large living systems [7] within the general framework of complex systems [5], while the scientific community agrees that an interdisciplinary approach is necessary.

All these reasonings have motivated the edited book [12] which collects, in the next eight chapters, surveys of the activity of scientists who are active in the aforementioned challenging research topic. Our chapter provides an introduction to the contents of the rest of the chapters, and its presentation is proposed in the next three sections:

Section 2 presents some general features of human crowds and a brief description of the rationale to be used in the modeling approach. These features are related to the selection of different scales which can be used in the modeling approach. Safety problems are also introduced in this section.

Section 3 provides a description of the contents of Chaps. 2, 3, 4, 5, 6, 7, 8 and 9 in the light of the previous section.

Section 4 takes advantage of the contents of the previous sections to develop a critical analysis and to look ahead to research perspectives.

2 On the Modeling of Crowd Dynamics

A possible definition of what a crowd is and some of its key features has been given in [36]. This article focuses on the evacuation dynamics, where the onset and propagation of stress conditions appear to be a common event in crisis situations. This dynamics is often difficult to understand and to model. Some specific definitions can be extracted from [36]:

- *Definition of crowd* Agglomeration of many people in the same area at the same time. The density of people is assumed to be high enough to cause continuous interactions, or reactions, with other individuals.
- *Collective intelligence* Emergent functional behaviors of a large number of individuals that result from interactions of walkers rather than from individual

reasoning or global optimization. Establishment of a qualitatively new behavior through nonlinear interactions of many individuals.

- *Panic breakdown of ordered, cooperative behavior of individuals* Panic is often characterized by attempted escape of many individuals from a real or perceived threat in situations of a perceived struggle for survival, which may end up in trampling or crushing.

These definitions shed light on three key elements to be accounted for in the modeling approach. First, the crowd is constituted by a sufficiently high number of individuals so that interactions are the main factors which drive the dynamics of the system. Second, a collective intelligence, or a self-organizing ability, emerges out of the said interactions which are nonlinearly additive. Finally, stress conditions, occasionally called "panic" in [36], may create collective behaviors that jeopardize pedestrians' safety.

The pioneer ideas of [36] have motivated an intense activity in the field of applied mathematics. In particular, the problem of understanding how individual behaviors are modified by stress conditions has been tackled in [10], and a strategy for validating crowd models has been proposed in [11].

More recently, studies have been carried out about the space propagation of emotional states driven by contagion-like interactions, similar to the phenomenon of the epidemics spreading [13, 15, 59]. Where this term has been used in analogy to the phenomenon of the epidemics spread. Control problems have also been introduced in [2] to show how the complex dynamics of a crowd can be controlled by external actions.

The literature on safety problems is of interest for engineers, physicists, and mathematicians (see, e.g., [51, 60]). The modeling of safety problems and crisis managing is generally related to evacuation dynamics where the pedestrians' level of stressful conditions is very high. A variety of papers are devoted to this specific topic (see, e.g., [9, 32, 36, 37, 51, 55, 58]).

A useful contribution to the modeling is given by experimental activity, for instance, the study of walking behaviors [46, 47], parameter estimation in well-defined models [26], self-organized dynamics [35], and collection of data on the overall behavior corresponding to the so-called velocity diagram [30, 44, 55–57], namely, mean velocity versus density.

The definitions, which have been reported above, can be used to identify a number of key features of human crowds. The following ones have been extracted from [7].

1. **Ability to express a strategy** Living entities have the ability to develop specific strategies generated by their organization ability. These strategies are not defined once and for all, but depend on the state of the entities in their surrounding environment as well as on the geometry and quality of the latter. These include abrupt changes of directions, visibility conditions, and many others.
2. **Heterogeneity** The said strategy is heterogeneously distributed, and it can also include different targets and groups, for instance, leaders who aim at driving all other entities to their own strategy. Note that the irrational behaviors of a few

entities can generate large deviations from the standard dynamics observed in situations where all entities behave rationally.

3. **Nonlinear interactions** Interactions are nonlinearly additive and nonlocal. In fact, not only immediate neighbors but also distant entities are involved. In some cases, the topological distribution of a fixed number of neighbors rather than all the entities in the visibility domain can play a prominent role in the output of social and mechanical interactions.
4. **Learning dynamics** Living entities receive inputs from the external environment and have the ability to learn from past experience. Accordingly, their strategic ability and the rules of interactions can evolve in time and space.
5. **Multiscale aspects** The mathematical approach always needs multiscale methods. Namely, a single observation and representation scale is not generally sufficient to describe the overall collective dynamics of living systems. For instance, the dynamics at the microscopic scale defines the conceptual basis toward the derivation of models at the mesoscopic scale. Models at the higher scale, corresponding to observable macroscopic quantities, can be obtained from kinetic models by letting the distance between individuals goes to zero.

Bearing all above in mind, let us now address the reader's attention to multiscale problems which appear as a general topic which pervades the contents of all chapters of this book.

As it is known, crowd dynamics modeling can be carried out at the three classical scales, namely, the microscopic, mesoscopic, and macroscopic scales, and lead to individual based, kinetic, and hydrodynamic models. More specifically:

- *Individual based models* are generally stated in terms of large systems of ordinary differential equations which model the dynamics of walkers represented by their individual position and velocity. Models are derived by describing the acceleration term, occasionally called force, by heuristic model of interactions between walkers located within the visibility area of each individually identified walker.

  The survey [33] provides the conceptual framework for the derivation of models, where the main modeling issue consists in modeling the acceleration term acting on each walker. An example is given by the celebrated social force model [34] which has been applied by various authors starting from [34] up to recent studies concerning the self organization ability of crowds [47].
- *Kinetic models* are in the form of integrodifferential equations which give the space and time evolution of a probability distribution function defined over the individual microscopic state of each walker, namely, its position and velocity. These models have been introduced in [8] for the dynamics in unbounded domain and further developed in [11] for a crowd in domains which include walls, exists, and obstacles. The space propagation of emotional state has been introduced in the already cited papers [13, 15, 59].

  The approach is closely related to the kinetic theory of gases [22], the main difference being that interactions are modeled by theoretical tools of game theory [20, 31, 43] rather than by rules of classical mechanics.

- *Hydrodynamic models* describe the dynamics of the dependent variables which are the local density and the local mean velocity, while the independent variables are time and position. The mathematical framework is defined by equations corresponding to the conservation of mass and linear momentum, where the acceleration term can be modeled by accounting for pedestrian's interactions. This term depends also on the geometry of the venue where pedestrians move.

  A simplified structure is defined by the equation corresponding to mass conservation only linked to a phenomenological model expressing how the local mean velocity varies depending on the local density and on the geometry of the venue. The literature on the models at the macroscopic scale is reviewed in [24], while their derivation from the underlying description at the microscopic scale delivered by kinetic models is discussed in [19] which is an important source of mathematical tools. A systematic approach to macroscopic crowd modeling has been started in [40, 41]. These seminal papers have been subsequently developed by various authors who have proposed important improvements, for instance [21].

Although concise, this literature overview allows us to propose some general rationale on crowd modeling which can contribute to enlighten some common features as well as some conceptual differences of the three classes of models.

The motivation of this discussion is the recurrent dispute among scientists on the choice of the most appropriate scale to be used in the modeling approach. It is often stated that only the microscopic scale is the most appropriate for systems with finite number of degrees, while the macroscopic scale requires unrealistic assumptions on the continuity of the matter and kills some heterogeneity features of the individual behaviors. The intermediate kinetic theory approach needs the assumption of continuity of the said probability distribution function over position and velocity of the walkers which is reasonable only when their number is sufficiently large.

Our viewpoint is that one has to look ahead to a multiscale approach, where all the modeling scales are involved. Indeed, this approach can be viewed as an important research challenge.

The following five key topics are deemed to contribute to a deeper understanding of the aforementioned multiscale vision.

Key Topic 1 – Modeling interactions and walking strategy Individual walkers have a visibility domain which depends on the quality and geometry of the venue. In specific conditions, for instance, in the presence of smoke, the visibility domain may be reduced. Each walker interacts with all the individuals in the said domain, and the interactions are nonlinearly additive and nonlocal.

Individual based interactions directly enter in the microscopic models as well as, in statistical sense, in the mesoscopic models. However, they should also be a key ingredient of hydrodynamic models. Indeed, interactions induce a walking strategy by which walkers continuously modify their direction of motion and adapt the speed to the local perceived density.

A minimal model, proposed in [10], indicates that the choice of the direction is continuously determined by four stimuli, namely, trend toward a target, search of

less crowded region, attraction toward the main stream, and search of trajectories that avoid the contact with walls. The selection depends on local density condition, on local emotional states, and on geometrical parameters such as the distance from targets and walls. Subsequently, pedestrians adapt their speed according to the density perceived in the new walking direction.

Key Topic 2 – Role of emotional states The walking strategy discussed in the Key Topic 1 depends on the emotional state of each walker which, following [10], can be modeled by a parameter u taking values in [0, 1], where $u = 0$ corresponds to absence of concentration on the search of an optimal walking strategy, while $u = 1$ corresponds to a maximal attraction toward the stream against the search of vacuum regions. This dynamics may create overcrowded areas and, as a consequence, leads to crisis situations.

This topic has been developed within the kinetic theory framework, but it can also be extended to the other modeling scales. Research activity specifically addressed to this topic is currently underway.

It is worth mentioning that an important development consists in modeling how initially localized stress conditions propagate in space. In fact, stress induces unsafe conditions, and crisis managers need knowing how this emotional state diffuses in space.

Key Topic 3 – Validation of models Validation of models is a challenging, definitely necessary, topic which precedes the application of models to real crowd flow problems. The main difficulty is that quantitative results are available in steady (equilibrium) flow conditions. However, models are required to provide quantitative results in real conditions which are generally unsteady and far from equilibrium. In addition, the behavior of the crowd is strongly dependent on the geometrical and quality features of the venue where walkers move.

Bearing all above conceptual difficulties in mind, a general rationale toward validation consists in requiring that models reproduce quantitatively empirical data for solutions corresponding to steady uniform flow and depict qualitatively emerging behaviors which are repetitively observed. In addition, models should include parameters that account for the specific role of the venue on the dynamics of the crowd.

Key Topic 4 – Analytic and computational problems The derivation and application of models pose challenging analytic and computational problems. These include:

(i) Qualitative analysis, namely, existence and regularity of solutions of initial-boundary value problems;

(ii) Asymptotic analysis toward the derivation of models at the higher scale from the underlying description at the lower scale;
(iii) Development of suitable computational methods, as models at different scales have a different differential structure which requires a specific numerical treatment.

Key Topic 5 – Management of crisis The objective of modeling and simulations needs to be finalized with respect to the specific cases under consideration.

Essentially, two cases can be distinguished, namely, the support to the training of crisis managers and the contribution to crisis management. In the former case, the aim of the computational modeling consists in providing simulations, where priority is given to the accurate description of the flow patterns for different geometries and qualities of the venue, while in the latter case, simulations should run, at least, in real time so that crisis managers can take rapid decisions and dynamically adapt evacuation plans to real conditions.

These five key topics provide a means of interpretation of the contents of the following chapters of our edited book. We will return to them in the last section where possible research perspectives are discussed.

Let us stress here that the five key problems discussed above provide a conceptual framework that naturally leads to propose a *multiscale vision* where models at the different scales are derived coherently. For instance, the derivation by kinetic theory methods requires a well-defined description of interactions at the microscopic scale, while the derivation of hydrodynamic models can be achieved by asymptotic methods applied to kinetic-type models by letting the distance between walkers goes to zero.

This vision suggests that, even if models are independently derived at each scale, the same modeling strategy has to be used in the derivation at each scale. Hence, what we have called *walking strategy* has to be treated by the same rules at each scale, possibly using analogous parameters. The overall strategy is a bottom-up process:

$$\textit{Microscopic scale} \quad \Rightarrow \quad \textit{Mesoscopic scale} \quad \Rightarrow \quad \textit{Macroscopic scale},$$

which corresponds to

$$\textit{Individual based models} \quad \Rightarrow \quad \textit{Kinetic models} \quad \Rightarrow \quad \textit{Hydrodynamic models}.$$

Some preliminary results are known in the literature. As an example, the first problem has been treated in [6] focusing on the derivation of hydrodynamic models from kinetic models for a crowd in unbounded domains. Arguably, the presence of walls and obstacles can modify the structure of the equations; however, this development has not yet been dealt with at all scales.

3 On the Contents of the Edited Book

The contents of the edited book [12] are front edge research topics in the modeling and application of crowd dynamics. As we shall see, the various chapters do not cover all possible issues, and many major scientific contributions are certainly still to come. These will be the subject of a next forthcoming edited book on the same field, scheduled as Volume 2.

The presentation of the next chapters is somehow referred to the key problems proposed in the preceding section. Indeed some chapters precisely focus on the said problems.

Bearing all above in mind, let us describe the specific topics dealt with by the chapters of this book by beginning from those which deal with the qualitative analysis of the behaviors of crowds from the viewpoint of psychologist and engineers and, afterward, analytic problems and applications.

Chapters 2 and 3 contribute to the development of topics that can bring important contributions to modeling by deeply discussing how the virtual reality may be used to collect empirical data [42], how the presence of smoke affects the dynamics of a crowd and has to be tackled to manage crisis situations [52], and how experimental data can be organized toward the calibration of models [54]. More specifically, the content of the chapters is as follows:

Chapter 2 [42] proposes a methodological approach to collect empirical data on crowd dynamics. The methods available to researchers typically need a compromise between ecological validity and experimental control. The goal of the chapter is to demonstrate that the approach therein called *virtual reality* (VR) offers a promising solution to the dilemma.

The first part of the chapter introduces VR as a research tool and analyzes its strengths and weaknesses. The second part covers a range of studies in which VR was used to study crowds, by beginning with a discussion of the differences between human behavior in real and virtual settings (e.g., walking and social interactions). Using the behavioral dynamics framework as a theoretical foundation, several studies are presented which demonstrate that people coordinate dynamically with their neighbors in a crowd. These studies are important contributions toward a data-driven approach to modeling human crowds. Then, a series of VR studies that cover various aspects of crowd behavior in emergency evacuation scenarios are introduced, covering topics such as evacuation decision-making, way-finding, and exit choice when people evacuate an area.

Chapter 3 [52] provides a detailed study on pedestrian movement in smoke-filled environments which is of paramount importance in fire safety engineering applications.

The chapter firstly presents an overview of the main concepts concerning pedestrian movement in smoke domains specifically focusing on evacuation dynamics. Several factors are discussed, including fire, pedestrians, and environmental factors. Subsequently, the authors provide an overview of the current capabilities

of pedestrian and evacuation models used in fire safety engineering applications, and future research directions in this specific field are envisioned.

Chapter 4 [54] reviews the state of the art of the interplay between empirical and theoretical studies of pedestrian dynamics.

Firstly, the main physical quantities characterizing the properties of a homogeneous crowd are introduced. Then, a brief summary of some important empirical findings is given. Finally, the properties of microscopic pedestrian models are critically analyzed. The authors emphasize the relevance of empirical results and show how they can be used for the validation and calibration of models.

Chapters 5 and 6 deal with analytic issues which are relevant when hydrodynamic models are applied to practical problems. It is shown in [3] that appropriate constraints on the conservation equations can reproduce interesting phenomena observed in crowd dynamics, while a detailed study of a generalized Wasserstein distance is discussed in [50].

Chapter 5 [3] presents analytic and computational studies on one-dimensional conservation laws with point constraints on the flux. Possible applications refer to the modeling of traffic flow through bottlenecks, such as exits in the context of pedestrians traffic and toll gates in vehicular traffic.

The authors introduce nonlocal constraints, which allow one to model the irrational behavior ("panic") near the exits observed in dense crowds and the capacity drop at tollbooths in vehicular traffic. Numerical schemes, based on finite volume methods, are developed, their convergence is proved, and their validations are done against explicit solutions. Numerical experiments show that constrained models are able to reproduce important features in traffic flow, such as capacity drop and self-organization.

Chapter 6 [50] revises some modeling, analysis, and simulation contributions for crowd dynamics using time-evolving measures. Two key features are strictly related to the use of measures: on one side, this setting permits to generalize both microscopic and macroscopic crowd models; on the other side, it allows an easy description of multiscale crowd models, e.g., crowds composed of leaders and followers. The main analytical tool for studying measure evolution is to endow the space of measures with the Wasserstein distance.

This chapter also describes recent contributions about crowd modeling with time-varying total mass. This requires to use a more flexible metric tool in the space of measures, which is referred to as generalized Wasserstein distance.

Chapters 7, 8, and 9 deal with crowd dynamics models which include some aspects of a multiscale vision proposed in the preceding section.

Chapter 7 [17] starts from a classical microscopic social force model for pedestrians [35] and extends it with an optimal path computation as, for instance, in Ref. [39]. The modeling accounts for nonlocal interactions and borrows some ideas from the classical kinetic theory and swarm modeling. Macroscopic hydrodynamic equations with a nonlocal interaction term are obtained by closure of conservation equations. The authors use, for the numerical simulations, mesh-free particle methods and finite volume methods on the different levels of the model hierarchy.

Chapter 8 [23] studies the dynamics of interacting agents from two distinct intermixed populations: one population includes active agents that follow a predetermined velocity field, while the second population contains exclusively passive agents, i.e., agents that have no preferred direction of motion. The orientation of their local velocity is affected by repulsive interactions with the neighboring agents and environment.

Two models that allow for a qualitative analysis of these mixed systems are presented as examples of possible case studies. It is shown that the residence times of this type of systems containing mixed populations are strongly affected by the interplay between these two populations. Finally, mathematical aspects concerning the well-posedness are carefully developed.

Chapter 9 [4] presents new ideas on the modeling of crowd dynamics at the microscopic scale. The authors succeed to go beyond the modeling approach based on the so-called force concept by introducing acceleration models that account for individual behaviors in different flow contexts. In more detail, a model for pedestrian dynamics is proposed to reproduce the rational behavior of individual agents by which each pedestrian undergoes a two-step time evolution based on a perception stage and a decision stage.

The contents are enlightened by figures descriptive of the dynamics and simulations that contribute to show the descriptive ability of the class of proposed models. In addition, it is shown, how the model can account for high density flow which is an important feature of crowd modeling.

4 Critical Analysis and Perspectives

This final section takes advantage of the review and critical analysis of the chapters in [12] to look ahead to possible research perspectives. The long list of possible research targets is narrowed down by only focusing on the multiscale vision proposed in the preceding section and by showing how this vision pervades all five key problems.

- **Interactions** The modeling of interactions is an essential step in the derivation of models. The multiscale vision suggests to model interactions by using the same rationale at each scale. Essentially this means that one has to invent structures suitable to retain, at each scale, the complexity features of the crowd as they appear in the said interactions.

  An important aspect consists in describing how people develop the strategy which accounts for the four stimuli previously mentioned when interactions also include the walkers' emotional state. Theoretical tools of game theory can be most likely used to model these interactions [8, 43].

  In principles, empirical data should be collected to support modeling, and, in this respect, many valuable papers show how empirical data can be used, for instance, [26–28, 39, 45, 48, 56]. It is worth stressing that a more extensive experimental activity is needed which focuses on individual interactions.

- **Emotional states** As it has been shown in [10], the level of emotional states can significantly affect the collective dynamics of human crowds and leads to very different pedestrians' flow patterns. Space and time propagation of the emotional state by a contagion-type dynamics is also expected to play a prominent role. This topic has been developed in [13] by the kinetic theory approach, while modeling of this complex dynamics should be possibly extended also to models derived at the microscopic and macroscopic scales.

  As already mentioned, an interesting development consists in modeling crowds, where groups of activists fight each other. Contagion dynamics might also be included which accounts for the possible passage between different groups.
- **Validation of models** An approach for the validation of models of large systems of interacting entities has been proposed in [7]. The basic requirement, specified in Key Topic 3, is the ability to quantitatively reproduce empirical data and qualitatively depict collective emerging behaviors.

  This approach has been used in [11], where the so-called velocity diagram has been reproduced by a model therein proposed, while segregation phenomena have been studied for the counterflow of walkers. It is important mentioning that the velocity diagram should be an output of interactions and not artificially inserted into the model.

  This study has been developed for kinetic-type models, while it should be extended to the case of individual-based and hydrodynamic models.
- **Analytic and computational problems** The derivation of macroscopic models from the underlying description at the microscopic scale is often obtained by heuristic averaging approximations that involve phenomenological models whose validity is generally claimed but not proved.

  Mathematicians are interested to the search of a unified approach to physical sciences as inspired by the sixth Hilbert problem [38]. In fluid dynamics, this problems has been interpreted as the derivation of hydrodynamic models from the description delivered by the Boltzmann equation [53].

  It has been shown in [14, 19] that the approach can be carried out also for certain populations of active particles including human crowds, and it has been proved in [6] for crowds in unbounded domain (see also [18]). An interesting research perspective consists in extending the tools of [19] and further developing the preliminary approach proposed in [6] to derive hydrodynamic models in the general case, namely, in the presence of walls and obstacles.

  Note that different computational methods are most likely needed at the different scales. More specifically, classical deterministic models can be used at the microscopic and macroscopic scales, while stochastic particle methods appear to be more appropriate in the case of kinetic theory models [16, 49].
- **Crisis management** The support that mathematical sciences can give to crisis managers has been mentioned several times in this chapter. A wide bibliography is reported in [9, 52], while some specific topics have also been tangentially treated in the chapters of our edited book. A possible use of artificial intelligence has been briefly discussed in [9].

This intense activity has enlightened the need of developing a systems approach to crowd modeling suitable to describe the dynamics in venues constituted of interconnected areas with different geometrical and qualitative features, possibly by using models with different granularity depending on the specific properties of each area.

In conclusion, the discussion above suggests that a multiscale approach is needed which allows one to switch between models developed at the different scales with the same unified principles. Hopefully, the contents of this edited book [12] can motivate researchers to develop future research activity and even to tackle this perspective.

References

1. G. Ajmone Marsan, N. Bellomo, and L. Gibelli, Stochastic evolutionary differential games toward a systems theory of behavioral social dynamics, *Math. Models Methods Appl. Sci.*, **26**, 1051–1093, (2016).
2. G. Albi, M. Bongini, E. Cristiano, and D. Kalise, Invisible control of self-organizing agents leaving unknown environments, *Siam J. Appl. Math.*, **76(4)**, 1683–1710, (2016).
3. B. Andreianov, C. Donadello, U. Razafison and M. D. Rosini, One-dimensional conservation laws with non-local point constraints on the flux, Chapter 5 in Crowd Dynamics, Volume 1 - Theory, Models, and Safety Problems, *Modeling and Simulation in Science, Engineering, and Technology*, Birkhäuser, New York, (2018).
4. R. Bailo, J. A. Carrillo, and P. Degond, Pedestrian models based on rational behaviour, Chapter 9 in Crowd Dynamics, Volume 1 - Theory, Models, and Safety Problems, *Modeling and Simulation in Science, Engineering, and Technology*, Birkhäuser, New York, (2018).
5. P. Ball, **Why Society is a Complex Matter**, Springer-Verlag, Heidelberg, (2012).
6. N. Bellomo and A. Bellouquid, On multiscale models of pedestrian crowds from mesoscopic to macroscopic, *Comm. Math. Sciences*, **13(7)**, 1649–1664, (2015).
7. N. Bellomo, A. Bellouquid, L. Gibelli, and N. Outada, **A Quest Towards a Mathematical Theory of Living Systems**, Birkhäuser, New York, (2017).
8. N. Bellomo, A. Bellouquid, and D. Knopoff, From the microscale to collective crowd dynamics, *Multiscale Model. Simul.*, **11**(3), 943–963, (2013).
9. N. Bellomo, D. Clarke, L. Gibelli, P. Townsend, and B.J. Vreugdenhil, Human behaviours in evacuation crowd dynamics: From modeling to "big data" toward crisis management, *Phys. Life Rev.*, **18**, 1–21, (2016).
10. N. Bellomo, and L. Gibelli, Toward a mathematical theory of behavioral-social dynamics for pedestrian crowds, *Math. Models Methods Appl. Sci.*, **25(13)**, 2417–2437, (2015).
11. N. Bellomo and L. Gibelli, Behavioral crowds: Modeling and Monte Carlo simulations toward validation, *Computers & Fluids*, **141**, 13–21, (2016).
12. N. Bellomo and L. Gibelli, **Crowd Dynamics, Volume 1 - Theory, Models, and Safety Problems**, *Modeling and Simulation in Science, Engineering, and Technology*, Birkhäuser, New York, (2018).
13. N. Bellomo, L. Gibelli, and N. Outada, On the interplay between behavioral dynamics and social interactions in human crowds, *Kinet. Relat. Mod.*, **12(2)**, 397–409, (2019).
14. A. Bellouquid and N. Chouhad, Kinetic models of chemotaxis towards the diffusive limit: asymptotic analysis, *Math. Models Methods Appl. Sci.*, **39**, 3136–3151, (2016).
15. A.L. Bertozzi, J. Rosado, M.B. Short, and L. Wang, Contagion shocks in one dimension, *J. Stat. Phys.*, **158**, 647–664, (2015).

16. G.A. Bird, **Molecular Gas Dynamics and the Direct Simulation of Gas Flows**, Oxford University Press, (1994).
17. R. Borsche, A. Klar, and F. Schneider, Numerical methods for mean-field and moment models for pedestrian flow, Chapter 7 in Crowd Dynamics, Volume 1 - Theory, Models, and Safety Problems, *Modeling and Simulation in Science, Engineering, and Technology*, Birkhäuser, New York, (2018).
18. M. Burger, P. Markowich, J.F. Pietschmann, Continuous limit of a crowd motion and herding Model: analysis and numerical simulations, *Kinet. Rel. Models*, **4(4)**, 1025–1047, (2011).
19. D. Burini and N. Chouhad, Hilbert method toward a multiscale analysis from kinetic to macroscopic models for active particles, *Math. Models Methods Appl. Sci.*, **27**, 1327–1353, (2017).
20. D. Burini, S. De Lillo, and L. Gibelli, Stochastic differential "nonlinear" games modeling collective learning dynamics, *Phys. Life Rev.*, **16**, 123–139, (2016).
21. J.-A. Carrillo, S. Martin, and M.-T. Wolfram An improved version of the Hughes model for pedestrian flow *Math. Model. Methods Appl. Sci.*, **26(04)**, 671–697, (2016).
22. C. Cercignani, R. Illner, and M. Pulvirenti, **The Kinetic Theory of a Diluted Gas**, Springer, Heidelberg, New York, (1993).
23. M. Colangeli, A. Muntean, O. Richardson and T. Thieu, Modelling interactions between active and passive agents moving through heterogeneous environments, Chapter 8 in Crowd Dynamics, Volume 1 - Theory, Models, and Safety Problems, *Modeling and Simulation in Science, Engineering, and Technology*, Birkhäuser, New York, (2018).
24. E. Cristiani, B. Piccoli, and A. Tosin, **Multiscale Modeling of Pedestrian Dynamics**, Springer, (2014).
25. E. Cristiani, F.S. Priuli, and A. Tosin, Modeling rationality to control self-organization of crowds: an environmental approach, *SIAM J. Appl. Math.*, **75(2)**, 605–629, (2015).
26. A. Corbetta, A. Mountean, and K. Vafayi, Parameter estimation of social forces in pedestrian dynamics models via probabilistic method, *Math. Biosci. Eng.*, **12**, 337–356, (2015).
27. P. Degond, C. Appert-Rolland, M. Moussaid, J. Pettré, and G. Theraulaz, A hierarchy of heuristic-based models of crowd dynamics, *J. Stat. Phys.*, **152**, 1033–1068, (2013).
28. P. Degond, C. Appert-Rolland, J. Pettré, and G. Theraulaz, Vision based macroscopic pedestrian models, *Kinetic Related Models*, **6**, 809–839, (2013).
29. J.-M. Epstein J.M., Modeling civil violence: An agent based computational approach, *Proc. Nat. Acad. Sci.*, **99**, 7243–7250, (2002).
30. Z. Fu, L. Luo, Y. Yang, Y. Zhuang, P. Zhang, L. Yang, H. Yang, J. Ma, K. Zhu, and Y. Li, Effect of speed matching on fundamental diagram of pedestrian flow, *Physica A*, **458**, 31–42, (2016).
31. H. Gintis, **Game Theory Evolving**, 2nd Ed., Princeton University Press, Princeton NJ, (2009).
32. M. Haghani, and M. Sarvi, Social dynamics in emergency evacuations: Disentangling crowds attraction and repulsion effects, *Physica A*, **475**, 24–34, (2017).
33. D. Helbing, Traffic and related self-driven many-particle systems, *Rev. Modern Phys.*, **73**, 1067–1141, (2001).
34. D. Helbing and P. Molnár, Social force model for pedestrian dynamics *Phys. Rev. E*, **51**, 4282–4286, (1995).
35. D. Helbing, P. Molnár, I.-J. Farkas, and K. Bolay, Self-organizing pedestrian movement, *Environ. Plan. B Plan. Des.*, **28(3)**, 361–383, (2001).
36. D. Helbing D. and A. Johansson, Pedestrian crowd and evacuation dynamics, *Enciclopedia of Complexity and System Science*, Springer, 6476–6495, (2009).
37. D. Helbing, A. Johansson, and H.-Z. Al-Abideen, Dynamics of crowd disasters: An empirical study, *Phys. Rev. E*, **75**, paper no. 046109, (2007).
38. D. Hilbert, Mathematical problems, *Bull. Amer. Math. Soc.*, **8(10)** (1902), 437–479.
39. S.P. Hoogendoorn, F. van Wageningen-Kessels, W. Daamen, and D.C. Duives, Continuum modelling of pedestrian flows: From microscopic principles to self-organised macroscopic phenomena, *Physica A*, **416**, 684–694, (2014).
40. R. L. Hughes A continuum theory for the flow of pedestrians, *Transp. Research B*, **36**, 507–536, (2002).

41. R.L. Hughes, The flow of human crowds, *Annu. Rev. Fluid Mech.*, **35**, 169–182, (2003).
42. M. Kinateder, T. D. Wirth, and W. H. Warren, Crowd Dynamics in Virtual Reality, Chapter 2 in Crowd Dynamics, Volume 1 - Theory, Models, and Safety Problems, *Modeling and Simulation in Science, Engineering, and Technology*, Birkhäuser, New York, (2018).
43. A. Lachapelle, M.T. Wolfram, On a mean field game approach modeling congestion and aversion in pedestrian crowds *Transportation Research B*, **45**, 1572–1589, (2011).
44. F. Martinez-Gil, M. Lozano, I. Garcia-Fernández and F. Fernández, Modeling, evaluation and scale on artificial pedestrians: A literature review, *ACM Computing Surveys*, In press (2018).
45. B. Maury, and J. Venel A discrete contact model for crowd motion, *ESAIM: M2AN*, **45**, 145–168, (2011).
46. M. Moussaïd, E.-G. Guillot, M. Moreau, J. Fehrenbach, O. Chabiron, S. Lemercier, J. Pettré, C. Appert-Rolland, P. Degond, and G. Theraulaz, Traffic instabilities in self-organized pedestrian crowds *PLoS Comput. Biol.*, **8(3)**, (2012).
47. M. Moussaïd, D. Helbing, S. Garnier, A. Johansson, M. Combe, and G. Theraulaz, Experimental study of the behavioural mechanisms underlying self-organization in human crowds, *Proc. Roy. Soc. B*, **276**, 2755–2762, (2009).
48. M. Moussaïd and G. Theraulaz, Comment les piétons marchent dans la foule. *La Recherche*, **450**, 56–59, (2011).
49. L. Pareschi and G. Toscani, **Interacting Multiagent Systems: Kinetic Equations and Monte Carlo Methods** Oxford University Press, Oxford, (2014).
50. B. Piccoli and F. Rossi, Measure-theoretic models for crowd dynamics, Chapter 6 in Crowd Dynamics, Volume 1 - Theory, Models, and Safety Problems, *Modeling and Simulation in Science, Engineering, and Technology*, Birkhäuser, New York, (2018).
51. F. Ronchi, F. Nieto Uriz, X. Criel, and P. Reilly, Modelling large-scale evacuation of music festival. *Fire Safety*, **5**, 11–19, (2016).
52. E. Ronchi and D. Nilsson Pedestrian Movement in Smoke: Theory, Data and Modelling Approaches, Chapter 3 in Crowd Dynamics, Volume 1 - Theory, Models, and Safety Problems, *Modeling and Simulation in Science, Engineering, and Technology*, Birkhäuser, New York, (2018).
53. L. Saint-Raymond, **Hydrodynamic limits of the Boltzmann equation**, Lecture Notes in Mathematics n.1971, Springer, Berlin, (2009).
54. A. Schadschneider, M. Chraibi, A. Seyfried, A. Tordeux, and J. Zhang, Pedestrian Dynamics - From Empirical Results to Modeling, Chapter 4 in Crowd Dynamics, Volume 1 - Theory, Models, and Safety Problems, *Modeling and Simulation in Science, Engineering, and Technology*, Birkhäuser, New York, (2018).
55. A. Schadschneider, W. Klingsch, H. Kläpfel, T. Kretz, C. Rogsch, and A. Seyfried, Evacuation Dynamics: Empirical Results, Modeling and Applications, *Encyclopedia of Complexity and System Scence*, 3142–3176, (2009).
56. A. Schadschneider and A. Seyfried, Empirical results for pedestrian dynamics and their implications for modeling. *Netw. Heterog. Media*, **6**, 545–560, (2011).
57. A. Seyfried, B. Steffen, W. Klingsch, and M. Boltes, The fundamental diagram of pedestrian movement revisited, *J. Stat. Mech.: Theory and Experiments*, **360**, 232–238, (2006).
58. H. Vermuyten, J. Belien, L. De Boeck, G. Reniers, and T. Wauters, A review of optimisation models for pedestrian evacuation and design problems, *Safety Science*, **87**, 167–178, (2016).
59. L. Wang, M.B. Short, and A.L. Bertozzi, Efficient numerical methods for multiscale crowd dynamics with emotional contagion, *Math. Models Methods Appl. Sci.*, **27**, 205–230, (2017).
60. N. Wijermans, C. Conrado, M. van Steen, C. Martella, and J.-L. Li, A landscape of crowd management support: An integrative approach, *Safety Science*, **86**, 142–164, (2016).

Crowd Dynamics in Virtual Reality

Max Kinateder, Trenton D. Wirth, and William H. Warren

Abstract Collecting empirical data on crowd dynamics is challenging. The methods available to researchers typically need to compromise between ecological validity and experimental control. The goal of this chapter is to demonstrate that virtual reality (VR) offers a promising solution to the dilemma. The first section of this chapter introduces VR as a research tool and touches on its strengths and weaknesses. The second section covers a range of studies in which VR was used to study crowds, beginning with a discussion of differences between human behavior in real and virtual settings (e.g., walking and social interactions). Using the *behavioral dynamics* framework as a theoretical foundation, several studies demonstrating that people coordinate dynamically with their neighbors in a crowd are presented, contributing toward a data-driven approach to modeling human crowds. Then, a series of VR studies that cover various aspects of crowd behavior in emergency evacuation scenarios are introduced, covering topics such as evacuation decision-making, way-finding, and exit choice when people evacuate in a crowd. Finally, the third section of this chapter offers an outlook on the road ahead, discussing some of the technical and methodological challenges for VR as a research tool.

M. Kinateder (✉)
Department of Psychological and Brain Sciences,
Dartmouth College, Hanover, NH, USA
e-mail: max.kinateder@nrc-cnrc.gc.ca

T. D. Wirth · W. H. Warren
Department of Cognitive, Linguistic & Psychological Sciences, Brown University,
Providence, RI, USA

L. Gibelli, N. Bellomo (eds.), *Crowd Dynamics, Volume 1*, Modeling
and Simulation in Science, Engineering and Technology,
https://doi.org/10.1007/978-3-030-05129-7_2

1 Introduction

Understanding crowd dynamics is a challenging endeavor. It is therefore not surprising that computational models of crowd dynamics vary significantly in complexity and granularity, ranging from physics-based approaches to attempts to model the dynamic interactions between individuals and groups based on social psychological theories [1]. To this day, it has been particularly challenging to connect advances in knowledge about human behavior in emergency situations to complex dynamics of crowd behavior, particularly in evacuation or other high-risk scenarios. Unfortunately, empirical data allowing for fine-grained analysis of interactions between individuals in a crowd is still hard to come by.

With the rise of affordable yet highly immersive virtual reality (VR) devices, researchers discovered VR as a promising tool for research on crowd behavior. Traditionally, VR refers to "real or simulated environment[s] in which the perceiver experiences telepresence" [2]. "Presence" denotes the experience of "being there," i.e., the feeling of being immersed in a virtual environment and forgetting about the real world [3, 4]. The more convincing a virtual environment is, the greater the sense of presence in the virtual world. Researchers in various areas have embraced VR as a tool because of its potential for presenting participants with immersive and interactive stimulus displays that are at the same time highly controlled. However, before accepting a novel tool, it is important to ask whether the tool can actually provide useful data. Indeed, the debate over the use of VR as a research tool for studying crowd dynamics, particularly in emergency situations, is ongoing [5].

Generally speaking, VR systems comprise computer-generated interactive visual and auditory simulations (and increasingly haptic/tactile, vestibular, even olfactory simulation [6–8]) of realistic environments. Virtual environments can be presented on a desktop computer screen [9, 10] and controlled with a mouse or joystick or more sophisticated displays such as a head-mounted display (HMD) or multiscreen cave automatic virtual environment (CAVE) system. In such advanced systems, users can freely move their whole body in the virtual space (see VR glossary for more detailed information).

We will begin this chapter with outlining the state of the art of VR systems, discuss the promises and limitations of VR with regard to crowd dynamics before we showcase several VR studies, and finish with a preview of future directions. The reader should note that VR has several applications relevant to crowd dynamics that are not covered in this chapter due to brevity. For instance, VR can be used to train emergency responders for crowd disasters or to visualize the results of crowd dynamic simulations for planning purposes. These are important and valid uses of the technology but go beyond the scope of this chapter. The same is true for emerging technologies such as Augmented Reality (AR) applications for crowd research. The interested reader is pointed to the following references for further reading [10–15].

VR Glossary
Avatar: A virtual representation of a human controlled by input from a real human user or "player."
Agent: A virtual human with interactive behavior controlled by a computer algorithm.
HMD: Head-mounted display; display device worn on the head that presents VR content stereoscopically. Typically, the head movements of the user are tracked, and the view is updated accordingly, creating the experience of being immersed in the virtual environment.
CAVE: Cave Automatic Virtual Environment; refers to VR technology that projects imagery on multiple walls, viewed through stereoscopic glasses. Users are immersed in the virtual environment and can move their whole body within the confines of the walls.
Presence refers to the experience of being fully "in" a virtual environment and to forget the real world. The more *immersive* a VR system, the stronger the experience of presence.
In *third-person view*, users have a bird's-eye view of the virtual scene and their avatar. In *first-person view*, they see the virtual scene "through the eyes" of their avatar.

1.1 When to (Not) Use VR

An important question for a researcher is to assess when VR is a suitable research tool, and when not. Studying how humans interact with each other in crowds or groups in the real world, especially in emergency scenarios, presents itself with several challenges. Each research method on crowd dynamics, e.g., questionnaire studies, laboratory experiments, field studies, and observations of real events, have their own strengths and weaknesses [16, 17]. In short, VR is a powerful tool that enables the experimental study of cause and effect in crowd dynamics (e.g., what factors cause individuals in a crowd to navigate one way or another). However, at least to date, it cannot be used to extract absolute values of locomotion parameters such as walking speed.

When trying to understand crowd dynamics, researchers often rely on data from surveillance footage of crowd events or laboratory studies of pedestrian groups. There are three challenges to this approach. First, while these data provide insights into global phenomena of crowd behavior (e.g., the patterns of movement that can be described at the crowd level), it is much harder to understand interpersonal interactions within a crowd, even though they ultimately shape global patterns of

motion (also see text box on the modeling cycle of crowd behavior) [21]. Most computational crowd modeling approaches treat crowds as a homogeneous mass in which all members of a crowd follow an identical set of rules, disregarding individual differences (e.g., in movement speed, response times, or mobility impairments), group behavior, and personal relations among individuals [1]. Second, studies with experimental control, i.e., experimental manipulations with control conditions or control groups, are rare, and thus it is difficult to identify cause and effect relations, which are crucial to a method's internal validity. In turn, a lack of internal validity makes it difficult to generalize findings from a specific scenario to other settings or populations (external validity; see text box on validity). Third, especially when studying potentially dangerous aspects of crowd behavior, researchers often need to trade the realism of a scenario for the safety of participants. For example, imagine a scenario in which you want to study crowd evacuation in a fire emergency. It is next to impossible to do this in a controlled laboratory experiment without risking the safety of participants.

Realistic computer-generated environments are thought to overcome some of these challenges by providing experimental control while simulating complex, visually realistic, and often hazardous scenarios in the safe environment of a laboratory. Immersing participants into a virtual crowd enables the researcher to test specific hypotheses about how individuals are influenced by a crowd and in turn shape global patterns of motion [21]. VR allows systematic manipulation of various aspects of crowd behavior while controlling for other factors. Complex questions, such as how crowd density and walking speed are related to, for example, the probability that an individual will misstep and fall, are thus accessible to experimental research with minimal risk to participants.

In addition to overcoming methodological challenges, VR opens new opportunities for crowd research. For instance, VR allows measuring additional variables, such as physiological responses during experiments. Interfaces with devices that record heart rate, skin conductance, or brain activity can be used to precisely synchronize crowd events with physiological and neural responses. In addition, participants can be tested repeatedly in identical scenarios, which allow studying both learning effects and easy replication of experimental setups. Another strength of VR is that it allows researchers to study vulnerable populations, either by simulating visual or mobility impairments, for example, or by testing participants who rely on mobility aids such as white canes or wheelchairs in a safe and controlled environment.

Validity

A method can be considered valid if it faithfully captures the relationships it was designed to measure. How credible and believable are VR experiments on crowd dynamics? Validity can be broken down into three subcategories.

(continued)

Internal validity refers to the degree a research tool can investigate cause and effect. Experimental stimulus control and manipulation are key aspects to internal validity [18].
External validity refers to the degree results of a study can be generalized beyond the scope of an immediate setting [19]. For example, can findings from a study on crowd behavior in tall buildings be generalized to other environments?
Ecological validity describes if behavior measured in an experiment holds true in the real world [20]. For example, does behavior observed in VR correspond to behavior in the real world?

2 VR Studies of Crowd Behavior

In this section we review a selection of empirical work that uses VR to study crowd dynamics. First, we give a brief overview of studies that compare pedestrian behavior in virtual and real environments to provide the reader with an understanding of the validity and limitations of VR for the purpose of crowd research. Next, we present research on basic aspects of crowd dynamics that has been carried out in VR. VR has been used to gain insights in complex interaction between members of a crowd, from social identity to how people move as a crowd in a coordinated fashion. Finally, we review VR studies that look specifically at human behavior in emergency situations and evacuation scenarios.

2.1 Comparing Virtual and Real Behavior

Is crowd behavior in VR comparable to crowd behavior in the real world? This is a key question, because a research tool is only valid if it produces results that generalize to real-world situations. The degree to which a method represents the real-world scenario that is being studied is often referred to as ecological validity (see text box on validity). Several studies have addressed questions around the ecological validity of VR experiments, and we present a selection further below.

There are some general differences between human behavior in virtual and physical environments that *can* limit the ecological validity of VR. First, in VR the virtual world is perceived through a display, and although users typically perform comparably in real world and matched stereoscopic virtual environments, some studies have found systematic biases in reported size and distance of objects in VR [22, 23]. However, distance biases appear to be reduced after a short period of active walking in the virtual environment [24, 25]. Second, navigation in VR is often implemented via interaction interfaces, such as a mouse, joystick, or game pad (see

below). How navigation and interaction with social and architectural environment are implemented influences the action opportunities of a user. Although there are many further differences between experiences and behavior in real and virtual environments, questions of self-propelled locomotion (i.e., walking) and social interactions between neighbors in a crowd seem particularly relevant in the context of this chapter.

2.1.1 Walking in VR

Some VR systems that fully immerse users can support physical self-propelled locomotion – that is, users can physically walk around inside the virtual environments. The most common and affordable of these systems use HMDs, so we focus on them here. Users wearing HMDs have been found to walk more slowly, take shorter stride lengths, and adopt a slightly different body posture compared to walking in a real environment [26–28]. In many VR systems, however, users navigate through the virtual environment with the help of an interaction interface such as a game pad. With such interfaces, users typically make sharper turns compared to walking in real life, and trajectories show no gait induced oscillations [29]. Interestingly, the overall shape of trajectories is qualitatively similar whether the user is walking, steering with a joystick, or steering by leaning in the desired direction [30]. In general, the values of locomotion parameters estimated from VR studies can't claim metric accuracy; for example, the raw walking speed values from VR studies should be interpreted with caution. However, relative effects between different conditions in VR are still meaningful.

2.1.2 Social Interactions in VR

Interactions between individuals in VR have been studied in a range of fields, exploring the opportunities and challenges of humans interacting with virtual representations of other humans (so-called avatars) or with computer-controlled virtual humans ("agents"). A particular challenge is studying social dynamics between individuals, because it is extremely difficult to control subtle social signals in experiments. VR allows experimenters to control many aspects of social interactions and to reduce the social information being exchanged to a manageable minimum. Luckily, humans are surprisingly good at identifying humanlike behavior, even in extremely minimalistic virtual environments [31, 32]. In fact, research on social interaction in VR has shown that people react toward computer-controlled virtual humans similarly to real people in social interactions, especially when the virtual humans are responsive [33, 34]. Simulating realistic social behavior such as collision avoidance in a crowd or simple social signals such as hand gestures and eye contact increases the sense of presence that users may experience in VR [35]. In recent years, VR has been used to study complex dyadic interactions, such as social mimicry (i.e., how we mimic each other's postures, facial expressions, gestures, and

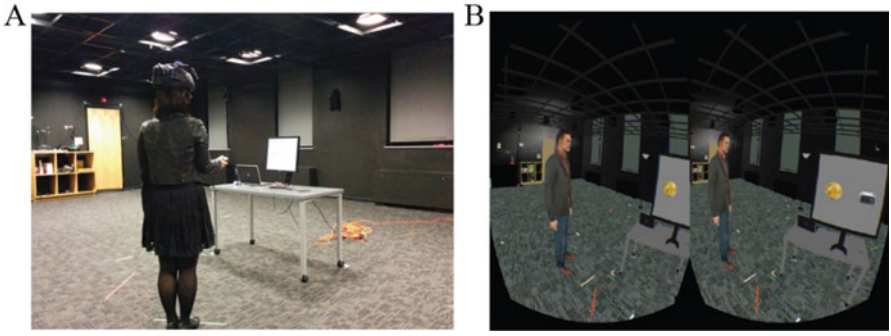

Fig. 1 (**a**) A participant in the real environment performing the bogus task in the control condition. The fire alarm over the entrance door in the background was activated during the experiment. (**b**) Stereo screenshot of the participant's view of the virtual environment during the fire alarm in the passive condition. (Images retrieved and adjusted with permission from [42])

other social signals), social cohesion (how close we feel to others), helping behavior during evacuation, and trust [36–40].

Studies of social dynamics and spatial behavior in matched real and virtual settings, however, are still relatively scarce. To investigate the role of social influence in emergency situations, we created a variation of the famous "smoke-filled room" experiment by Darley and Latané [41], who first reported on the so-called bystander effect: People are less likely to help in an emergency when others in the scene remain passive. In our study [42], participants were performing a bogus task when a fire alarm sounded. In the control condition, participants were alone at the time, whereas two other groups of participants worked on the bogus task with a confederate next to them. When the fire alarm went off, the confederate either ignored the fire alarm and continued to work on the task (passive bystander condition) or left the room through an emergency exit (active bystander condition). Importantly, half of the participants were tested in a real-world setting and the other half in a matched virtual environment with a virtual confederate (Fig. 1). In both cases, participants with an active bystander were more likely to evacuate, and those with a passive bystander less likely to evacuate, than the control group, consistent with the bystander effect. Importantly, this pattern was observed in both the real and virtual environments, although the overall response to the virtual alarm was reduced.

2.1.3 Comparing Crowd Dynamics in Real and Virtual Environments

Studies that systematically compare crowd dynamics in virtual and real environments are still relatively scarce. However, results from several recent studies found that VR experiments yield meaningful insights for real-world crowd dynamics. One study focused on dynamic interactions between individuals and found comparable

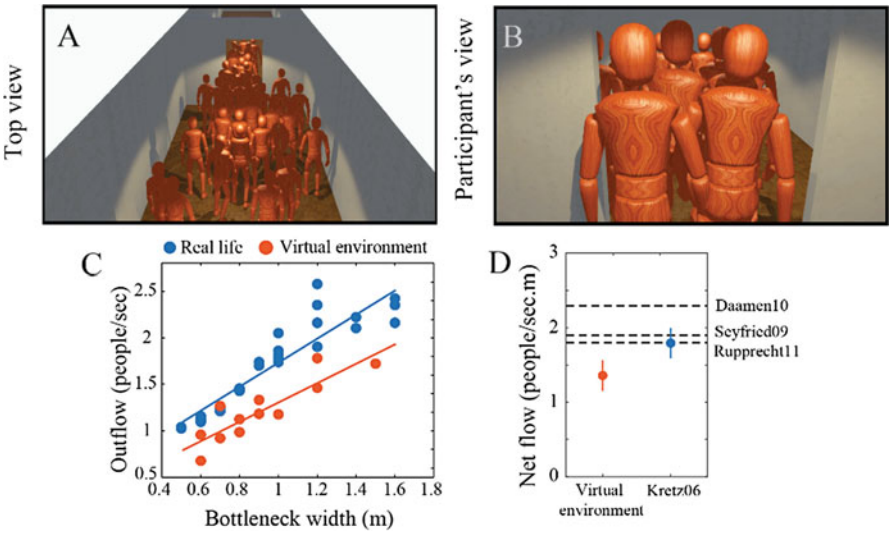

Fig. 2 Example of VR crowd evacuation study. (**a**) Third-person view of a virtual crowd moving through a bottleneck. (**b**) First-person view of a participant of the same scenario. Comparison of VR and real-world data: (**c**) outflow as a function of aperture width; (**d**) virtual crowd flow in comparison to reference studies (see original publication for further details; image retrieved and adjusted with permission; [43])

behavioral patterns in virtual and real crowds. Using a desktop VR setup, several participants were immersed in the same virtual environment at the same time and could interact with the avatars of the other participants (Fig. 2a, b). The authors found that participants showed similar avoidance maneuvers when faced with oncoming traffic (e.g., steer to the right) compared to data obtained from real-world experiments. Similarly, when groups of participants moved through a bottleneck, outflow speed increased monotonically with aperture width in both the virtual and real world (Fig. 2c); however, overall outflow of participants was lower in VR compared to a number of reference studies (Fig. 2d) [43].

Another series of experiments compared navigation trajectories within a crowd using different input modalities to real-world reference trajectories [44]. In particular, the authors tested whether participants would accurately estimate collision risk, anticipate, and engage in collision avoidance with virtual agents in similar ways as in the real world. The results showed that VR experiments can produce reliable trajectories that are comparable to real-world data. However, there were some quantifiable differences: First, there was a systematic bias in participants' collision estimates (VR collisions were estimated to be later than real ones), and participants slightly overcompensated their trajectories to avoid collisions in VR.

The Modeling Cycle
Sumpter, Mann, and Perna (2012) provide a comprehensive outline for the variety of approaches one might take toward modeling collective behavior (including crowd behavior) [45]. The differences can be broken down into the *level of description* and the *modeling approach*.

Level of Description
Local: Here researchers are primarily concerned with the "microscopic" interactions between individuals within the collective and their relationship with their environment. For an experimental example involving locust swarms, see [4].
Global: Here scientists are completely unconcerned with the behavior of the individual components of the system but focus on the "macroscopic" behavior of ensembles or populations of individuals. At this macroscale, researchers describe the states and phase transitions of the system as a whole and the patterns that emerge.
Local-to-Global: This micro-to-macro perspective starts by characterizing the behaviors and "rules of engagement" at a local level and seeks to explain the global patterns that emerge based on these local behaviors. A prominent example of this is the *self-propelled particle model* [10, 15].
Global-to-Local: Researchers who take a macro-to-micro perspective begin with observations at the global level and then infer hypothetical rules that could give rise to the observed global patterns. Rather than explore the entire parameter space of individual behaviors, this method seeks to limit the parameter space.

Modeling Approach
Theory Driven: The self-propelled particle model is an example of theory-driven research, where the local rules are based on theories about the kind of behavior that gives rise to the global pattern [10].
Data Driven: Rather than hypothesizing the nature of an individual's behavior, a data-driven approach derives the rules of engagement by experimental means. The behavioral dynamics perspective is an example of a data-driven approach [46].
Model Selection: This approach is taken by many researchers, who are interested in testing how well their model, and other models, can account for real-world data. A model-selection approach is essential to compare alternative models, providing crucial evidence about the adequacy of competing explanations of real behavior.

Note that in all the comparison studies described here, the behavioral data in VR and real-world scenarios are not identical, and the researchers observed systematic quantifiable differences between locomotion parameters in virtual and real scenarios. This should not be surprising given the differences between a virtual and real scenario, ranging from the appearance of the environment, how navigation and interaction are implemented, to the fact that participants in VR are usually aware that the virtual scenario is necessarily a simulation controlled by the experimenter. The key takeaway here is not absolute but relative ecological validity: Results in VR studies are not wildly different from those in real laboratory studies, and similar effects are typically observed in both cases. This indicates that VR is a useful tool for the study of crowd dynamics, but users, especially those developing crowd simulations for real-world applications, need to be careful when implementing VR results in their models.

2.2 Crowd Dynamics in VR

To understand why we use VR to study crowd dynamics, we begin with some background on how global behavior might emerge from the dynamic interaction between a pedestrian and their environment. A theoretical framework that is designed to analyze and model these interactions is *behavioral dynamics* [46].

The behavioral dynamics approach to the control of behavior comes from a history of the coevolution of dynamical systems and theories of action in the late twentieth century [47–49]. By the early 1980s, dynamical systems theory had found its way into explanations of behavior, by using systems of differential equations to model and replicate the dynamic patterns exhibited in motor coordination. The paradigmatic examples of this were finger-wagging experiments, in which the author showed that with the right differential equations, one could describe the simple but elegant coordinative patterns of a person rhythmically oscillating their index fingers at the same time [50]. Warren (2006) saw the potential of this approach for explaining more complex behaviors in which an individual dynamically interacts with a changing environment [46].

The behavioral dynamics approach aims to account for the organization of complex behavior without appealing to a central controller or internal representations of the behavior (Fig. 3). This perspective rejects the assumption, common in psychology and cognitive science, that behavior is generated by a central controller which deploys action plans to accomplish everyday tasks [46]. The behavioral dynamics approach naturally extends to both intra- and interpersonal behaviors such as collective crowd motion by modeling each individual interacting with their respective environment.

There are four key components of the behavioral dynamics perspective. First, an individual possesses a physical body that is embedded in a physical environment, both of which provide essential constraints on behavior. Second, perceptual information about the environment and the individual-environment relationship

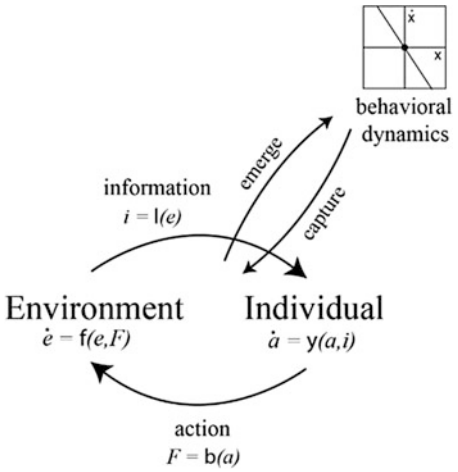

Fig. 3 Depiction of the behavioral dynamics perspective [46]. The individual interacts with the information from the environment and is cyclically connected to the environment by acting upon it. The behavioral dynamics exist by nature of the interaction between the individual and the environment, and they capture, i.e., describe, the interactions. (Image retrieved and adjusted with permission from [46])

enables the control of behavior. Third, control involves mapping the relevant information variables into the relevant control variables, and this mapping depends on the task at hand. And fourth, the resulting behavior is self-organized, emerging from interactions in the individual-environment system under the relevant physical, informational, and task constraints [46].

To model behavior, this framework proposes that a pattern of behavior can be described by a system of differential equations. The individual and environment are treated as a pair of coupled dynamical systems, with informational and mechanical couplings. The individual's actions exert forces that change the state of the environment according to physical laws, which in turn generate information (spatiotemporal patterns in optic, acoustic, haptic, olfactory, etc. fields) according to what Gibson (1979) called ecological laws [51]. Reciprocally, information is detected by the individual and serves to modulate the state of the action system according to laws of control, which are specific to the task at hand. This cyclical interaction between individual and environment generates a trajectory through the "state space" of behavioral variables – the behavioral dynamics. This is where the system of differential equations comes in, for it describes a vector field with attractor states that correspond to task goals and repellers that correspond to avoided states. Successful emergent behavior at this level serves to lock in control laws and tune their parameters at the lower level. Control laws, which map information variables to control variables, can thus be learned and used for the "online" control of behavior, without assuming a centralized controller or a priori representation (see Fig. 3 for an illustration of the behavioral dynamics framework) [46].

Recently, the behavioral dynamics framework has been applied to modeling collective crowd behavior [21]. Each pedestrian in a crowd is treated as an individual interacting with a dynamic "environment" that includes other moving pedestrians. The crux of the problem lies in deciphering the local "rules of engagement," i.e., the lawlike relationship that exists between individuals of a crowd, that give rise

to the global patterns of crowd motion. Research in virtual reality has been used to derive these local rules (or, more precisely, control laws) experimentally [48, 52]. Within Sumpter, Mann, and Perna's (2012) framework, this can be considered a *local-to-global*, *data-driven* modeling approach (see textbox; [45]). The success of the behavioral dynamics approach rests on its ability to model self-organized collective behavior, where local interactions between individuals combine to yield emergent coordinative patterns, such as coherent motion and lane formation.

2.2.1 Behavioral Dynamics in VR

Warren and colleagues employ the behavioral dynamics approach using VR, designing experiments to find the rules that give rise to collective motion in humans (Fig. 4) [53, 54]. One of the first steps in finding the "rules of engagement" is to figure out what information an individual is using from their environment to control their behavior. A primary study that set the paradigm was designed to investigate the nature of coordination in crowds based on the visual information about an agent's movement [52, 53, 55].

Three hypotheses were tested in a recent series of studies [52]. All three experiments were conducted with participants in an untethered HMD VR system, in which they could walk freely around a 10 × 12m tracking space. In VR, participants walked through a simple flat environment, and a crowd of virtual agents was generated in front of them. On control trials, the crowd of agents would walk straight ahead, at a constant speed with a constant direction of travel (or heading), and the

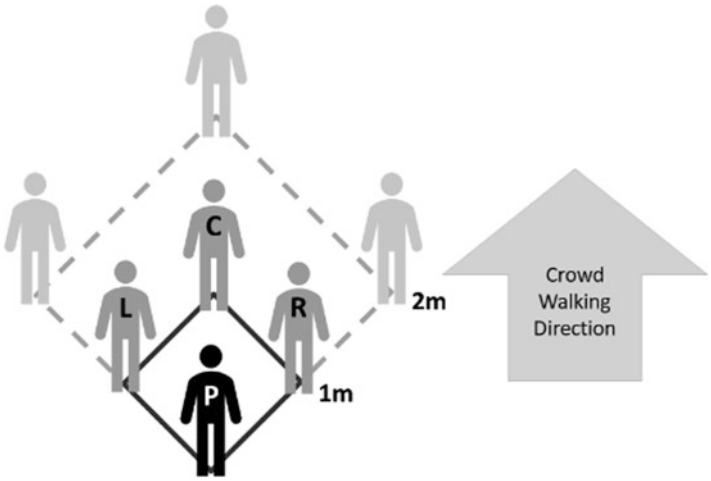

Fig. 4 Diagram of the Rio and Warren 2014 experimental paradigm of investigating pedestrian interactions in virtual crowds [53]. Several agents are placed in front of the participant in VR, and then programed to walk in specific ways. The path that the crowd takes and the starting conditions of the experiment are dependent on the research question at hand

participant would be told to "walk with the crowd." In test trials, either 0, 3, 6, 9, or 12 agents in the crowd were "manipulated" to either change their speed or to turn 10° to the left or the right. The first experiment addressed the hypothesis of *superposition* that the influence of multiple neighbors is combined linearly. This was achieved by manipulating subsets of agents in a virtual crowd and observing how the participant responded to increasing number of subset size. The second investigated the role of *distance*, expecting that the influence of members of the crowd who are further away would be less than the influence of members who are close by. This experiment manipulated the distance of half the crowd, making the crowd average distance either altogether closer or further. The third experiment investigated the role of *eccentricity*, meaning that those members of the crowd who are in front of the participant should influence them the most, and those who are at the sides should influence the participant to a lesser extent, producing an elliptical shape of influence. This was tested by manipulating agents in particular wedges in front of the participant, where the most central wedge would be expected to illicit the largest response.

The first two hypotheses were supported, finding evidence that the influence of a crowd is linearly combined and that the influence decreases with distance. There was no observed effect of eccentricity, however, suggesting that members of a crowd influence a participant if they are within the field of view. Naturally, there are visual variables such as occlusion and optical expansion/contraction that emerge by the physical nature of the crowds. Visual variables such as the effects of expansion and contraction can theoretically be accounted for by nature of the distance parameter that was discovered through the experiments, and more experiments are underway to specifically investigate the role of such variables and account for them in the model.

The authors further investigated how visual coupling in crowds can be used to model behavior of real crowd "swarms" [52]. To test this, participants were split into two separate groups in two different data collection sessions. The participants were instructed to walk about the room on a random path at a normal speed, while staying together as a group, and to do this until they were told to stop. Their movements were tracked using a motion capture camera system, and their trajectories were then analyzed to see how the groups moved together through space. The analyzed behavior was then fit to a model, showing that the rules abstracted from the behavioral dynamics perspective (of visual coordination) successfully simulate real human behaviors [52]. The main finding of the study can be understood by looking at the heat map of mean absolute heading difference as a function of distance between individuals (Fig. 5). The heat map shows that over the course of the given trial, participants had more similar headings to those who were near to them and increasingly different headings compared to those who were further away [52]. This result reinforces the studies done in VR, showing that individuals coordinate with those who are closest to them and that the coordination strength decreases as individuals get further away.

Warren and colleagues are currently investigating more "rules of engagement" in VR. These experiments isolate variables that could contribute toward how individuals interact with those around them. For example, experiments have been

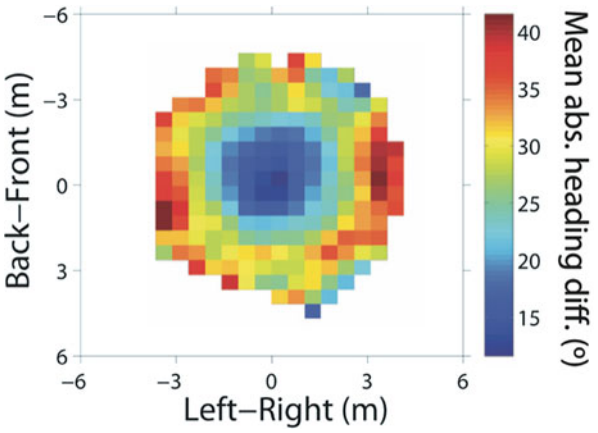

Fig. 5 The heat map represents the spatial heading relationship (where heading is defined as the direction of travel) between each individual in a human "swarm" and every other individual in the swarm with respect to their distance at any moment during the trials. The relationship is then averaged to show that individuals are closely aligned with those most immediately near them and that the alignment similarity falls off with distance. (Reprinted from [52])

done to determine if the density of a crowd modulates a participant's interactions with the agents around them. The results support claims that collective behavior in humans can be better governed by density-dependent models, rather than density-independent models [54]. As more rules are experimentally derived, more information can be accounted for in the model allowing for a local-to-global understanding of how human collective motion is self-organized.

2.3 VR Studies of Crowd Evacuation Behavior

The following section highlights several studies in which VR was used to investigate crowd dynamics in the context of emergency evacuation. The common motivation to use VR in most of the studies was to be able to control precisely what participants would see and how that would affect their behavior. The reader should note that the technology of the VR systems varied significantly across studies and consequently so did the experience of the participants.

An early crowd evacuation study performed in a CAVE system investigated how the availability of exits and the number of agents affected evacuation success and evacuation time in a simulated emergency in an underground transportation system. Although the behavioral results were unclear, this study was one of the first to combine the techniques of crowd simulation with behavioral input from human participants in VR [56].

More recently, Bode and colleagues studied how people choose exits in a variety of crowd evacuation scenarios [9, 39, 57, 58]. One study compared effects of static information (signage), dynamic information (crowd behavior), and verbal instructions, as well as a combination of these factors on participants' exit choice. Participants viewed the scenario from a top-down view of a rectangular enclosure with two exits, and their task was to choose one of the exits. The authors found main effects of static information but not the other two factors. However, when the factors were tested in combination (e.g., when signage and crowd movement contradicted each other or pointed to the same exit), the authors found several interactions, suggesting that exit choice, in particular during evacuation in crowds, is subject to a complex set of influences [9].

Another study by this group in a similar virtual environment compared how knowledge of exit width and evacuation route length, together with dynamic aspects of crowd evacuation (e.g., change in visible congestion at an exit) affected route choice [58]. Participants again controlled an avatar in a top-down virtual environment and had to choose between two exits during a simulated crowd evacuation. The authors manipulated the length of the two egress routes, width of the exits, as well as additional time pressure. The results revealed that participants generally preferred taking a wider exit compared to a narrower exit. However, in a more fine-grained analysis, the authors found that dynamic information detected from the movements of the crowd (e.g., the number of agents choosing a particular exit, or their movement speed) better accounted for their observations than the static information alone. The results suggested that crowd dynamics play a crucial role in exit choice during evacuations. Interestingly, the authors also found that adding time pressure as a proxy for simulated stress led to more rigid decision-making; participants were less likely to adjust their initial exit choice even, when information was available regarding the speed at which the simulated crowd moved through the two doors (Fig. 6).

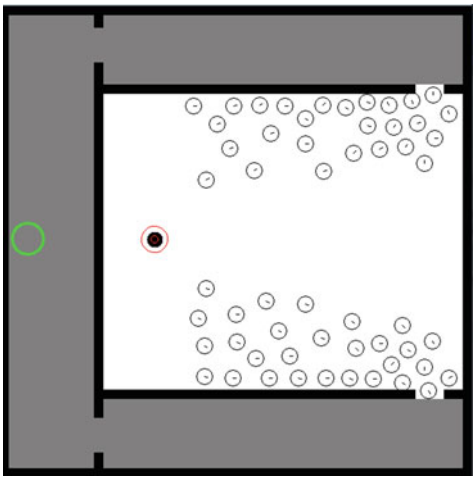

Fig. 6 Screenshot from Bode et al. [57]. Participants control an avatar (black solid dot with red circle) and are tasked to leave the room as quickly as possible together with a crowd of virtual agents (unfilled circles). They need to choose between two possible exits (top or bottom left) and reach the target area (green circle). (Reprinted with permission from [57])

In general, the studies by Bode et al. used a minimalistic virtual environment, and the reader might rightfully ask how much can be learned about real-world evacuation behavior. The authors explicitly address this concern and point out that their claim is not that people walk exactly like avatars controlled by mouse clicks. However, given that virtual behavior is often comparable to real-world behavior and the degree of experimental control in their studies, the results can lead us to hypotheses that merit further study in larger and more realistic settings.

To investigate the combined effects of observing the behavior of others and exit familiarity, we tested participants using an untethered HMD system that allowed participants to freely walk within a space of 12 by 12 meters (Fig. 1a). Participants entered and then explored a square room that simulated an art gallery, when a fire alarm was triggered. They could then decide between two equidistant emergency exits, one using the same door they used for entering the room and another, unknown exit. Participants were more likely to exit through the more familiar emergency exit. However, in experimental conditions, in which participants saw virtual agents egressing either through the familiar or unfamiliar exit, participants tended to follow the agents. The effect of the agents on exit choice was stronger, when participants saw two instead of one agent exiting, suggesting, social influence in evacuation situation scales with the number of observed people [59].

As mentioned previously (Fig. 2), another recent study tested egress behavior in a virtual crowd under time pressure, with not just one but 36 participants interacting in a shared desktop VR environment with first-person views [43]. Participants were asked to evacuate a room through a maze of virtual corridors. When under time pressure, they kept shorter interpersonal distance between their avatars and collided with each other more frequently, compared to a control condition without time pressure. This increase in crowd density was most commonly observed at corridor junctions, near exits, and at dead ends in the maze (Fig. 7). Interestingly, participants were more likely to follow the majority of the crowd with an increase in density, suggesting that the strength of social influence within a crowd increases as a function of crowd density, the number of people visible, or both.

Another indication that interactions between crowd dynamics and spatial navigation during fire evacuation are complex was documented in a recent study [60]. This study made use of another avenue to data afforded by VR: online surveys. In this study, data from over 1500 participants was collected in an online survey, providing a rich database. Participants watched videos of six different scenarios of a room with two exits and some smoke from a first-person view and saw a crowd of virtual humans egressing through the exits (Fig. 8). Interestingly, most of them indicated that they would follow the crowd majority toward an exit but also noted that an exit became less attractive the more virtual humans were observed near the exit.

In a recent experiment, the authors of this chapter combined the approaches presented in the previous studies. Participants wore an untethered HMD that allowed them to actively walk in the virtual environment and were immersed in a virtual crowd within a room that contained two exits. A fire alarm sounded, the virtual agents moved toward the exits, and the participant's task was to evacuate through one of the two exits. This experiment manipulated the size of the crowd, which

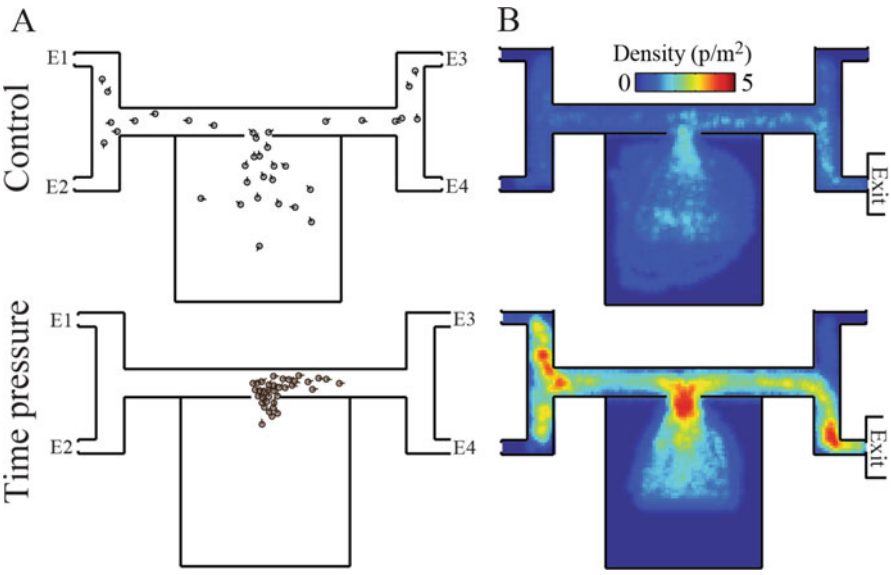

Fig. 7 Exemplary results from [43]. (**A**) Snapshot of participants navigating toward the exits (E1 to E4) in a virtual maze in a control condition (top) and under simulated time pressure (bottom). (**B**) Crowd density hotspots distributed across the virtual maze (see original publication for further details; reprinted with permission from [43])

Fig. 8 Screenshot of first-person participant view of the simulated emergency scenario from [60] (see original publication for further details; reprinted with permission)

consisted of 10 or 20 agents, and the proportion of agents egressing through one exit, which varied from 50% to 100% of the crowd, in 10% increments. This manipulation allowed us to disentangle the influence of the absolute and relative number of agents going to one exit and the effect of crowding near one exit. The results showed that for both crowd sizes, participants chose an egress more or less randomly when no clear majority of the crowd opted for one of the exits. In the small crowd, as a greater proportion of agents went to one exit, participants increasingly followed the majority, whereas in the larger crowd, participants initially avoided the more crowded exit and followed the majority only when all agents went to one exit. These data and the results of the previously discussed studies underline that evacuation behavior in a crowd depends in complex ways on the dynamics of the situation.

3 The Road Ahead

In recent years, researchers have pushed the boundaries of the abilities of computational models of crowd dynamics, ranging from biomechanics [61], physiological/metabolic processes [62, 63], to cognitive aspects [64, 65]. Yet, Haghani and Sarvi (2018) observed an imbalance in the crowd dynamics knowledge base [17]; while openly observable data is already quite rich and researchers have begun to tackle more and more complex questions in recent years, they found that research on the interplay between latent variables such as psychological (e.g., perceived risk, emotional states, or personality traits) and physiological states that influence, for example, motion trajectories, time, and decision-making during crowd evacuation scenarios has only scratched the surface [17]. Consequently, perceptual, cognitive, and other psychological processes that produce observable behavior are typically not included, and, not surprisingly, most crowd evacuation models only represent human decision-making in relatively simplistic manners and often ignore aspects such as cognitive bias in evacuation decision-making [66, 67]. VR has the potential to provide detailed insights into aspects of crowd dynamics that are otherwise hard to observe. For example, in the related field of moral decision-making, VR has been used to study eye movements and physiological responses in moral dilemmas [68, 69].

What does the future hold for VR as a research tool in crowd dynamics? Although increasing computing power and graphics development will allow immersing participants into ever more realistic simulations, there are still some significant challenges ahead. For one, virtual environments need to be immersive enough so that participants experience a sufficient degree of presence. A recent study found that more lifelike behaviors displayed by agents in a virtual crowd as well as higher levels of interactivity increased participants' self-reported presence in the virtual environment. In addition, adding realistic social responses to the behavioral repertoire of agents (e.g., avoiding collisions with participants or greeting) prompted participants to display similar behaviors [35].

Another important step ahead seems to be the integration of immersive VR tools and computational models of crowd evacuation that react dynamically and in real time to user behavior. Currently, these tools are not widely used for research, but they could contribute to closing the gap between experimental data from individual participants and global models of crowd dynamics. For instance, researchers could test how a simulated dynamic crowd influences an individual in a variety of conditions (e.g., different levels of crowd density or time pressure). Ultimately this approach would allow to link the behavior of members in a crowd to global patterns of motion.

References

1. A. Templeton, J. Drury, and A. Philippides, "From Mindless Masses to Small Groups: Conceptualizing Collective Behavior in Crowd Modeling," *Rev Gen Psychol,* vol. 19, pp. 215–229, Sep 2015.
2. J. Steuer, "Defining Virtual Reality - Dimensions Determining Telepresence," *Journal of Communication,* vol. 42, pp. 73–93, Fal 1992.
3. M. Slater, B. Spanlang, and D. Corominas, "Simulating Virtual Environments within Virtual Environments as the Basis for a Psychophysics of Presence," *Acm Transactions on Graphics,* vol. 29, p. 92, Jul 2010.
4. S. Bazazi, J. Buhl, J. J. Hale, M. L. Anstey, G. A. Sword, S. J. Simpson*, et al.*, "Collective motion and cannibalism in locust migratory bands," *Curr Biol,* vol. 18, pp. 735–739, May 20 2008.
5. E. Ronchi, A. Corbetta, E. Galea, M. Kinateder, E. D. Kuligowski, D. McGrath*, et al.*, "New approaches to evacuation modelling," in *Symposium of the International Association for Fire Safety Science*, Lund, Sweden, 2017, pp. 1–78.
6. W. Barfield and E. Danas, "Comments on the use of olfactory displays for virtual environments," *Presence: Teleoperators and Virtual Environments,* vol. 5, pp. 109–121, 1996.
7. E. Richard, A. Tijou, P. Richard, and J.-L. Ferrier, "Multi-modal virtual environments for education with haptic and olfactory feedback," *Virtual Reality,* vol. 10, pp. 207–225, 2006.
8. F. Hülsmann, N. Mattar, J. Fröhlich, and I. Wachsmuth, "Wind and Warmth in Virtual Reality–Requirements and Chances," in *Proceedings of the Workshop Virtuelle & Erweiterte Realität 2013*, 2013.
9. N. W. Bode, A. U. Kemloh Wagoum, and E. A. Codling, "Human responses to multiple sources of directional information in virtual crowd evacuations," *J R Soc Interface,* vol. 11, p. 20130904, Feb 6 2014.
10. A. Czirok and T. Vicsek, "Collective behavior of interacting self-propelled particles," *Physica a-Statistical Mechanics and Its Applications,* vol. 281, pp. 17–29, Jun 15 2000.
11. Y. Q. Song, J. H. Gong, Y. Li, T. J. Cui, L. Q. Fang, and W. C. Cao, "Crowd evacuation simulation for bioterrorism in micro-spatial environments based on virtual geographic environments," *Safety Science,* vol. 53, pp. 105–113, Mar 2013.
12. E. B. Hsu, Y. Li, J. D. Bayram, D. Levinson, S. Yang, and C. Monahan, "State of virtual reality based disaster preparedness and response training," *PLoS Curr,* vol. 5, Apr 24 2013.
13. R. Lovreglio, "A Review of Augmented Reality Applications for Building Evacuation," presented at the 17th International Conference on Computing in Civil and Building Engineering, Tampere, Finland, 2018.
14. R. Lovreglio, V. Gonzalez, Z. Feng, R. Amor, M. Spearpoint, J. Thomas*, et al.*, "Prototyping Virtual Reality Serious Games for Building Earthquake Preparedness: The Auckland City Hospital Case Study," *arXiv preprint arXiv:1802.09119,* 2018.

15. T. Vicsek, A. Czirok, E. Ben-Jacob, I. I. Cohen, and O. Shochet, "Novel type of phase transition in a system of self-driven particles," *Phys Rev Lett,* vol. 75, pp. 1226–1229, Aug 7 1995.
16. M. Kinateder, E. Ronchi, D. Nilsson, M. Kobes, M. Muller, P. Pauli, *et al.*, "Virtual Reality for Fire Evacuation Research," *Federated Conference on Computer Science and Information Systems, 2014,* vol. 2, pp. 313–321, 2014.
17. M. Haghani and M. Sarvi, "Crowd behaviour and motion: Empirical methods," *Transportation Research Part B-Methodological,* vol. 107, pp. 253–293, Jan 2018.
18. J. M. Loomis, J. J. Blascovich, and A. C. Beall, "Immersive virtual environment technology as a basic research tool in psychology," *Behavior Research Methods Instruments & Computers,* vol. 31, pp. 557–564, Nov 1999.
19. W. R. Shadish, T. D. Cook, and D. T. Campbell, "Experimental and quasi-experimental designs for generalized causal inference," 2002.
20. C. A. Anderson and B. J. Bushman, "External validity of "trivial" experiments: The case of laboratory aggression," *Review of General Psychology,* vol. 1, pp. 19–41, 1997.
21. W. H. Warren, "Collective motion in human crowds," *Current Directions in Psychological Science,* 2018.
22. J. K. Stefanucci, S. H. Creem-Regehr, W. B. Thompson, D. A. Lessard, and M. N. Geuss, "Evaluating the Accuracy of Size Perception on Screen-Based Displays: Displayed Objects Appear Smaller Than Real Objects," *Journal of Experimental Psychology-Applied,* vol. 21, pp. 215–223, Sep 2015.
23. C. J. Lin and B. H. Woldegiorgis, "Egocentric distance perception and performance of direct pointing in stereoscopic displays," *Appl Ergon,* vol. 64, pp. 66–74, Oct 2017.
24. B. J. Mohler, S. H. Creem-Regehr, and W. B. Thompson, "The influence of feedback on egocentric distance judgments in real and virtual environments," in *Proceedings of the 3rd symposium on Applied perception in graphics and visualization*, 2006, pp. 9–14.
25. A. R. Richardson and D. Waller, "Interaction with an immersive virtual environment corrects users' distance estimates," *Hum Factors,* vol. 49, pp. 507–17, Jun 2007.
26. B. J. Mohler, J. L. Campos, M. Weyel, and H. H. Bülthoff, "Gait parameters while walking in a head-mounted display virtual environment and the real world," in *Proceedings of Eurographics*, 2007, pp. 85–88.
27. J. H. Hollman, R. H. Brey, T. J. Bang, and K. R. Kaufman, "Does walking in a virtual environment induce unstable gait?: An examination of vertical ground reaction forces," *Gait & Posture,* vol. 26, pp. 289–294, 2007.
28. P. W. Fink, P. S. Foo, and W. H. Warren, "Obstacle Avoidance During Walking in Real and Virtual Environments," *Acm Transactions on Applied Perception,* vol. 4, p. 2, Jan 2007.
29. T. Y. Grechkin, J. M. Plumert, and J. K. Kearney, "Dynamic affordances in embodied interactive systems: the role of display and mode of locomotion," *IEEE Trans Vis Comput Graph,* vol. 20, pp. 596–605, Apr 2014.
30. G. Cirio, A. H. Olivier, M. Marchal, and J. Pettre, "Kinematic evaluation of virtual walking trajectories," *IEEE Trans Vis Comput Graph,* vol. 19, pp. 671–80, Apr 2013.
31. M. Auvray, C. Lenay, and J. Stewart, "Perceptual interactions in a minimalist virtual environment," *New Ideas in Psychology,* vol. 27, pp. 32–47, Apr 2009.
32. T. Froese, H. Iizuka, and T. Ikegami, "Embodied social interaction constitutes social cognition in pairs of humans: a minimalist virtual reality experiment," *Sci Rep,* vol. 4, p. 3672, Jan 14 2014.
33. M. Garau, M. Slater, D. P. Pertaub, and S. Razzaque, "The responses of people to virtual humans in an immersive virtual environment," *Presence-Teleoperators and Virtual Environments,* vol. 14, pp. 104–116, Feb 2005.
34. J. N. Bailenson, J. Blascovich, A. C. Beall, and J. M. Loomis, "Equilibrium theory revisited: Mutual gaze and personal space in virtual environments," *Presence-Teleoperators and Virtual Environments,* vol. 10, pp. 583–598, Dec 2001.
35. M. Kyriakou, X. N. Pan, and Y. Chrysanthou, "Interaction with virtual crowd in Immersive and semi-Immersive Virtual Reality systems," *Computer Animation and Virtual Worlds,* vol. 28, pp. e1729-n/a, Sep-Oct 2017.

36. B. Tarr, M. Slater, and E. Cohen, "Synchrony and social connection in immersive Virtual Reality," *Sci Rep,* vol. 8, p. 3693, Feb 27 2018.
37. J. Hale and A. F. D. Hamilton, "Testing the relationship between mimicry, trust and rapport in virtual reality conversations," *Scientific Reports,* vol. 6, p. 35295, Oct 14 2016.
38. J. Hale, M. E. Payne, K. M. Taylor, D. Paoletti, and C. H. A. F. De, "The virtual maze: A behavioural tool for measuring trust," *Q J Exp Psychol (Hove),* vol. 71, pp. 989–1008, Apr 2018.
39. N. W. Bode, J. Miller, R. O'Gorman, and E. A. Codling, "Increased costs reduce reciprocal helping behaviour of humans in a virtual evacuation experiment," *Sci Rep,* vol. 5, p. 15896, Nov 6 2015.
40. L. Gamberini, L. Chittaro, A. Spagnolli, and C. Carlesso, "Psychological response to an emergency in virtual reality: Effects of victim ethnicity and emergency type on helping behavior and navigation," *Computers in Human Behavior,* vol. 48, pp. 104–113, Jul 2015.
41. B. Latane and J. M. Darley, "Group inhibition of bystander intervention in emergencies," *J Pers Soc Psychol,* vol. 10, pp. 215–21, Nov 1968.
42. M. Kinateder and W. H. Warren, "Social Influence on Evacuation Behavior in Real and Virtual Environments," *Frontiers in Robotics and Ai,* vol. 3, Jul 25 2016.
43. M. Moussaid, M. Kapadia, T. Thrash, R. W. Sumner, M. Gross, D. Helbing*, et al.*, "Crowd behaviour during high-stress evacuations in an immersive virtual environment," *J R Soc Interface,* vol. 13, Sep 2016.
44. A. H. Olivier, J. Bruneau, G. Cirio, and J. Pettre, "A Virtual Reality platform to study crowd behaviors," *Conference on Pedestrian and Evacuation Dynamics 2014 (Ped 2014),* vol. 2, pp. 114–122, 2014.
45. D. J. Sumpter, R. P. Mann, and A. Perna, "The modelling cycle for collective animal behaviour," *Interface Focus,* vol. 2, pp. 764–73, Dec 6 2012.
46. W. H. Warren, "The dynamics of perception and action," *Psychol Rev,* vol. 113, pp. 358–89, Apr 2006.
47. M. T. Turvey, "Coordination," *Am Psychol,* vol. 45, pp. 938–53, Aug 1990.
48. H. Haken, "Synergetics," *Physics Bulletin,* vol. 28, p. 412, 1977.
49. J. Kelso, "Dynamic patterns: The self-organization of brain and behavior," ed: Cambridge, MA: MIT Press, 1995.
50. H. Haken, J. A. Kelso, and H. Bunz, "A theoretical model of phase transitions in human hand movements," *Biol Cybern,* vol. 51, pp. 347–56, 1985.
51. J. Gibson, "The theory of affordances The Ecological Approach to Visual Perception (pp. 127–143)," ed: Boston: Houghton Miffin, 1979.
52. K. W. Rio, G. C. Dachner, and W. H. Warren, "Local interactions underlying collective motion in human crowds," *Proceedings of the Royal Society B-Biological Sciences,* vol. 285, May 16 2018.
53. K. Rio and W. H. Warren, "The visual coupling between neighbors in real and virtual crowds," in *Conference on Pedestrian and Evacuation Dynamics 2014 (Ped 2014)*, 2014, pp. 132–140.
54. T. D. Wirth and W. H. Warren, "The visual neighborhood in human crowds: Metric vs. Topological Hypotheses," *Journal of Vision,* vol. 16, pp. 982–982, 2016.
55. K. W. Rio, "Mapping the visual coupling between neighbors in real and virtual crowds," *Brown University,* 2015.
56. A. Shendarkar, K. Vasudevan, S. Lee, and Y. J. Son, "Crowd simulation for emergency response using BDI agents based on immersive virtual reality," *Simulation Modelling Practice and Theory,* vol. 16, pp. 1415–1429, Oct 2008.
57. N. W. F. Bode and E. A. Codling, "Human exit route choice in virtual crowd evacuations," *Animal Behaviour,* vol. 86, pp. 347–358, Aug 2013.
58. N. W. Bode, A. U. Kemloh Wagoum, and E. A. Codling, "Information use by humans during dynamic route choice in virtual crowd evacuations," *R Soc Open Sci,* vol. 2, p. 140410, Jan 2015.

59. M. Kinateder, B. Comunale, and W. H. Warren, "Exit choice in an emergency evacuation scenario is influenced by exit familiarity and neighbor behavior," *Safety Science,* vol. 106, pp. 170–175, 2018.
60. R. Lovreglio, A. Fonzone, and L. Dell'Olio, "A mixed logit model for predicting exit choice during building evacuations," *Transportation Research Part a-Policy and Practice,* vol. 92, pp. 59–75, Oct 2016.
61. P. Thompson and D. McGrath, "Exploring the Biomechanics of Walking and Crowd „Flow"," presented at the Human Behaviour in Fire Symposium, Cambridge, UK, 2015.
62. M. Delin, J. Norén, E. Ronchi, K. Kuklane, A. Halder, and K. Fridolf, "Ascending stair evacuation: walking speed as a function of height," *Fire and Materials,* vol. 41, pp. 514–534, 2017.
63. K. Kuklane and A. Halder, "A model to estimate vertical speed of ascending evacuation from maximal work capacity data," *Safety Science,* vol. 89, pp. 369–378, Nov 2016.
64. M. Kinateder, E. D. Kuligowski, P. A. Reneke, and R. D. Peacock, "Risk perception in fire evacuation behavior revisited: definitions, related concepts, and empirical evidence," *Fire Sci Rev,* vol. 4, p. 1, 2015.
65. E. D. Kuligowski, S. M. Gwynne, M. J. Kinsey, and L. Hulse, "Guidance for the Model User on Representing Human Behavior in Egress Models," *Fire Technol,* vol. 53, pp. 649–672, Mar 2017.
66. M. J. Kinsey, S. M. V. Gwynne, E. D. Kuligowski, and M. Kinateder, "The Impact of Cognitive Biases On Decision-making During Fire Evacuation," *Fire Technology,* 2018.
67. M. J. Seitz, A. Templeton, J. Drury, G. Köster, and A. Philippides, "Parsimony versus reductionism: how can crowd psychology be introduced into computer simulation?," *Review of General Psychology,* vol. 21, p. 95, 2017.
68. A. Skulmowski, A. Bunge, K. Kaspar, and G. Pipa, "Forced-choice decision-making in modified trolley dilemma situations: a virtual reality and eye tracking study," *Front Behav Neurosci,* vol. 8, p. 426, 2014.
69. C. D. Navarrete, M. M. McDonald, M. L. Mott, and B. Asher, "Virtual morality: emotion and action in a simulated three-dimensional "trolley problem"," *Emotion,* vol. 12, pp. 364–70, Apr 2012.

Pedestrian Movement in Smoke: Theory, Data and Modelling Approaches

Enrico Ronchi and Daniel Nilsson

Abstract The understanding of pedestrian movement in smoke-filled environments is of significant importance in fire safety engineering applications. This chapter presents an overview of the main concepts concerning pedestrian movement in smoke, with a particular emphasis on the adverse effects that it can have on pedestrian evacuation. Several factors are discussed, including fire, pedestrian and environmental factors. Factors associated with the presence of fire relate to the impact of reduced visibility conditions, the presence of asphyxiant/irritant gases and cognitive and emotional influences are also explored. Pedestrian factors include walking speed and pedestrian movement abilities, visual acuity and physical exertion. Environmental factors include geometric complexity, the interaction with way-finding and signage systems, inclination of floor/ground or inclines (similar to stairs), stairs and surface materials. An overview of the current capabilities of pedestrian and evacuation models used in fire safety engineering applications is also presented along with recommendations for future areas of research in the domain of pedestrian movement in smoke.

1 Introduction

The study of pedestrian behaviour in smoke-filled environments is of great importance in the fire engineering context, as the fire safety design process often relies on the prediction of human behaviour during evacuation in case of emergency. This is often done using a performance-based design approach [1], which relies on the estimation of the required safe evacuation time (RSET) which is compared to the

E. Ronchi (✉)
Department of Fire Safety Engineering, Lund University, Lund, Sweden
e-mail: enrico.ronchi@brand.lth.se

D. Nilsson
Department of Civil and Natural Resources Engineering, University of Canterbury, New Zealand

L. Gibelli, N. Bellomo (eds.), *Crowd Dynamics, Volume 1*, Modeling and Simulation in Science, Engineering and Technology,
https://doi.org/10.1007/978-3-030-05129-7_3

time available for safe evacuation (ASET). The estimation of the RSET can be made using hand calculations or pedestrian evacuation models [2].

During the design of complex infrastructures, such as transportation systems (e.g. metro and train stations, road and rail tunnels, airports, etc.) or complex indoor buildings (e.g. shopping malls, industrial premises, etc.), engineering tools are adopted to investigate the fire safety conditions in given design scenarios [3]. In this context, pedestrian behavioural scenarios [4, 5] needs to be identified and studied.

In order to perform this analysis, a necessary step is the assessment of the ability of pedestrians to evacuate. While the study of pedestrian movement and crowd dynamics have been largely investigated for smoke-free environments [6, 7], a limited number of data collection efforts have been conducted to obtain information concerning the behaviour and movement of pedestrians in smoke [8]. This is in contrast with the current need of fire protection engineers, which may need to perform life safety assessments in which pedestrians may need to walk in smoke-filled environments.

The adverse effects of smoke on the pedestrian ability to reach a safe place may vary. This chapter intends to identify and categorize those effects and review the existing methodologies adopted for representing these effects in models. This is associated with a review of the existing experimental data sets available in the literature for the analysis of pedestrian movement in smoke. These may refer to both raw experimental data sets as well as empirical correlations provided by researchers which relate human behaviour outcomes and the conditions of the emergency scenarios in which they are located.

The main existing theories and data available today in the literature on pedestrian movement in smoke are provided in this chapter. This includes the consideration of several factors which may impact pedestrian movement behaviour and the subsequent evacuation performance. The factors associated with the fire scenarios are introduced and discussed, followed by a description of the pedestrian characteristics which may affect evacuation performance in smoke. Furthermore, environmental factors which affect pedestrian movement in such scenarios are reviewed and analysed.

This chapter also presents an overview of the current modelling assumptions, methodologies and approaches adopted for the representation of pedestrian movement in smoke within evacuation models. The main context of application of such models is fire safety engineering. Nevertheless, most of the information provided here can be translated to other contexts in which pedestrians are exposed to hazardous conditions, i.e. hazardous scenarios associated with a toxic gas dispersion where smoke is an issue [9, 10].

Recommendations concerning the directions of future research in this area are given. They relate to future data collection efforts that may be undertaken in order to collect relevant data for improved modelling representation of human behaviour in smoke-filled environments.

2 Theory and Data

Although movement through smoke in case of fire should be avoided, there are situations where it is difficult to completely avoid. Examples include fires in single-bore rail or road tunnels due to the lack of compartmentation. In single-bore tunnels, some pedestrians are typically forced to move in an environment with smoke in case of a fire evacuation emergency, which has been clearly shown by road tunnel fire accidents from around the world [11–13].

In cases where movement through smoke is unavoidable, the designer needs to consider how smoke influences the pedestrian movement process. Among other things, the impact of smoke on movement speed and way-finding of evacuees needs to be considered. This need has led to a set of research studies in the area of movement and way-finding in smoke. Much of this research takes its starting point in the now classical experiments by Jin [14].

Jin's pioneering research [14] consisted of experiments in a smoke-filled corridor with two types of fire smoke, namely, irritant smoke from a wood crib fire and non-irritant smoke from burning kerosene. At the end of the corridor, there was an emergency exit sign, and participants moved towards the sign, while their movement speed was measured. The experiment resulted in data on movement in irritant and non-irritant fire smoke. Jin's pioneering research shows that low visibility can reduce movement speed but also that irritant species can further reduce the speed. Hence, both visibility and irritancy are important factors to consider in fire safety design.

Since Jin's experiments, many research projects have aimed at further exploring human behaviour and movement in smoke-filled environments [15–27]. In many of these experiments, the smoke has been artificially generated non-fire smoke, although irritants have sometimes been added, e.g. acetic acid [15, 26, 28]. Some experiments have, however, used real fire smoke, specifically when the influence of fire species on cognition or emotion is the focus of the study [20, 21].

Previous research in the area of pedestrian movement in smoke seems to suggest that the problem can be divided into three distinct areas, namely, (1) fire factors, (2) pedestrian factors and (3) environmental factors. In the following subsections, each of these factors is briefly covered, and relevant research is highlighted.

2.1 Fire Factors

The fire itself can be a driving force behind poor evacuation condition, including smoke-filling, in case of fire incidents. From a design perspective, fire is typically described as an energy release rate (kW) as a function of time [29]. Among other things, the production rates of aerosols, i.e. solid and liquid particles suspended in air, and species also need to be set for a design fire. From a pedestrian movement perspective, aerosols are the main contributors to low visibility, whereas species

generated by fire can contribute to eye irritation, negative cognitive and emotional influence and loss of the ability to self-evacuate.

2.1.1 Visibility

Reduced visibility is believed to be one of the most important factors influencing the reduction of speed when moving through fire smoke. The visibility is related to the density of the smoke, which is often expressed as the proportion of light obscured by smoke, called the extinction coefficient. The extinction coefficient can be expressed according to Eq. 1 [30].

$$K_s = -\frac{1}{L} \cdot \ln \frac{I}{I_0} \tag{1}$$

where:

K_s = extinction coefficient (m^{-1})
L = distance travelled by light (m)
I/I_0 = fraction between intensity of light after travelling the distance L and initial intensity of the light (−)

Visibility is often expressed in terms of the visibility distance, which is the maximum distance at which an item can be seen through smoke. The correlation between visibility distance and extinction coefficient is often expressed according to Eq. 2 [29, 31].

$$S = \frac{A}{K_s} \tag{2}$$

where:

S = visibility distance (m)
A = 3 for light-reflecting items and 8 for light-emitting items
K_s = extinction coefficient (m^{-1})

The constant *A* assumes different values for light-reflecting and light-emitting items. However, it should be pointed out that Eq. 2 is only strictly valid for cases where no ambient light sources are present, i.e. when an item is seen thought smoke in a dark environment.

For movement in fire smoke, it is important to distinguish between the two cases of movement towards a light-reflecting item versus a light-emitting item [8]. When moving towards a light-emitting item, e.g. a lamp, the visibility distance of the item will be longer than the visibility distance of the adjacent light-reflecting walls. If people move towards the lamp, they will be able to see that there is no obstacle

between them and the lamp. In this case, the correlation for light-emitting items is most relevant for estimating visibility distance. For other cases, i.e. when people are moving towards light-reflecting items, the correlation for light-reflecting items is most relevant for estimating the visibility distance.

When pedestrians move in fire smoke, it is assumed that they will typically reduce their speed as a function of reduced visibility to avoid potentially dangerous collisions with obstacles, e.g. building features or other people, or to reduce the risk of falling. This is supported by observations of people's behaviour patterns when moving through smoke, which often involves crouching and protection of body and head with their hands or arms [15, 28, 32].

The movement speed starts to reduce once the visibility distance prohibits free movement, i.e. when people are no longer able to move at their unimpeded speed without risking injury. In theory, this means that there is an upper visibility distance where a person moving at her preferred speed will start to reduce her movement speed. At shorter visibility distances, the movement speed reduces as the visibility becomes lower, until a lower visibility distance is reached. The lower visibility distance typically corresponds to smoke logged conditions, i.e. a situation similar to movement in complete darkness. Below the lower visibility distance, people move at a constant low movement speed [30].

A compilation of the available experiments concerning movement speeds in relation to different extinction coefficients is presented in Fig. 1.

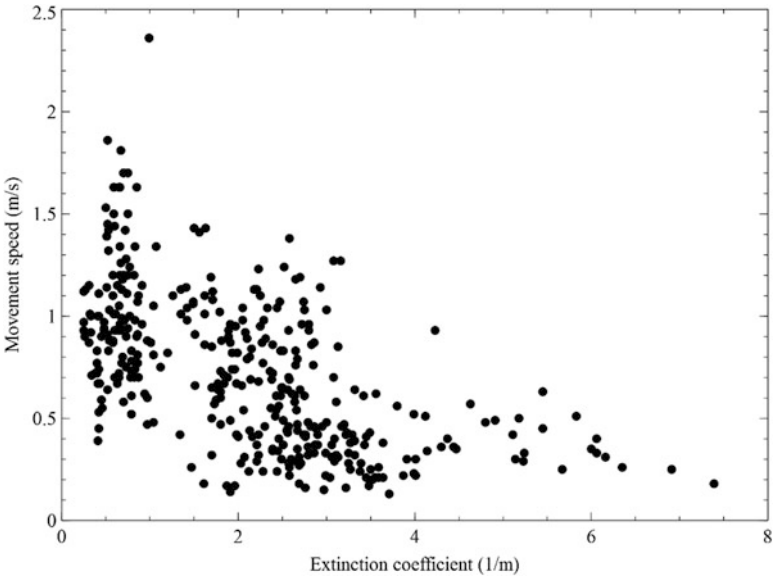

Fig. 1 Summary of aggregated experimental data sets [14–16, 28, 32, 33] concerning movement speeds vs extinction coefficient in smoke-filled environments

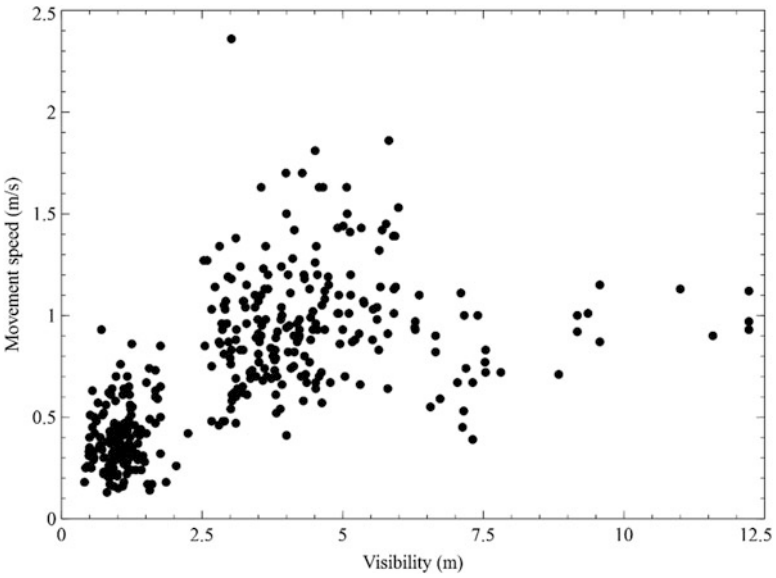

Fig. 2 Summary of aggregated experimental data sets [14–16, 28, 32, 33] concerning movement speeds vs visibility in smoke-filled environments

Considering the assumptions made to transform extinction coefficient into visibility (i.e. taking into consideration light-reflecting in comparison with light-emitting items), it is possible to present experimental data as in Fig. 2 [8].

2.1.2 Irritancy

Species from fires are known to cause eye irritation, which makes it difficult to see and hence may reduce the movement speed of pedestrians. Although selected research has focused on real irritant fire smoke, e.g. smoke from wood fires [14, 22, 34], guidance on how to consider the effect of irritancy on movement speed in smoke is scarce. However, an empirical correlation for predicting the combined influence of irritants on walking speed in smoke has been proposed in the literature [35] (see Eq. 3).

$$R = \frac{\left(e^{-\left(\frac{1000x}{b}\right)^2}\right) + (-0.2x + 0.2)}{1.2} \tag{3}$$

where:

R = the fractional reduction of movement speed
$b = 160$
x = fractional effective concentration (FEC) [35], which includes HCl, HBr, HF, SO_2, NO_2, acrolein and formaldehyde (called FIC in [35])

2.1.3 Cognitive and Emotional Influences

Although it has been shown that fire smoke does influence people both cognitively and emotionally [20, 21], there is currently a lack of guidance on how to incorporate this influence in design. The reason for this is that many past experiments have examined aspects that are difficult to generalize to the situation of movement and decision-making in smoke-filled environments. One example is an experiment that examined how people moving through a corridor filled with smoke from a burning wood fire were able to answer a series of questions [14]. Another example is an experiment where participants played a precision game, similar to the classical board game called operation, while being exposed to worsening smoke conditions from a burning wood fire [21]. Although both these experiments clearly showed that people are both emotionally and cognitively influenced by fire smoke, they failed to explore how this influence can be extrapolated to extended periods of movement through smoke.

2.1.4 Tenability

Although products from fire, e.g. soot obscuring vision or toxic/irritant species, may initially only influence movement speeds and cognitive functions, an increased exposure may eventually render the pedestrians incapable of self-evacuation. As most structures and buildings today rely on self-evacuation, pedestrians are typically considered lost from a design perspective if they are incapable of evacuating on their own. The point at which the ability to self-evacuate is lost is usually called incapacitation [35, 36].

The most common approach for estimating incapacitation in the area of fire safety is described in an ISO standard [36]. This standard takes into account incapacitation due to (1) radiant and convected heat, (2) asphyxiant gases, (3) sensory/upper respiratory irritants and (4) visual obscuration due to smoke. Perhaps the most important and prominent for movement through smoke are the asphyxiant gases and sensory/upper respiratory irritants.

In the standard [36], the two asphyxiant gases that are given the most attention are carbon monoxide (CO) and hydrogen cyanide (HCN). These two species accumulate in the body, i.e. follow a dose concept, and prevent the uptake or use of oxygen. Incapacitation is expressed in terms of the Fractional Effective Dose (FED), which is expressed as an equation taking into account the combined dose of CO and HCN. This equation can be modified to also take account of increased uptake due to increased breathing rate at high carbon dioxide levels. The way the FED equation is expressed in the standard [36], FED equals 1.0 corresponds to incapacitation of 50% of the population, which can also be expressed as incapacitation of a pedestrian of average susceptibility. In design, FED equals 0.3 is therefore sometimes used, which corresponds to incapacitation of 11.4% of the population.

Irritant gases are also treated in the ISO standard [36], and a correlation for fractional effective concentration (FEC) is presented. Similar to the FED concept,

FED equals 1.0 corresponds to incapacitation of 50% of the population and FED equals 0.3 corresponds to incapacitation of 11.4% of the population. The main difference between FED and FEC is that FEC is not a dose that accumulates in the body but a combined concentration of irritant species leading to incapacitation. The species specifically highlighted in the standard are HCl, HBr, HF, SO_2, NO_2, acrolein and formaldehyde.

2.2 Pedestrian Factors

The characteristics of pedestrians can influence their way to move through fire smoke. For example, the movement speed of an individual in clear conditions might be linked to its movement speed in smoke. In addition, a person's vision and physical abilities (intended as the stamina associated with exertion) might also be important in some situations.

2.2.1 Unimpeded Movement Speed

Many studies have shown that people move at different normal movement speeds [37, 38], which in the context of movement through smoke is called the unimpeded speed. Research has attempted to investigate how the unimpeded speed is related to the movement speed in smoke, i.e. if the reduction of speed is absolute or fractional. One example is the experiment performed in the Northern Link tunnel in Stockholm [26, 32]. In this experiment, participants walked both in a smoke-filled and a smoke-free tunnel. However, the study did not yield conclusive results regarding absolute or fractional reduction of the unimpeded movement speed when moving in smoke [39].

2.2.2 Visual Acuity

Given to the assumption that people slow down in smoke partly due to limited visual distance, it is reasonable to assume that people's visual acuity will influence the reduction of movement speed in smoke. For example, a pedestrian with vision impairment might move slower in smoke than an evacuee with 20/20 vision [15]. Visual acuity has therefore been the focus of experiments. One example is a Japanese study where participants with different visual acuity moved through a corridor under different illumination levels [33]. In one set of sub-experiments, smoke was also introduced in the corridor. In spite of this study, the influence of visual acuity on movements is still a relatively unexplored area of research.

2.2.3 Physical Exertion

In some instances, the physical exertion of pedestrians may influence their movement through smoke. The variability of physical performance of different pedestrians might be particularly important in those cases where they need to move up a slope or a hill (or walk long distances), which may lead to exhaustion associated to cardiorespiratory capacity or muscle fatigue [40, 41]. As physical exertion and fitness may vary significantly within a population, this is a factor that needs to be considered in the design process. Repetitive muscular activities may be associated with local muscle fatigue which can impede pedestrian movement capabilities [42].

Experimental research has been conducted to assess the biomechanical aspects of the pedestrian evacuation task by measuring physiological variables studying electromyographic muscle activity, an indicator of fatigue to evaluate performance [43]. Energy expenditure in pedestrian evacuation tasks has also been investigated by measuring oxygen uptake (VO_2) and heart rate [40, 44]. Those variables are useful to estimate physical work capacity during the pedestrian evacuation task. In case of moderate-intensity work which is below the lactate threshold, the oxygen uptake rises slowly until it reaches a stable value. This would be the situation at the beginning of the pedestrian evacuation movement. In case the physical activity is performed at a higher level than the lactate threshold, the maximum oxygen uptake threshold is reached. In this situation, a progressive loss of skeletal muscle work efficiency can occur [45].

2.3 Environmental Factors

Some environments are simply easier to navigate through smoke than others. For example, a very complex environment, e.g. a labyrinth, may require advanced route choices [16, 17, 19], which a simple room with one exit might not. Also, in a geometry where people are likely to follow a wall for a very long time, e.g. a tunnel, they might easily miss exits located at a 90-degree angle [15]. The environment is therefore important to consider in relation to movement through smoke.

2.3.1 Geometric Complexity

Movement and way-finding in smoke can be particularly challenging if the geometry is complex and difficult to navigate. One incident that clearly illustrated this difficulty is the MS Scandinavian Star incident [46]. Many passengers on MS Scandinavian Star were forced to evacuate through smoke, and some had a difficult time finding their way in the labyrinth of corridors on lower decks. A handful of diseased passengers were even found in dead-end corridor configurations. The problems found in the MS Scandinavian Star incident has led to research on way-finding in smoke-filled complex geometries in general and ships in particular [17–19].

Another situation where evacuees can easily miss emergency exits is during evacuation of smoke-filled tunnels. Research has shown that people tend to follow the tunnel wall when evacuating smoke-filled tunnels and pedestrians seem to rely more on their perception of touch than their vision [15]. This means that they can sometimes miss emergency exits located at the opposite tunnel wall unless they are encouraged to let go of the wall and head for the exit [15].

In both geometrically complex buildings and tunnels, smoke has been shown to negatively influence movement and way-finding. For these types of environments, additional help might be needed for people to find their way to safety. One solution might be to use way-finding systems, which are discussed in the following section (see Sect. 2.3.2).

2.3.2 Way-Finding Systems

One potential solution to the problems linked to a geometric complexity mentioned in Sect. 2.3.1 is to install way-finding systems that guide people in smoke [19, 47]. However, the design of such systems is not self-evident, as the designer often makes assumptions about interpretation and behaviour, and is not able to incorporate the mindset of the evacuees in the design process [48]. It has therefore been argued that the only way to ensure that a way-finding system works as intended is to test it in experiments [49]. Numerous studies have therefore involved experiments with the aim of testing and refining way-finding systems for smoke logged conditions. These experiments have been performed both in Virtual Reality (VR) [47] and physical environments [15, 17, 19, 28, 32, 50].

In recent years, a significant body of research has focused on the design of way-finding systems for road and rail tunnels. This research has shown that visual systems work, but that acoustic systems may be an even better alternative for guiding pedestrians to emergency exits. One system that has proven to work well in tunnels consists of a speaker at the emergency exit that plays a sound and a voice message, thereby encouraging people to move towards the exit. These types of systems, sometimes called sound beacons, have also been tested in other experiments [51–53] and have the potential to also work in ordinary building. However, research has shown that some sound beacon systems are difficult to understand without education [52].

In the wake of the previously mentioned MS Scandinavian Star incident, research in Norway focused on the use of way-finding systems in passenger ships [16, 46]. Both tactile and visual systems were evaluated and were shown to be an effective way of guiding people to safety in spite of complex geometries.

2.3.3 Inclination, Stairs and Surface Material

As mentioned in Sect. 2.1.3, exertion can play a significant role during the evacuation process. This is believed to be particularly important in cases where

evacuees need to move long distances upstairs or slopes, which is perhaps mainly relevant for underground facilities, e.g. road tunnels, rail tunnels and underground stations. For example, Norwegian road tunnels may have an inclination of more than 5% [54], and many new metro projects contain deep station that are 70 metres or more below the surface [55]. In these cases, the physical exertion of evacuees must be considered.

The surface material that evacuees walk on during evacuation might also influence the moment in smoke, and an uneven or coarse surface is expected to slow down movement. This can be particularly important for rail tunnels where the surface material may consist of large stones or macadam. Relatively limited research has yet to focus on movement through smoke on coarse surfaces, but performed research has not yet been able to show a significant reduction of speed on macadam compared to even surfaces [15].

3 Modelling Pedestrian Movement in Smoke

Modelling the impact of smoke on pedestrian movement should ideally take into consideration the different issues presented above. Models may make use of different data sets from experimental studies (as the ones discussed in Sect. 2) which investigate the factors associated with the movement of people in case of evacuation in smoke-filled environments.

The most sophisticated pedestrian and evacuation models used in fire safety engineering present the opportunity to couple fire simulations and pedestrian simulations. This means that the evolving conditions of the fire scenario (e.g. smoke movement) can be used to affect pedestrian movement. Different approaches can be used to represent the impact of the fire conditions in a modelling framework. The majority of evacuation models on the market used in fire safety engineering applications implement fire model results from an external fire model [56, 57], i.e. the smoke impact intended as visibility conditions and gas concentrations are imported into an evacuation model after preperforming a fire simulation. Another set of models are natively coupled, i.e. fire and evacuation simulations can be run at the same time, e.g. FDS + Evac [58]. Nevertheless, most of the existing models allow only a one-way coupling, which means that smoke can impact the movement and behaviours of pedestrians, while the action of pedestrians, e.g. opening a door, do not generally impact smoke movement [59].

Existing pedestrian and evacuation modelling tools employed to represent the impact of smoke on pedestrian movement can be categorized in relation to a series of modelled impacts, namely, (1) modelling the impact of reduced visibility conditions on movement speed, (2) modelling the impact of smoke on route/exit choice and (3) modelling the interaction with safety systems. All these impacts may be represented explicitly (i.e. the model includes a sub-model for a direct representation of the pedestrian behaviours linked to a given scenario) or implicitly, i.e. the model does

not include a specific sub-model to consider the given scenario, but it includes enough flexibility to represent it through other variables.

The impact of asphyxiants and irritants on pedestrian movement is typically not yet explicitly modelled, i.e. pedestrian and evacuation models may consider the adverse impact of toxic products in smoke by calculating FED [35], but the growing dose of asphyxiants is generally not assumed to affect pedestrian movement. This limitation is mostly due to the scarce knowledge on the negative effects that asphyxiant products may have on different pedestrians and the fact that acceptable design solutions are generally well below relatively high values of FED; thus, they will be often not considered as scenarios to be fully modelled with a pedestrian simulator. In other words, fire safety engineers generally perform pedestrian simulations with the assumption that toxicity and irritancy will not substantially affect the performance of pedestrian during evacuation.

For example, several international guidance documents indicate the threshold of FED = 0.3 [36, 60] as critical conditions for rejection of a fire engineering design during a deterministic analysis. Nevertheless, there is limited knowledge concerning the possibly adverse effects of toxic and irritant smoke, especially given the possible variation in the susceptibility that different individuals may have. Sub-models (see Sect. 2.1.4) may be included for the representation of the thresholds corresponding to certain irritant effects of smoke, i.e. intense pain in the eyes, the ability to keep eyes open, etc. that can reduce movement abilities [35]. Nevertheless, such effects are generally not considered explicitly while modelling their effect on pedestrian movement, but they are calculated separately to consider the tenability of the environmental conditions in which movement takes place.

To date, a limited number of studies [40] investigate the impact of physical exertion on pedestrian movement. Different types of models have been presented to relate movement speeds to physical exertion [40, 61–63]. Those models may be conceptual frameworks, i.e. considering the relationship between the motivation of pedestrians to move in relation to their fatigue level and the presence of others [61] or models merely based on physical performance. The latter models [40, 41] have been proposed to relate physical variables (e.g. oxygen uptake) with pedestrian evacuation abilities. Despite these recent research efforts in this area, current pedestrian evacuation models do not generally include dedicated sub-models for the representation of physical exertion of each pedestrian and the subsequent evacuation performance associated with it [64].

For all these reasons, the main aspects considered in this section concerning pedestrian evacuation simulations in smoke are the impact of reduced visibility conditions on pedestrian movement and the interaction with safety systems, i.e. the way-finding process.

3.1 Modelling the Impact of Reduced Visibility Conditions

The representation of the impact of reduced visibility conditions relates to the implementation and interpretation of existing experimental data sets into pedestrian and evacuation modelling tools. The impact of different visibility conditions can be used to simulate reduced movement speeds, generally representing those conditions as smoke extinction coefficient (as this variable is not dependent on the observed object, see Sect. 2.1.1) or visibility. Regardless of the data set(s) employed as a base for the correlation between extinction coefficient or visibility and movement speed, it is crucial to understand that the reduction in movement speed will also depend on the manner in which these data sets are interpreted by the modelling framework. In fact, there are currently two contrastive approaches to represent the reduction of pedestrian movement speed in smoke [39], namely:

1. A fractional reduction of speed
2. An absolute reduction of speed

The modelling interpretation with an absolute reduction refers to the case in which pedestrians reduce their movement speed all in the same way regardless of their unobstructed speed in clear conditions. The main variable affecting the obstructed movement speed (i.e. movement speed in smoke) is the visibility conditions in which they walk. The modelling interpretation with a fractional reduction considers instead a reduction in movement speed which is linked to both the visibility conditions as well as the initial unobstructed movement speed that people will have in smoke-free conditions [26].

In addition, it is also important to understand that different modelling interpretations can be made for the choice of the minimum movement speeds that pedestrians will adopt in the lower range of visibility conditions (i.e. almost complete darkness). In such scenarios, the simulated movement speed will depend on the assumption made by the model developer (or the model user, depending on how default settings can be controlled [65]) in the choice of the minimum speed. Three approaches are currently adopted by models to represent the minimum threshold of the impact of smoke on pedestrian movement, namely:

1. The model does not implement any minimum speed, and each pedestrian will reduce their speed in relation to the decreasing visibility conditions.
2. The model includes a constant minimum speed, and each pedestrian will reduce their speeds as a function of decreasing visibility conditions until a minimum constant threshold is reached. This corresponds to a set minimum speed in thick smoke (i.e. complete darkness).
3. The model implements a variable minimum speed which depends on the individual characteristics of the pedestrians (e.g. their unimpeded movement speed).

There is a link between the three minimum speeds assumed and the associated behavioural hypotheses which they represent. The movement of people in poor

visibility conditions can be made referring to the assumption that smoke affects movement speeds in any conditions (Method 1, see also Sect. 2.2). Secondly, it is possible to assume that movement speeds can be affected by smoke up to a certain constant threshold, i.e. movement speeds will not reduce below a certain constant minimum. This corresponds to the assumption that the whole population will have a common reduced movement speed corresponding to the visibility conditions of complete darkness (Method 2). The order of magnitude of such constant minimum speed is generally between 0.2 and 0.3 m/s depending on the data set used for reference (e.g. Jin [30]). The third assumption is that the minimum movement speed is affected by the individual characteristics of people, i.e. there is no common minimum movement speed, but this is variable in relation to the ability of people of moving in almost complete darkness.

These assumptions relating to the absolute/fractional interpretation and the minimum movement speeds in almost complete darkness yield five different interpretations, which are presented in Eqs. 4, 5, 6, 7 and 8 [39]. The same type of equations can be presented considering the reduced visibility conditions expressed as visibility (applying Eq. 2 in Sect. 2.1.1 and assuming a certain visibility factor).

$$\begin{aligned} v_i^s &= v_i^0\,(K_s) \quad \text{OR} \\ v_i^s &= v_i^0(S) \end{aligned} \tag{4}$$

$$\begin{aligned} v_i^s &= \text{Max}\left\{v_{min},\, v_i^0 c\,(K_s)\right\} \quad \text{OR} \\ v_i^s &= \text{Max}\left\{v_{min},\, v_i^0 c(S)\right\} \end{aligned} \tag{5}$$

$$\begin{aligned} v_i^s &= \text{Max}\left\{v_{min}(i),\, v_i^0 c\,(K_s)\right\} \quad \text{OR} \\ v_i^s &= \text{Max}\left\{v_{min}(i),\, v_i^0 c(S)\right\} \end{aligned} \tag{6}$$

$$\begin{aligned} v_i^s &= \text{Max}\left\{v_{min},\, v_i\,(K_s) \pm \Delta\right\} \quad \text{OR} \\ v_i^s &= \text{Max}\left\{v_{min},\, v_i(S) \pm \Delta\right\} \end{aligned} \tag{7}$$

$$\begin{aligned} v_i^s &= \text{Max}\left\{v_{min}(i),\, v_i^0\,(K_s) \pm \Delta\right\} \quad \text{OR} \\ v_i^s &= \text{Max}\left\{v_{min}(i),\, v_i^0(S) \pm \Delta\right\} \end{aligned} \tag{8}$$

Each equation is associated with a different data set interpretation:

v_i^s = movement speed in smoke of each individual i
v_i^0 = unobstructed movement speed in clear conditions of each individual i
K_s = extinction coefficient
S = visibility
v_{min} = minimum speed in dense smoke
$v_{min}(i)$ = minimum speed in dense smoke of each individual i
c = fraction of the unobstructed movement speed
Delta = variation of movement speeds

1. Fractional/no minimum speed interpretation. In this case the movement speed in smoke v_i^s of each individual person i is a fraction of the unobstructed movement speed in clear conditions v_i^0. This reduction can be a function of the extinction coefficient Ks (or visibility S). This interpretation corresponds to several curves of reduction of movement speed given reduced visibility conditions in relation to the characteristics of the individuals under consideration (i.e. their unobstructed movement speed). In this case, there is no minimum threshold of movement speed regardless of the visibility conditions.
2. Fractional/constant minimum speed interpretation. This case considers a reduction of the initial unobstructed movement speed v_i^0 obtained considering a fraction c (where $0 < c \leq 1$) of the unobstructed speed depending on the extinction coefficient K_s (or visibility S). In very scarce visibility conditions (almost darkness), pedestrians walk all at the same minimum speed $v_{i,min}$ (in the range for instance of 0.2–0.3 m/s). Several curves of reduction of movement speed given reduced visibility conditions are produced in accordance to the characteristics of the individuals (i.e. their unobstructed movement speed), but the curves will all have a threshold of minimum movement speed.
3. Fractional/variable minimum speed interpretation. In this case, the obstructed movement speed in smoke v_i^s of each individual person i is a fraction c (where $0 < c \leq 1$) of the unobstructed movement speed in clear conditions v_i^0, depending on the extinction coefficient K_s (or visibility S). The minimum speed in dense smoke assumes a variation in the speeds; thus, the minimum movement speed $v_{min}(i)$ varies in relation to the characteristics of each individual person i, e.g. $v_{min}(i)$ can be obtained as a fraction g of the initial unobstructed movement speed v_i^0, and thus $v_{min}(i) = g v_i^0$. This interpretation corresponds to several curves of reduction of movement speeds given reduced visibility, and the minimum speed depends on the characteristics of each person. Models [58] may also assume that this variable minimum speed is a fraction g of the unobstructed movement speed, e.g. $v_{i,min}(i) = g\ v_{i,min}$. This means that a minimum threshold is used for each individual person, i.e. the obstructed movement speed in smoke will not go below a certain minimum individual value.
4. Absolute/constant minimum speed interpretation. The obstructed movement speed in smoke v_i^s of each individual person i depends on the visibility conditions, expressed as extinction coefficient K_s (or visibility S), considering a certain variation Δ of movement speeds around the average value. This means that the movement speed reduction is not dependent from the unobstructed movement speed in smoke-free conditions v_i^0. In almost complete darkness, pedestrians walk at a constant minimum speed v_{min} (in the range, for instance, of 0.2–0.3 m/s). Therefore, a single movement speed reduction curve is produced for all pedestrians under consideration. The resulting reduced movement speeds of each pedestrian will then be along the line of the curve employed, which includes a threshold of minimum speed within a certain range of variation Δ.

5. Absolute/variable minimum speed interpretation. The obstructed movement speed in smoke v_i^s of each individual person i depends only on the visibility conditions, expressed as extinction coefficient K_s (or visibility S), considering a certain variation Δ of movement speeds around the average value. This means that movement speed in smoke does not depend on the unobstructed movement speed in smoke-free conditions v_i^0. The movement in very dense smoke is reproduced considering a variable speed reduction among pedestrians, i.e. $v_{min}(i)$ depends on the characteristics of each individual pedestrian, e.g. $v_{min}(i)$ can be obtained as a fraction g of the initial unobstructed movement speed v_i^0; thus, $v_{min}(i) = g v_i^0$. A single-speed reduction curve is used for all pedestrians, with the exception of the lower part of the curve which makes use of different minimum values of movement speed based on the individual movement abilities of the pedestrians in dark smoke.

Considering these modelling interpretations as a starting point for the representation of the speed reduction of people in reduced visibility conditions, different empirical correlations have been presented in relation to several variables, such as:

1. The empirical data set(s) considered for building the correlation (see Sect. 2).
2. The assumptions of considering a reference for the reduction of movement speed in smoke, visibility [8] or extinction coefficient [35, 58, 66].
3. The range of visibility conditions in which movement speed is considered to start being affected by the presence of smoke. A value corresponding to 3 m of visibility [8] has been recently suggested as threshold for starting considering a reduction of speed due to smoke, i.e. better visibility conditions would not correspond to a reduction of the unobstructed movement speed.
4. The method to treat uncertainties and represent pedestrian movement, either deterministic or stochastic [67]. This last aspect would be used to assume correlations which may be based on fixed constant movement speeds/relationships or using pseudorandom sampling from distributions [68].

It should be noted that the presence of smoke can also affect movement speeds implicitly [69], i.e. movement speeds can be reduced assuming the impact of smoke on other behavioural variables, such as (1) redirection of movement path [15] and (2) posture change, e.g. crawling [70]. Most of existing models do not generally include the option to represent complex behaviours such as stop and go, zig-zag or posture changes. Models allowing such type of complex behaviours [66] generally require model user's action aimed at calibrating the conditions in which such behaviours occur or implementing manually a specific set of actions/behaviour. Therefore, the redirection of movement and posture changes are generally implicitly represented by considering the so called modelling speed, which is a speed calculated for each person by dividing the distance between two points by the total time, including the duration of the stops made by pedestrians, possible zig-zag movement or posture changes which may yield a delay in reaching the destination. This modelling speed is provided [15] to consider implicitly the broader impact of smoke on movement,

and it is in contrast with the movement speed, which is instead calculated by dividing the total distance walked in the space by the time employed, excluding all other behavioural factors (e.g. stops) which may impact the movement speed. Therefore, most models represent explicitly only upright pedestrian movement along an almost straight path in smoke. The actual movement path of a pedestrian in smoke might not be straight as the model may include a movement modelling algorithm which considers the navigation around other pedestrians and obstacles, e.g. the social force model [6] or the steering model [71].

Crawling movement in smoke (which could actually take place given the possible presence of a hot descending smoke layer) has received limited research attention [70, 72], with an empirical relationship between crowd crawling speed and crawling density that has been expressed by Kadi [73] as follows:

$$\text{Crawling speed} = 0.7973 + 0.2909\text{D}–0.1503\text{D}^2 \tag{9}$$

where:

D = crawling crowd density (pedestrians/m^2)

3.2 Modelling Way-Finding in Smoke

Models which allow a coupled fire and pedestrian/evacuation simulation may include different algorithms and sub-models for the representation of wayfinding (i.e. pedestrian route/exit choice) in smoke. Those models may take into account different variables which affect this choice. The starting condition is generally an algorithm based on general assumptions of route choice which is used to represent the movement paths and the target/destinations of pedestrians. Such types of algorithms may be based on different assumptions, namely, (1) the simulation of the shortest path, (2) the simulation of the quickest path (i.e. accounting for the queueing time of pedestrians, (3) a deterministic user-defined choice of the movement paths and (4) paths based on different conditions, such as the presence of smoke, signage systems (e.g. exit signs, way-finding lights), etc. [74].

The most sophisticated models represent this choice by considering the interaction between pedestrians and different environmental conditions, such as the presence of smoke and the signage system (e.g. an exit sign, a way-finding guidance system). Pedestrian choices can also be affected by several variables, such as modelling the familiarity with the environment (e.g. according to affiliation theory [75], people tend to move towards familiar places). In particular, modelling the impact that signage can have in smoke on route choice presents several challenges, as different aspects would need to be modelled within a simulator. Firstly, it is important to simulate if signage is visible or not (given the design of the signage and environmental conditions, which may include reduced visibility due to smoke). Signage objects can be light-reflecting or self-emitting [30, 76] (see Sect. 2.1.1), and its visibility may depend on several factors such as its location, characteristics,

configuration and ambient/external lighting. Different frameworks have been used to represent this process (e.g. the theory of affordances [49, 77, 78].

A set of four steps can be used for the simulation of the process of using the information provided by a signage system. It should be noticed that these four steps may be used for the simulation of the interaction of a single pedestrian with a signage system. Nevertheless a more complete representation of the route/exit choice should also model social influence [79–81], i.e. how the information and the interaction of each pedestrian in a group influence each other's decisions or how the choices made by other pedestrians in the surroundings can affect each individual choice.

The first step (Step 1) is to simulate if the signage under consideration is visible or not to the pedestrians. The visibility of signage in smoke-filled environments has been investigated for more than half a century [82]. Nevertheless, existing research does not fully consider the visibility levels reached by signage in different smoke-filled environmental conditions, which may also take into consideration the design of the signage and other factors such as the colours and properties of smoke and lighting conditions [31]. The visibility of signage should consider not only the environmental conditions and the property of the signage but also the intrinsic properties of the signage system (e.g. signage design, colour and location). This is also linked with the simulation of the interaction between pedestrians and line of sights, an issue which has been investigated and addressed in pedestrian simulations [83].

The second step (Step 2) consists of assessing if the signage is noticed by the pedestrians. This step assumes that a sign might be visible but not be noticed by a pedestrian or a group of pedestrians. The noticeability of a signage system might depend on different fire, environmental and pedestrian factors such as the familiarity of the pedestrians with the signage and the environment [75], the location and characteristics of the signage system [77], etc.

The third step (Step 3) refers to the ability of the signage to provide the intended information, i.e. if the signage message is understood. Different attributes of the interactions of pedestrians with signage systems can be represented within pedestrian models. Most of existing models do not represent explicitly the interaction between the information provided (and how it is provided) and the actions of the pedestrians. They instead often rely on implicit deterministic or probabilistic approaches which allow the model user to represent the likelihood of understanding the information given to the pedestrians.

The last step (Step 4) relates to the actual use of the information given by the signage system, given this has been understood. In other words, this is the final action taken by the pedestrians, i.e. the use of a given route or exit.

The representation of these steps can take place adopting different modelling strategies [84, 85], including approaches based on a cellular automata modelling approach [86–88], agent-based modelling [89–91] or game theory [7, 92, 93]. In this context, research studies [86] have investigated how to include the impact of different variables (including the presence of way-finding installations) using different modelling approaches.

4 Discussion

The analysis of existing data sets, theories and modelling approaches currently adopted to investigate pedestrian movement in smoke allow a reflection on the contrasting factors which may play a role in the representation of this phenomenon. In some instances, modelling research has been trying to represent variables for which there is still limited knowledge, mostly due to the scarce quantity of experimental data sets available.

As a result of this lack of knowledge, pedestrian and evacuation models used in fire safety engineering practice may use significantly different assumptions to represent the impact of smoke on pedestrian movement. To date, there is no clear understanding on whether the reduction of movement speed in smoke due to reduced visibility conditions should be represented as an absolute or fractional reduction of the movement speed in clear conditions. This is mostly due to the fact that experimental participants generally move only in smoke-filled environments (with the exception of one experimental data set in which they move both in smoke-free and smoke-filled conditions [32]). Also, a significant proportion of the experimental studies conducted to study this variable [14, 15, 25, 32, 50] has been made in relatively simple environments (e.g. corridors or tunnels); thus, the pedestrian movement in smoke in complex geometrical configurations still needs to be fully investigated.

The relationship between the motivation to move, the physical exertion and the presence of smoke has received limited research attention. Most models adopted today are self-driven particle models [94], i.e. they are based on the assumption that pedestrians have a constant initial speed (although that may be subjected to perturbations of different nature [74]). This assumption does not fully allow to represent some of the variables which may have a key role in pedestrian movement in smoke, such as the level of perceived urgency and risk perception in general [95]. In addition, studies have so far investigated mostly physiological factors and perceived exertion affecting pedestrian movement in smoke-free conditions [40]. This leads to the need to study the interaction of perceived and actual physical exertion in smoke.

While theoretical models that investigate how movement speeds are affected by the relationship between motivation and exertion levels have been presented [61], such models do not consider the additional behavioural and physical variables associated with the presence of smoke. Pedestrians may indeed adopt movement speeds in smoke as a result of a combination of different factors, which may contribute in different manners, namely:

1. Factors associated with an increase in speed (e.g. perceived urgency, interaction with way-finding systems and lighting)
2. Factors associated with a decrease in speed (e.g. reduced visibility conditions, the presence of irritants and asphyxiants, physical exertion)

3. Factors that may have a decreasing or increasing impact on movement speed depending on the specific scenario conditions (e.g. social influence and group interactions, motivation to move)

From a fire engineering design perspective, factors 2 and 3 are the ones that should receive more attention (as they are heading to worsening conditions).

Several factors currently need further investigation in order to have a better understanding of pedestrian movement in smoke. One aspect that would need to be experimentally investigated is the study of the impact of social influence during pedestrian movement in smoke-filled environments. In fact, although a few attempts have been made on understanding how pedestrians interact with each other in smoke [96, 97], to date, limited data sets exist which investigate human behaviour during such type of group movement scenarios [24]. Aspects that need to be investigated include both how movement speeds and behaviours change in a group (i.e. people may tend to walk all at the speed of the lowest person in the group) and route/exit choice (as there may be leaders and followers in the group). This latter aspect has been investigated and modelled for smoke-free conditions [98], but it has not been addressed yet with dedicated experimental studies for smoke-filled environments.

Scarce research has also been conducted on the impact of radiation and temperature on pedestrian movement [99]. Also in this case, a few modelling attempts and guidance [36] have been provided to represent the impact of the evolving conditions, but this feature is generally currently not implemented in pedestrian evacuation models used in fire safety engineering [100]. Some of the sub-incapacitating effects of fire smoke also need to be assessed more thoroughly, as at the moment there is limited knowledge on the impact that asphyxiants and irritants may have on human cognition (which can subsequently affect pedestrian movement and way-finding abilities). This lack of knowledge is linked to the difficulties associated with developing and validating such type of sub-models, both given the scarcity of existing data sets from real pedestrian and evacuation movement events and the ethical limitations associated with such type of experimental data collection. This issue inevitably limits the validity of models for the representation of pedestrian movement in smoke and the applicability of existing tools in engineering practice.

Regarding the impact of surface materials, current experimental research studies [15] have been investigating such variables assuming people wearing comfortable clothing/shoes. This condition is not necessarily fully representative of a real scenario (where people may wear heels or clothes who limit their movement). Such limitation should be taken into consideration when applying such type of data sets and considered in future research studies.

Concerning route/exit choice in smoke, the modelling literature includes a set of approaches for its representation. While existing tools often represent enough flexibility to represent different conditions and scenarios, their predictive capabilities are often directly linked to the calibration effort made by the model user and by the correspondence between the assumptions/data sets used by the model developer and the scenario under consideration by the use. Future route/exit choice models should instead take into consideration more sophisticated interactions between

pedestrians and the environment (e.g. signage, the presence of others, etc.) and have such interactions based on experimental data sets rather than on fully theoretical algorithms/assumptions (i.e. quickest or shortest path, etc.). In fact, while initial attempts to model complex decision-making in terms of route/exit choice have been performed [83, 92], further studies are needed to perform further validation of the predicted behaviour. Such models should also take into account the impact of the presence of smoke on possible changes of pedestrian behaviour, i.e. the use of walls that pedestrians may do to orientate themselves during movement in smoke or complex leader/follower interactions. Similarly, the impact of visual acuity on pedestrian movement in smoke has received relatively limited research attention [33].

5 Conclusion

This chapter has introduced the fundamental theories, data sets and models concerning pedestrian movement in smoke. To date, most of the existing experimental data sets focus on the relationship between movement speed and reduced visibility conditions. Other factors such as fire-, pedestrian- or environmental-related factors can be taken into consideration, but there is a generally limited knowledge on their impact on pedestrian movement. A variety of modelling approaches today exist for the representation of pedestrian movement. The main aspects taken into consideration are the reduction of movement speed due to low visibility and way-finding in smoke.

Acknowledgements The authors wish to acknowledge Håkan Frantzich and Karl Fridolf for the joint research activities conducted in the area of pedestrian movement in smoke.

References

1. B. J. Meacham, “An introduction to performance-based fire safety analysis and design with applications to structural fire safety,” in *Building To Last*, 1997, pp. 529–533.
2. E. D. Kuligowski, “Computer Evacuation Models for Buildings,” in *SFPE Handbook of Fire Protection Engineering*, M. J. Hurley, D. T. Gottuk, J. R. Hall, K. Harada, E. D. Kuligowski, M. Puchovsky, J. L. Torero, J. M. Watts, and C. J. Wieczorek, Eds. New York, NY: Springer New York, 2016, pp. 2152–2180.
3. S. Erik Magnusson, H. Frantzich, and K. Harada, “Fire safety design based on calculations: Uncertainty analysis and safety verification,” *Fire Saf. J.*, vol. 27, no. 4, pp. 305–334, Nov. 1996.
4. D. A. Purser and M. Bensilum, “Quantification of behaviour for engineering design standards and escape time calculations,” *Saf. Sci.*, vol. 38, no. 2, pp. 157–182, Jul. 2001.
5. D. Nilsson and R. Fahy, “Selecting Scenarios for Deterministic Fire Safety Engineering Analysis: Life Safety for Occupants,” Springer New York, 2016, pp. 2047–2069.
6. D. Helbing and P. Molnár, “Social force model for pedestrian dynamics,” *Phys. Rev. E*, vol. 51, no. 5, pp. 4282–4286, May 1995.

7. N. Bellomo, D. Clarke, L. Gibelli, P. Townsend, and B. J. Vreugdenhil, "Human behaviours in evacuation crowd dynamics: From modelling to 'big data' toward crisis management," *Phys. Life Rev.*, May 2016.
8. K. Fridolf, D. Nilsson, H. Frantzich, E. Ronchi, and S. Arias, "Människors gånghastighet i rök: Förslag till representation vid brandteknisk projektering [Human walking speed in smoke: recommendations for representation in fire engineering design]," SP Sverige, Sweden, 2016.
9. R. Lovreglio, E. Ronchi, G. Maragkos, T. Beji, and B. Merci, "A dynamic approach for the impact of a toxic gas dispersion hazard considering human behaviour and dispersion modelling," *J. Hazard. Mater.*, vol. 318, pp. 758–771, Nov. 2016.
10. M. J. Assael and K. E. Kakosimos, *Fires, explosions, and toxic gas dispersions: effects calculatioan and risk analysis*. CRC Press, 2010.
11. T. Statens Haverikommisjon, "Rapport om brann i vogntog på RV23, Oslofjordtunnelen, 23 juni 2011 [Report on the fire in a road tunnel on the RV23 Oslofjordtunnel, 23rd of June 2011]," SHT, 2013/05, 2013.
12. T. Statens Haverikommisjon, "Report on fire in a heavy goods vehicle in the Gudvanga tunnel on the E16 road in Aurland on 5 August 2013," Norway, 2015/02, 2015.
13. P. Duffé and M. Marec, "Task Force for Technical Investigation of the 24 March 1999 Fire in the Mont Blanc Vehicular Tunnel." Minister of the Interior - Ministry of Equipment, Transportation and Housing, 1999.
14. T. Jin, "Visibility through fire smoke," *J. Fire Flammabl.*, vol. 9, no. 2, pp. 135–155, 1978.
15. K. Fridolf, E. Ronchi, D. Nilsson, and H. Frantzich, "Movement speed and exit choice in smoke-filled rail tunnels," *Fire Saf. J.*, vol. 59, pp. 8–21, Jul. 2013.
16. G. Jensen, "Römming i röyk: Fullskala test av ledesystemer, personlig röykvern og atferd [Evacuating in Smoke: Full Scale Tests on Emergency Egress Information Systems and Human Behaviour in Smoky Conditions]," IGP AS, Trondheim, Norway, 1993.
17. T. Paulsen, "The effect of escape route lnforemation on mobility and way finding under smoke logged conditions," *Fire Saf. Sci.*, vol. 4, pp. 693–704, 1994.
18. A. Heskestad and K. S. Pedersen, "Escape Through Smoke: Assessment of Human Behavior and Performance of Wayguidance Systems," in *Proceedings of the First International Symposium on Human Behaviour in Fire, Belfast, UK*, 1998, pp. 631–638.
19. A. W. Heskestad, "Performance in smoke of wayguidance systems," *Fire Mater.*, vol. 23, no. 6, pp. 375–381, Nov. 1999.
20. T. Jin and T. Yamada, "Experimental study on human emotional instability in smoke filled corridor: part 2," *J. Fire Sci.*, vol. 8, no. 2, pp. 124–134, 1990.
21. T. Jin, "Studies of emotional instability in smoke from fires," *J. Fire Flammabl.*, vol. 12, no. 2, pp. 130–142, 1981.
22. T. Jin and T. Yamada, "Experimental Study On Effect Of Escape Guidance In Fire Smoke By Travelling Flashing Of Light Sources," *Fire Saf. Sci.*, vol. 4, pp. 705–714, 1994.
23. M. Wright, G. Cook, and G. Webber, "The effects of smoke on people's walking Speeds using overhead lighting and Wayguidance provision," in *Proceedings of the 2nd international symposium on human behaviour in fire. MIT, Boston*, 2001, pp. 275–284.
24. H. Frantzich, "Utrymning av tunnelbanetåg: Experimentell utvärdering av möjligheten att utrymma i spårtunnel [Metro tunnel evacuation: Experimental evaluation of the possibility of a space in the tram tunnel]," Karlstad, Sweden, 2000.
25. M. Seike, N. Kawabata, and M. Hasegawa, "Experiments of evacuation speed in smoke-filled tunnel," *Tunn. Undergr. Space Technol.*, vol. 53, pp. 61–67, Mar. 2016.
26. K. Fridolf, E. Ronchi, D. Nilsson, and H. Frantzich, "The relationship between obstructed and unobstructed walking speed: Results from an evacuation experiment in a smoke filled tunnel," presented at the 6th Human Behaviour in Fire Symposium 2015, Downing College, Cambridge, UK, 2015, pp. 537–548.
27. K. Fujii, T. Sano, and Y. Ohmiya, "Effect of Emergency Sign and Illumination on Walking Speed in Smoke-Filled Corridor," presented at the 6th International Symposium on Human Behaviour in Fire, UK, 2015, pp. 561–571.

28. H. Frantzich and D. Nilsson, "Utrymning genom tät rök: beteende och förflyttning [Evacuation in dense smoke: behaviour and movement] Technical Report 3126." Lund: Department of Fire Safety Engineering and Systems Safety, 2003.
29. B. Karlsson and J. Quintiere, *Enclosure fire dynamics*. CRC press, 1999.
30. T. Jin, "Visibility and Human Behavior in Fire Smoke," in *SFPE Handbook of Fire Protection Engineering (3rd edition)*, Di Nenno P., Quincy, MA (USA): National Fire Protection Association, 2008, pp. 2–42 – 2–53.
31. G. W. Mulholland, "Smoke production and properties," *SFPE Handb. Fire Prot. Eng.*, vol. 3, pp. 2–258, 1995.
32. E. Ronchi, K. Fridolf, H. Frantzich, D. Nilsson, A. L. Walter, and H. Modig, "A tunnel evacuation experiment on movement speed and exit choice in smoke," *Fire Saf. J.*, Jun. 2017.
33. Y. Akizuki, K. Yamao, and T. Tanaka, "Experimental Study On Walking Speed In Escape Route Considering Luminous Condition, Smoke Density And Evacuee'S Visual Acuity," in *Seventh Asia-Oceania Symposium on Fire Science and Technology*, Hong Kong, 2007, p. 10.
34. T. Jin, "Studies On Human Behavior And Tenability In Fire Smoke," *Fire Saf. Sci.*, vol. 5, pp. 3–21, 1997.
35. D. A. Purser and J. L. McAllister, "Assessment of Hazards to Occupants from Smoke, Toxic Gases, and Heat," in *SFPE Handbook of Fire Protection Engineering*, M. J. Hurley, D. T. Gottuk, J. R. Hall, K. Harada, E. D. Kuligowski, M. Puchovsky, J. L. Torero, J. M. Watts, and C. J. Wieczorek, Eds. New York, NY: Springer New York, 2016, pp. 2308–2428.
36. International Standards Organization, "ISO 13571:2012 - Life-threatening components of fire – Guidelines for the estimation of time to compromised tenability in fires." 2012.
37. J. J. Fruin, *Pedestrian Planning and Design*, (Revised Edition). Elevator World, Inc, Mobile, AL, 1987.
38. A. Seyfried, B. Steffen, W. Klingsch, T. Lippert, and M. Boltes, "The Fundamental Diagram of Pedestrian Movement Revisited — Empirical Results and Modelling," in *Traffic and Granular Flow'05*, A. Schadschneider, T. Pöschel, R. Kühne, M. Schreckenberg, and D. E. Wolf, Eds. Berlin, Heidelberg: Springer Berlin Heidelberg, 2007, pp. 305–314.
39. E. Ronchi, S. M. V. Gwynne, D. A. Purser, and P. Colonna, "Representation of the Impact of Smoke on Agent Walking Speeds in Evacuation Models," *Fire Technol.*, vol. 49, no. 2, pp. 411–431, Apr. 2013.
40. E. Ronchi *et al.*, "Ascending evacuation in long stairways: Physical exertion, walking speed and behaviour," Department of Fire Safety Engineering, Lund University, Lund, Sweden, 3192, 2015.
41. A. Halder *et al.*, "Limitations of oxygen uptake and leg muscle activity during ascending evacuation in stairways," *Appl. Ergon.*, vol. 66, pp. 52–63, Jan. 2018.
42. A. Halder *et al.*, *Energy costs and leg muscle activities in ascending stairs*. 2015.
43. C. Hanon, C. Thepaut-Mathieu, C. Hausswirth, and J. M. Le Chevalier, "Electromyogram as an indicator of neuromuscular fatigue during incremental exercise," *Eur. J. Appl. Physiol.*, vol. 78, no. 4, pp. 315–323, Aug. 1998.
44. J. H. T. Lam, J. K. K. Yuen, E. W. M. Lee, and R. Y. Y. Lee, "Experimental study on upward movement in a high-rise building," *Saf. Sci.*, vol. 70, pp. 397–405, Dec. 2014.
45. T. J. Barstow, "Characterization of VO2 kinetics during heavy exercise.," *Med. Sci. Sports Exerc.*, vol. 26, no. 11, pp. 1327–1334, 1994.
46. A. Robinson, "The Scandinavian Star Incident: A Case Study," *Fire Eng. J.*, vol. 59, pp. 36–38, 1999.
47. G. Cosma, E. Ronchi, and D. Nilsson, "Way-finding lighting systems for rail tunnel evacuation: A virtual reality experiment with Oculus Rift®," *J. Transp. Saf. Secur.*, vol. 8, no. sup1, pp. 101–117, Jun. 2016.
48. D. Nilsson, H. Frantzich, E. Ronchi, K. Fridolf, A. Lindgren Walter, and H. Modig, "Integrating evacuation research in large infrastructure tunnel projects - Experiences from the Stockholm Bypass Project," *Fire Saf. J.*, Aug. 2017.
49. D. Nilsson, *Exit choice in fire emergencies: influencing choice of exit with flashing lights*. Lund, Sweden: Dept. of Fire Safety Engineering and Systems Safety, Lund University, 2009.

50. D. Nilsson, M. Johansson, and H. Frantzich, "Evacuation experiment in a road tunnel: A study of human behaviour and technical installations," *Fire Saf. J.*, vol. 44, no. 4, pp. 458–468, May 2009.
51. L. C. Boer and S. J. van Wijngaarden, "Directional sound evacuation from smoke-filled tunnels," presented at the Safe & Reliable Tunnels. Innovative European Achievements, Prague, Czech Republic, 2004.
52. L. Boer and D. Withington, "Auditory guidance in a smoke-filled tunnel," *Ergonomics*, vol. 47, no. 10, pp. 1131–1140, Aug. 2004.
53. L. D. Mellert and U. Welte, "Acoustical Guidance in Road Tunnels," presented at the 6th International Conference Tunnel Safety and Ventilation, Graz, 2012, pp. 187–194.
54. H. akan Frantzich, D. Nilsson, and K. Rød, "Utrymning och tekniska installationer i vägtunnlar med dubbelriktad trafik," *Lund Brand. Lunds Tek. Högsk.*, 2016.
55. Förvaltning för utbyggd tunnelbana, "Tunnelbana till Nacka och söderort, Stockholm." Stockholms Läns Landsting, 2016.
56. Mott MacDonald Simulation Group, "Simulation of Transient Evacuation and Pedestrian MovementS. STEPS User Manual v5.3." 2016.
57. Thunderhead Engineering, "Pathfinder - Technical Reference." 2018.
58. T. Korhonen and S. Hostikka, "Fire Dynamics Simulator with Evacuation: FDS+Evac Technical Reference and User's Guide," VTT Technical Research Center of Finland, Working paper 119, 2009.
59. E. Galea, Z. Wang, A. Veeraswamy, F. Jia, P. Lawrence, and J. Ewer, "Coupled Fire/Evacuation Analysis of the Station Nightclub Fire," *Fire Saf. Sci.*, vol. 9, pp. 465–476, 2008.
60. British Standards, "PD 7974-0:2002 Application of fire safety engineering principles to the design of buildings. Guide to design framework and fire safety engineering procedures." BSI, 2002.
61. E. Ronchi, P. A. Reneke, and R. D. Peacock, "A conceptual fatigue-motivation model to represent pedestrian movement during stair evacuation," *Appl. Math. Model.*, vol. 40, no. 7–8, pp. 4380–4396, Apr. 2016.
62. J. Koo, B.-I. Kim, and Y. S. Kim, "Estimating the effects of mental disorientation and physical fatigue in a semi-panic evacuation," *Expert Syst. Appl.*, vol. 41, no. 5, pp. 2379–2390, 2014.
63. M. W. Denny, "Limits to running speed in dogs, horses and humans," *J. Exp. Biol.*, vol. 211, no. 24, pp. 3836–3849, 2008.
64. E. Ronchi and D. Nilsson, "Fire evacuation in high-rise buildings: a review of human behaviour and modelling research," *Fire Sci. Rev.*, vol. 2, no. 1, p. 7, 2013.
65. S. M. V. Gwynne, E. Kuligowski, M. Spearpoint, and E. Ronchi, "Bounding defaults in egress models," *Fire Mater.*, Nov. 2013.
66. E. R. Galea, "BuildingExodus. User manual v6.1." 2014.
67. D. Alvear, O. Abreu, A. Cuesta, and V. Alonso, "A new method for assessing the application of deterministic or stochastic modelling approach in evacuation scenarios," *Fire Saf. J.*, vol. 65, pp. 11–18, Apr. 2014.
68. R. Machado Tavares and E. Ronchi, "Uncertainties in evacuation modelling: Current flaws and future improvements," presented at the 6th Human Behaviour in Fire Symposium 2015, Downing College, Cambridge, UK, 2015, pp. 185–196.
69. S. M. V. Gwynne and K. E. Boyce, "Engineering Data," in *SFPE Handbook of Fire Protection Engineering*, M. J. Hurley, D. T. Gottuk, J. R. Hall, K. Harada, E. D. Kuligowski, M. Puchovsky, J. L. Torero, J. M. Watts, and C. J. Wieczorek, Eds. New York, NY: Springer New York, 2016, pp. 2429–2551.
70. R. A. Kady and J. Davis, "The effect of occupant characteristics on crawling speed in evacuation," *Fire Saf. J.*, vol. 44, no. 4, pp. 451–457, May 2009.
71. C. W. Reynolds, "Steering Behaviors For Autonomous Characters," presented at the Game developers conference, 1999, pp. 763–782.
72. R. Nagai, M. Fukamachi, and T. Nagatani, "Evacuation of crawlers and walkers from corridor through an exit," *Phys. Stat. Mech. Its Appl.*, vol. 367, pp. 449–460, Jul. 2006.

73. R. A. Kady, "The development of a movement–density relationship for people going on four in evacuation," *Saf. Sci.*, vol. 50, no. 2, pp. 253–258, Feb. 2012.
74. E. Ronchi and D. Nilsson, "Basic Concepts and Modelling Methods," in *Evacuation Modeling Trends*, A. Cuesta, O. Abreu, and D. Alvear, Eds. Cham: Springer International Publishing, 2016, pp. 1–23.
75. J. D. Sime, "Movement toward the Familiar: Person and Place Affiliation in a Fire Entrapment Setting," *Environ. Behav.*, vol. 17, no. 6, pp. 697–724, Nov. 1985.
76. E. Ronchi, D. Nilsson, and S. M. V. Gwynne, "Modelling the Impact of Emergency Exit Signs in Tunnels," *Fire Technol.*, vol. 48, no. 4, pp. 961–988, Apr. 2012.
77. E. Carattin, R. Lovreglio, E. Ronchi, and D. Nilsson, "Affordance-based evaluation of signage design for areas of refuge," in *14th International Conference and Exhibition on Fire Science and Engineering*, Royal Holloway College, University of London, UK, 2016.
78. J. J. Gibson, *The Ecological approach to visual perception*. Hillsdale (N.J.): Lawrence Erlbaum Associates, 1986.
79. M. Deutsch and H. B. Gerard, "A study of normative and informational social influences upon individual judgment.," *J. Abnorm. Soc. Psychol.*, vol. 51, no. 3, pp. 629–636, 1955.
80. M. Hewstone and R. Martin, "Social Influence," in *Introduction to Social Psychology*, 4th ed., London, UK: Blackwell Publishing, 2008.
81. M. Kinateder *et al.*, "Social influence on route choice in a virtual reality tunnel fire," *Transp. Res. Part F Traffic Psychol. Behav.*, vol. 26, pp. 116–125, Sep. 2014.
82. D. Rasbash, "The efficiency of hand lamps in smoke," *IFE J*, vol. 11, no. 1, p. 46, 1951.
83. H. Xie, L. Filippidis, E. R. Galea, D. Blackshields, and P. J. Lawrence, "Experimental study of the effectiveness of emergency signage," in *Proceedings of the 4th international symposium on human behaviour in fire, Robinson College, Cambridge, UK*, 2009, pp. 13–15.
84. E. Vilar, F. Rebelo, P. Noriega, J. Teles, and C. Mayhorn, "The influence of environmental features on route selection in an emergency situation," *Appl. Ergon.*, vol. 44, no. 4, pp. 618–627, Jul. 2013.
85. W. Liao, A. U. Kemloh Wagoum, and N. W. F. Bode, "Route choice in pedestrians: determinants for initial choices and revising decisions," *J. R. Soc. Interface*, vol. 14, no. 127, p. 20160684, Feb. 2017.
86. R. Lovreglio, E. Ronchi, and D. Nilsson, "Calibrating floor field cellular automaton models for pedestrian dynamics by using likelihood function optimization," *Phys. Stat. Mech. Its Appl.*, vol. 438, pp. 308–320, Nov. 2015.
87. S. Bandini, F. Rubagotti, G. Vizzari, and K. Shimura, "A Cellular Automata Based Model for Pedestrian and Group Dynamics: Motivations and First Experiments," in *Parallel Computing Technologies*, vol. 6873, V. Malyshkin, Ed. Berlin, Heidelberg: Springer Berlin Heidelberg, 2011, pp. 125–139.
88. N. Pelechano and A. Malkawi, "Evacuation simulation models: Challenges in modeling high rise building evacuation with cellular automata approaches," *Autom. Constr.*, vol. 17, no. 4, pp. 377–385, May 2008.
89. E.-W. Augustijn-Beckers, J. Flacke, and B. Retsios, "Investigating the effect of different pre-evacuation behavior and exit choice strategies using agent-based modeling," *Procedia Eng.*, vol. 3, pp. 23–35, Jan. 2010.
90. L. Tan, M. Hu, and H. Lin, "Agent-based simulation of building evacuation: Combining human behavior with predictable spatial accessibility in a fire emergency," *Inf. Sci.*, Sep. 2014.
91. D. Shikhalev, K. Wagoum, A. Ulrich, and R. Khabibulin, "Development of a safest routing algorithm for evacuation simulation in case of fire," in *6th International Conference on Agents and Artificial Intelligence*, 2014, vol. 1.
92. H. Ehtamo, S. Heliövaara, T. Korhonen, and S. Hostikka, "Game Theoretic Best-Response Dynamics For Evacuees' Exit Selection," *Adv. Complex Syst.*, vol. 13, no. 01, pp. 113–134, Feb. 2010.
93. S. M. Lo, H. C. Huang, P. Wang, and K. K. Yuen, "A game theory based exit selection model for evacuation," *Fire Saf. J.*, vol. 41, no. 5, pp. 364–369, Jul. 2006.

94. T. Vicsek, A. Czirók, E. Ben-Jacob, I. Cohen, and O. Shochet, "Novel Type of Phase Transition in a System of Self-Driven Particles," *Phys. Rev. Lett.*, vol. 75, no. 6, pp. 1226–1229, Aug. 1995.
95. M. T. Kinateder, E. D. Kuligowski, P. K. Reneke, and R. D. Peacock, "A Review of Risk Perception in Building Fire Evacuation," National Institute of Standards and Technology, NIST TN 1840, Sep. 2014.
96. E. N. M. Cirillo and A. Muntean, "Dynamics of pedestrians in regions with no visibility— A lattice model without exclusion," *Phys. Stat. Mech. Its Appl.*, vol. 392, no. 17, pp. 3578–3588, Sep. 2013.
97. E. N. M. Cirillo and A. Muntean, "Can cooperation slow down emergency evacuations?," *Comptes Rendus Mécanique*, vol. 340, no. 9, pp. 625–628, Sep. 2012.
98. T. Korhonen and S. Heliovaara, "FDS+Evac: Herding Behavior and Exit Selection," *Fire Saf. Sci.*, vol. 10, pp. 723–734, 2011.
99. S. Bae, J.-H. Choi, C. Kim, W. Hong, and H. S. Ryou, "Development of new evacuation model (BR-radiation model) through an experiment," *J. Mech. Sci. Technol.*, vol. 30, no. 7, pp. 3379–3391, Jul. 2016.
100. E. D. Kuligowski, R. D. Peacock, and B. L. Hoskins, "A Review of Building Evacuation Models, 2nd Edition, NIST Technical Note 1680." National Institute of Standards and Technology, 2010.

Pedestrian Dynamics: From Empirical Results to Modeling

Andreas Schadschneider, Mohcine Chraibi, Armin Seyfried, Antoine Tordeux, and Jun Zhang

Abstract In this contribution, we review the state of the art of the interplay between empirical and theoretical studies of pedestrian dynamics. First, we introduce the main physical quantities characterizing the properties of a homogeneous crowd. A brief summary of some important empirical findings is given. Finally, we discuss the properties of microscopic pedestrian models. Different classifications of the models are proposed. We emphasize the relevance of empirical results and show how they can be used for validation and calibration.

1 Introduction

Modeling of pedestrian dynamics has become more and more relevant in recent years due to urbanization of cities. The increasing number of large-scale events underlines the need for accurate tools for planning and management in order to avoid crowd disasters where many people may get injured or even killed. The models implemented in such tools need to be validated and, in order to

A. Schadschneider (✉)
Institut für Theoretische Physik, Universität zu Köln, Köln, Germany
e-mail: as@thp.uni-koeln.de

M. Chraibi · A. Seyfried
Institute of Advanced Simulation, Forschungszentrum Jülich GmbH, Jülich, Germany
e-mail: m.chraibi@fz-juelich.de; a.seyfried@fz-juelich.de

A. Tordeux
School of Mechanical Engineering and Safety Engineering, University of Wuppertal, Wuppertal, Germany
e-mail: tordeux@uni-wuppertal.de

J. Zhang
State Key Laboratory of Fire Science, University of Science and Technology of China, Hefei, China
e-mail: junz@ustc.edu.cn

L. Gibelli, N. Bellomo (eds.), *Crowd Dynamics, Volume 1*, Modeling and Simulation in Science, Engineering and Technology,
https://doi.org/10.1007/978-3-030-05129-7_4

make accurate quantitative predictions, calibrated properly. This can only be achieved if reliable empirical data exist. Therefore, in recent years, more and more research groups have performed laboratory experiments with pedestrians to obtain trustworthy quantitative information about pedestrian motion and investigate qualitative phenomena. Obviously, laboratory experiments have both advantages and disadvantages compared to observational studies. On one hand, they are easily reproducible and can also be verified. In laboratory experiments, the pedestrian can be equipped with different kinds of sensors allowing to obtain accurate data. The studies are not being influenced by external uncontrollable factors like weather or light. On the other hand, it remains unclear if the test persons behave exactly in the same way as in everyday situations. Certain scenarios cannot be studied due to ethical and safety issues, e.g., extremely high densities or excessive pushing in bottlenecks. Nevertheless, laboratory experiments have improved our knowledge about pedestrian traffic considerably in the last 10 years, especially in "normal" situations.

This improvement has also consequences for the modeling of pedestrian dynamics. Although some aspects are still discussed controversially, we now have access to rich and reliable data for validation and calibration purposes. This has led to the improvement of existing models as well as the introduction of new modeling approaches.

In this contribution we give a short overview of the empirical results that are usually used to test model predictions in Sect. 2. Here we distinguish between quantitative results such as the fundamental diagram (flow-density relation) and collective effects that can be observed microscopically (e.g., lane formation or clogging). In Sect. 3 we propose a classification of the modeling approaches based on the interaction mechanism and the main variables of the description. Hereby, we will focus on microscopic models of pedestrian dynamics, i.e., models that distinguish individual agents and their motion. This allows to distinguish acceleration-based, velocity-based, and decision-based models. Then in Sect. 4, we discuss how the modeling approaches can be tested both qualitatively and quantitatively, where the empirical results in Sect. 2 will play an important role.

2 Empirical Results

Studies of empirical properties of pedestrian motion and evacuation have a long history that can be traced back more than 100 years when researchers started to study the influences of emergency exits [30]. At the beginning, most data were obtained in different places by field observation. For example, some researchers blended themselves into the crowd measuring their own speed in the stream to represent the speed of the corresponding pedestrian flow. Another popular method is filming pedestrian motion in public transportation places like subway stations and sidewalks and then analyzing their macroscopic characteristics by visual observation and manual counting. These earlier studies supply abundant data for pedestrian dynamics both on a quantitative and qualitative level. However, the common problem of these data

is their precision and reliability. It is not known whether data from individuals can be used to represent global properties of pedestrian flow or not. Visual observation and manual counting on sequences of videos may lead to large errors for the final results, especially quantitatively. In addition, other factors influencing pedestrian movement cannot be determined or excluded from these results. In this situation, in the last 20 years, a new approach became more and more popular which emphasizes the role of controlled experiments with large groups of pedestrians. With the development of computer science and image processing techniques and low prices of consumer electronics, e.g., video cameras, it is possible to obtain empirical data with higher precision and improved quality.

A main goal of any theory of pedestrian dynamics is a quantitative description of the observed phenomena. This requires definition of observable quantities that provide an accurate description of the relevant properties of pedestrian streams. In the following we introduce the most relevant observable and also discuss potential problems in measuring them. Many of these quantities are also used in related areas, for example, vehicular traffic.

2.1 Observables: Flow, Density, and Velocity

2.1.1 Flow

The pedestrian flow J is defined by the number of pedestrians crossing a fixed location of a facility per unit of time. In most cases, it is considered as a scalar quantity where only the flow normal to some cross section is taken into account. The flow can be measured in different ways. In the simplest method, the times t_i at which pedestrians pass a fixed measurement location are determined. The flow J is then related to the time gaps $\Delta t_i = t_{i+1} - t_i$ between two consecutive pedestrians i and $i + 1$ by

$$J = \frac{1}{\langle \Delta t \rangle} \qquad \text{with} \qquad \langle \Delta t \rangle = \frac{1}{N} \sum_{i=1}^{N} (t_{i+1} - t_i) = \frac{t_{N+1} - t_1}{N}\,, \tag{1}$$

which allows to estimate J for a given number N of observed pedestrians. Another approach uses the cumulative flow function $N(t)$ where pedestrians passing the cross section are numbered consecutively.[1] Taking the continuous limit, the time evolution of $N(t)$ allows to determine the flow as the time derivative $J_0 = N'(t)$. For a discrete time interval T, the flow is given by (see Fig. 1)

$$J_T = \frac{\Delta N}{T}, \qquad \text{with} \qquad \Delta N = N(t) - N(t + T). \tag{2}$$

[1] Formally, $N(t) = \sum_i \mathbb{1}_{t_i < t}$, with $\mathbb{1}_A = 1$ if A holds and $\mathbb{1}_A = 0$ otherwise.

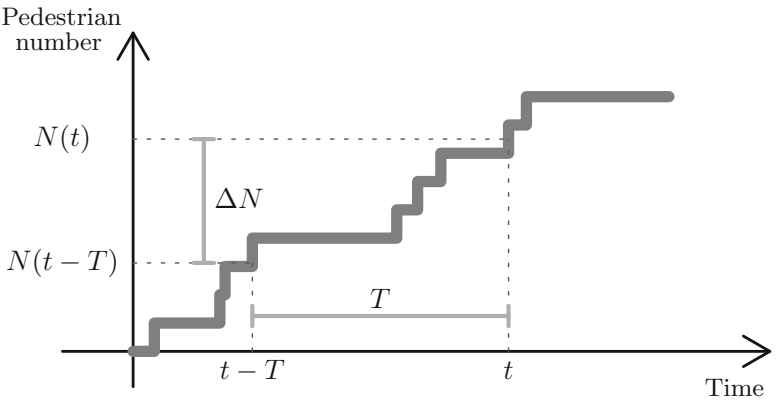

Fig. 1 Illustration of the cumulative flow function $N(t)$ and its relation to the flow on a time interval T

The flow of a pedestrian stream can also be measured by using ideas from fluid dynamics. The flow through a facility of width b is determined by the average density ρ and the average speed v of a pedestrian stream as

$$J = \rho\, v\, b = J_s b, \tag{3}$$

where the *specific flow*[2]

$$J_s = \rho\, v \tag{4}$$

gives the flow per unit-width. Equation (4) is usually called *hydrodynamic relation*.

These two definitions of the flow can lead to problems related to the way how velocities, densities, or time gaps are measured. When Eq. (1) is used, the flow is usually measured as time average at a certain location. In contrast, density measurements used in Eq. (3) are determined as an instantaneous mean value averaging over space. The underestimation of fast-moving pedestrians by the spatial average compared to the time average of the flow at a single measurement location can lead to a bias.[3] Furthermore most experimental studies that determine the flow using (3) for technical reasons combine an *average* velocity of a single pedestrian over time with an *instantaneous* density. However, the mean values only correspond when the average velocity of all pedestrians contributing to the density at a certain instant is considered. This procedure would be very time-consuming and has not been realized in practice up to now. Moreover, spatial averages are influenced by the

[2]In strictly one-dimensional motion often a line density (dimension: 1/length) is used. Then the *flow* is given by $J = \rho v$.

[3]For a discussion of this effect for the case of vehicular traffic, see e.g. [57, 73, 96].

fact that the dimension of the test section is usually of the same order of magnitude as the extent of the pedestrians. All these factors can contribute to the observed large differences in different measurements (see also the discussion in Sect. 2.3).

2.1.2 Density

In pedestrian dynamics, various quantities have been proposed that are related to different notions of density. Fruin [43] has proposed to quantify the pedestrian load of a facility by the *pedestrian area module* which is given by the reciprocal of the density. The *inter-person distance* introduced by Thompson and Marchant [174] is measured between center coordinates of the assessing and obstructing persons. For a pedestrian stream of evenly spaced persons, Thompson and Marchant [174] call $\sqrt{\frac{1}{\rho}}$ the *average inter-person distance*. In [61] the local density is obtained by averaging over a circular region of radius R

$$\rho(\mathbf{r}, t) = \sum_i f(\mathbf{r}_i(t) - \mathbf{r}), \tag{5}$$

where $\mathbf{r}_i(t)$ are the positions of the pedestrians i in the neighborhood of $\mathbf{r}$ and $f(\ldots)$ is a Gaussian, distance-dependent weight function. The kernel function f depends on a bandwidth parameter for calibration. In the *Voronoi method* [168], which has the advantage of not needing additional parameters, the kernels are uniform on the cells given by the Voronoi diagram (see Fig. 2).

Predtechenskii and Milinskii [139] use a density definition that differs from the ones given above. They consider the ratio of the sum of the projection area f_i of the bodies and the total area of the pedestrian stream A, defining the (dimensionless) density $\tilde{\rho}$ as

$$\tilde{\rho} = \frac{\sum_i f_i}{A}. \tag{6}$$

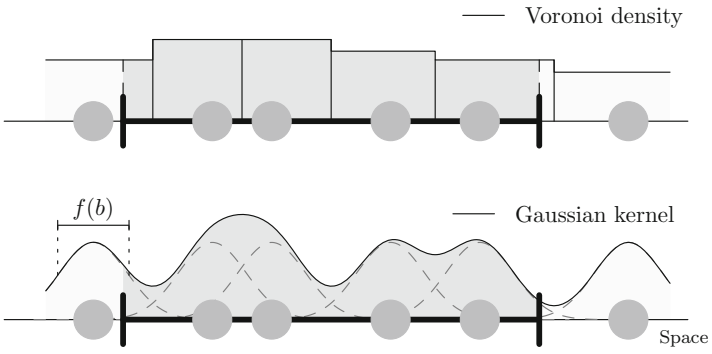

Fig. 2 Examples of Voronoi and Gaussian kernel estimations for the density of pedestrians in one dimension. The Gaussian kernel estimation depends on a bandwidth parameter b for calibration

This quantity is known as *occupancy* in the context of vehicular traffic. Since the projection area f_i depends strongly on the type of person (e.g., it is much smaller for a child than an adult), the densities for different pedestrian streams consisting of the same number of persons and the same stream area can be quite different.

2.1.3 Mean Speed

As for flow and density, there exist various methods to measure the mean speed. For instance, the time mean speed averages the speeds of pedestrians over the time, while the space mean speed averages the speed over the space. Space mean time is generally determined by measuring the traveled distance of the pedestrians over two successive photographs of the environment. Time mean is derived from the crossing times of two consecutive points. It is important to notice that in general space and time mean speeds are not identical. This statement, closely related to double-loop detector measurement technique, has been pointed out early for traffic flow [183]. However, the difference can be substantial for pedestrian flows as well [82]. The time mean speed does not allow to recover the traveled time of the pedestrian nor the hydrodynamic relation (4) borrowed from fluid dynamics the harmonic average should be used instead to recover (asymptotically) the space mean speed [183] and so travel time and hydrodynamic relation.

The difference between the space and time mean speeds can be nicely tackled thanks to trajectories. Let us denote d_i the traveled distance and t_i the traveled time of pedestrian trajectories in the space-time diagram. The speed of pedestrian i is therefore $v_i = d_i/t_i$. According to Edie [33], a natural way to estimate the mean speed of the trajectories consists in dividing the total traveled distance by the total travel time:

$$V_E = \frac{\sum_i d_i}{\sum_i t_i}. \tag{7}$$

Let us fix now the traveled distance to a fix value d (estimation of the mean speed on a horizontal band in the time-space diagram of the trajectories, see Fig. 3). Such a methodology is the one used above with entry and exit times. One gets the harmonic mean

$$V_E = \frac{\sum_i d}{\sum_i t_i} = \frac{n}{\sum_i 1/v_i}. \tag{8}$$

If we fix the traveled time to a fixed value t (estimation of the speeds from two successive photographs of the system, this corresponds to estimation of the mean speed on a vertical band in the time-space diagram of the trajectories; see Fig. 3); then one gets

$$V_E = \frac{\sum_i d_i}{\sum_i t} = \frac{1}{n}\sum_i v_i. \tag{9}$$

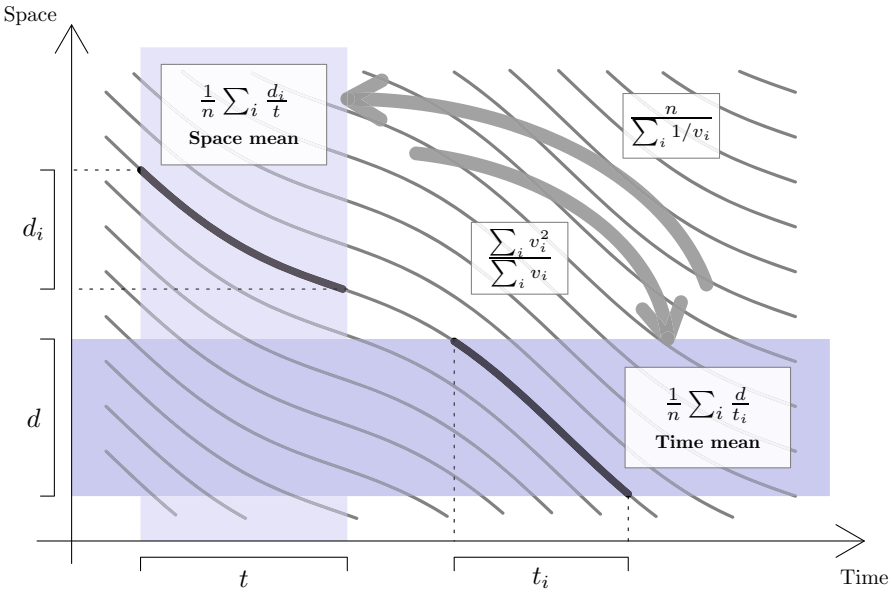

Fig. 3 Illustration for the measurements of the mean speed for trajectories with a fixed time interval (space mean speed, vertical band) and a fixed distance (time mean speed, horizontal band), and the harmonic and contraharmonic means allowing to recover asymptotically one definition from the other

As expected, Edie's definition for the mean speed of trajectories corresponds to the space mean speed.

2.2 Collective Phenomena

Pedestrian dynamics shows a large variety of collective effects and self-organization phenomena. Although these are macroscopic phenomena, they are a consequence of microscopic interactions between individuals. Therefore they can be viewed as benchmark tests for any model of pedestrian dynamics.

2.2.1 Jamming and Clogging

At high densities, often jamming and clogging phenomena are observed in pedestrian crowds. Jamming is observed when the inflow exceeds the capacity. This often happens at locations with reduced capacity. Such bottlenecks are encountered frequently in every facility, e.g., at exits (Fig. 4), other kinds of narrowings, and stairs. Most jamming phenomena are a consequence of the exclusion principle and

Fig. 4 Clogging in front of a bottleneck

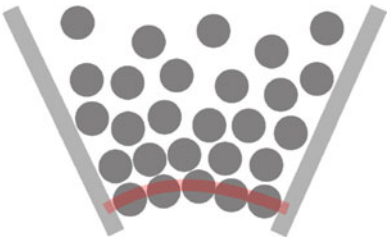

Fig. 5 Formation of an arch (red line) stabilized by friction in a funnel. Similar arches are observed in pedestrian evacuations near a bottleneck (e.g., an exit)

do not depend strongly on the microscopic dynamics of the particles. Exclusion here means that space occupied by one particle is not available for others. A detailed understanding of the conditions under which clogging occurs is important for many practical applications. In fact, clogging in pedestrian crowds has many similarities with clogging in other particulate systems, e.g., granular matter. For the latter it has been shown that so-called arching phenomena occur in the flow through narrow openings (Fig. 5) [186]. Arches are self-stabilizing structures that are formed under contact of the particles due to friction effects. Similar structures were already observed in [138] in front of doors under high pressure. Experimental studies on clogging at bottlenecks can be found in [49, 114].

Jamming can also be observed in pedestrian streams moving in opposite directions (counterflow). Here oppositely moving individuals can mutually block each other's forward motion. At high densities or high inflows, it is not possible to turn around and move back which then leads to a gridlock.

2.2.2 Density Waves, Stop-and-Go Waves

Density variations that are quasiperiodic density variations in space and time are usually called density wave. They are, e.g., observed in densely crowded corridors

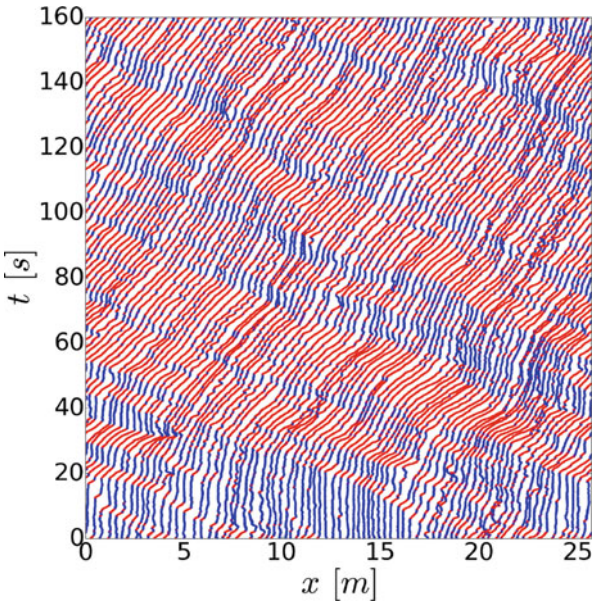

Fig. 6 Trajectories of pedestrians on a section during an experiment on a corridor with periodic boundary conditions [16]. The initial configuration is uniform. However, stop-and-go waves occur and propagate after some time. Here the trajectories of stopped or slowly moving pedestrians are shown in blue, whereas those of moving pedestrians are presented in red

in subway stations as well as during experiments (see [160, 161] and Fig. 6). Here phenomena similar to stop-and-go vehicular traffic are observed. These can also be observed in controlled experiments of single-file motion [137, 161] and in large crowds, e.g., on the Jamaraat Bridge during the Hajj pilgrimage 2006 in Mecca [60]. As in vehicular traffic, density fluctuations in single-file motion move backward opposite to the movement direction of the pedestrians. A kind of phase separation into standing and slowly moving pedestrians is observed. In contrast, in highway traffic, a separation into standing and fast-moving cars is found (neglecting a narrow transition layer) which is usually explained by the so-called slow-to-start behavior of cars [3]. This fundamental difference indicates that in pedestrian motion additional mechanisms must be relevant which have not yet been fully understood.

2.2.3 Lane Formation

When two groups of people move in opposite directions (counterflow), often dynamically varying lanes are formed consisting of pedestrians moving in the same direction (Fig. 7) [124, 127, 188]. This reduces strongly the probability of collisions with oncoming pedestrians which is more comfortable and allows higher walking speeds. It should be noted that the occurrence of lane formation does not require a preference of moving on one side. It also occurs in situations without left or right preference. Although cultural differences for the preferred side are observed, they are not essential for the phenomenon itself but have an influence on the kind of lanes formed and their order. The number of lanes can vary considerably with

Fig. 7 Bidirectional flow with two comparative lanes in each flow direction

the total width of the flow and is usually not constant in time. The number of lanes in opposite directions can be different corresponding to a kind of spontaneous symmetry breaking.

Lane formation can be described quantitatively, e.g., by the band index [188] which is basically the ratio of pedestrians in lanes to their total number. Another characterization can be obtained from (transversal) velocity profiles at fixed positions [14]. Since similar phenomena have been observed in other physical systems, e.g., colloidal mixtures driven by an external field [17, 32, 141], the order parameter $\phi = \frac{1}{N}\left\langle \sum_{j=1}^{N} \phi_j \right\rangle$ introduced there has been adopted for pedestrian streams. Here $\phi_j = 1$ if the lateral distance to all other particles of the other type is larger than a typical density-dependent length scale and $\phi_j = 0$ otherwise. Although lane formation is one of the most important benchmark tests for any model, quantitative empirical studies are rather rare [85, 188, 195]. At high densities, several theoretical models predict a jamming transition, i.e., the transition to a state where no movement is possible anymore (gridlock) [98]. However, so far there is no conclusive empirical evidence for this transition. From the existing experiments, it can be concluded that such a transition – if it exists – will occur at densities larger than 3.5 persons/m^2 [195].

2.2.4 Other Collective Effects

At bottlenecks, e.g., doors, oscillatory changes of the direction of motion in counterflow are frequently observed. The flow direction is stable until a pedestrian who wants to move in the opposite direction is able to pass through the bottleneck making it easier for others to follow her.

Various collective patterns of motion can be observed at intersections. Usually they lead to a higher efficiency of motion. Typical examples are (short-lived) roundabouts that are formed dynamically. Even though they require small detours, they can be advantageous by allowing for a "smoother" motion.

2.2.5 Emergency Situations, "Panic"

Collective phenomena observed in emergency situations have often been misleadingly attributed to "panic behavior." However, there is no universally accepted definition of "panic." Instead, social scientists discuss the underlying theory about collective behavior of crowds formulated by Le Bon [94] critically (see, e.g., [110, 157]). Certain aspects are usually associated with this concept [72, 167], e.g., competition for scarce or dwindling resources (e.g., safe space or access to an exit). It is often assumed that this leads to selfish, asocial, or even irrational behavior and contagion that affects large groups. A closer investigation of many crowd disasters has revealed that most of these characteristics either have not been observed at all or have played no role for the outcome [71, 144]. Often the reason for these accidents is much simpler, e.g., a capacity of the facility that is too small. Therefore the term "panic" should be avoided as it implicitly puts the blame on the victims, *crowd disaster* being a more appropriate characterization.

2.3 Fundamental Diagram

The fundamental diagram, describing the relation among density ρ, velocity v, and flow J, is basic input in applications for the design and dimensioning of pedestrian facilities [43, 125, 138]. Furthermore it is a quantitative benchmark for models of pedestrian dynamics [25, 75, 111, 165]. In general, there is a widespread consensus that velocity decreases with increasing density. However, the relation is affected by several factors including culture and population differences [18, 61, 113], differences between uni- and multidirectional flow [92, 124, 140], short-ranged fluctuations [140], the type of traffic [127], different types of facilities, etc. In this section, we will mainly discuss the fundamental diagrams of pedestrian flows in different types of geometries.

2.3.1 Single-File Movement in Circuit

For the pedestrian movement along a line, the speed for walking pedestrians depends linearly on the step size [184] and the inverse of the density [164]. In most studies for this case, the density is defined as the inverse of headway and therefore with the unit of pedestrians per meter. External factors like lateral interference and curvature effects of the path have little influence on the fundamental diagram in the density

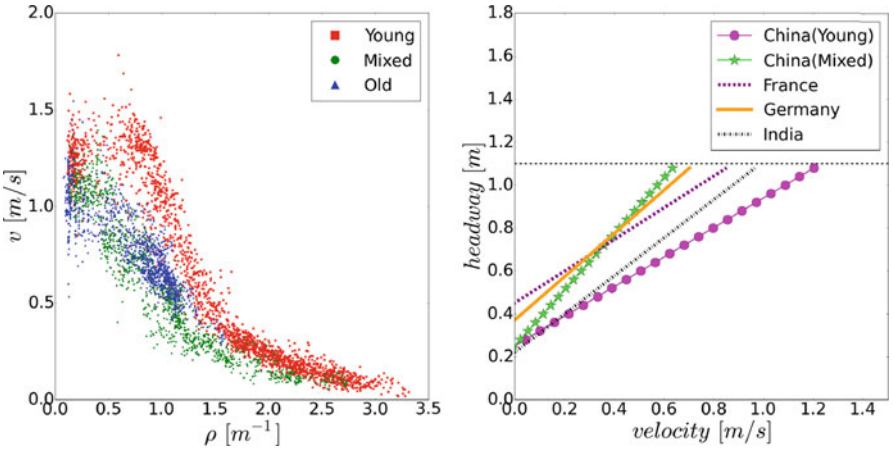

Fig. 8 Fundamental diagrams for single-file movement of pedestrians in a circuit (left) and comparison of linear fits of the headway-velocity relation in the strongly constrained regime for experiments from different countries [16]

domains considered [164, 197]. However, the influence of cultural differences [18, 101] and the composition of crowd should not be ignored. For example, the speed of Indians is less dependent on density than the speed of Germans. For a crowd composed of young students with nearly the same age, the speed is always higher than that of a mixed group of elder and young test persons at the same density range (see Fig. 8). When considering directly the relation between the headway and velocity, different linear regimes are obtained, and the corresponding slope for each regime represents the adaptation time. Instead of changing continuously, the adaptation time takes three discrete values [69]. However, for a homogeneous group composed of young students, only two adaptation times are observed [16]. Figure 8 shows linear fits of the headway-velocity relation in the strongly constrained regime in different countries.

2.3.2 Pedestrian Movement in Straight Corridor

Corridors are simple and common elements in almost all types of pedestrian facilities designed for uni- and bidirectional pedestrian flow. The fundamental diagram both for uni- and bidirectional flow in corridor with different widths can be unified into one diagram for specific flow [56, 124, 127, 128, 193] (see Fig. 9, left). When comparing the fundamental diagrams of uni- and bidirectional pedestrian streams, clear differences can be observed especially for densities higher than 1.0 m^{-2} (see Fig. 9, right) [92, 124, 195]. The flow becomes almost independent of the density and shows a plateau. The maximal specific flow is lower in bidirectional flow. Regarding the influence of the flow ratio of bidirectional streams, it seems not to be an independent factor influencing the fundamental diagram. However, no

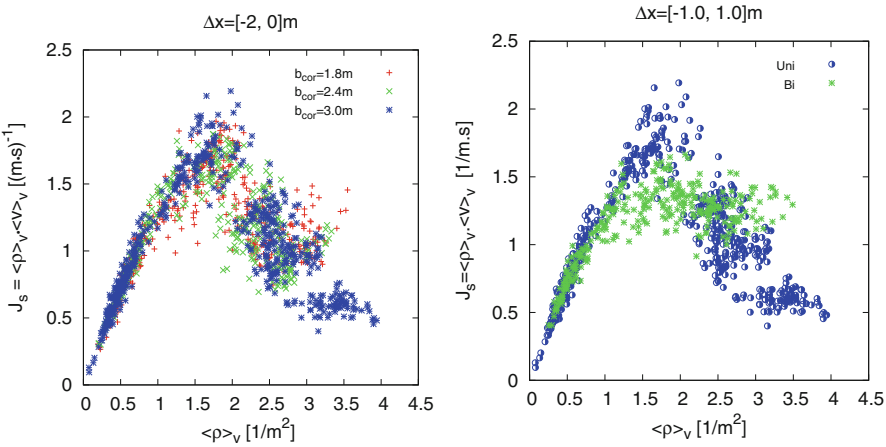

Fig. 9 Fundamental diagrams for pedestrian movement in a straight corridor. The left results are obtained from unidirectional movement in corridors with three different widths [193], while in the right, the fundamental diagrams of uni- and bidirectional flow are compared [195]

consensus is reached up to now [2, 36, 93, 179]. Surprisingly some studies found that the sum of flow and counterflow in corridors is larger than the unidirectional flow and that, for equally distributed loads, it can be twice the unidirectional flow [85].

2.3.3 Pedestrian Movement Through Bottlenecks

For the characterization of the performance of bottlenecks, two cases have to be distinguished. In the free flow case, the flow through the bottleneck is identical to the incoming flow. In the congested case, the incoming flow exceeds the capacity (the maximal possible flow) of the bottleneck. Then congestion occurs, and the density in front of the bottleneck increases. The density in front of the bottleneck is higher than that inside the bottleneck [26, 138, 162]. Surprisingly, several experiments have found that the maximal flow at bottlenecks can exceed the maximum of the empirical fundamental diagram [115, 120]. This is not fully understood up to now as it contradicts a rather general result from non-equilibrium physics [135, 149]. Possible explanations are finite-size effects or psychological factors.

In case of congestion, pedestrians can cooperate or compete while entering the bottleneck. One strategy to successfully enter a bottleneck in a competitive situation is pushing, which could lead to blockages (clogs) limiting the flow through the bottleneck. Here we focus on pedestrian movement in cooperative situations. One of the most important practical issues is how the capacity of the bottleneck increases with the width which has already been studied at the beginning of the twentieth century [30, 38]. A stepwise increase of capacity with the width is up to

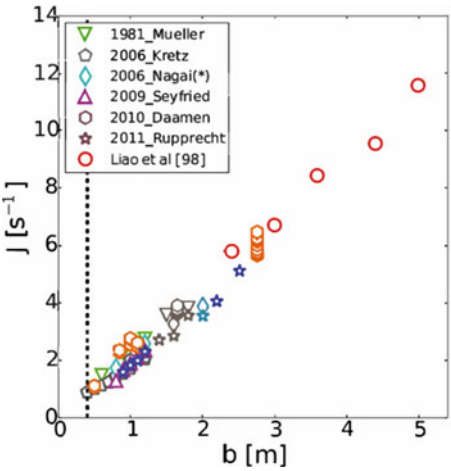

Fig. 10 Influence of the width of a bottleneck on the flow. Experimental data [114, 115, 120, 162] of different types of bottlenecks and initial conditions. The black dashed line corresponds to $b = 0.4$ m. The flow shows a linear dependency of bottleneck width. The widths of Nagai et al. [120] are scaled by $b = b_{\text{desk}} + 0.4$ m [99]

now an assumption made in several building codes and design recommendations [119, 133]. The empirical results in [65, 66] also imply a stepwise increase of capacity. However, the investigation was restricted to two values of the width. When more values of the bottleneck width are considered from different laboratory experiments [87, 114, 115, 120, 162], it is found that the flow does not necessarily depend on the number of lanes. On the contrary, the capacity is given by the maximum of the fundamental diagram, and a linear function of the width is assumed in [43, 125, 138, 175, 184] (see Fig. 10). The exact geometry of the bottleneck has only a minor influence on the flow [162], while a high initial density in front of the bottleneck can increase the resulting flow values [120]. The width of the passage [146] and the existence of an obstacle [59, 189] in front of the bottleneck also influence the flow through the bottleneck. Shorter bottlenecks allow higher flows than longer ones [100, 153, 160]. The total flow at bottlenecks with bidirectional movement is higher than it is for unidirectional flows [59]. Population with disabled pedestrians could lead to a lower flow and that with mainly children leads to the highest flow [27].

2.3.4 Pedestrian Movement on Stairs

Stairs in multi-storey or high-rise buildings are a major determinant for the evacuation time. Generally, they have to be considered as bottlenecks for pedestrian flow due to their physical dimension which is often smaller than other parts of a building. Unlike on horizontal planes, the speed has to be reduced, and pedestrians become fatigued more quickly while moving on stairs. The free speed has been shown to depend on the incline [43–45, 53], environment conditions (comfortable, normal, dangerous) [139], age and gender [43], tread width [41], length of a stair [86], and health condition, especially disablement [10].

Consequently, there are more degrees of freedom (e.g., upward and downward movement, the influence of riser height and tread length, exhaustion effects for upward motion, etc.) which influence the fundamental diagram of movement on stairs compared to the movement on flat terrain. Different fundamental diagrams for stairs are presented in four well-known planning handbooks for pedestrian facilities and evacuation routes [43, 125, 138, 184]. Figure 11 shows the fundamental diagram for up- and downward movement on stairs collected by Burghardt et al. [12] from [11, 20, 40, 41, 53, 56, 67, 86, 91, 158, 171, 172, 190]. These empirical data are obtained from different conditions (e.g., different locations and slopes of the stairs, different measurement methods, etc.). A linear increase of the specific flow is observable with minor differences of the incline at low densities for both up- and downward motions. However, the flow decreases with increasing slope of stairs [12, 53]. In the experiment of [12], the density range where the specific flow reaches the maximum is larger for downward than for upward motion. For downward motion the specific flow at the external staircase fades into a plateau for densities higher than $2.0\,\mathrm{m}^{-2}$. For the stairs located in the lower tier of the grandstand, the specific flow increases with higher densities, while in the upper tier, a decrease of flow appears.

2.3.5 Other Geometries

Pedestrian flow through other structures like T-junctions or crossings is more complex than for the elements described in the previous subsections. In T-junctions, depending on the situation, bottleneck flow, merging flow, or splitting flow is possible. For motion around corners, it is still not known how the effective width of the corridor reduces and changes with increasing inflow. The existing empirical data shows that the fundamental diagrams of streams in front and behind the turning at the corner agree well and are in accordance with that from T-junction flow behind the merging [192]. The fundamental diagram obtained in the main stream is different from that in branches [194]. At crossings, pedestrians from different directions have different preferred velocities and different orientations. Therefore the local velocity or flow cannot be measured in the usual way. Adapted definitions have been proposed [15, 97]. Surprisingly, the fundamental diagrams for bidirectional flow and four-directional crossing flow show no apparent difference in the density ranges covered in the experiments. However, there are indications that measurement methods, motivation of pedestrians, and experimental setup may have a strong influence.

3 Classification of Models

Models of pedestrian dynamics can be classified on different levels according to the relevant timescale (Fig. 12). The *strategic level* describes long-term decisions on the activities that pedestrians like to perform. The *tactical level* concerns short-term

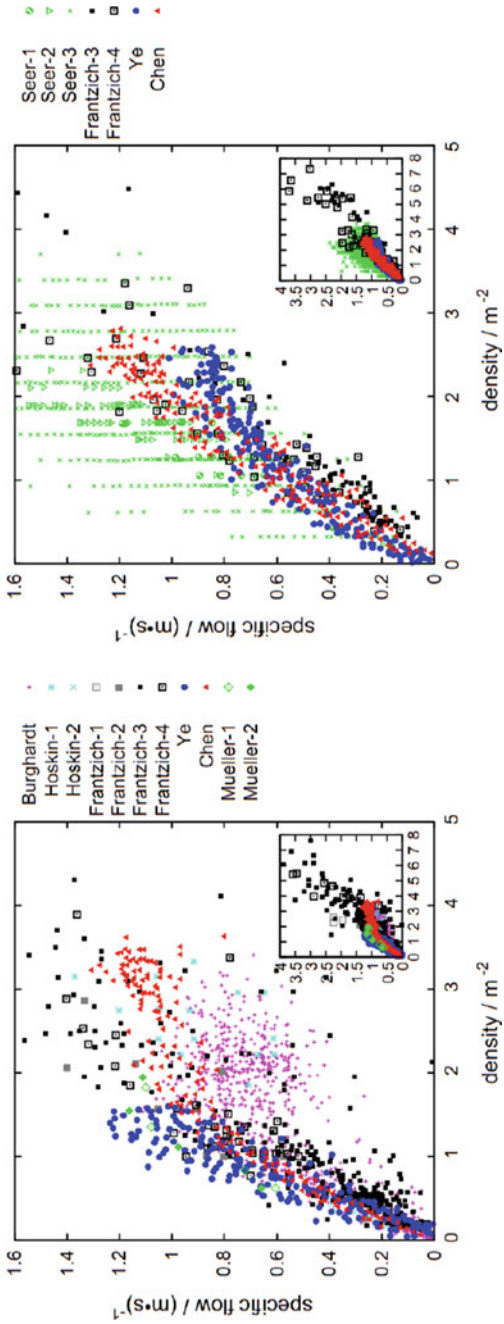

Fig. 11 Fundamental diagram for pedestrian movement on stairs (left, downward; right, upward) [12]

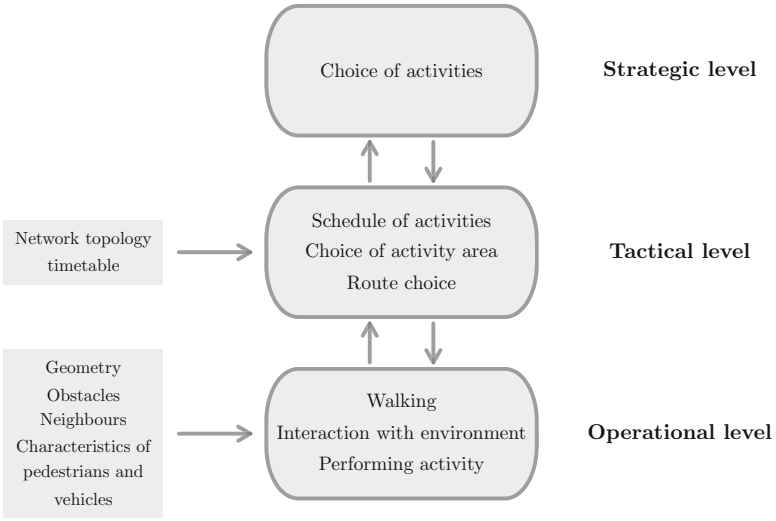

Fig. 12 The different levels of modeling of pedestrian behavior [24, 64]

decisions made by the pedestrians, especially the route choice taking into account potential obstacles, the density of the pedestrian crowd, etc. The strategic and tactical levels can be summarized as extrinsic factors for the pedestrian motion. Their modeling would require information from disciplines like sociology and psychology.

In the following our focus will be on the *operational level* which describes the actual walking behavior of pedestrians, e.g., their immediate decisions necessary to avoid collisions. Modeling on the operational level usual makes use of physics-based approaches where pedestrians are treated as particles that interact with each other and with the environment. They are then formulated in mathematical form that allows quantitative predictions. The goal is to find models which are as simple as possible but at the same time can reproduce "realistic" movement dynamics. Extensions to "intelligent" particles are possible and often referred to as *multi-agent systems*. They usually capture parts of the tactical or even strategic level, e.g., by taking into account goals and desires of the agents.

On the operational level, the various modeling approaches can be further classified. First, *heuristic models* can be distinguished from *first-principle models*. Heuristic models typically include several interaction terms that are considered to be relevant. They are parametrized by model parameters which can be used to fit empirical data. In contrast, first-principle models are derived from certain postulates considered to be fundamental.

Next, *microscopic models* can be distinguished from *macroscopic models*. In macroscopic models, the state of the system is described by time and space averages of the density, velocity, and flow which are derived from the trajectories of the persons. Therefore different individuals cannot be distinguished. However,

microscopic models represent each individual separately which allows to introduce individual properties in a natural way. Pedestrian motion is usually described by three basic variables, namely, space (position), time, and state variable (e.g., velocities). Each of these variables can either be discrete (i.e., an integer number) or continuous (i.e., a real number). In fact, combinations are possible, e.g., a continuous space combined with discrete time as in so-called coupled map lattices. The most common choices are approaches where all variables are discrete, e.g., cellular automata models, and models where all variables are continuous as in the social-force models. In this contribution we will mainly focus on microscopic approaches.

Microscopic models of pedestrian dynamics can be viewed as interacting many-particle systems. They can be classified by the relevant variable used to determine the motion and the way for implementing the interactions among pedestrians, e.g., acceleration- and velocity-based models. In *acceleration-based models*, the interactions are typically described by the so-called *social forces*: agents "feel" the force exerted by others and the infrastructure. This is inspired by the observation that the presence of others leads to deviations from straight motion. In analogy to Newtonian mechanics, a force is made responsible for these accelerations. In addition, physical forces are relevant, e.g., when persons are in contact. In *velocity-based models*, speed and direction of motion are determined from the positions of the surrounding neighbors and obstacles by taking into account collision avoidance and speed optimization principles. In the simplest case, the speed is proportional to the distance to the next agent/obstacle in front, while the chosen direction of motion maximizes the speed to the desired destination. Both acceleration- and velocity-based models emphasize the extrinsic properties and their relevance for the motion of the agents. However, in *rule-based models* (or *decision-based models*), pedestrians make "decisions" based on the current (local) situation in their neighborhood, their goals, etc. The rules are often justified by psychology. Consequently, these kind of models can be interpreted as *position-based models*, since their dynamics is not determined by acceleration nor velocity. A typical example for decision-based models is cellular automata.

Besides, the dynamics of pedestrians can either be deterministic or contain stochastic elements. For deterministic models the future movement is completely determined by the present state. In contrast, in stochastic models, pedestrians can react differently in the same situation. The alternatives are chosen with certain probabilities that are usually determined from the current state. Stochastic behavioral rules often generate a rather realistic representation. They reflect the lack of knowledge of the underlying physical processes that determine the decision-making. This "intrinsic" stochasticity is to be distinguished from external "noise" that sometimes is added to the *macroscopic* observables, like the position or velocity which is often used to avoid certain unrealistic configurations, like completely blocked states. Here the overall behavior is very similar to the deterministic case. However, for intrinsic stochasticity, the deterministic limit usually has very different properties.

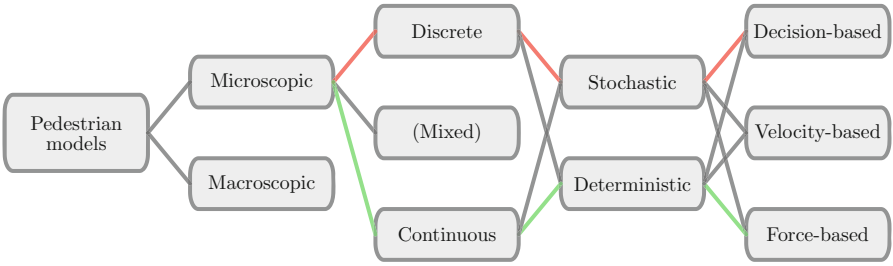

Fig. 13 Based on the proposed model classification, a large number of different approaches can be distinguished. Here we show only (part of) the classification scheme for microscopic models. The most common approaches are discrete, stochastic, rule-based models (red) and continuous, deterministic acceleration-based models (green)

Figure 13 shows the variety of model classes obtained from this classification. There are examples for almost every class shown here. In the following we will describe some model classes in more detail.

3.1 Acceleration-Based Models

In 1975 Hirai and Tarui proposed the first known microscopic acceleration-based model to investigate the movement of pedestrians in a 2D space [63]. In their seminal work, the authors investigated several aspects of human's behavioral motion. On one side, the proposed model considered the movement of pedestrians on the "operative level," where pedestrians move in the direction of an assigned goal while avoiding collisions with other pedestrians or obstacles. On the other side, the model incorporates different aspects of the "tactical level" of human behavior as well, e.g., group behavior and the influence of guiding signs on agent's wayfinding – aspects which recently caught the attention of the community of pedestrian dynamics with several emerging studies.

The equation of motion of the *Hirai-Tarui model (HT model)* is

$$m_i \frac{d^2\mathbf{x}_i}{dt^2} + \nu_i \frac{d\mathbf{x}_i}{dt} = \mathbf{f}_{1i} + \mathbf{f}_{2i} + \mathbf{f}_{3i}, \tag{10}$$

where m_i, ν_i, and $\mathbf{x}_i$ are the mass, coefficient of viscosity, and position of the individual i, respectively. $\mathbf{f}_{1i}$, $\mathbf{f}_{2i}$, and $\mathbf{f}_{3i}$ are external forces acting upon the individual i, implementing different modeling concepts. $\mathbf{f}_{1i}$ is a force required by the individual i to form a group together with other individuals and to move forward, while $\mathbf{f}_{2i}$ is a force exerted by the environment around the individual i. $\mathbf{f}_{3i}$ is a random force acting upon the individual i to consider uncertainties in the modeled behavior. The mean forces $\mathbf{f}_{ji}$ $((j = 1, \cdots, 3))$ are defined as a superposition of other forces, expressing different ideas.

The "group" force, for instance, consists of three components:

$$\mathbf{f}_{1i} = \mathbf{f}_{ai} + \mathbf{f}_{bi} + \mathbf{f}_{ci}, \tag{11}$$

where $\mathbf{f}_{ai}$ is a driving force causing i to move forward with constant speed. $\mathbf{f}_{bi}$ is an interaction force acting between the individual i and other individuals. Depending on the distance between two pedestrians, it can be attractive of repulsive. Finally, $\mathbf{f}_{ci}$ is the group force which acts only if some individuals move together in a restricted domain.

Both forces $\mathbf{f}_{ai}$ and $\mathbf{f}_{ci}$ depend on distance as well as angle. This expresses the observation that the influence of other pedestrians on i is greater in its direction of motion than in transversal direction. No forces act on individuals from behind.

In analogy to the "group force," the "environmental" force $\mathbf{f}_{2i}$ is defined as the sum of other forces, each with s specific intent:

$$\mathbf{f}_{2i} = \mathbf{f}_{wi} + \sum_{k} (\mathbf{f}_{eik} + \mathbf{f}_{fik}) + \mathbf{f}_{gi} + \mathbf{f}_{hi}, \tag{12}$$

where $\mathbf{f}_{wi}$ is a repulsive force acting from other static objects like walls and obstacles. Its magnitude is inversely proportional to the distance perpendicular to the wall.

The forces $\mathbf{f}_{eik}$ and $\mathbf{f}_{fik}$ are attractive and act within a semicircular domain around a guiding sign or symbol k. Formally both forces are identical. The main difference is that, while the first force acts only if k is in the visibly field of i, the second force will still be active if i "memorizes" it. In all cases it is assumed that i still moves to the nearest exit.

$\mathbf{f}_{gi}$ is an attraction force pulling individuals near the exit. When this force is active, the sign forces $\mathbf{f}_{eik}$ and $\mathbf{f}_{fik}$ are not. The last force $\mathbf{f}_{hi}$ is a constant force causing pedestrians to move away from "dangerous" areas.

The last main term in the model $\mathbf{f}_{3i}$ is a random force acting upon i. Its direction varies stochastically, and its magnitude is a function of the distance between i and the wall.

Hirai and Tarui showed that their model exhibits, to some extent, realistic evacuation behavior in a simplified train station. The authors validated their model with respect to experiments performed on rats, making the assumption that human behavior in "panic"-like situations may be comparable to animal dynamics. They showed that the tactical component of the model at least exhibits comparable results to the empirical data. Some patterns in the behavior of the simulated crowd have been found to be satisfactory and in agreement with the rat experiments. Although the model was not elaborated further, it shows some original concepts that were investigated lately in different works, e.g., group behavior, route choice modeling, attraction to a site, memory effects of objects, etc.

The HT model inspired several acceleration-based models which became one of the most used and well-studied classes of models.As a prominent example, we

mention the social-force model [62] which describes the movement of pedestrians in two-dimensional space by means of superposition of driving and repulsive forces:

$$\frac{d^2\mathbf{x}_i}{dt^2} = \mathbf{f}\Big(\mathbf{v}_i, \Delta\mathbf{v}_{ij}, \Delta x_{ij}\Big) + \frac{\mathbf{v}_i^{(0)} - \mathbf{v}_i}{\tau}, \tag{13}$$

where $\mathbf{f}$ is the sum of the interactions of i with its environment and τ is a time constant. Here, the driving force describes, in contrast to the HT model, an exponential velocity relaxation. The interactions with the environment ($\mathbf{f}$) are composed of several components. We can distinguish between "social" forces responsible for collision avoidance and "contact forces" designed to avoid excessive overlapping among pedestrians, especially in high densities.

For a review of the state of the art of the social-force model and its derivatives, we refer to [19].

3.2 Velocity-Based Models

In velocity-based (VB) models, the velocity is instantaneously adjusted to the neighborhood and the environment with no inertia or an implicit implementation of a reaction time. Such a modeling approach is largely inspired by motion planning in robotics, since robots move with almost no inertia and react instantaneously to a command. Generally speaking, VB approaches are based on visual considerations (local interaction) and optimization techniques under collision avoidance constraints. Mathematically, VB models are differential equations of first order. A typical example is

$$\frac{d\mathbf{x}_i}{dt} = \mathbf{V}\big(\mathbf{x}_j - \mathbf{x}_i, \mathbf{v}_j\big). \tag{14}$$

Here the velocity is a function $\mathbf{V}$ depending on the relative positions $\mathbf{x}_j - \mathbf{x}_i$ and velocities $\mathbf{v}_j$ of the neighbors j.

In *velocity obstacle models* [37], the velocity is determined by minimizing the deviation to the desired speed while avoiding collision. The collision possibilities are evaluated over horizon times by assuming constant velocities of the neighbors and carrying out the velocity obstacle cones VO(i) (see Fig. 14). No collision occurs when the velocity is set outside the cones. The velocity is then the solution of the optimization problem

$$\mathbf{V}_i = \underset{\mathbf{v}\notin\{\mathrm{VO}(i)\}}{\arg\min} \|\mathbf{v} - \mathbf{v}_0\|, \tag{15}$$

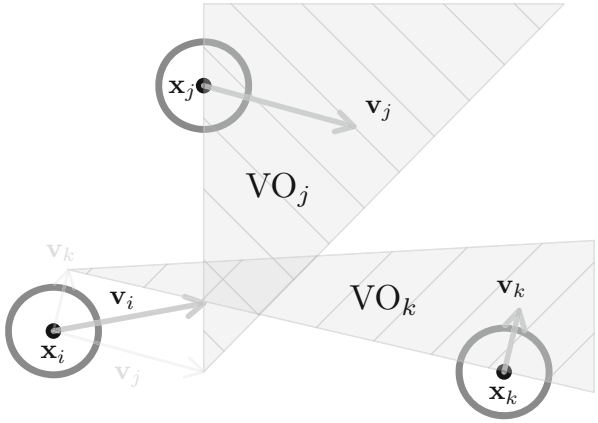

Fig. 14 Velocity obstacle cones VO(i) for the pedestrian i. No collision occurs when the velocity is set outside the cones

which minimizes the deviation to the desired speed $\mathbf{v}_0$. Similar optimization problems coupled to exclusion constraints in case of contact are solved in [108, 109] for evacuation dynamics.

Discretizations of velocity obstacle models can describe undesired ping-pong oscillatory effects when two pedestrians are switching from one direction to another at each time step. This phenomenon results from the implicit definition of velocities in the model (the speed of a pedestrian depends on the speed of the neighbor and vice versa). The *reciprocal velocity obstacle* (RVO) model allows to avoid this undesired behavior by taking into account the fact that the neighbors make similar collision avoidance reasoning [181]. However, this formulation only guarantees hard-core body exclusion under specific conditions. The *optimal reciprocal collision avoidance* (ORCA) overcomes this limitation and provides sufficient and efficient conditions for moving agents to avoid collisions among one another [180]. ORCA modeling approach and its variants are frequently used to describe pedestrian dynamics (see, e.g., [54, 55, 74, 112, 130]).

Other VB models consider the velocity as the product of a speed V (scalar) by a direction $\mathbf{e}$ (such that $\|\mathbf{e}\| = 1$)

$$\frac{d\mathbf{x}_i}{dt} = V\big(\mathbf{x}_j - \mathbf{x}_i, \mathbf{v}_j\big)\,\mathbf{e}\big(\mathbf{x}_j - \mathbf{x}_i, \mathbf{v}_j\big). \tag{16}$$

Both speed V and direction $\mathbf{e}$ depend on the relative positions of the neighbors and their velocities. In the optimal velocity VB approach, the speed depends, in analogy to optimal velocity (OV) models in traffic, on the minimal distance in front [176], while the direction is, as in acceleration-based models, a sum of exponential repulsion with the neighbors [31]. If $\mathbf{e}_i$ is the direction of the pedestrian i, $\mathbf{e}_{i,j}$ the direction from j to i and $s_{i,j} = \|\mathbf{x}_j - \mathbf{x}_i\|$ the spacing distance between pedestrians i and j and if the pedestrians are considered as discs of diameter ℓ, then the

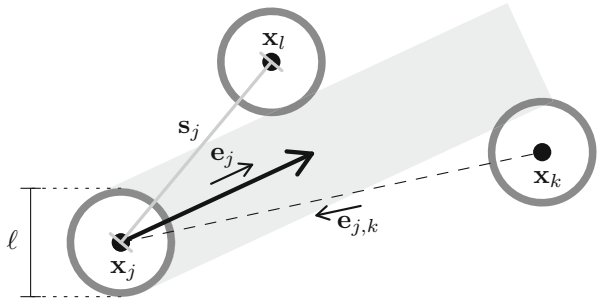

Fig. 15 Minimal spacing in front. The pedestrians in front of the pedestrian i (i.e., into the gray area) are the set $J = \{j, \mathbf{e}_i \cdot \mathbf{e}_{i,j} \leq 0 \text{ and } \mathbf{e}_i^{\perp} \cdot \mathbf{e}_{i,j} \leq \ell / s_{i,j}\}$, while the minimum spacing in front is $s_i = \min_{j \in J} s_{i,j}$

pedestrians in front of the pedestrian i are the set $J = \{j, \mathbf{e}_i \cdot \mathbf{e}_{i,j} \leq 0 \text{ and } \mathbf{e}_i^{\perp} \cdot \mathbf{e}_{i,j} \leq \ell / s_{i,j}\}$ (see Fig. 15). The optimal velocity VB model with exponential repulsion is

$$V_i = V(\min_{j \in J} s_{i,j}) \quad \text{and} \quad \mathbf{e}_i = \frac{1}{N} \left(\frac{\mathbf{v}_0}{\|\mathbf{v}_0\|} + A \sum_j \exp(-s_{i,j}/B) \right). \tag{17}$$

Here N is a normalization constant, and V is the optimal velocity function. Any positive OV function V depending on the minimal spacing in front ensures collision-free dynamics as soon as $V(s) = 0$ for all $s \leq \ell$, independently to the direction model [176]. Note that in contrast to VB models described above, the velocity in this model solely depends on the relative positions of the neighbors, and not on their velocities, making the system of velocities explicitly defined (i.e., no ping-pong effect in the simulation).

VB models do not incorporate relaxation or delay mechanisms. However, relaxation and diffusion processes can be introduced by using specific noises in the dynamics. Classically the noise is white in acceleration-based models (see, e.g., [62]). In velocity-based models, the noise is a Brownian one relaxed at the second order to describe the autocorrelation of the speed residuals [178]. Simulation results show that the relaxed noises allow to describe oscillating traffic waves (stop-and-go dynamics). Thus this modeling ansatz of stop-and-go waves for pedestrian dynamics is noise-induced. It contrasts with the modeling of stop-and-go for traffic flow, generally done by means of instability and phase transitions.

3.3 Decision-Based Models

Decision-based models or *rule-based models* belong to a class of models which are not defined using differential equations. As indicated by the name, their dynamics is based on decisions that the pedestrians make to determine their

motion (e.g., position, velocity). Since decisions are made at discrete times, time is typically discrete in this class, i.e., $t = n\Delta t$ (with an integer n). Usually the time step Δt is identified with the reaction time of the pedestrians and thus of the order $0.1 - 0.5$ s. It can be used for calibration which is essential to make quantitative predictions. In the spirit of the previous subsections, such models could be termed "zeroth-order models" since their dynamics is not based on differential equations.

3.3.1 Cellular Automata

Arguably the best known subclass of decision-based models are *cellular automata (CA)*. CA are discrete in space, time and the state variable(s) (e.g. the velocity). The most common spatial discretization is based on quadratic cells, but also other cell forms have been used. The cell size can be related to the maximal densities observed in dense crowds which determines the minimal space requirement of one person. This space requirement can be identified with the cell size if each cell in the CA can only be occupied by one person (exclusion principle). A typical maximal density of 6.25 persons/m^2 [184] leads to a cell size of 40×40 cm^2. The discrete time is in computer simulations usually realized through a *parallel* or *synchronous* update where all pedestrians move at the same time.

Most CA models for pedestrian dynamics are based on a stochastic dynamics defined in terms of rules that specify the transition probabilities for the motion to one of the neighboring cells (Fig. 16). In the simplest case, the potential target cells are nearest neighbors (*von Neumann neighborhood*), but more general definitions of the neighborhood are used frequently (*Moore neighborhood*). Models can be distinguished by the specification of the probabilities for motion. For deterministic models, only one probability is nonzero.

Most CA models for pedestrian dynamics are based on two-dimensional extensions of the paradigmatic asymmetric simple exclusion process (ASEP) (see [8, 29,

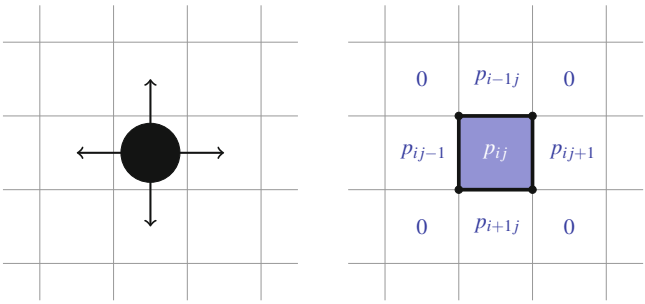

Fig. 16 Possible directions of motion and the corresponding transition probabilities p_{ij} for the case of a von Neumann neighborhood

156] for reviews) or models for vehicular traffic [5, 22, 123] based on the ASEP. Pedestrians are represented by particles subject to the exclusion principle. The motion to neighboring cells is based on transition probabilities that are determined by (1) the desired direction of motion, (2) interactions with other pedestrians, and (3) interactions with the infrastructure (walls, doors, etc.).

One of the earliest CA models was introduced by Blue and Adler [6, 7]. It is based on a multilane variant of the of the Nagel-Schreckenberg model [123] of highway traffic with lane-changing rules similar to those in [142]. The update is deterministic and performed in four steps which are applied to all pedestrians in parallel: (1) choosing a preferred lane, (2) performing lane changes, (3) adjustment of the velocity based on the headway in the new lane, and (4) motion according to the velocity determined in (3). Head-on conflicts occurring in counterflow situations are resolved such that with some probability, opposing pedestrians are allowed to exchange positions within one time step. Other early CA models can be found in [47, 80, 116].

Most cellular automaton models are based on stochastic dynamics. When interpreting simulation results, one has to keep in mind that these models are designed in such a way that the average over different realizations of the stochastic process should be realistic. Considering just a single realization can be misleading. However, for large crowds even then one usually obtains rather realistic results due to self-averaging effects. Furthermore the stochastic nature of the dynamics allows to determine probability distributions of quantities like evacuation times in a natural way.

3.3.2 Floor Field Model

The *floor field model* [13, 14, 78, 148] is probably the most popular CA model for pedestrian dynamics. In contrast to simpler CA models, the transition probabilities to neighboring cells are no longer fixed but vary dynamically. This is motivated by the process of chemotaxis [4] used, e.g., by ants for communication. In the floor field model [14], pedestrians also create a virtual trace in contrast to the chemical trace in chemotaxis. This virtual trace might be interpreted as some abstract representation of the path in the mind of the pedestrians. One important advantage of this approach is that interactions become purely local. The number of interaction terms grows only linearly with the number of pedestrians even in complex geometries. This allows for efficient simulations without supercomputers.

The local interactions are specified by so-called *floor fields*. The transition probabilities depend on the strength of the floor fields in the target cells such that transitions in the direction of larger fields are preferred. The *dynamic floor field* D_{ij} is basically the virtual trace created by moving pedestrians which in turn influence the motion of other individuals. It has its own dynamics where diffusion and decay lead to a dilution and finally the vanishing of the trace after some time. The *static floor field* S_{ij} is constant in time. It takes into account the effects of the (static) environment and allows to model, e.g., preferred areas, walls, and other obstacles. It

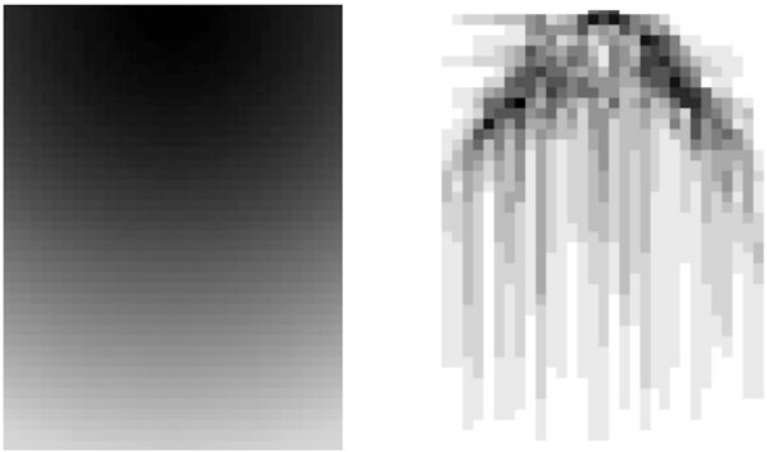

Fig. 17 Left: Static floor field for the simulation of an evacuation from a large room with a single door. The door is located in the middle of the upper boundary, and the field strength is increasing with increasing intensity. Right: Snapshot of the dynamical floor field created by pedestrians leaving the room

is nonzero even in the absence of pedestrians. A typical examples is shown in Fig. 17 for the simulation of evacuations from a room with a single door. The strength of the static floor field decreases with increasing distance from the door. This makes the motion into the direction of the door more preferable.

The relative influence of both floor fields is controlled by coupling constants k_S and k_D. Strong coupling to the static field leads to pedestrians choosing the shortest path to the exit. This corresponds to a "normal" situation. If the coupling to the dynamic field dominates, strong herding behavior is observed where pedestrians try to follow the lead of others which is typical for emergency situations. The generic form of the transition probability p_{ij} to a neighboring cell (i, j) is given by

$$p_{ij} = N \exp\left(k_D D_{ij}\right) \exp\left(k_S S_{ij}\right)(1 - n_{ij})\xi_{ij} \,. \tag{18}$$

D_{ij} and S_{ij} are the strengths of the dynamic and static field at cell (i, j), respectively. $n_{ij} = 0, 1$ is the number of persons in cell $((i, j)$. The factor $(1 - n_{ij})$ forbids motion to occupied cells according to the exclusion principle. The obstacle number

$$\xi_{ij} = \begin{cases} 0 & \text{for forbidden cells (e.g. walls)} \\ 1 & \text{else} \end{cases} \tag{19}$$

allows to forbid transition to wall cells, etc. Finally, N is a normalization constant that ensures the sum of all transition probabilities for a pedestrian is 1.

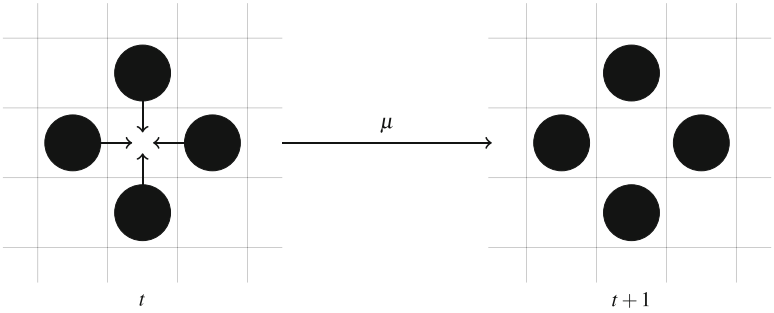

Fig. 18 Refused movement due to the friction parameter μ

The use of a parallel update leads to conflicts where different pedestrians want to move to the same destination cell. These conflicts are not a technical problem for the simulations but should be interpreted as an important part of the dynamics [76]. It has been shown [77] that the behavior becomes more realistic if not all conflicts are resolved. Instead of choosing one pedestrian that is allowed to move whereas the others stay at their positions, with some probability μ, called friction parameter, the movement of *all* involved pedestrians is denied [77] (see Fig. 18). This leads to a more realistic description of clogging effects, e.g., at bottlenecks. Although friction is a local effect, it can have a strong influence on macroscopic quantities like flow and evacuation time, especially in evacuation scenarios.

The floor field model has been extended in different ways. To increase the spatial resolution which is limited by the cell size, models with smaller cells have been proposed [75] where pedestrians correspond to extended particles that occupy more than one cell (e.g., four cells). Furthermore a spatial anisotropy is introduced by the lattice structure. As a consequence straight motion in directions not parallel to the lattice axis is difficult to achieve. This can be reduced by a proper choice of the transition probabilities [14, 155] or by allowing motion further than just to nearest-neighbor cells [75, 84, 88, 103].

Many variants of the floor field model have been introduced which include other types of interactions. For counterflow situations, the inclusion of anticipation effects [126, 169] leads to a more realistic behavior. Another interesting extension is the inclusion of game theory, e.g., in the resolution of conflicts [9] or the choice of exits in an evacuation [102].

3.3.3 Other CA Models and Related Approaches

Besides the floor field model, many other cellular automata models have been proposed for the description of pedestrian dynamics, e.g., the Fukui-Ishibashi model [46, 47] which is based on a two-dimensional variant of the ASEP. The motion in the Fukui-Ishibashi model is deterministic; only sidestepping to avoid oppositely moving pedestrian is stochastic. An asymmetric variant where walkers prefer lane

changes to the right has been proposed in [116]. Further modifications include different update types [35], simultaneous (exchange) motion of pedestrians standing "face-to-face" [70], or the possibility of backstepping [106]. The influence of the shape of the particles has been investigated in [121]. Also other geometries [118, 170] and extensions to full two-dimensional motion have been studied in various modifications [105, 106, 117].

The Gipps-Marksjös model [52] anticipated the idea of social forces (see Sect. 3.1). Interactions between pedestrians are assumed to be repulsive, and the actual motion is determined by the competition between this repulsion and the gain of approaching the destination. The model dynamics is deterministic, and updating is done sequentially to avoid conflicts.

Lattice-gas models are conceptually very similar to cellular automata models where the main difference is the position of the particles. The definition of the dynamics is analogous, but in lattice-gas models, the pedestrians are located on the vertices of the lattice, whereas they are located on the faces of the lattice in CA. Some lattice-gas models of pedestrian dynamics take inspiration from lattice gases introduced for the description of classical hydrodynamics [42], e.g., the model introduced by Marconi and Chopard [107] which is based on a sequence of collision and propagation steps.

Real-coded cellular automata (RCA) [187] have been proposed in order to solve some problems related to the discretization of space. In RCA, in contrast to genuine CA, the velocities of the pedestrians are not discrete, and they can move in any direction. This makes the motion isotropic irrespective of the lattice structure.

In the *Optimal Steps Model* [159], the motion of a pedestrian is discretized to reflect the movement in steps. However, space is not discrete but continuous. This allows natural grid-free trajectories without introducing differential equations or complex steering behaviors.

4 Performance of Models: Quantitative and Qualitative "Benchmarking"

4.1 Stability Analysis

An often observed collective phenomenon that emerges in crowds, especially when the density exceeds a certain threshold, is stop-and-go waves [150]. Although some space-continuous models [34, 95, 136, 161] reproduce partly this phenomenon, some models generally fail to describe pedestrian dynamics in jam situations correctly. Instead, quite often unrealistic behavior like backward motion or overtaking ("tunneling") is observed in some situations, especially in one-dimensional single-file movement. Recently it has been shown [23] that this is not a consequence of numerical problems in the treatment of the differential equations, but an indication of inherent problems of the models, at least for certain classes.

In vehicular traffic, the formation of jams and the dynamics of traffic waves have been studied intensively [22, 51, 122, 129]. Traffic jams in simulations occur as a result of phase transitions from a stable homogeneous configuration to an unstable configuration. That means it should be possible to calibrate model parameters such that systems in unstable regimes can be simulated. Otherwise, a reproduction of jams is impossible, and the model can be qualified as unrealistic. For each parameter set that leads to an unstable homogeneous state, it has to be verified by simulations whether this instability corresponds to realistic behavior (i.e., the occurrence of jams) or unrealistic behavior (e.g., overlapping of particles).

By investigating the linear instability of a continuous model in an homogeneous steady state, it is possible to roughly identify an adequate parameter set that may lead to reproduction of inhomogeneous states.

From an empirical point of view, the stop-and-go waves that were observed in experiments under laboratory conditions [95, 136] have a short pseudo-period. Hence, it is not clear if these waves disappear after a long time or remain. However, by means of simulation of validated models, it is possible to investigate this assumption.

4.2 Verification and Validation

The concepts of *verification* and *validation* are often confounded. According to [147], verification is the process of assuring if the computer programming and implementation of a mathematical model are correct. At this stage no statement about the quality of the underlying model can be made. In the context of pedestrian dynamics, verification is performed by means of simple tests mostly based on common sense. In [68] several verification tests were recommended to assess the quality of simulations of ships. For evacuation simulation other tests were proposed within the framework of RiMEA [143] and further developed to include evacuation under smoke conditions [145].

Validation is the process of assessing the performance of the model (not its numerical implementation) with respect to empirical findings, that is, to what extent the model can describe the system in a realistic way. Here, it should be emphasized that the empirical data used as reference, whether they are derived from experiments under laboratory conditions or field studies, reflect the properties of the crowd in *normal* conditions.

Several benchmarks and metrics were developed in the past to assess the reliability of mathematical models for pedestrian dynamics and hence evaluate to what extent they can be used to address safety-related questions. One can distinguish between qualitative and quantitative validations. Most of models that guarantee a certain volume exclusion are able to describe qualitatively well some of those phenomena, e.g., lane formation [191, 196], oscillations at bottlenecks [58, 196], the "faster-is-slower" effect [90, 131], and clogging at bottlenecks [58, 191], that sometimes are difficult to verify empirically [50, 132]. Quantitative validation

features comparisons with empirical data in the form of the relationship between density and flow [152, 163] or evacuation times. In [89] an approach based on data binning and cumulative distribution functions to assess the discrepancy of two data clouds (fundamental diagrams) was proposed. Given observation points of speed and density from experiments $\{[\rho_i^{\text{data}}, v_i^{\text{data}}]\}$ and simulations $\{[\rho_i^{\text{model}}, v_i^{\text{model}}]\}$, the degree of similarity among these two point clouds is measured. For this purpose N equally spaced density intervals are defined

$$V_j^{\text{src}} = \{v_i^{\text{src}} : \rho_i^{\text{src}} \in [\rho_j, \rho_{j+1}], i = 1, \ldots, N^{\text{src}}\}, \tag{20}$$

where $j = 1, \ldots, N$, src $= \{\text{data, model}\}$ and N^{src} is the number of observations. By means of the cumulative distribution functions both for the experiment, $F_{V_j^{\text{data}}}(x)$, and for the simulations, $F_{V_j^{\text{model}}}(x)$, the Kolmogorov-Smirnov distance is calculated as

$$D_j = \sup_x |F_{V_j^{\text{data}}}(x) - F_{V_j^{\text{model}}}(x)|, \; j = 1, \ldots, N. \tag{21}$$

Finally, the weighted arithmetic mean of distances D_j is used as a quantitative metric estimating the similarity of two data clouds

$$D^* = \frac{\sum_{j=1}^{N} (N_j^{\text{data}} + N_j^{\text{model}}) D_j}{N^{\text{data}} + N^{\text{model}}}, \tag{22}$$

where N_j^{data} and N_j^{model} are the number of observations in the jth bin for data and model, respectively. In other words, metric D^* quantifies the degree of success (or failure) of the validation process.

With this approach a new quantity (also called *validity factor*) is introduced which enables a verification as well as a validation of most models in an automatic way. The degree of success of the considered pedestrian model is henceforth quantified and can be used in an iterative process to calibrate and enhance the model's performance.

5 Summary

We have reviewed the present state of the art of modeling of pedestrian and evacuation dynamics focusing on microscopic models. In recent years the interplay between empirical results and theoretical models has become more and more important. Many groups have carried out laboratory experiments under controlled conditions that can, in principle, be easily repeated. Nevertheless, there is still no consensus even about quantitative behavior and sometimes the qualitative shape of basic relations like the fundamental diagram or the dependence of the flow through bottlenecks on their width.

Modeling approaches are often inspired by the physics of many-particle systems building on similarities with hydrodynamics or granular materials. Indeed, most phenomena observed in pedestrian streams have analogies in these classes of physical systems. However, quite different model classes can be distinguished and investigated separately.

We have proposed a classification on the basis of the relevant state variable that is determined by the system dynamics as defined by the equation of motion. This allows to distinguish acceleration-based, velocity-based, and decision-based models. In the latter the new position is determined based on rules representing the decisions made by pedestrians during motion, whereas in the first two classes the dynamics is given by an ordinary differential equation of second and first order, respectively.

Overall there are hundreds of different models and model variants in each class. They can further be distinguished, e.g., by the type of dynamics which can be deterministic or stochastic. Currently, still new models are proposed, often for the description of rather specific scenarios. A conceptually different approach is based on the idea of machine learning for the prediction of pedestrian movement. In contrast to physical models, data-driven approaches are deliberately complex and have a large number of parameters without direct physical interpretation. Their calibration (called *training* in this context) generally requires a very large amount of data. When accurately trained, the very high plasticity of the prediction models allows in principle to describe any type of patterns. Examples for this relatively new approach can be found, e.g., in [1, 21, 28, 39, 104, 177].

An aspect that is currently becoming more and more relevant concerns the human factor in pedestrian dynamics. As humans, pedestrians are subject of psychology and sociology which is often only considered in a simplified way in current models [166, 173]. Psychology considers single pedestrians and their behavior and experiences. For pedestrian dynamics, the influence of senses (viewing, hearing, tactile) on the movement as well as cognitive abilities like wayfinding is relevant. Sociology treats pedestrians as entities belonging to a group (families or friends) sharing a social identity (e.g., protester or police) or following social norms (e.g., waiting in a queue instead of pushing toward an overloaded exit). Thus many norms and rules exist which should be considered for a realistic modeling of the movement of crowds, groups, or single pedestrians. Understanding the relevance of these aspects remains one of the challenges the theory of pedestrian dynamics has to face in the future.

References

1. Alahi, A., Goel, K., Ramanathan, V., Robicquet, A., Fei-Fei, L., and Savarese, S. Social LSTM: Human trajectory prediction in crowded spaces. In *2016 IEEE Conference on Computer Vision and Pattern Recognition (CVPR)* (2016), pp. 961–971.
2. Alhajyaseen, W. K. M., Nakamura, H., and Asano, M. Effects of bi-directional pedestrian flow characteristics upon the capacity of signalized crosswalks. *Procedia - Social and Behavioral Sciences 16* (2011), 526–535.

3. Barlovic, R., Santen, L., Schadschneider, A., and Schreckenberg, M. Metastable states in cellular automata for traffic flow. *Eur. Phys. J. B 5* (1998), 793–800.
4. Ben-Jacob, E. From snowflake formation to growth of bacterial colonies. Part II. Cooperative formation of complex colonial patterns. *Contemp. Phys. 38* (1997), 205–241.
5. Biham, O., Middleton, A. A., and Levine, D. Self-organization and a dynamical transition in traffic-flow models. *Phys. Rev. A 46* (1992), R6124.
6. Blue, V. J., and Adler, J. L. Cellular automata microsimulation of bi-directional pedestrian flows. *J. Trans. Research Board 1678* (2000), 135–141.
7. Blue, V. J., and Adler, J. L. Flow capacities from cellular automata modeling of proportional spilts of pedestrians by direction. In Schreckenberg and Sharma [154].
8. Blythe, R., and Evans, M. R. Nonequilibrium steady states of matrix product form: a solver's guide. *J. Phys. A 40* (2007), R333.
9. Bouzat, S., and Kuperman, M. N. Game theory in models of pedestrian room evacuation. *Phys. Rev. E 89* (2014), 032806.
10. Boyce, K. E., Shields, T. J., and Silcock, G. W. H. Toward the Characterization of Building Occupancies for Fire Safety Engineering: Capabilities of Disabled People Moving Horizontally and on an Incline. *Fire Technology 35* (1999), 51–67.
11. Burghardt, S., Seyfried, A., and Klingsch, W. Improving egress design through measurement and correct interpretation of the fundamental diagram for stairs. In *Developments in Road Transportation* (2010), M. Panda and U. Chattaraj, Eds., Macmillan Publishers India Ltd, pp. 181–187.
12. Burghardt, S., Seyfried, A., and Klingsch, W. Performance of stairs - fundamental diagram and topographical measurements. *Transportation Research Part C: Emerging Technologies 37* (2013), 268–278.
13. Burstedde, C., Kirchner, A., Klauck, K., Schadschneider, A., and Zittartz, J. Cellular automaton approach to pedestrian dynamics – applications. In Schreckenberg and Sharma [154], pp. 87–98.
14. Burstedde, C., Klauck, K., Schadschneider, A., and Zittartz, J. Simulation of pedestrian dynamics using a two-dimensional cellular automaton. *Physica A 295* (2001), 507–525.
15. Cao, S., Seyfried, A., Zhang, J., Holl, S., and Song, W. Fundamental diagrams for multidirectional pedestrian flows. *Journal of Statistical Mechanics: Theory and Experiment 2017* (2017), 033404.
16. Cao, S., Zhang, J., Salden, D., Ma, J., Shi, C., and Zhang, R. Pedestrian dynamics in single-file movement of crowd with different age compositions. *Phys. Rev. E 94* (2016), 012312.
17. Chakrabarti, J., Dzubiella, J., and Löwen, H. Reentrance effect in the lane formation of driven colloids. *Phys. Rev. E 70* (2004), 012401.
18. Chattaraj, U., Seyfried, A., and Chakroborty, P. Comparison of pedestrian fundamental diagram across cultures. *Advances in Complex Systems 12*, 3 (2009), 393–405.
19. Chen, X., Treiber, M., Kanagaraj, V., and Li, H. Social force models for pedestrian traffic - state of the art. *Transport Reviews 38* (2018), 625–653.
20. Chen, X., Ye, J., and Jian, N. Relationships and characteristics of pedestrian traffic flow in confined passageways. *Transportation Research Record: Journal of the Transportation Research Board 2198* (2010), 32–40.
21. Chen, Y., Everett, M., Liu, M., and How, J. P. Socially aware motion planning with deep reinforcement learning. In *Proceedings of the 2017 IEEE International Conference on Intelligent Robots and Systems (IROS)* (2017), pp. 1343–1350.
22. Chowdhury, D., Santen, L., and Schadschneider, A. Statistical physics of vehicular traffic and some related systems. *Physics Reports 329* (2000), 199–329.
23. Chraibi, M. Oscillating behavior within the social force model. *arXiv:1412.1133* (2014).
24. Daamen, W. *Modelling Passenger Flows in Public Transport Facilities*. PhD thesis, Technical University of Delft, 2004.

25. DAAMEN, W., BOVY, P. H. L., AND HOOGENDOORN, S. P. Modelling pedestrians in transfer stations. In Schreckenberg and Sharma [154], pp. 59–73.
26. DAAMEN, W., AND HOOGENDOORN, S. P. Flow-density relations for pedestrian traffic. In Schadschneider et al. [151], pp. 315–322.
27. DAAMEN, W., AND HOOGENDOORN, S. P. Capacity of doors during evacuation conditions. *Procedia Engineering 3* (2010), 53–66.
28. DAS, P., PARIDA, M., AND KATIYAR, V. K. Analysis of interrelationship between pedestrian flow parameters using artificial neural network. *Journal of Modern Transportation 23* (2015), 298–309.
29. DERRIDA, B. An exactly soluble non-equilibrium system: The asymmetric simple exclusion process. *Phys. Rep. 301* (1998), 65–83.
30. DIECKMANN, D. *Die Feuersicherheit in Theatern*. Jung (München), 1911. in German.
31. DIETRICH, F., AND KÖSTER, G. Gradient navigation model for pedestrian dynamics. *Phys. Rev. E 89* (2014), 062801.
32. DZUBIELLA, J., HOFFMANN, G. P., AND LÖWEN, H. Lane formation in colloidal mixtures driven by an external field. *Phys. Rev. E 65* (2002), 021402.
33. EDIE, L. Discussion of traffic stream measurements and definitions. In *Proc. 2nd Int. Symp. Theory of traffic flow* (1963), J. Almond, Ed., pp. 139–154.
34. EILHARDT, C., AND SCHADSCHNEIDER, A. Stochastic headway dependent velocity model for 1d pedestrian dynamics at high densities. *Transportation Research Procedia 2* (2014), 400–405.
35. FANG, W., YANG, L., AND FAN, W. Simulation of bi-directional pedestrian movement using a cellular automata model. *Physica A 321* (2003), 633–640.
36. FELICIANI, C., AND NISHINARI, K. Empirical analysis of the lane formation process in bidirectional pedestrian flow. *Phys. Rev. E 94* (2016), 032304.
37. FIORINI, P., AND SHILLER, Z. Motion planning in dynamic environments using velocity obstacles. *The International Journal of Robotics Research 17* (1998), 760–772.
38. FISCHER, H. *Über die Leistungsfähigkeit von Türen, Gängen und Treppen bei ruhigem, dichtem Verkehr*. Dissertation, Technische Hochschule Dresden, 1933. in German.
39. FRAGKIADAKI, K., LEVINE, S., FELSEN, P., AND MALIK, J. Recurrent network models for human dynamics. In *Proceedings of the 2015 IEEE International Conference on Computer Vision (ICCV)* (Washington, DC, USA, 2015), ICCV '15, IEEE Computer Society, pp. 4346–4354.
40. FRANTZICH, H. A model for performance-based design of escape routes. Tech. Rep. 1011, Department of Fire Safety Engineering, Lund Institute of Technology, 1994.
41. FRANTZICH, H. Study of movement on stairs during evacuation using video analysing techniques. Tech. rep., Department of Fire Safety Engineering, Lund Institute of Technology, 1996.
42. FRISCH, U., HASSLACHER, B., AND POMEAU, Y. Lattice-gas automata for the Navier-Stokes equation. *Phys. Rev. Lett. 56* (1986), 1505–1508.
43. FRUIN, J. J. *Pedestrian Planning and Design*. Metropolitan Association of Urban Designers and Environmental Planners, New York, 1971.
44. FUJIYAMA, T., AND TYLER, N. An explicit study on walking speeds of pedestrians on stairs. In *10th International Conference on Mobility and Transport for Elderly and Disabled People* (Hamamatsu, Japan, May 2004).
45. FUJIYAMA, T., AND TYLER, N. Pedestrian speeds on stairs: An initial step for a simulation model. In *Proceedings of 36th Universities' Transport Studies Group Conference* (2004).
46. FUKUI, M., AND ISHIBASHI, Y. Jamming transition in cellular automaton models for pedestrians on passageway. *J. Phys. Soc. Jpn. 68* (1999), 3738–3739.
47. FUKUI, M., AND ISHIBASHI, Y. Self-organized phase transitions in cellular automaton models for pedestrians. *J. Phys. Soc. Jpn. 68* (1999), 2861–2863.
48. GALEA, E. R., Ed. *Pedestrian and Evacuation Dynamics 2003* (London, 2003), CMS Press.
49. GARCIMARTÍN, A., PARISI, D. R., PASTOR, J. M., MARTÍN-GÓMEZ, C., AND ZURIGUEL, I. Flow of pedestrians through narrow doors with different competitiveness. *Journal of Statistical Mechanics: Theory and Experiment* (2016), 043402.

50. Garcimartín, A., Zuriguel, I., Pastor, J. M., Martín-Gómez, C., and Parisi, D. R. Experimental evidence of the "faster is slower" effect. *Transportation Research Procedia 2* (2014), 760–767.
51. Gazis, D. C. The origins of traffic theory. *Op Res. 1* (2002), 69–77.
52. Gipps, P. G., and Marksjö, B. A micro-simulation model for pedestrian flows. *Mathematics and Computers in Simulation 27* (1985), 95–105.
53. Graat, E., Midden, C., and Bockholts, P. Complex evacuation; effects of motivation level and slope of stairs on emergency egress time in a sports stadium. *Safety Science 31* (1999), 127–141.
54. Guy, S., Chhugani, J., Kim, C., Satish, S., Lin, M., Manocha, D., and Dubey, P. Clearpath: Highly parallel collision avoidance for multi-agent simulation. *Proceedings of the 2009 ACM SIGGRAPH/Eurographics Symposium on Computer Animation* (2009), 177–187.
55. Guy, S., Lin, M., and Manocha, D. Modeling collision avoidance behavior for virtual humans. *Proceedings of the 9th International Conference on Autonomous Agents and Multiagent Systems 2* (2010), 575–582.
56. Hankin, B. D., and Wright, R. A. Passenger flow in subways. *Operational Research Quarterly 9* (1958), 81–88.
57. Helbing, D. Traffic and related self-driven many-particle systems. *Rev. Mod. Phys. 73* (2001), 1067.
58. Helbing, D. Collective phenomena and states in traffic and self-driven many-particle systems. *Computational Materials Science 30* (2004), 180–187.
59. Helbing, D., Buzna, L., Johansson, A., and Werner, T. Self-organized pedestrian crowd dynamics: Experiments, simulations, and design solutions. *Transportation Science 39* (2005), 1–24.
60. Helbing, D., Johannson, A., and Al-Abideen, H. H. Z. Crowd turbulence: the physics of crowd disasters. In *The Fifth International Conference on Nonlinear Mechanics (ICNM-V)* (Shanghai, June 2007), pp. 967–969.
61. Helbing, D., Johansson, A., and Al-Abideen, H. Z. The dynamics of crowd disasters: An empirical study. *Phys. Rev. E 75* (2007), 046109.
62. Helbing, D., and Molnár, P. Social force model for pedestrian dynamics,. *Phys. Rev. E 51* (1995), 4282–4286.
63. Hirai, K., and Tarui, K. A simulation of the behavior of a crowd in panic. In *Proc. of the 1975 International Conference on Cybernetics and Society* (San Francisco, 1975), pp. 409–411.
64. Hoogendoorn, S. P., Bovy, P. H. L., and Daamen, W. Microscopic pedestrian wayfinding and dynamics modelling. In Schreckenberg and Sharma [154], pp. 123–154.
65. Hoogendoorn, S. P., and Daamen, W. Pedestrian behavior at bottlenecks. *Transportation Science 39 2* (2005), 147–159.
66. Hoogendoorn, S. P., Daamen, W., and Bovy, P. H. L. Microscopic pedestrian traffic data collection and analysis by walking experiments: Behaviour at bottlenecks. In Galea [48], pp. 89–100.
67. Hoskin, K. J., and Spearpoint, M. Crowd characteristics and egress at stadia. In *Human Behaviour in Fire* (London, 2004), T. J. Shields, Ed., Proceedings of the third International Symposium on Human Behaviour in Fire, Ulster, Belfast, Intersience, pp. 367–376.
68. International Maritime Organization. Guidelines for evacuation analysis for new and existing passenger ships, 2007.
69. Jelić, A., Appert-Rolland, C., Lemercier, S., and Pettré, J. Properties of pedestrians walking in line: Fundamental diagrams. *Phys. Rev. E 85* (2012), 036111.
70. Jian, L., Lizhong, Y., and Daoling, Z. Simulation of bi-direction pedestrian movement in corridor. *Physica 354* (2005), 619–628.
71. Johnson, N. R. Panic at "The Who Concert Stampede": An Empirical Assessment. *Social Problems 34* (1987), 362–373.
72. Keating, J. P. The myth of panic. *Fire Journal* (May 1982), 57–62.
73. Kerner, B. S. *The Physics of Traffic*. Springer, 2004.

74. KIM, S., STEPHEN, G., GUY, S., LIU, W., WILKIE, D., LAU, R., LIN, M., AND MANOCHA, D., BRVO: Predicting pedestrian trajectories using velocity-space reasoning. *The International Journal of Robotics Research 34* (2014), 201–217.
75. KIRCHNER, A., KLÜPFEL, H., NISHINARI, K., SCHADSCHNEIDER, A., AND SCHRECKENBERG, M. Discretization effects and the influence of walking speed in cellular automata models for pedestrian dynamics. *Journal of Statistical Mechanics: Theory and Experiment* (2004), P10011.
76. KIRCHNER, A., NAMAZI, A., NISHINARI, K., AND SCHADSCHNEIDER, A. Role of conflicts in the floor field cellular automaton model for pedestrian dynamics. In Galea [48], p. 51.
77. KIRCHNER, A., NISHINARI, K., AND SCHADSCHNEIDER, A. Friction effects and clogging in a cellular automaton model for pedestrian dynamics. *Phys. Rev. E 67* (2003), 056122.
78. KIRCHNER, A., AND SCHADSCHNEIDER, A. Simulation of evacuation processes using a bionics-inspired cellular automaton model for pedestrian dynamics. *Physica A 312* (2002), 260–276.
79. KLINGSCH, W., ROGSCH, C., SCHADSCHNEIDER, A., AND SCHRECKENBERG, M., Eds. *Pedestrian and Evacuation Dynamics 2008* (Berlin Heidelberg, 2010), Springer.
80. KLÜPFEL, H., MEYER-KÖNIG, T., WAHLE, J., AND SCHRECKENBERG, M. Microscopic simulation of evacuation processes on passenger ships. In *Theory and Practical Issues on Cellular Automata* (Berlin Heidelberg, 2000), S. Bandini and T. Worsch, Eds., Springer.
81. KNOOP, V. L., AND DAAMEN, W., Eds. *Traffic and Granular Flow '15* (2009), Springer, Berlin Heidelberg.
82. KNOOP, V., HOOGENDOORN, S.P., AND VAN ZUYLEN, H. Empirical differences between time mean Speed and space mean speed. In C. Appert-Rolland, F. Chevoir, P. Gondret, S. Lassarre, J.-P. Lebacque, and M. Schreckenberg, editors, Traffic and Granular Flow '07. Springer-Verlag Berlin Heidelberg (2009), 351–356.
83. KOZLOV, V., BUSLAEV, A., BUGAEV, A., YASHINA, M., SCHADSCHNEIDER, A., AND SCHRECKENBERG, M., Eds. *Traffic and Granular Flow '11* (Heidelberg, 2013), Springer.
84. KRETZ, T. *Pedestrian Traffic - Simulation and Experiments*. PhD thesis, Universität Duisburg-Essen, 2007.
85. KRETZ, T., GRÜNEBOHM, A., KAUFMAN, M., MAZUR, F., AND SCHRECKENBERG, M. Experimental study of pedestrian counterflow in a corridor. *Journal of Statistical Mechanics: Theory and Experiment* (2006), P10001.
86. KRETZ, T., GRÜNEBOHM, A., KESSEL, A., KLÜPFEL, H., MEYER-KÖNIG, T., AND SCHRECKENBERG, M. Upstairs walking speed distributions on a long stairway. *Safety Science 46* (2008), 72–78.
87. KRETZ, T., GRÜNEBOHM, A., AND SCHRECKENBERG, M. Experimental study of pedestrian flow through a bottleneck. *J. Stat. Mech.* (2006), P10014.
88. KRETZ, T., AND SCHRECKENBERG, M. The F.A.S.T.-model. *Lect. Notes Comp. Sci. 4173* (2006), 712.
89. KURTC, V., CHRAIBI, M., AND TORDEUX, A. Automated quality assessment of space-continuous models for pedestrian dynamics. In *Traffic and Granular Flow '17* (2017).
90. LAKOBA, T. I., KAUP, D. J., AND FINKELSTEIN, N. M. Modifications of the Helbing-Molnár-Farkas-Vicsek social force model for pedestrian evolution. *Simulation 81* (2005), 339–352.
91. LAM, W. H. K., AND CHEUNG, C. Y. Pedestrian speed/flow relationships for walking facilities in hong kong. *Journal of Transportation Engineering 126* (2000), 343–349.
92. LAM, W. H. K., LEE, J. Y. S., CHAN, K. S., AND GOH, P. K. A generalised function for modeling bi-directional flow effects on indoor walkways in Hong Kong. *Transportation Research Part A: Policy and Practice 37* (2003), 789–810.
93. LAM, W. H. K., LEE, J. Y. S., AND CHEUNG, C. Y. A study of the bi-directional pedestrian flow characteristics at Hong Kong signalized crosswalk facilities. *Transportation 29* (2002), 169–192.
94. LE BON, G. *Lois Psychlogiques De l'Évolution Des Peuples*. Alcan, Paris, 1895.
95. LEMERCIER, S., JELIC, A., KULPA, R., HUA, J., FEHRENBACH, J., DEGOND, P., APPERT-ROLLAND, C., DONIKIAN, S., AND PETTRÉ, J. Realistic following behaviors for crowd simulation. *Computer Graphics Forum* (2012), 489–498.

96. Leutzbach, W. *Introduction to the Theory of Traffic Flow*. Springer, Berlin, 1988.
97. Lian, L., Mai, X., Song, W., Richard, Y. K. K., Wei, X., and Ma, J. An experimental study on four-directional intersecting pedestrian flows. *Journal of Statistical Mechanics: Theory and Experiment* (2015), P08024.
98. Lian, L., Song, W., Richard, Y. K. K., and Wu, C. Experimental study of high-density pedestrian flow field characteristics at a crossing. In Knoop and Daamen [81], pp. 57–64.
99. Liao, W., Seyfried, A., Zhang, J., Boltes, M., Zheng, X., and Zhao, Y. Experimental study on pedestrian flow through wide bottleneck. *Transportation Research Procedia 2* (2014), 26–33.
100. Liddle, J., Seyfried, A., Klingsch, W., Rupprecht, T., Schadschneider, A., and Winkens, A. An experimental study of pedestrian congestions: Influence of bottleneck width and length. In *Traffic and Granular Flow 2009* (2009). arXiv:0911.4350.
101. Liu, X., Song, W., and Zhang, J. Extraction and quantitative analysis of microscopic evacuation characteristics based on digital image processing. *Physica A 388*, 13 (2009), 2717–2726.
102. Lo, S., Huang, H., Wang, P., and Yuen, K. A game theory based exit selection model for evacuation. *Fire Safety Journal 41* (2006), 364–369.
103. Luo, L., Fu, Z., Cheng, H., and Yang, L. Update schemes of multi-velocity floor field cellular automaton for pedestrian dynamics. *Physica A 491* (2018), 946–963.
104. Ma, Y., Lee, E. W. M., and Yuen, R. K. K. An artificial intelligence-based approach for simulating pedestrian movement. *IEEE Transactions on Intelligent Transportation Systems 17* (2016), 3159–3170.
105. Maniccam, S. Traffic jamming on hexagonal lattice. *Physica A321* (2003), 653–664.
106. Maniccam, S. Effects of back step and update rule on congestion of mobile objects. *Physica A 346* (2005), 631–650.
107. Marconi, S., and Chopard, B. A multiparticle lattice gas automata model for a crowd. *Lect. Notes Comp. Sci. 2493* (2002), 231–238.
108. Maury, B., and Venel, J. A discrete contact model for crowd motion. *ESAIM: Mathematical Modelling and Numerical Analysis 45* (2011), 145–168.
109. Maury, B., Venel, J., Olivier, A.-H., and Donikian, S. A mathematical framework for a crowd motion model. *Comptes Rendus de l'Académie des Sciences - Series I 346* (2008), 1245–1250.
110. McPhail, C., and Tucker, C. Collective behaviour. In *Handbook of Symbolic Interactionism*, L. Reynolds and H.-K. NJ., Eds. Walnut Creek, Altamira, 2003, pp. 721–741.
111. Meyer-König, T., Klüpfel, H., and Schreckenberg, M. Assessment and analysis of evacuation processes on passenger ships by microscopic simulation. In Schreckenberg and Sharma [154], pp. 297–302.
112. Mordvintsev, A., Krzhizhanovskaya, V., Lees, M., and Sloot, P. Simulation of city evacuation coupled to flood dynamics. In *Pedestrian and Evacuation Dynamics 2012* [185], pp. 485–499.
113. Morrall, J. F., Ratnayake, L. L., and Seneviratne, P. N. Comparison of CBD pedestrian characteristics in Canada and Sri Lanka. *Transportation Research Record 1294* (1991), 57–61.
114. Muir, H. C., Bottomley, D. M., and Marrison, C. Effects of motivation and cabin configuration on emergency aircraft evacuation behavior and rates of egress. *Intern. J. Aviat. Psych. 6*, 1 (1996), 57–77.
115. Müller, K. *Zur Gestaltung und Bemessung von Fluchtwegen für die Evakuierung von Personen aus Bauwerken auf der Grundlage von Modellversuchen*. PhD thesis, Technische Hochschule Otto von Guericke Magdeburg, 1981.
116. Muramatsu, M., Irie, T., and Nagatani, T. Jamming transition in pedestrian counter flow. *Physica A 267* (1999), 487–498.
117. Muramatsu, M., and Nagatani, T. Jamming transition in two-dimensional pedestrian traffic. *Physica A 275* (2000), 281–291.
118. Muramatsu, M., and Nagatani, T. Jamming transition of pedestrian traffic at crossing with open boundary conditions. *Physica A 286* (2000), 377–390.

119. MVStättV - Erläuterungen: Musterverordnung über den Bau und Betrieb von Versammlungsstätten, Erläuterungen, Juni 2005. www.is-argebau.de.
120. NAGAI, R., FUKAMACHI, M., AND NAGATANI, T. Evacuation of crawlers and walkers from corridor through an exit. *Physica A 367* (2006), 449–460.
121. NAGAI, R., AND NAGATANI, T. Jamming transition in counter flow of slender particles on square lattice. *Physica A 366* (2006), 503–512.
122. NAGATANI, T. The physics of traffic jams. *Reports on Progress in Physics 65*, 9 (2002), 1331–1386.
123. NAGEL, K., AND SCHRECKENBERG, M. A cellular automaton model for freeway traffic. *J. Phys. I France 2* (1992), 2221–2229.
124. NAVIN, P. D., AND WHEELER, R. J. Pedestrian flow characteristics. *Traffic Engineering 39* (1969), 31–36.
125. NELSON, H. E., AND MOWRER, F. W. Emergency movement. In *SFPE Handbook of Fire Protection Engineering*, P. J. DiNenno, Ed., third ed. National Fire Protection Association, Quincy MA, 2002, ch. 14, pp. 367–380.
126. NOWAK, S., AND SCHADSCHNEIDER, A. Quantitative analysis of pedestrian counterflow in a cellular automaton model. *Phys. Rev. E 85* (2012), 066128.
127. OEDING, D. Verkehrsbelastung und Dimensionierung von Gehwegen und anderen Anlagen des Fußgängerverkehrs. Forschungsbericht 22, Technische Hochschule Braunschweig, 1963.
128. OLDER, S. J. Movement of pedestrians on footways in shopping streets. *Traffic Engineering and Control 10* (1968), 160–163.
129. OROSZ, G., WILSON, R. E., AND STEPAN, G. Traffic jams: dynamics and control. *Proc. R. Soc. A 1957* (2010), 4455–4479.
130. PARIS, S., PETTRÉ, J., AND DONIKIAN, S. Pedestrian reactive navigation for crowd simulation: a predictive approach. *Computer Graphics Forum 26* (2007), 665–674.
131. PARISI, D. R., AND DORSO, C. O. Morphological and dynamical aspects of the room evacuation process. *Physica A 385* (2007), 343–355.
132. PARISI, D. R., SORIA, S. A., AND JOSENS, R. Faster-is-slower effect in escaping ants revisited: Ants do not behave like humans. *Safety Science 72* (2015), 274–282.
133. PAULS, J. L., FRUIN, J. J., AND ZUPAN, J. M. Minimum stair width for evacuation, overtaking movement and counterflow - technical bases and suggestions for the past, present and future. In Waldau et al. [182], pp. 57–69.
134. PEACOCK, R. D., KULIGOWSKI, E. D., AND AVERILL, J. D., Eds. *Pedestrian and Evacuation Dynamics* (2011), Springer Berlin Heidelberg.
135. POPKOV, V., AND SCHÜTZ, G. Steady-state selection in driven diffusive systems with open boundaries. *Europhys. Lett. 48* (1999), 257–263.
136. PORTZ, A., AND SEYFRIED, A. Modeling stop-and-go waves in pedestrian dynamics. In *PPAM 2009, Part II* (2010), R. Wyrzykowski, J. Dongarra, K. Karczewski, and J. Wasniewski, Eds., Springer-Verlag Berlin Heidelberg, pp. 561–568.
137. PORTZ, A., AND SEYFRIED, A. Analyzing stop-and-go waves by experiment and modeling. In *Pedestrian and Evacuation Dynamics 2010* [134], pp. 577–586.
138. PREDTECHENSKII, V. M., AND MILINSKII, A. I. *Planing for foot traffic flow in buildings*. Amerind Publishing, New Dehli, 1978. Translation of: Proekttirovanie Zhdanii s Uchetom Organizatsii Dvizheniya Lyuddskikh Potokov, Stroiizdat Publishers, Moscow, 1969.
139. PREDTETSCHENSKI, W., AND MILINSKI, A. *Personenströme in Gebäuden – Berechnungsmethoden für die Modellierung*. Müller, Köln-Braunsfeld, 1971.
140. PUSHKAREV, B., AND ZUPAN, J. M. Capacity of walkways. *Transportation Research Record 538* (1975), 1–15.
141. REX, M., AND LÖWEN, H. Lane formation in oppositely charged colloids driven by an electric field: Chaining and two-dimensional crystallization. *Phys. Rev. E 75* (2007), 051402.
142. RICKERT, M., NAGEL, K., SCHRECKENBERG, M., AND LATOUR, A. Two lane traffic simulations using cellular automata. *Physica A 231* (1996), 534–550.
143. RiMEA - Richtlinie für Mikroskopische Entfluchtungs-Analysen, www.rimea.de (2007).

144. Rogsch, C., Schreckenberg, M., Tribble, E., Klingsch, W., and Kretz, T. Was it panic? An overview about mass-emergencies and their origins all over the world for recent years. In Klingsch et al. [79], pp. 743–755.
145. Ronchi, E., Kuligowski, E. D., Reneck, P. A., Peacock, R. D., and Nilsson, D. The process of verification and validation of building fire evacuation models. Tech. rep., National Institute of Standards and Technology, November 2013.
146. Rupprecht, T., Klingsch, W., and Seyfried, A. Influence of geometry parameters on pedestrian flow through bottleneck. In Peacock et al. [134], pp. 71–80.
147. Sargent, R. G. Verification and validation of simulation models. *Journal of Simulation 7* (2013), 12–24.
148. Schadschneider, A. Cellular automaton approach to pedestrian dynamics – theory. In Schreckenberg and Sharma [154], pp. 75–86.
149. Schadschneider, A., Chowdhury, D., and Nishinari, K. *Stochastic Transport in Complex Systems - From Molecules To Vehicles*. Elsevier, Amsterdam, 2010.
150. Schadschneider, A., Klingsch, W., Kluepfel, H., Kretz, T., Rogsch, C., and Seyfried, A. Evacuation dynamics: Empirical results, modeling and applications. In *Encyclopedia of complexity and system science*, R. A. Meyers, Ed., vol. 5. Springer, Berlin, Heidelberg, 2009, pp. 3142–3176.
151. Schadschneider, A., Pöschel, T., Kühne, R., Schreckenberg, M., and D.E.Wolf, Eds. *Traffic and Granular Flow '05* (Berlin Heidelberg New York, 2007), Springer.
152. Schadschneider, A., and Seyfried, A. Empirical results for pedestrian dynamics and their implications for cellular automata models. In *Pedestrian Behavior: Data Collection and Applications*, H. Timmermans, Ed. Emerald Group Publishing Limited, 2009, ch. 2, pp. 27–43.
153. Schadschneider, A., and Seyfried, A. Empirical results for pedestrian dynamics and their implications for modeling. *Networks and Heterogeneous Media 6* (2011), 545–560.
154. Schreckenberg, M., and Sharma, S. D., Eds. *Pedestrian and Evacuation Dynamics* (Berlin Heidelberg, 2002), Springer.
155. Schultz, M., and Fricke, H. Stochastic transition model for discrete agent movements. *Lect. Notes Comp. Sci. 6350* (2010), 506–512.
156. Schütz, G. M. Exactly solvable models for many-body systems. In *Phase Transitions and Critical Phenomena, Vol. 19*, C. Domb and J. L. Lebowitz, Eds. Academic Press, 2001.
157. Schweingruber, D., and Wohlstein, R. T. The madding crowd goes to school: Myths about crowds in introductory sociology textbooks. *Teaching Sociology 33* (2005), 136–153.
158. Seer, S. Bauer, D. B. N., and Ray, M. Estimating pedestrian movement characteristics for crowd control at public transport facilities. In *11th International IEEE Conference on Intelligent Transport Systems* (2008), pp. 742–747.
159. Seitz, M. J., and Köster, G. Natural discretization of pedestrian movement in continuous space. *Phys. Rev. E 86* (2012), 046108.
160. Seyfried, A., Boltes, M., Kähler, J., Klingsch, W., Portz, A., Rupprecht, T., Schadschneider, A., Steffen, B., and Winkens, A. Enhanced empirical data for the fundamental diagram and the flow through bottlenecks. In Klingsch et al. [79], pp. 145–156.
161. Seyfried, A., Portz, A., and Schadschneider, A. Phase coexistence in congested states of pedestrian dynamics. *Lect. Notes Comp. Sci. 6350* (2010), 496–505.
162. Seyfried, A., Rupprecht, T., Passon, O., Steffen, B., Klingsch, W., and Boltes, M. Capacity estimation for emergency exits and bootlenecks. In *Interflam 2007 - Conference Proceedings* (2007), pp. 247–258.
163. Seyfried, A., and Schadschneider, A. Fundamental diagram and validation of crowd models. *Lect. Notes Comp. Sci. 5191* (2008), 563–566.
164. Seyfried, A., Steffen, B., Klingsch, W., and Boltes, M. The fundamental diagram of pedestrian movement revisited. *J. Stat. Mech.* (2005), P10002.
165. Seyfried, A., Steffen, B., and Lippert, T. Basics of modelling the pedestrian flow. *Physica A 368* (2006), 232–238.

166. Sieben, A., Schumann, J., and Seyfried, A. Collective phenomena in crowds - where pedestrian dynamics need social psychology. *PLOS ONE 12* (2017), 1–19.
167. Sime, J. The concept of panic. In *Fire and Human Behavior*. David Fulton Publishers, 1993, ch. 5, pp. 63–82.
168. Steffen, B., and Seyfried, A. Methods for measuring pedestrian density, flow, speed and direction with minimal scatter. *Physica A 389* (2010), 1902–1910.
169. Suma, Y., Yanagisawa, D., and Nishinari, K. Anticipation effect in pedestrian dynamics: Modeling and experiments. *Physica A 391* (2011), 248–263.
170. Tajima, Y., and Nagatani, T. Clogging transition of pedestrian flow in T-shaped channel. *Physica A 303* (2002), 239–250.
171. Tanaboriboon, Y., Hwa, S. S., and Chor, C. H. Pedestrian characteristics study in Singapore. *Journal of Transportation Engineering 112* (1986), 229–235.
172. Templer, J. A. *The Staircase: Studies of Hazards, Falls, and Safer Design*. The MIT Press, 1992.
173. Templeton, A., Drury, J., and Philippides, A. From mindless masses to small groups: Conceptualizing collective behavior in crowd modeling. *Review of General Psychology 19*, 3 (2015), 215–229.
174. Thompson, P. A., and Marchant, E. W. Simulex; Developing new computer modelling techniques for evaluation. In *Fire Safety Science – Proceedings of the Fourth International Symposium* (Interscience Communications Ltd, West Yard House, Guildford Grove, London, 1994), T. Kashiwagi, Ed., The International Association for Fire Safety Science, pp. 613–624.
175. Tian, W., Song, W., Ma, J., Fang, Z., Seyfried, A., and Liddle, J. Experimental study of pedestrian behaviors in a corridor based on digital image processing. *Fire Safety Journal 47* (2012), 8–15.
176. Tordeux, A., Chraibi, M., and Seyfried, A. Collision-free speed model for pedestrian dynamics. In *Traffic and Granular Flow '15* [81], pp. 225–232.
177. Tordeux, A., Chraibi, M., Seyfried, A., and Schadschneider, A. Prediction of pedestrian speed with artificial neural networks. *Traffic and Granular Flow '17* (to be published, arXiv:1801.09782).
178. Tordeux, A., and Schadschneider, A. White and relaxed noises in optimal velocity models for pedestrian flow with stop-and-go waves. *J. Phys. A: Math. Theor. 49* (2016), 185101.
179. Transportation Research Board. Highway capacity manual. Tech. rep., Transportation Research Board, Washington DC, 2000.
180. van den Berg, J., Guy, S., Lin, M., and Manocha, D. Reciprocal n-body collision avoidance. *Robotics Research: The 14th International Symposium ISRR* (2011), 3–19.
181. van den Berg, J., Lin, M., and Manocha, D. Reciprocal velocity obstacles for real-time multi-agent navigation. *2008 IEEE International Conference on Robotics and Automation* (2008), 1928–1935.
182. Waldau, N., Gattermann, P., Knoflacher, H., and Schreckenberg, M., Eds. *Pedestrian and Evacuation Dynamics 2005* (Berlin, 2006), Springer.
183. Wardrop, J. Some theoretical aspects of road traffic research. *Proceedings of the Institution of Civil Engineers 1* (1952), 325–362.
184. Weidmann, U. Transporttechnik der Fußgänger - Transporttechnische Eigenschaften des Fußgängerverkehrs (Literaturauswertung) . Schriftenreihe des IVT 90, ETH Zürich, 1993. Zweite, ergänzte Auflage, in German.
185. Weidmann, U., Kirsch, U., and Schreckenberg, M., Eds. *Pedestrian and Evacuation Dynamics 2012* (Zürich, 2014), Springer Berlin Heidelberg.
186. Wolf, D., and Grassberger, P., Eds. *Friction, Arching, Contact Dynamics* (Singapore, 1996), World Scientific.
187. Yamamoto, K., Kokubo, S., and Nishinari, K. Simulation for pedestrian dynamics by real-coded cellular automata (RCA). *Physica A379* (2007), 654–660.
188. Yamori, K. Going with the flow: Micro-macro dynamics in the macrobehavioral patterns of pedestrian crowds. *Psychological Review 105* (1998), 530–557.

189. YANAGISAWA, D., KIMURA, A., TOMOEDA, A., RYOSUKE, N., SUMA, Y., OHTSUKA, K., AND NISHINARI, K. Introduction of frictional and turning function for pedestrian outflow with an obstacle. *Phys. Rev. E 80* (2009), 036110.
190. YE, J., CHEN, X., YANG, C., AND WU, J. Walking behavior and pedestrian flow characteristics for different types of walking facilities. *Transportation Research Record: Journal of the Transportation Research Board 2048* (2008), 43–51.
191. YU, W., CHEN, R., DONG, L., AND DAI, S. Centrifugal force model for pedestrian dynamics. *Phys. Rev. E 72* (2005), 026112.
192. ZHANG, J., KLINGSCH, W., RUPPRECHT, T., SCHADSCHNEIDER, A., AND SEYFRIED, A. Empirical study of turning and merging of pedestrian streams in T-junction. In *Fourth International Symposium on Agent-Based Modeling and Simulation (ABModSim-4)* (Vienna, Austria, 2012).
193. ZHANG, J., KLINGSCH, W., SCHADSCHNEIDER, A., AND SEYFRIED, A. Transitions in pedestrian fundamental diagrams of straight corridors and T-junctions. *Journal of Statistical Mechanics: Theory and Experiment* (2011), P06004.
194. ZHANG, J., KLINGSCH, W., SCHADSCHNEIDER, A., AND SEYFRIED, A. Experimental study of pedestrian flow through a T-junction. In Kozlov et al. [83].
195. ZHANG, J., KLINGSCH, W., SCHADSCHNEIDER, A., AND SEYFRIED, A. Ordering in bidirectional pedestrian flows and its influence on the fundamental diagram. *Journal of Statistical Mechanics: Theory and Experiment* (2012), P02002.
196. ZHANG, Q., AND HAN, B. Simulation model of pedestrian interactive behavior. *Physica A 390* (2011), 636–646.
197. ZIEMER, V., SEYFRIED, A., AND SCHADSCHNEIDER, A. Congestion dynamics in pedestrian single-file motion. In Knoop and Daamen [81], pp. 89–96.

One-Dimensional Conservation Laws with Nonlocal Point Constraints on the Flux

Boris Andreianov, Carlotta Donadello, Ulrich Razafison, and Massimiliano Daniele Rosini

Abstract We review recent results and present new ones on one-dimensional conservation laws with point constraints on the flux. Their application is, for instance, the modeling of traffic flow through bottlenecks, such as exits in the context of pedestrians' traffic and tollgates in vehicular traffic. In particular, we consider nonlocal constraints, which allow to model, e.g., the irrational behavior ("panic") near the exits observed in dense crowds and the capacity drop at tollbooths in vehicular traffic. Numerical schemes for the considered applications, based on finite volume methods, are designed, their convergence is proved, and their validations are done with explicit solutions. Finally, we complement our results with numerical examples, which show that constrained models are able to reproduce important features in traffic flow, such as capacity drop and self-organization.

1 Introduction

This chapter deals with macroscopic modeling of traffic flows, both for pedestrians and vehicles, below referred to as agents. The literature on macroscopic models for traffic flows is already vast and characterized by contributions covering statement of problems, modeling aspects, qualitative analysis, and numerical simulations motivated by their real-life applications. Macroscopic models of traffic flows

B. Andreianov
LMPT, CNRS UMR 7350, Université de Tours, Tours, France
e-mail: boris.andreianov@lmpt.univ-tours.fr

C. Donadello · U. Razafison
Laboratoire de Mathématiques CNRS UMR 6623, Université Bourgogne Franche-Comté, Besançon, France
e-mail: carlotta.donadello@univ-fcomte.fr; ulrich.razafison@univ-fcomte.fr

M. D. Rosini (✉)
Department of Mathematics and Computer Science, University of Ferrara, Ferrara, Italy
e-mail: rsnmsm@unife.it

L. Gibelli, N. Bellomo (eds.), *Crowd Dynamics, Volume 1*, Modeling and Simulation in Science, Engineering and Technology,
https://doi.org/10.1007/978-3-030-05129-7_5

are nowadays a consolidated and nonetheless continuously expanding field of mathematical research from both the theoretical and applied point of view, as the surveys [9, 38, 42, 46] and the books [29, 44] demonstrate.

The macroscopic variables (that translate the discrete nature of traffic into continuous variables) are the density of agents ρ, the velocity v, and the density flow f. By definition

$$f = \rho\, v. \tag{1}$$

Furthermore, the conservation of the number of agents is expressed by the scalar conservation law (CL)

$$\rho_t + f_x = 0. \tag{2}$$

We have to impose a further condition to close system (1), and (2) of two equations and three unknowns. However, (1), and (2) are the only accurate physical laws in traffic flow theory and any other assumption results from an approximation of empirical observations. In fact, traffic modeling cannot be an exact science, e.g., Newtonian physics, because traffic flows are influenced by psychological effects. Nevertheless, good macroscopic models help to understand nontrivial properties of traffic flows, to predict and optimize them.

There are two approaches to close system (1), and (2), which correspond to first- and second-order models. First-order models close system (1), and (2) by expressing one of the three variables in terms of the remaining two. The prototype of the first-order models is the Lighthill, Whitham [35], and Richards [43] (LWR) model, which assumes that the velocity depends on the density alone, namely, $v = V(\rho)$. The function V belongs to $\mathbf{C^1}([0, \rho_{\max}]; [0, v_{\max}])$ and is non-increasing with $V(0) = v_{\max}$ and $V(\rho_{\max}) = 0$, where $v_{\max}$ is the maximal speed and $\rho_{\max}$ is the maximal density. As a result, LWR is expressed by the scalar CL

$$\rho_t + [\rho\, V(\rho)]_x = 0. \tag{3}$$

Second-order models close system (1), and (2) by adding a CL as third constitutive equation. The most celebrated second-order model is the Aw, Rascle [8], and Zhang [48] model (ARZ). Away from the vacuum $\rho = 0$, ARZ writes

$$\begin{pmatrix} \rho \\ y \end{pmatrix}_t + \left[\left(\frac{y}{\rho} - p(\rho) \right) \begin{pmatrix} \rho \\ y \end{pmatrix} \right]_x = \begin{pmatrix} 0 \\ 0 \end{pmatrix}, \tag{4}$$

where $y = (v + p(\rho))\, \rho$ is called generalized momentum. The "pressure" function $p\colon \mathbb{R}_+ \to \mathbb{R}_+$ plays the role of an anticipation factor, taking into account agents' reactions to the traffic in front of them.

From the modeling point of view, the main drawback of LWR is the fact that agents adjust instantaneously their velocities according to the density they are

experiencing (which implies infinite acceleration) and take into account the slightest change in the density. This behavior contradicts the empirical observations. Also, experimental data show that the fundamental diagram (ρ, f) is given by a cloud of points rather than being the support of a map $\rho \mapsto [\rho\, V(\rho)]$, see [20, Figure 1.1] or [14, Figure 3.1]. ARZ can be interpreted as a generalization of LWR, possessing a family of fundamental diagram curves, rather than a single one. For this reason ARZ avoids the drawbacks of LWR listed above. Moreover, the empirical tests in [26] show that in many cases, ARZ is significantly more accurate than LWR.

From the mathematical point of view, however, the analysis of ARZ requires a higher degree of technicalities because system (4) degenerates into just one equation at the vacuum. As observed in [31], taking initial data away from the vacuum does not forbid the emergence of vacuum in the solutions; in this case the solutions do not depend continuously on the initial data and experience a sudden increase of the total variation as the vacuum appears.

Goatin [30] bypasses these drawbacks of LWR and ARZ by coupling the two models. The resulting phase transition model (PT) describes the free-flow phase Ω_{f} with LWR and the congested phase Ω_{c} with ARZ. This PT model has been generalized in [10–12, 24].

An underlying assumption of all the models considered above (LWR, ARZ, PT) is that agents move in a homogeneous environment. However, in real life, agents typically move in inhomogeneous spaces characterized by "obstacles" that hinder the density flow, such as bottlenecks and traffic lights. The effect of such obstacles can be represented by introducing point constraints on the density flow

$$f(t, x_i) \leq Q_i \tag{5}$$

at the locations x_i of obstacles, where Q_i are their capacities, namely, the maximal density flows allowed through them. The concept of point constraints was first introduced in the framework of crowd dynamics in [23] and in [21] for vehicular traffic. The point constraint (5) is called nonlocal if Q_i depends in a nonlocal way on the density and local otherwise. We briefly summarize the literature on conservation laws with point constraints recalling that:

- LWR with a local point constraint is studied analytically in [21, 23] and numerically in [7, 16, 19, 22];
- LWR with a nonlocal point constraint is studied analytically in [2, 5] and numerically in [3];
- ARZ with a local point constraint is studied analytically in [6, 25, 28] and numerically in [1];
- PT with a local point constraint is analytically studied in [10, 12, 24].

In the present chapter, we shortly review the above results. For simplicity in the exposition, we consider below only the case of one obstacle placed at $x = 0$.

Despite the theory of point constraints is stated in a general mathematical framework (see, for instance, [44, Chapter 6]), according to the authors' knowledge, it is so far applied only in two frameworks: crowd dynamics [2, 3, 5, 18, 19, 23] and

vehicular traffic [1, 6, 7, 10, 12, 16, 21, 22, 24, 25, 28]. However, it is easy to envisage its application in other fields of research, such as biology (e.g., to model flows of biological substances across cell membranes), biomedicine (e.g., to model blood flows in vessels through thromboses), Internet traffic engineering (e.g., to model flows of data through routers or proxies), etc.

This chapter is organized as follows. Section 2 deals with the Cauchy problem for constrained LWR (3), and (5) in case the constraint is a function of the density, nonlocally both in time and space. The resulting problem is investigated analytically in Sect. 2.1 and numerically in Sect. 2.2. In Sect. 2.3, we construct exact and approximate solutions to some explicit cases. Section 3 deals with the Cauchy problem for constrained ARZ (4), and (5) in case the constraint is a function of time. The well-posedness is then considered in Sect. 3.1. In Sect. 3.2 we construct an exact solution to an explicit case. Section 4 deals with the Cauchy problem for constrained PT (3), (4), and (5) in case the constraint is constant. The well-posedness is then considered in Sect. 4.1. In Sect. 4.2 we construct an exact solution to an explicit case.

2 Nonlocally Constrained LWR

In this section we study the Cauchy problem for LWR (3) subject to a point constraint on the density flow (5)

$$\rho_t + f(\rho)_x = 0, \qquad x \in \mathbb{R},\ t \in (0,T], \tag{6a}$$

$$f(\rho)(t,0^{\pm}) \le Q(t), \qquad t \in (0,T], \tag{6b}$$

$$\rho(0,x) = \rho_0(x), \qquad x \in \mathbb{R}. \tag{6c}$$

Above $T > 0$ is the time horizon, ρ_0 is the initial datum, and $f(\rho) = \rho\, V(\rho)$ is the flux. Moreover Q is the maximal density flow allowed through $x = 0$ and has the form

$$Q(t) = \mathsf{Q}[\rho](t) \ \text{ for a.e. } t \in [0,T], \tag{7}$$

where the operator

$$\mathsf{Q}\colon \mathbf{C^0}(0,T;\mathbf{L^1}) \longrightarrow \mathbf{L^1}(0,T)$$

may be nonlocal both in time and space. Above

$$\mathbf{C^0}(0,T;\mathbf{L^1}) = \mathbf{C^0}\big([0,T];\mathbf{L^1}(\mathbb{R};[0,\rho_{\max}])\big) \quad \text{and}$$
$$\mathbf{L^1}(0,T) = \mathbf{L^1}\big((0,T);[0,f_{\max}]\big)$$

are, respectively, endowed with the distances induced by the norms

$$\|\rho\|_{\mathbf{C^0}(0,T;\mathbf{L^1})} = \max_{t\in[0,T]} \int_{\mathbb{R}} |\rho(t,x)|\,\mathrm{d}x \text{ and } \|Q\|_{\mathbf{L^1}(0,T)} = \int_0^T |Q(t)|\,\mathrm{d}t.$$

2.1 Existence and Uniqueness Results

We split the definition of solution to (6), and (7) into two points in the following.

Definition 1 A couple $(\rho, Q) \in \mathbf{C^0}([0,T];\mathbf{L^1_{loc}}(\mathbb{R};[0,\rho_{\max}])) \times \mathbf{L}^\infty(0,T)$ is an entropy solution to (6), and (7) if the following conditions hold:

(i) The function ρ is an entropy solution of constrained Cauchy problem (6), i.e., for every test function $\phi \in \mathbf{C^\infty_c}([0,T)\times\mathbb{R};\mathbb{R}_+)$ and constant $k \in [0,\rho_{\max}]$

$$\int_{\mathbb{R}}\left[\int_{\mathbb{R}_+}\left[|\rho-k|\phi_t + \operatorname{sign}(\rho-k)\big(f(\rho)-f(k)\big)\phi_x\right]\mathrm{d}t + |\rho_0(x)-k|\,\phi(0,x)\right]\mathrm{d}x \tag{8a}$$

$$+2\int_{\mathbb{R}_+}\left[1-\frac{Q(t)}{\max_{[0,\rho_{\max}]} f}\right] f(k)\,\phi(t,0)\,\mathrm{d}t \geq 0, \tag{8b}$$

and the left and right traces $t \mapsto \gamma^{\pm} f(\rho)(t)$ of $f(\rho)$ at $x = 0$ fulfill

$$\gamma^{\pm} f(\rho)(t) \leq Q(t) \text{ for a.e. } t \in [0,T]\,. \tag{8c}$$

(ii) The function Q is linked to ρ by relation (7).

Item (i) is precisely [7, Definition 2.1], which is a minor generalization of [21, Definition 3.2]. Line (8a) constitutes the classical Kruzhkov entropy condition (see [33]) suitable for a conservation law without any constraint condition, namely, for (6a), and (6c). Lines (8b) and (8c) account for constraint (6b). Recall that assumption (**GNL**) given below ensures that the strong traces $t \mapsto \gamma^{\pm}\rho(t)$ exist; hence $f(\rho)(t,0^{\pm})$ coincides with $f(\rho(t,0^{\pm}))$ (see [40]). In the sequel, we write $f(\rho)(t,0^{\pm})$ for $\gamma^{\pm} f(\rho)(t)$ and $\rho(t,0^{\pm})$ for $\gamma^{\pm}\rho(t)$.

Definition 2 Two constraint operators Q_1 and Q_2 are equivalent if $\mathsf{Q}_1[\rho] = \mathsf{Q}_2[\rho]$ for any entropy solution ρ of (6), and (7) corresponding to Q_1 or Q_2.

The existence results for (6), and (7) obtained in [5, 19, 21] rely on the wave-front tracking (WFT) method; see [15, 32] and the references therein. Such method is tailored to the specific expressions of Q and can be hardly generalized to even slight modification of Q. For this reason, as in [4], we provide below a rigorous set of

general hypotheses, which guarantee existence and uniqueness of entropy solutions for wide classes of constraint operators, via the application of splitting or fixed-point methods. More precisely, we assume that ρ_0 is in $\mathbf{L^1}(\mathbb{R};[0,\rho_{\max}])$ (due to the finite speed of propagation, property for (3), the extension to $\mathbf{L^\infty}(\mathbb{R};[0,\rho_{\max}])$ is straightforward; see [5, Theorem 2.1]). On the flux f, we always assume that

$$\begin{array}{l} f \text{ belongs to } \mathbf{Lip}([0,\rho_{\max}];\mathbb{R}_+) \text{ and is bell}-\text{shaped, that is, } f(0)=0=\\ f(\rho_{\max}) \text{ and there exists } \rho_c\in(0,\rho_{\max}) \text{ such that } f'(\rho)\,(\rho_c-\rho)>0\\ \text{for a.e. } \rho\in[0,\rho_{\max}]; \end{array} \tag{\textbf{f}}$$

some of our results require the additional assumption

$$\begin{array}{l} \text{for any} \rho_1,\rho_2\in[0,\rho_{\max}] \text{ such that } \rho_1<\rho_2, \text{ the restriction of } f \text{ to}\\ [\rho_1,\rho_2] \text{ is not affine.} \end{array} \tag{\textbf{GNL}}$$

By (**f**) we have that $f_{\max}=\max_{[0,\rho_{\max}]} f$ satisfies $f_{\max}=f(\rho_c)$. On Q we assume that it is "history dependent," that is

$$\begin{array}{l} \text{if } \rho_1,\rho_2\in\mathbf{C^0}(0,T;\mathbf{L^1}) \text{ coincide on } [0,t]\times\mathbb{R}, \text{ then } \mathsf{Q}[\rho_1] \text{ and } \mathsf{Q}[\rho_2]\\ \text{coincide on } [0,t], \end{array} \tag{$\mathbf{Q}^{\mathrm{hd}}$}$$

and that for any $t\in[0,T]$ the restriction $\mathsf{Q}_t\colon \mathbf{C^0}(0,t;\mathbf{L^1})\to\mathbf{L^1}(0,t)$ of Q to $\mathbf{C^0}(0,t;\mathbf{L^1})$ is such that

$$\begin{array}{l} \mathsf{Q}_t \text{ is Lipschitz continuous, and there exists a non}-\text{decreasing map } \omega\in\\ \mathbf{C^0}(\mathbb{R}_+;\mathbb{R}_+) \text{ such that } \omega(0)=0 \text{ and for any } \rho_1,\rho_2\in\mathbf{C^0}(0,T;\mathbf{L^1})\\ \qquad \|\mathsf{Q}_t[\rho_1]-\mathsf{Q}_t[\rho_2]\|_{\mathbf{L^1}(0,t)}-\omega(t-\tau)\,\|\rho_1-\rho_2\|_{\mathbf{C^0}(0,t;\mathbf{L^1})}\le 0,\\ \text{where } \tau=\max\{s\in[0,t]\colon \rho_1=\rho_2 \text{ in } \mathbf{C^0}(0,s;\mathbf{L^1})\}. \end{array} \tag{$\mathbf{Q}^{\mathrm{Lip}}$}$$

By ($\mathbf{Q}^{\mathrm{hd}}$) we have that Q_t, $t\in[0,T]$, can be defined by letting $\mathsf{Q}_t[\rho]$ as the restriction to $[0,t]$ of $\mathsf{Q}[\mathscr{E}[\rho]]$, where $\mathscr{E}[\rho]\in\mathbf{C^0}(0,T;\mathbf{L^1})$ is an arbitrary extension of $\rho\in\mathbf{C^0}(0,t;\mathbf{L^1})$.

Before stating our main results, let us recall the uniform Lipschitz continuity estimate obtained in [7, Proposition 2.10].

Lemma 1 *For any $Q_1,Q_2\in\mathbf{L^\infty}(0,T)$ and $t\in[0,T]$, the corresponding entropy solutions $\rho_1,\rho_2\in\mathbf{C^0}(0,t;\mathbf{L^1})$ to (6) with time horizon t satisfy*

$$\|\rho_1-\rho_2\|_{\mathbf{C^0}(0,t;\mathbf{L^1})}\le 2\,\|Q_1-Q_2\|_{\mathbf{L^1}(0,t)}.$$

We have the following well-posedness result.

Theorem 1

1. *If* Q *verifies* ($\mathbf{Q}^{\mathrm{Lip}}$)*, then constrained Cauchy problem* (6)*, and* (7) *admits one and only one entropy solution.*
2. *The conclusion of 1 still holds true if* Q *is equivalent to a constraint that verifies* ($\mathbf{Q}^{\mathrm{Lip}}$).

Proof By ($\mathbf{Q}^{\mathrm{Lip}}$) and Lemma 1, the Banach-Picard fixed-point argument yields both existence and uniqueness of solutions on a sufficiently small time interval. Bootstrapping the construction, we achieve the global existence result.

In practice, verification of assumption ($\mathbf{Q}^{\mathrm{Lip}}$) may be tedious; for this reason we provide the following.

Proposition 1 *A constraint operator* Q *satisfies* ($\mathbf{Q}^{\mathrm{Lip}}$) *if there exists a constant* $C > 0$ *such that one of the following conditions is satisfied:*

1. *for all* $t \in [0, T]$, Q_t *verifies* $\|\mathsf{Q}[\rho_1] - \mathsf{Q}[\rho_2]\|_{\mathbf{L^1}(0,t)} \leq C \, \|\rho_1 - \rho_2\|_{\mathbf{L^1}(0,t;\mathbf{L^1})}$;
2. *for all* $t \in [0, T]$, Q_t *verifies* $\|\mathsf{Q}[\rho_1] - \mathsf{Q}[\rho_2]\|_{\mathbf{L}^\infty(0,t)} \leq C \, \|\rho_1 - \rho_2\|_{\mathbf{C^0}(0,t;\mathbf{L^1})}$.

While uniqueness seems to require some kind of Lipschitz continuity of Q, existence results can be obtained in much more generality. In fact, under assumption (**GNL**), it is enough to require that

$$\mathsf{Q} \text{ can be extended to a continuous map from } \mathbf{L^1}(0, T; \mathbf{L^1}) \text{ to } \mathbf{L^1}(0, T), \quad (\mathbf{Q}^{\mathrm{cont}})$$

whereas if (**GNL**) does not hold, then it is enough to require that

$$\mathsf{Q} \text{ is continuous and compact from } \mathbf{C^0}(0, T; \mathbf{L^1}) \text{ to } \mathbf{L^1}(0, T). \qquad (\mathbf{Q}^{\mathrm{comp}})$$

Above

$$\mathbf{L^1}(0, T; \mathbf{L^1}) = \mathbf{L^1}\big((0, T) \times \mathbb{R}; [0, \rho_{\max}]\big) \text{ and } \mathbf{L}^\infty(0, T) = \mathbf{L}^\infty\big((0, T); [0, f_{\max}]\big)$$

are, respectively, endowed with the distances induced by the norms

$$\|\rho\|_{\mathbf{L^1}(0,T;\mathbf{L^1})} = \int_0^T \int_{\mathbb{R}} |\rho(t, x)| \, \mathrm{d}x \, \mathrm{d}t \quad \text{and} \quad \|Q\|_{\mathbf{L}^\infty(0,T)} = \operatorname{ess\,sup}_{t \in (0,T)} |Q(t)|.$$

More precisely, we have the following existence result.

Theorem 2 *Constrained Cauchy problem* (6)*, and* (7) *admits at least one entropy solution if one of the following conditions is satisfied:*

(a) Q *satisfies* ($\mathbf{Q}^{\mathrm{comp}}$).
(b) f *satisfies* (**GNL**) *and* Q *satisfies* ($\mathbf{Q}^{\mathrm{cont}}$).

The same conclusion holds if Q *is equivalent to a constraint operator that satisfies* (a) *or* (b).

Proof In case (b), compactness of families of functions (ρ_Δ) solving (6a) in $x \neq 0$ is obtained by using the results in [39]. In case (a), compactness of the corresponding (Q_Δ) (and consequently that of (ρ_Δ)) is straightforward. In both cases, the Schauder fixed-point argument can be used to resolve the coupling between ρ and Q in (6), and (7).

Notice that the embeddings $\mathbf{L^1}(0,T;\mathbf{L^1}) \supset \mathbf{C^0}(0,T;\mathbf{L^1})$ and $\mathbf{L^\infty}(0,T) \subset \mathbf{L^1}(0,T)$ are continuous. Moreover, since the topology of $\mathbf{L^1}(0,T;\mathbf{L^1})$ is weaker than that of $\mathbf{C^0}(0,T;\mathbf{L^1})$, ($\mathbf{Q}^{\mathrm{cont}}$) and ($\mathbf{Q}^{\mathrm{comp}}$) are not directly comparable.

In the spirit of Proposition 1, let us point out that the compactness assumption on Q can follow from the stronger assumption of compactness of Q as operator from $\mathbf{C^0}(0,T;\mathbf{L^1})$ to $\mathbf{L^\infty}(0,T)$.

2.2 Finite Volume Approximation

In this section we describe the numerical scheme [4] based on finite volume method that we use to solve (6), and (7) and prove its convergence to entropy solutions under the general assumptions ($\mathbf{Q}_\Delta^{\mathbf{cons}}$) and ($\mathbf{Q}_\Delta^{\mathbf{comp}}$) given below.

Let Δx and Δt be the constant space and time steps, respectively. Introduce the points $x_{j+1/2} = j\Delta x$, the cells $K_j = [x_{j-1/2}, x_{j+1/2})$ and the cell centers $x_j = (j-1/2)\Delta x$ for $j \in \mathbb{Z}$. Let j_c be the index such that $x_{j_c+1/2}$ is the location of the constraint. Define $N = \lfloor T/\Delta t \rfloor$ and for $n \in \mathbb{N} \cap [0,N]$ introduce the time discretization $t^n = n\Delta t$. For $n \in \mathbb{N} \cap [0,N]$ and $j \in \mathbb{Z}$, we denote by ρ_j^n the approximation of the average of $\rho(t^n,\cdot)$ on the cell K_j, namely

$$\rho_j^0 = \frac{1}{\Delta x}\int_{K_j} \rho_0(x)\,\mathrm{d}x \qquad \text{and} \qquad \rho_j^n \simeq \frac{1}{\Delta x}\int_{K_j} \rho(t^n,x)\,\mathrm{d}x \qquad \text{if } n>0.$$

The discretized initial datum ρ_Δ^0 is defined by

$$\rho_\Delta^0(x) = \rho_j^0 \qquad \text{for } x \in K_j, \tag{9}$$

convergences to ρ_0 in $\mathbf{L^1}(\mathbb{R})$ and obeys the same $\mathbf{L^\infty}$ bounds as ρ_0.

Let $(\rho_\Delta, Q_\Delta)\colon [0,T]\times\mathbb{R} \to [0,\rho_{\max}]\times[0,f_{\max}]$ be an approximate solution with

$$\rho_\Delta(t,x) = \sum_{n=1}^{N} \rho_\Delta^n(x)\,\chi_{(t^{n-1},t^n]}(t), \qquad Q_\Delta(t) = \sum_{n=1}^{N} Q_\Delta^n\,\chi_{(t^{n-1},t^n]}(t),$$

where $(\rho_\Delta^n, Q_\Delta^n)$ is a discrete function computed by executing the following algorithm, based on a suitable discretization Q_Δ of Q that satisfies ($\mathbf{Q}^{\mathrm{hd}}$).

0. Initialization. We start with ρ_Δ^0 given in (9) and $Q_\Delta^0 = \mathsf{Q}_\Delta[\rho_\Delta^0](0)$.
1. For each $n \in [0, N-1] \cap \mathbb{N}$,

   A. A finite volume method [7] for constrained Cauchy problem (6) is

$$\rho_j^{n+1} = \rho_j^n - \frac{\Delta t}{\Delta x}\left(\mathscr{F}_{j+1/2}^n - \mathscr{F}_{j-1/2}^n\right), \tag{10}$$

   where

$$\mathscr{F}_{j+1/2}^n = \begin{cases} \mathfrak{F}\left(\rho_j^n, \rho_{j+1}^n\right) & \text{if } j \neq j_c, \\ \min\left\{\mathfrak{F}\left(\rho_j^n, \rho_{j+1}^n\right), Q_\Delta^n\right\} & \text{if } j = j_c, \end{cases} \tag{11}$$

   is a monotone, consistent numerical flux, namely

   - $\mathfrak{F} \in \mathbf{Lip}([0, \rho_{\max}]^2; \mathbb{R})$ with Lipschitz constant $\mathrm{Lip}(\mathfrak{F})$,
   - $\mathfrak{F}(a, a) = f(a)$ for any $a \in [0, \rho_{\max}]$,
   - $[0, \rho_{\max}]^2 \ni (a, b) \mapsto \mathfrak{F}(a, b) \in [0, f_{\max}]$ is non-decreasing with respect to a and non-increasing with respect to b,

   and Q_Δ^n is an approximation of $Q(t^n)$.

   B. Given $(\rho_\Delta^k)_{k=1,\dots,n}$ with $\rho_\Delta^n(x) = \rho_j^n$ for $x \in K_j$, we compute $Q_\Delta^n \in [0, f_{\max}]$ by discretizing relation (7):

$$Q_\Delta^n = \mathsf{Q}_\Delta\left[\mathscr{E}^n[\rho_\Delta^n]\right](t^n), \tag{12}$$

   where $\mathscr{E}^n[\rho_\Delta^n](t, x) = \sum_{k=1}^n \rho_\Delta^k(t - t^{k-1}, x)\, \mathbf{1}_{(t^{k-1}, t^k]}(t)$.

We use the $\mathbf{L^1}(0, T)$-norm for Q_Δ and with the $\mathbf{L^\infty}(0, T; \mathbf{L^1})$-norm for ρ_Δ, both norms being computed from the above expressions of Q_Δ and ρ_Δ as functions of t and (t, x), respectively.

In the following we assume that the approximations of Q given by Q_Δ are consistent

$$\left.\begin{array}{l} \|Q_\Delta - Q\|_{\mathbf{L^1}(0,T)} \to 0 \\ \|\rho_\Delta - \rho\|_{\mathbf{L^1}(0,T;\mathbf{L^1})} \to 0 \\ Q_\Delta = \mathsf{Q}_\Delta[\rho_\Delta] \end{array}\right\} \Longrightarrow Q = \mathsf{Q}[\rho] \qquad (\mathbf{Q}_\Delta^{\mathbf{cons}})$$

and the following asymptotic compactness property

$$\left.\begin{array}{l} (\rho_\Delta) \text{ is bounded in } \mathbf{L^\infty}(0, T; \mathbf{L^1}) \\ Q_\Delta = \mathsf{Q}_\Delta[\rho_\Delta] \end{array}\right\} \Longrightarrow (Q_\Delta) \text{ is compact in } \mathbf{L^1}(0, T). \quad (\mathbf{Q}_\Delta^{\mathbf{comp}})$$

Here and in the sequel, by compactness of (Q_Δ), we mean the possibility to extract a convergent subsequence in $\mathbf{L^1}(0,T)$, i.e., the relative compactness.

As in [7, Proposition 4.2], under the CFL condition

$$\mathrm{Lip}(\mathfrak{F})\ \frac{\Delta t}{\Delta x} \le \frac{1}{2},$$

we have the $\mathbf{L}^\infty$-stability of the scheme (10), (11), and (12), that is

$$0 \le \rho_\Delta(t,x) \le \rho_{\max} \qquad \text{for a.e. } (t,x) \in (0,T)\times\mathbb{R}.$$

We have the following convergence results of our scheme.

Theorem 3 *Let* Q *verify* ($\mathbf{Q}^{\mathrm{Lip}}$) *and* (ρ, Q) *be the unique entropy solution of* (6), *and* (7).

1. *If* Q *admits an approximation* Q_Δ *that satisfies* ($\mathbf{Q}_\Delta^{\mathbf{cons}}$) *and* ($\mathbf{Q}_\Delta^{\mathbf{comp}}$). *Then* (ρ_Δ, Q_Δ) *constructed by the scheme* (10), (11), *and* (12) *converges to* (ρ, Q) *as* $\Delta t, \Delta x \to 0$.
2. *The conclusion of 1. still holds true if* Q *is equivalent to a constraint that verifies* ($\mathbf{Q}^{\mathrm{Lip}}$) *and admits an approximation that satisfies* ($\mathbf{Q}_\Delta^{\mathbf{cons}}$) *and* ($\mathbf{Q}_\Delta^{\mathbf{comp}}$), *then the approximate solution constructed by the corresponding scheme* (10), (11), *and* (12) *converges to* (ρ, Q) *as* $\Delta t, \Delta x \to 0$.

2.3 Examples

In this section we give some examples of constraint operators satisfying the hypothesis of Theorem 1. This means that the associated constrained Cauchy problems are well-posed. Below $q \in \mathbf{Lip}([0,\rho_{\max}];(0,f_{\max}])$ is non-increasing, $w \in \mathbf{L}^\infty(\mathbb{R}_-;\mathbb{R}_+)$ is non-decreasing with $\|w\|_{\mathbf{L^1}(\mathbb{R}_-)} = 1$ and $\mathrm{supp}(w) = [-\mathrm{i}_w, 0]$, $\mathrm{i}_w > 0$, $\kappa \in \mathbf{Lip}(\mathbb{R}_+;\mathbb{R}_+)$ is non-increasing with $\|\kappa\|_{\mathbf{L^1}(\mathbb{R}_+)} = 1$ and $\mathrm{supp}(\kappa) = [0,\tau]$, $\tau > 0$, which express the dependence of the constraint level on the subjective density, the space non-locality, and the time non-locality (memory), respectively. We also assume that w belongs to $\mathbf{Lip}((-\infty,0);\mathbb{R}_+)$ but can be/is discontinuous at $x = 0$. The numerical simulations are performed using the Ruzanov fux [45]:

$$\mathfrak{F}(a,b) = \frac{f(a)+f(b)}{2} - \frac{b-a}{2}\max(|f'(a)|,|f'(b)|).$$

Example 1 If $w \in \mathbf{C_c^1}(\mathbb{R};\mathbb{R}_+)$ and $\mathfrak{K} \in \mathbf{C^2}(\mathbb{R}_+;\mathbb{R}_+)$ is the primitive of κ such that $\mathfrak{K}(0) = 0$, then the nonlocal (both in time and space) constraint operators

$$\mathsf{Q}_1[\rho](t) = q\left(\int_{\mathbb{R}_-}\int_0^t w(x)\,\kappa(t-s)\,\rho(s,x)\,\mathrm{d}s\,\mathrm{d}x\right), \tag{13}$$

$$\mathsf{Q}_2[\rho](t) = q\Bigg(\int_{\mathbb{R}_-} \left[w(x)\, \mathfrak{K}(t)\, \rho_0(x) + w'(x) \int_0^t \mathfrak{K}(t-s)\, f(\rho)(s,x)\, \mathrm{d}s \right] \mathrm{d}x$$
$$- w(0^-) \int_0^t \mathfrak{K}(t-s)\, f(\rho)(s,0^-)\, \mathrm{d}s \Bigg), \tag{14}$$

are well defined and equivalent. Such operators correspond to the case of a maximal density flow at $x = 0$ which depends on the values of ρ in $\mathrm{supp}(\kappa(t-\cdot)) \times \mathrm{supp}(w)$. The monotonicity assumption on w (on κ) implies that the capacity is more affected by the "closest" ("more recent") values of ρ. Let also

$$\mathsf{Q}_3[\rho](t) = q\left(\sum_{0<t_i\le t} [t_i - t_{i-1}]\, \kappa(t-t_{i-1}) \left[\int_{\mathbb{R}_-} w(x)\, \rho(t_i,x)\, \mathrm{d}x \right] \right), \tag{15}$$

$$\mathsf{Q}_4[\rho](t) = q\Bigg(\sum_{y_i<0} [y_{i+1} - y_i]\, w(y_i) \left[\int_0^t \kappa(t-s)\, \rho(s,y_{i+1})\, \mathrm{d}s \right] \Bigg), \tag{16}$$

which are discretized versions of Q_1, with $t_i < t_{i+1}$ and $y_0 \le y_i < y_{i+1} \le y_{M+1} = 0$.

Such operators can model, for instance, the traffic through tollbooths if the number of open gates is decided according to online data. One might think that both Q_1 and Q_2 correspond to data collected by a video camera registering the area given by $\mathrm{supp}(w)$, Q_3 corresponds to data collected by a photo camera that shoots photos at times t_i of the area given by $\mathrm{supp}(w)$, and Q_4 corresponds to data collected by local sensors located at y_i. In each of these cases, $\mathrm{supp}(\kappa)$ is the period of time the data are taken into account.

In Fig. 1 we represent the exact solution ρ corresponding to the constraint operator Q_1, $f(\rho) = (1-\rho)\,\rho$ (hence $v_{\max} = 1$ and $\rho_{\max} = 1$), $w(x) = 2(1+x)\,\chi_{[-1,0]}(x)$, $\kappa(t) = 2(1-t)\,\chi_{[0,1]}(t)$, $\rho_0(x) = \chi_{[-6,-1.2]}(x)$ and

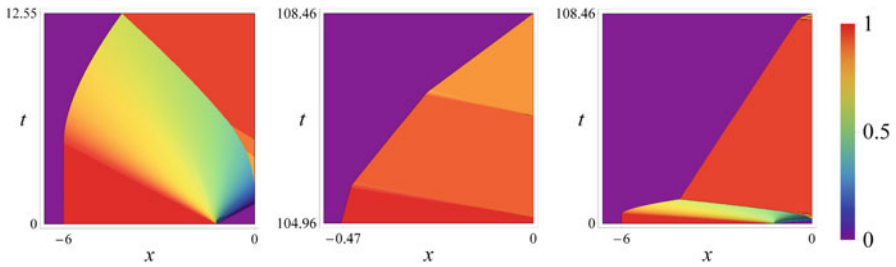

Fig. 1 The solution ρ described in Example 1

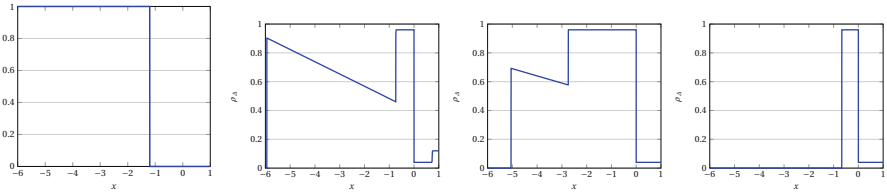

(a) (b) (c) (d)

Fig. 2 The approximate solution $x \mapsto \rho_\Delta(t,x)$ at different times for $\Delta x = 10^{-3}$ and $\Delta t = 4 \times 10^{-4}$. (**a**) $\rho_\Delta(0,x)$. (**b**) $\rho_\Delta(5.878,x)$. (**c**) $\rho_\Delta(10,x)$. (**d**) $\rho_\Delta(100,x)$

Table 1 Relative $\mathbf{L^1}$-error at time $t = 10$, for the constraints Q_1 and Q_2

	Q_1 defined in (13)		Q_2 defined in (14)	
Space step	$\mathbf{L^1}$-error	Rate of convergence	$\mathbf{L^1}$-error	Rate of convergence
600	9.68×10^{-3}	–	1.07×10^{-2}	–
1200	5.06×10^{-3}	0.935	5.64×10^{-3}	0.923
2400	2.73×10^{-3}	0.913	3.03×10^{-3}	0.91
6000	1.24×10^{-3}	0.891	1.37×10^{-3}	0.892
12000	6.56×10^{-4}	0.892	7.28×10^{-4}	0.892
24000	3.36×10^{-4}	0.902	3.8×10^{-4}	0.898

$$q(\xi) = \begin{cases} q_0 & \text{if } 0 \le \xi < \xi_1, \\ q_1 & \text{if } \xi_1 \le \xi < \xi_2, \\ q_2 & \text{if } \xi_2 \le \xi \le 1, \end{cases} \tag{17}$$

with $q_0 = 0.16$, $q_1 = 0.1056$, $q_2 = 0.0384$, $\xi_1 \sim 0.508$, $\xi_2 \sim 0.6911$. The approximate solution $x \mapsto \rho_\Delta(t,x)$ is represented at different fixed times t in Fig. 2. Table 1 lists the relative $\mathbf{L^1}$-errors

$$\left[\sum_j \left|\rho(t^n, x_j) - \rho_j^n\right|\right] \Big/ \left[\sum_j \left|\rho(t^n, x_j)\right|\right]$$

at time $t^n = 10$ between the exact and approximate solutions computed with the constraint operators Q_1 and Q_2 for different numbers of space cells and for a fixed time step $\Delta t = 10^{-4}$. The relative $\mathbf{L^1}$-errors are similar; hence the solutions corresponding to Q_1 and Q_2 are essentially the same, and in fact Q_1 and Q_2 are very close to one another. This is not surprising, indeed, the constraint operators Q_1 and Q_2 are equivalent in the sense of Definition 2. We recall that equivalent constraints lead to the same solutions. Thus, the schemes based on the respective discretizations of Q_1 and Q_2 should be seen as different approximations of one and the same continuous problem.

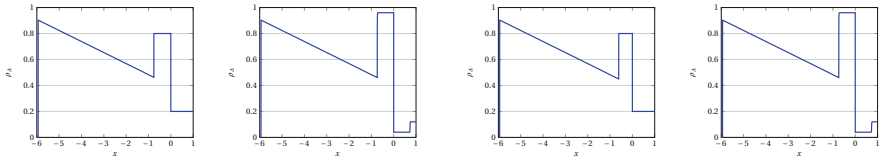

(a) (b) (c) (d)

Fig. 3 Solutions $x \mapsto \rho_\Delta(10, x)$ corresponding to Q_3 and Q_4 for $\Delta x = 10^{-3}$ and $\Delta t = 4 \times 10^{-4}$. (**a**) $x \mapsto \rho_\Delta(5.878, x)$ for $t_0 = 0$, $t_1 = 2$ and $t_3 = 5$. (**b**) $x \mapsto \rho_\Delta(5.878, x)$ for all $t_i = i\,\Delta t$, $i = 0, \ldots, 14695$. (**c**) $x \mapsto \rho_\Delta(5.878, x)$ for $y_0 = -1.1$ and $y_1 = 0$. (**d**) $x \mapsto \rho_\Delta(5.878, x)$ for all $y_i = -6 + i\,\Delta x$, $i = 1, \ldots, 7000$

We focus on the constraint operators Q_3 and Q_4. For each of them, we perform two types of simulations: one by taking a small number of discretized times or positions (see Fig. 3a, c) and one by taking all the times and positions of the discretization (see Fig. 3b, d). Notice a good agreement between Fig. 3b, d, and Fig. 2c. As expected, the constraint operator that corresponds to the case where data are collected by a video camera is the more efficient since the two other may underestimate the importance of the congestion before the exit.

Example 2 The *capacity drop* of a bottleneck when a high density accumulates upstream is reproduced in [5] by the constraint operator

$$\mathsf{Q}_1[\rho](t) = q\big(\Xi^1(t)\big), \qquad \Xi^1(t) = \int_{\mathbb{R}_-} w(x)\,\rho(t,x)\,\mathrm{d}x, \tag{18}$$

where Ξ^1 is *subjective density* at the bottleneck. Existence and uniqueness results for this model are proved in [5, Theorem 3.1]. Since ($\mathbf{Q}^{\mathrm{hd}}$) is obvious and ($\mathbf{Q}^{\mathrm{Lip}}$) follows from Proposition 1, thanks to Theorem 1 we can give a shorter alternative proof, which requires weaker hypotheses on q and w. However this proof does not give any hint on the behavior of the entropy solution nor a priori bounds of its total variation, unlike to the (much longer) arguments of [5]. Observe that we do not need to assume (**GNL**).

According to this model, even a small density may form a queue provided a sufficiently high density is approaching from behind. This drawback is tempered by considering a memory effect and choosing $\mathsf{Q}_2[\rho](t) = q\big(\Xi^2(t)\big)$ with

$$\Xi^2(t) = \min\left\{\int_{\mathbb{R}_-} w(x)\,\rho(t,x)\,\mathrm{d}x,\ \alpha f_-^{-1}\left(\int_0^t \kappa(t-s)\,f(\rho)(s,0^-)\,\mathrm{d}s\right)\right\}, \tag{19}$$

being $\alpha \in (0, \rho_{\max}/\rho_c]$ a constant and f_- the restriction of f to $[0, \rho_c]$. Indeed, if, for instance, $\alpha = \sqrt{5}$, the numerical domain is $[-6, 1]$, $f(\rho) = (1-\rho^2)^2\,\rho$, $\rho_0(x) = \chi_{[-1,-0.1]}(x)$ and

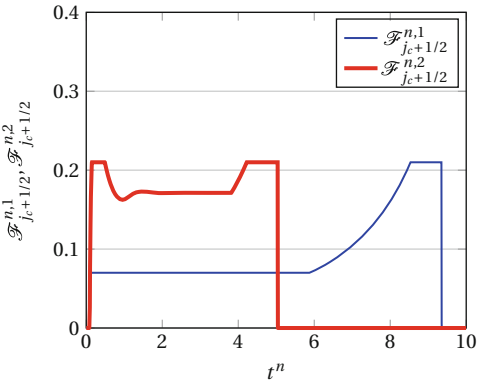

Fig. 4 The fluxes at the exit $\mathscr{F}^{n,1}_{j_c+1/2}$ and $\mathscr{F}^{n,2}_{j_c+1/2}$ corresponding to the constraints (18) and (19), respectively, for $\Delta x = 10^{-3}$ and $\Delta t = 4 \times 10^{-4}$

$$q(\xi) = \begin{cases} q_0 & \text{if } 0 \le \xi < \xi_1, \\ \dfrac{(q_0 - q_1)\xi + q_1\xi_1 - q_0\xi_2}{\xi_1 - \xi_2} & \text{if } \xi_1 \le \xi < \xi_2, \\ q_1 & \text{if } \xi_2 \le \xi \le 1, \end{cases}$$

with $q_0 = 0.21$, $q_1 = 0.07$, $\xi_1 = 0.3$, $\xi_2 = 0.7$, then, at least in this case, the constraint operator (19) does not present the drawback pointed out for the constraint operator (18); see Fig. 4. Moreover, Fig. 4 shows that the constraint operator (19) qualitatively reproduces also the self-organization. Indeed, the flux in red first increases until it reaches the maximum level of the efficiency of the exit, and then it falls down, and after a very short period, it increases without reaching the maximum level of the efficiency: this is the effect of self-organization [17, 47].

A further drawback of (18) is that it does not take into account memory effects of inertia kind; in fact Ξ^1 is the solution of the ordinary differential equation (ODE)

$$\dot{\Xi}(t) = \int_{\mathbb{R}_-} w'(x)\big[f(\rho)(t,x) - f(\rho)(t,0^-)\big]\mathrm{d}x,$$

hence Ξ^1 uniquely depends on the instantaneous values of ρ. This drawback is tempered by choosing Ξ^3 or Ξ^4 solutions in $\mathscr{D}'([0,T))$ of the Cauchy problems for ODEs

$$\Xi^3: \begin{cases} \dot{\Xi}(t) = \max\left\{\int_{\mathbb{R}_-} w'(x)\big[f(\rho)(t,x) - f(\rho)(t,0^-)\big]\mathrm{d}x, -\delta\,\Xi(t)\right\}, \\ \Xi(0) = \Xi_0[\rho_0], \end{cases} \tag{20}$$

$$\Xi^4: \begin{cases} \dot{\Xi}(t) = \max\left\{\int_{\mathbb{R}_-} w'(x)\big[f(\rho)(t,x) - f(\rho)(t,0^-)\big]\mathrm{d}x, -\delta\right\}, \\ \Xi(0) = \Xi_0[\rho_0], \end{cases} \tag{21}$$

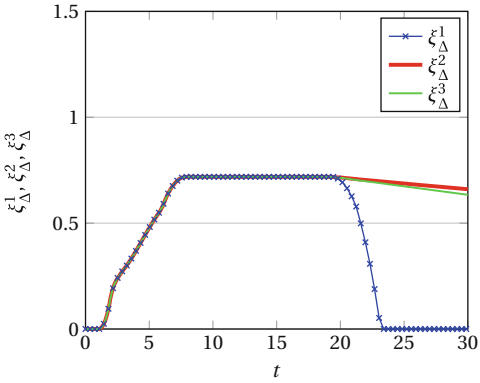

Fig. 5 The approximate functions Ξ^1_Δ, Ξ^3_Δ, Ξ^4_Δ of Ξ^1, Ξ^3, Ξ^4 defined in (18), (20), and (21) for $\Delta x = 10^{-3}$ and $\Delta t = 4 \times 10^{-4}$

where $\Xi_0 \colon \mathbf{L^1}(\mathbb{R}) \to \mathbb{R}$ and $\delta > 0$ is a constant. Indeed, if $\delta = 8 \times 10^{-3}$, the numerical domain is $[-6, 1]$, $f(\rho) = (1 - \rho^2)^2\, \rho$, $\rho_0(x) = \chi_{[-5.75,-2]}(x)$, q is given by (17) with $q_0 = 0.21$, $q_1 = 0.168$, $q_2 = 0.021$, $\xi_1 = 0.566$, $\xi_2 = 0.731$, then, at least in this case, the constraint operators associated to (20) and (21) do not present the drawback pointed out for the constraint operator (18); see Fig. 5.

3 Locally Constrained ARZ

This section is devoted to the study of ARZ (4)

$$\begin{pmatrix} \rho \\ y \end{pmatrix}_t + \left[\left(\frac{y}{\rho} - p(\rho) \right) \begin{pmatrix} \rho \\ y \end{pmatrix} \right]_x = \begin{pmatrix} 0 \\ 0 \end{pmatrix}, \tag{22}$$

where the density ρ and the generalized momentum y are such that (ρ, y) belongs to $\mathscr{Y} = \{(\rho, y) \in \mathbb{R}^2_+ \colon 0 \le \rho\, p(\rho) \le y\}$. Recall that $p \colon \mathbb{R}_+ \to \mathbb{R}_+$ accounts agents' reactions to the state of traffic in front of them. We assume that p belongs to $\mathbf{C^0}(\mathbb{R}_+; \mathbb{R}_+) \cap \mathbf{C^2}((0, \infty); \mathbb{R}_+)$ and satisfies

$$p(0) = 0, \quad p'(\rho) > 0 \quad \text{and} \quad p'(\rho) + \rho\, p''(\rho) > 0 \quad \text{for every } \rho > 0,$$

$$\lim_{\rho \downarrow 0} \left[\rho^2 p'(\rho) \right] = 0, \qquad \lim_{\rho \downarrow 0} \left| \frac{\rho\, p''(\rho)}{p'(\rho)} \right| < \infty.$$

Typical choice is $p(\rho) = \rho^\gamma$, $\gamma > 0$; see [8].

ARZ can be interpreted as a generalization of LWR, possessing a fundamental diagram (ρ, f) which is a two-dimensional manifold rather than a one-dimensional manifold as for LWR. This is consistent with experimental data (see, for instance, [20, Figure 1.1] or [14, Figure 3.1]), according to which the fundamental diagram (ρ, f) is given by a cloud of points rather than being the support of a map $\rho \mapsto V(\rho)\, \rho$.

To any Lagrangian marker $w = y/\rho$, we can associate the fundamental diagram curve $\rho \mapsto (w - p(\rho))\,\rho$, which has maximal slope w and intersects $f = 0$ at the vacuum $\rho = 0$ and at $\rho = p^{-1}(w)$. Since $w = w(t, x)$ satisfies the equation $w_t + v\, w_x = 0$, the vehicle initially at $x_0 \in \mathbb{R}$ is characterized at any time $t > 0$ by the Lagrangian marker $w(0, x_0)$ and has, therefore, maximal speed $w(0, x_0)$ and length $1/p^{-1}(w(0, x_0))$. For this reason, ARZ can also be interpreted as a generalization of LWR to the case of a multi-population traffic.

Away from the vacuum, system (22) is strictly hyperbolic, $\lambda_1 < \lambda_2$, the first characteristic field is genuinely nonlinear, $\nabla\lambda_1 \cdot R_1 < 0$, and the second characteristic field is linearly degenerate, $\nabla\lambda_2 \cdot R_2 = 0$, where $\lambda_1 = \frac{y}{\rho} - p(\rho) - \rho\, p'(\rho)$, $\lambda_2 = \frac{y}{\rho} - p(\rho)$ are the eigenvalues of the Jacobian matrix of the flux and $R_1 = (\rho, y)$, $R_2 = (\rho, y + \rho^2 p'(\rho))$ are the corresponding eigenvectors.

At the vacuum, system (22) degenerates into just one equation. In particular, the solutions to (22) fail to depend continuously on the initial data in any neighborhood of $\rho = 0$ (see [8]); moreover, the solutions may experience a sudden increase of the total variation as the vacuum appears (see [31]).

A theory for traffic flow away from the vacuum is not of practical interest. Indeed, a trivial example of vacuum formation is downstream of a traffic light when it is red. Moreover, vacuum might appear even without the action of a traffic light when, for instance, slow and fast vehicles initially in $(-\infty, 0]$ and $(0, \infty)$, respectively, move at their maximal speed. For this reason we extend the flux to the vacuum by introducing $F\colon \mathscr{Y} \to \mathbb{R}_+$ defined by

$$F(\rho, y) = \begin{cases} (0, 0) & \text{if } \rho = 0, \\ \left[\frac{y}{\rho} - p(\rho)\right](\rho, y) & \text{if } \rho \neq 0. \end{cases}$$

Moreover, we introduce the change of variables

$$\rho = \mathfrak{r}(v, w), \qquad\qquad y = \mathfrak{r}(v, w)\, w,$$

where the components of (v, w) are the Riemann invariant coordinates (velocity and Lagrangian marker, respectively) and $\mathfrak{r}(v, w) = p^{-1}(w - v)$. The main motivation for this change of variables stems from the fact that the total variation of the solutions in these coordinates does not increase; see [27, 31, 37] where this property is exploited to prove existence results for ARZ. Furthermore, at the vacuum, the entropy pairs defined below in (24) are well defined in the (v, w) coordinates and multivalued in the (ρ, y) coordinates.

In the new variables, $\mathscr{Y}$ becomes $\mathscr{W} = \{(v, w) \in \mathbb{R}^2_+ \colon v \leq w\}$. Notice that the vacuum $\rho = 0$ corresponds in the (ρ, y) variables to the point $(\rho, y) = (0, 0)$ and in the (v, w) variables to the half line $\mathscr{W}_0 = \{(v, w) \in \mathscr{W} \colon v = w\}$. Let $\mathscr{W}_0^c = \mathscr{W} \setminus \mathscr{W}_0$ be the set of the non-vacuum states.

The Cauchy problem for ARZ (22) subject to a point constraint on the density flow (5) writes in the new variables

$$Y(v,w)_t + F\big(Y(v,w)\big)_x = (0,0), \qquad x \in \mathbb{R},\ t \in (0,T], \tag{23a}$$

$$f(v,w)(t,0^{\pm}) \le Q(t), \qquad t \in (0,T], \tag{23b}$$

$$(v,w)(0,x) = (v_0,w_0)(x), \qquad x \in \mathbb{R}, \tag{23c}$$

where $T > 0$ is the time horizon, $Y(v,w) = (\mathfrak{r}(v,w), \mathfrak{r}(v,w)\,w)$, $(v_0,w_0) \in \mathbf{L}^{\infty}(\mathbb{R};\mathscr{W})$ is the initial datum, $Q(t)$ is the maximal density flow allowed at $x=0$ at time $t>0$, and $f(v,w) = \mathfrak{r}(v,w)\,v$.

3.1 Existence and Uniqueness Results

Before stating the definition of entropy solution to (23), we introduce the family of entropy-entropy flux pairs

$$\mathrm{E}_k(v,w) = \begin{cases} 0 & \text{if } v \le k,\\ 1 - \frac{p^{-1}(w-v)}{p^{-1}(w-k)} & \text{if } v > k, \end{cases} \qquad \mathrm{F}_k(v,w) = \begin{cases} 0 & \text{if } v \le k,\\ k - \frac{f(v,w)}{p^{-1}(w-k)} & \text{if } v > k, \end{cases} \tag{24}$$

and the "compensation term"

$$\mathrm{N}_k(v,w,Q) = \begin{cases} f(v,w)(t,0)\left[\frac{k}{Q(t)} - \frac{1}{p^{-1}([w(t,0)-k]^+)}\right]^+ & \text{if } Q(t) \neq 0,\\ k & \text{otherwise}. \end{cases}$$

Definition 3 We say that $(v,w) \in \mathbf{L}^{\infty}(\mathbb{R}_+;\mathbf{BV}(\mathbb{R};\mathscr{W})) \cap \mathbf{C}^{\mathbf{0}}(\mathbb{R}_+;\mathbf{L}^{\mathbf{1}}_{\mathbf{loc}}(\mathbb{R};\mathscr{W}))$ is a constrained entropy solution to (23) if the following conditions hold:

(i) (v,w) is a weak solution of Cauchy problem (23a), and (23c), i.e., $(v,w)(0,x) = (v_0,w_0)(x)$ for a.e. $x \in \mathbb{R}$ and for any test function $\phi \in \mathbf{C}^{\infty}_{\mathbf{c}}((0,\infty)\times\mathbb{R};\mathbb{R})$

$$\iint_{\mathbb{R}_+\times\mathbb{R}} \mathfrak{r}(v,w)\big[\phi_t + v\,\phi_x\big]\,(1,w)\,\mathrm{d}x\,\mathrm{d}t = (0,0).$$

(ii) (v,w) satisfies constraint (23b), namely, $f(v,w)(t,0^{\pm}) \le Q(t)$ for a.e. $t>0$ and for any test function $\phi \in \mathbf{C}^{\infty}_{\mathbf{c}}((0,\infty)\times\mathbb{R};\mathbb{R}_+)$ and constant $k>0$

$$\iint_{\mathbb{R}_+\times\mathbb{R}} \big[\mathrm{E}_k(v,w)\,\phi_t + \mathrm{F}_k(v,w)\,\phi_x\big]\mathrm{d}x\,\mathrm{d}t + \int_{\mathbb{R}_+} \mathrm{N}_k(v,w,Q)\,\phi(t,0)\,\mathrm{d}t \ge 0. \tag{25}$$

Conditions (25) originate from the classical definition of entropy solutions to hyperbolic systems of conservation laws, [34, 36]. The entropies $\mathtt{E}_k$ are not convex with respect to the variables (v, w) (they are convex only with respect to the conservative variable ρ); however, given any Riemann datum not involving the vacuum state, the entropy inequalities (25) select precisely the solutions prescribed by the Aw-Rascle and Zhang Riemann solver.

We recall the existence results for unconstrained Cauchy problem (23a), and (23c) obtained in [27] away from the vacuum and in [31, 37] for solutions attaining also the vacuum state.

Some remarks on $\mathtt{N}_k$ are in order. First, $\mathtt{N}_k$ compensates the possible additional entropy dissipation at $x = 0$ due to the constraint. Second, it makes sense to consider the traces $f(v, w)(t, 0^{\pm})$ and $w(t, 0^{\pm})$. This is obvious as we assume that the solution (v, w) is in $\mathbf{L}^{\infty}(\mathbb{R}_+; \mathbf{BV}(\mathbb{R}; \mathscr{W}))$; therefore we can introduce both the left measure theoretic trace $(v, w)(t, 0^-)$, implicitly defined by

$$\lim_{\varepsilon \downarrow 0} \frac{1}{\varepsilon} \int_{\mathbb{R}_+} \int_{-\varepsilon}^{0} \left\| v(t,x) - v(t,0^-) \right\| \phi(t,x)\, \mathrm{d}x\, \mathrm{d}t = 0 \qquad \text{for all } \phi \in \mathbf{C}_{\mathbf{c}}^{\infty}(\mathbb{R}^2; \mathbb{R}),$$

$$\lim_{\varepsilon \downarrow 0} \frac{1}{\varepsilon} \int_{\mathbb{R}_+} \int_{-\varepsilon}^{0} \left\| w(t,x) - w(t,0^-) \right\| \phi(t,x)\, \mathrm{d}x\, \mathrm{d}t = 0 \qquad \text{for all } \phi \in \mathbf{C}_{\mathbf{c}}^{\infty}(\mathbb{R}^2; \mathbb{R}),$$

and the right measure theoretic trace $(v, w)(t, 0^+)$, which is defined analogously. Moreover, if $w(t, 0^-)$ and $w(t, 0^+)$ differ then $x \mapsto (v, w)(t, x)$ has a stationary contact discontinuity at $x = 0$ and therefore $\mathtt{N}_k(v, w, Q) = 0$ because $f(v, w)(t, 0^{\pm}) = 0$.

Condition (25) does not ensure uniqueness of solutions involving a vacuum state. For this reason at vacuum, we adopt the selection criterion for **BV**-entropy solutions requiring that for any $t > 0$ and $x \in \mathbb{R}$

$$\begin{pmatrix} v(t,x^-) \\ w(t,x^-) \\ v(t,x^+) \\ w(t,x^+) \end{pmatrix} \in \left\{ \begin{pmatrix} v_\ell \\ w_\ell \\ v_r \\ w_r \end{pmatrix} \in \mathscr{W}^2 : \begin{array}{c} (v_\ell, w_\ell) \in \mathscr{W}_0 \\ (v_r, w_r) \in \mathscr{W}_0 \end{array} \right\} \Rightarrow \begin{pmatrix} v_\ell \\ w_\ell \end{pmatrix} = \begin{pmatrix} v_r \\ w_r \end{pmatrix} \Bigg\} . \quad (26)$$

Remark 1 The solutions we consider in this section, and in general all solutions associated to constant or piecewise constant in time constraints and **BV**-regular initial conditions, are in $\mathbf{L}^{\infty}(\mathbb{R}_+; \mathbf{BV}(\mathbb{R}; \mathscr{W}))$; see [6]. However since $\mathtt{N}_k$ can be written as the product of $f(v, w)$ by a function of w and Q, and w enjoys the renormalization property, [41], the weak traces at $x = 0$ of $\mathtt{N}_k = \mathtt{N}_k(v, w, Q)$ exist; see [1, 6] for details. This property gives hope to extend the existence results presented here to general time-variable constraints and then to nonlocal constraints, in the spirit of the LWR-based models discussed in Sect. 2.

We collect the basic properties of constrained entropy solutions in the following.

Proposition 2 *If (v, w) is a constrained entropy solution of (23), then:*

1. *Any discontinuity of $Y(v, w)$ satisfies the Rankine-Hugoniot jump conditions.*
2. *Any discontinuity of $Y(v, w)$ away from $x = 0$ satisfies the classical Lax entropy inequalities.*
3. *If $x \mapsto Y(v, w)(t_0, x)$, $t_0 > 0$, has a nonclassical shock discontinuity, then $f(v, w)(t_0, 0^{\pm}) = Q(t_0)$.*

Denote by **PC** the set of piecewise constant functions with a finite number of jumps. Let $(\widetilde{v}(Q), \widetilde{w}(Q))$ be the point of the curve $f(v, w) = Q$ with the lowest w coordinate, $J\colon\ (0, \infty) \times \mathbb{R}_+ \to \mathbb{R}_+$ be defined by

$$J(Q, w) = \begin{cases} \check{v}(Q, w) - \hat{v}(Q, w) & \text{if } w \in \left[\widetilde{w}(Q), \infty\right), \\ 0 & \text{if } w \in \left[0, \widetilde{w}(Q)\right), \end{cases}$$

and for any $w \geq \widetilde{w}(Q)$, let

$$\hat{v}(Q, w) = \min\left\{v \in (0, w) : \mathfrak{r}(v, w)\, v = Q\right\},$$
$$\check{v}(Q, w) = \max\left\{v \in (0, w) : \mathfrak{r}(v, w)\, v = Q\right\}.$$

Notice that $\widetilde{v}(Q)^2/Q = p'\left(Q/\widetilde{v}(Q)\right)$ and $\widetilde{w}(Q) = \widetilde{v}(Q) + p\left(Q/\widetilde{v}(Q)\right)$.

Theorem 4 *Let $(v_0, w_0) \in \mathbf{BV}(\mathbb{R}; \mathscr{W})$ satisfy (26) and $Q \in \mathbf{PC}\left(\mathbb{R}_+; \mathbb{R}_+\right)$ be such that $x \mapsto J\left(Q(0), w_0(x)\right)$ has bounded total variation in $\mathbb{R}_-$ and*

$$K_0 = \sum_{\substack{t>0 \text{ s.t.} \\ Q(t^-)\neq Q(t+)}} \sup_{y\in\mathbb{R}_-} \left|\mathrm{TV}\left(J\left(Q(t^-), w_0\right); (-\infty, y]\right) - \mathrm{TV}\left(J\left(Q(t^+), w_0\right); (-\infty, y]\right)\right|$$

is bounded. Then constrained Cauchy problem (23) admits a constrained entropy solution $(v, w) \in \mathbf{C^0}\left(\mathbb{R}_+; \mathbf{BV}\left(\mathbb{R}; \mathscr{W}\right)\right)$ and for all $t, s \in \mathbb{R}_+$

$$\mathrm{TV}\Big((v, w)(t)\Big) \leq C, \quad \|(v, w)(t) - (v, w)(s)\|_{\mathbf{L^1}} \leq L\ |t - s|\,, \quad \|(v, w)(t)\|_{\mathbf{L}^\infty} \leq V_0,$$

where

$$V_0 = \|(v_0, w_0)\|_{\mathbf{L}^\infty(\mathbb{R})}, \qquad L = C\ \max\left\{V_0,\ p^{-1}(V_0)\ p'\left(p^{-1}(V_0)\right)\right\}$$
$$C = \mathrm{TV}(v_0, w_0) + 3\mathrm{TV}\Big(J\Big(Q(0), w_0\Big); \mathbb{R}_-\Big) + 2V_0 + 3\,(K_1 + K_2)\,.$$

Above, K_1 and K_2 are constants that may depend on K_0.

The proof is based on the WFT algorithm restarted at every time Q has a jump. The main obstacle for generalizing the existence result to general time-dependent Q is the dependence of the Temple functional on Q via $J(Q, \cdot)$.

3.2 Example

In this section we apply model (23) to simulate the traffic on a road in the presence of a traffic light placed at $x = 0$. More specifically, let $w_2 > w_1 > 0$, and consider two types of vehicles, the "slow vehicles" characterized by the Lagrangian marker w_1 and the "fast vehicles" characterized by the Lagrangian marker w_2. Observe that the maximum speed of the fast vehicles is w_2 and that one of the slow vehicles is w_1. Moreover, the length of the fast vehicles, $1/p^{-1}(w_2)$, is lower than that one of the slow vehicles, $1/p^{-1}(w_1)$; see Fig. 6.

Place at $x = 0$ a traffic light that turns from red to green at time $t = 0$. Assume that at time $t = 0$ all the vehicles are at rest in $[x_1, 0)$; more precisely, assume that the slow vehicles are uniformly distributed in $[x_1, x_2)$ with density $p^{-1}(w_1)$ and the fast vehicles are uniformly distributed in $[x_2, 0)$ with density $p^{-1}(w_2)$. The resulting problem is (23) with initial datum

$$v_0(x) = \begin{cases} w_1 & \text{if } x \le x_1, \\ 0 & \text{if } x_1 \le x < 0, \\ w_2 & \text{if } x > 0, \end{cases} \qquad w_0(x) = \begin{cases} w_1 & \text{if } x \le x_2, \\ w_2 & \text{if } x > x_2, \end{cases}$$

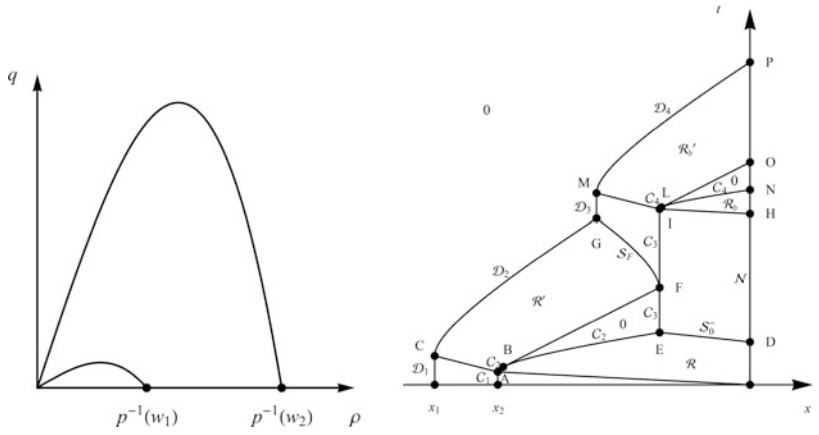

Fig. 6 Left: The fundamental diagrams $\rho \mapsto f(w_1 - p(\rho), w_1)$ and $\rho \mapsto f(w_2 - p(\rho), w_2)$ corresponding to the slow and fast vehicles, respectively. Right: The solution constructed in Sect. 3.2. Above "0" stands for the vacuum

and constraint

$$Q(t) = \left(\max_{\rho \in [0,\, p^{-1}(w_2)]} f(w_2 - p(\rho), w_2) \right) \chi_{(0,t_D)\cup(t_H,t_P)}(t).$$

The above expression for Q means that the traffic light is green for $t \in (0, t_D) \cup (t_H, t_P)$; otherwise it is red.

Below we furnish a detailed construction of the resulting solution; see Figs. 6 and 7. We first consider three Riemann problems at $(t, x) \in \{0\} \times \{x_1, x_2, 0\}$ and obtain that from $x = x_1$ starts a stationary discontinuity $\mathscr{D} = \mathscr{D}_1$ from the vacuum state (w_1, w_1) to $(0, w_1)$, from $x = x_2$ starts a stationary contact discontinuity $\mathscr{C} = \mathscr{C}_1$ from $(0, w_1)$ to $(0, w_2)$, and from $x = 0$ starts a rarefaction $\mathscr{R}$ centered in $(t, x) = (0, 0)$ and taking values

$$\mathscr{R}\colon \quad \rho_{\mathscr{R}}\left(x/t\right) = \Re\left(w_2 - x/t\right), \quad w_{\mathscr{R}}\left(x/t\right) = w_2, \quad \text{for } x/t \in \left[\lambda_1\left(0, w_2\right), w_2\right],$$

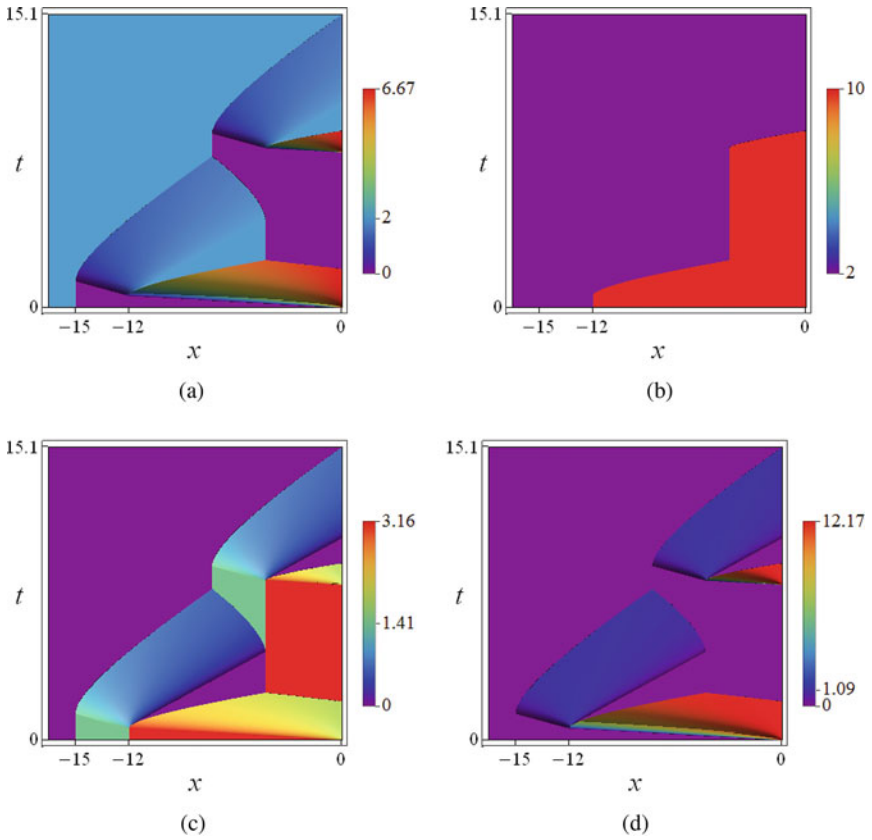

Fig. 7 The solution constructed in Sect. 3.2. (**a**) $(t, x) \mapsto v(t, x)$. (**b**) $(t, x) \mapsto w(t, x)$. (**c**) $(t, x) \mapsto \rho(t, x)$. (**d**) $(t, x) \mapsto f(t, x)$

where $\mathfrak{R}$ is the inverse function of $\rho \mapsto p(\rho) + \rho\, p'(\rho)$. Let then

$$\mathscr{D} = \mathscr{D}_1 : \qquad x_{\mathscr{D}_1}(t) = x_1,$$
$$\mathscr{C} = \mathscr{C}_1 : \qquad x_{\mathscr{C}_1}(t) = x_2.$$

We prolong then the solution by considering the Riemann problems at each interaction as follows:

- The contact discontinuity $\mathscr{C}$ starts to interact with the rarefaction $\mathscr{R}$ from $A = (t_A, x_A) = (x_2/\lambda_1(0, w_2), x_2)$; as a result, $\mathscr{C}$ accelerates according to the following ordinary differential equation

$$\mathscr{C} = \mathscr{C}_2 : \qquad \dot{x}_{\mathscr{C}_2}(t) = v_{\mathscr{R}}\left(x_{\mathscr{C}_2}(t)\big/t\right), \qquad x_{\mathscr{C}_2}(t_A) = x_A. \tag{27}$$

  The contact discontinuity $\mathscr{C}$ stops to interact with the rarefaction $\mathscr{R}$ at $B = (t_B, x_B)$ implicitly given by $x_B = x_{\mathscr{C}_2}(t_B)$ and $v_{\mathscr{R}}(x_B/t_B) = w_1$; then the vacuum state (w_1, w_1) appears in $\{(t, x) \colon x_B + (t - t_B)\, w_1 < x < x_{\mathscr{C}_2}(t)\}$. Observe that (27) still holds after time $t = t_B$ because the speed of propagation of any discontinuity from any vacuum state to $(v_*, w_*) \in \mathscr{W}_0^c$ is v_*. Notice that $\mathscr{C}$ is not a contact discontinuity after time $t = t_B$.
- Each point of $\mathscr{C}(t)$, $t_A \le t \le t_B$, is the center of a rarefaction appearing on its left. Denote by $\mathscr{R}'$ the juxtaposition of these rarefactions. In order to compute the values attained by $\mathscr{R}'$, it is sufficient to recall that the velocity v is conserved across the contact discontinuity $\mathscr{C}(t)$, $t_A \le t \le t_B$, and that the density ρ in $\mathscr{R}'$ is constant along

$$\mathscr{P} : \qquad x = x_{\mathscr{C}_2}(t_0) + \lambda_1\left(v_{\mathscr{R}}\left(x_{\mathscr{C}_2}(t_0)\big/t_0\right), w_1\right)(t - t_0). \tag{28}$$

  Hence, the value of $\rho_{\mathscr{R}'}$ at any point (t, x) of the rarefaction $\mathscr{R}'$ is equal to $\mathfrak{r}(v_{\mathscr{R}}, w_1)$ computed at the point $(t_0, x_{\mathscr{C}_2}(t_0))$, with $t_0 = \mathscr{P}(t, x)$, obtained by projecting (t, x) to a point of $\mathscr{C}$ along (28):

$$\mathscr{R}' : \quad \rho_{\mathscr{R}'}(t, x) = p^{-1}\left(w_1 - v_{\mathscr{R}}\left(x_{\mathscr{C}_2}\left(\mathscr{P}(t, x)\right)\big/\mathscr{P}(t, x)\right)\right), \quad w_{\mathscr{R}'}(t, x) = w_1.$$

  Observe that by definition $\mathscr{P}(t, x) \in [t_A, t_B]$ for all (t, x) in $\mathscr{R}'$.
- The rarefaction $\mathscr{R}'$ reaches the stationary discontinuity $\mathscr{D}$ in $C = (t_C, x_C) = (t_A + (x_1 - x_2)\big/\lambda_1(0, w_1), x_1)$. As a result of its interaction with $\mathscr{R}'$, the discontinuity $\mathscr{D}$ starts to accelerate

$$\mathscr{D} = \mathscr{D}_2 : \qquad \dot{x}_{\mathscr{D}_2}(t) = v_{\mathscr{R}'}\left(t, x_{\mathscr{D}_2}(t)\right), \qquad x_{\mathscr{D}_2}(t_C) = x_C.$$

- At time $t = t_D$, such that $t_D > t_B$ and $\mathscr{C}_2(t_D) < 0$, the traffic light turns to red. Hence, at $D = (t_D, 0)$, the solution has a shock $\mathscr{S}_0^-$ with negative speed, a stationary nonclassical shock $\mathscr{N}$ from $(0, w_2)$ to the vacuum state (w_2, w_2), and

a shock $\mathscr{S}_0^+$ with positive speed. Since $\mathscr{S}_0^-$ and $\mathscr{S}_0^+$ interact with the rarefaction $\mathscr{R}$, we have that

$$\mathscr{S}_0^-: \qquad \dot{x}_{\mathscr{S}_0^-}(t) = \frac{q_{\mathscr{R}}\left(x_{\mathscr{S}_0^-}(t)/t\right)}{\rho_{\mathscr{R}}\left(x_{\mathscr{S}_0^-}(t)/t\right) - p^{-1}(w_2)}, \qquad x_{\mathscr{S}_0^-}(t_D) = 0,$$

$$\mathscr{S}_0^+: \qquad \dot{x}_{\mathscr{S}_0^+}(t) = v_{\mathscr{R}}\left(x_{\mathscr{S}_0^+}(t)/t\right), \qquad x_{\mathscr{S}_0^+}(t_D) = 0.$$

- The discontinuity $\mathscr{C}$ and the shock $\mathscr{S}_0^-$ meet in E, which is implicitly given by $x_{\mathscr{C}_2}(t_E) = x_E = x_{\mathscr{S}_0^-}(t_E)$. Observe that

$$x_E = x_2 + \frac{t_D}{p^{-1}(w_2)} \max\left\{f\left(w_2 - p(\rho), w_2\right) : \rho \in [0, p^{-1}(w_2)]\right\}.$$

  As a result of this interaction, $\mathscr{S}_0^-$ disappears and $\mathscr{C}$ becomes stationary

$$\mathscr{C} = \mathscr{C}_3: \qquad x_{\mathscr{C}_3}(t) = x_E.$$

- The discontinuity $\mathscr{C}$ meets again the rarefaction $\mathscr{R}'$ in $F = (t_F, x_F) = (t_B + (x_E - x_B)/w_1, x_E)$. As a result of this interaction, from F starts a backward shock $\mathscr{S}_F$, while $\mathscr{C}$ becomes a stationary contact discontinuity. Since $\mathscr{S}_F$ interacts with $\mathscr{R}'$, we have that

$$\mathscr{S}_F: \quad \dot{x}_{\mathscr{S}_F}(t) = f_{\mathscr{R}'}\left(t, x_{\mathscr{S}_F}(t)\right) \Big/ \left(\rho_{\mathscr{R}'}\left(t, x_{\mathscr{S}_F}(t)\right) - p^{-1}(w_1)\right), \quad x_{\mathscr{S}_F}(t_F) = x_F.$$

- The discontinuity $\mathscr{D}$ and the shock $\mathscr{S}_F$ meet in G, which is implicitly given by $x_{\mathscr{D}_2}(t_G) = x_G = \mathscr{S}_F(t_G)$. Observe that $x_G = (x_1 - x_2) + x_E$. As a result of this interaction, $\mathscr{S}_F$ disappears and $\mathscr{D}$ becomes stationary

$$\mathscr{D} = \mathscr{D}_3: \qquad x_{\mathscr{D}_3}(t) = x_G.$$

- If at time $t = t_H$, with $t_H > t_G$, the traffic light turns to green. Then we have a rarefaction $\mathscr{R}_\flat$ centered in $H = (t_H, 0)$ and taking values

$$\mathscr{R}_\flat: \quad \begin{cases} \rho_{\mathscr{R}_\flat}(t, x) = \mathfrak{R}\left(w_2 - x/(t - t_H)\right), \\ w_{\mathscr{R}_\flat}(t, x) = w_2, \end{cases} \qquad \text{for } x/t - t_H \in [\lambda_1(0, w_2), w_2],$$

- The contact discontinuity $\mathscr{C}$ starts to interact with the rarefaction $\mathscr{R}_\flat$ in $I = (t_I, x_I) = (t_H + \alpha\, t_A, \alpha\, x_2)$, where $\alpha = x_E/x_2$. As a result, analogously to the interaction in A, $\mathscr{C}$ accelerates and a rarefaction $\mathscr{R}'_\flat$ appears on its left. Hence

$$\mathscr{C} = \mathscr{C}_4: \quad x_{\mathscr{C}_4}(t) = \alpha\, x_{\mathscr{C}_2}\left((t - t_H)/\alpha\right), \tag{29}$$

$$\mathscr{P}_\flat: \qquad \mathscr{P}_\flat(t,x) = \alpha\, \mathscr{P}\left((t-t_H)/\alpha, x/\alpha\right) + t_H,$$

$$\mathscr{R}'_\flat: \qquad \begin{cases} \rho_{\mathscr{R}'_\flat}(t,x) = p^{-1}\left(w_1 - v_{\mathscr{R}}\left(x_{\mathscr{C}_4}\left(\mathscr{P}_\flat(t,x)\right)/\left(\mathscr{P}_\flat(t,x) - t_H\right)\right)\right), \\ w_{\mathscr{R}'_\flat}(t,x) = w_1. \end{cases}$$

- The contact discontinuity $\mathscr{C}$ stops to interact with the rarefaction $\mathscr{R}_\flat$ from $L = (t_L, x_L) = (t_H + \alpha\, t_B, \alpha\, x_B)$ and the vacuum state (w_1, w_1) appears in $\{(t,x)\colon x_L + (t-t_L)\, w_1 < x < x_{\mathscr{C}_4}(t)\}$. Observe that (29) still holds after time $t = t_L$. Notice that $\mathscr{C}$ is not a contact discontinuity after time $t = t_L$.
- The rarefaction $\mathscr{R}'_\flat$ reaches the stationary discontinuity $\mathscr{D}$ in $M = (t_M, x_M) = (t_I + (x_G - x_E)/\lambda_1(0, w_1), x_G)$. As a result of its interaction with $\mathscr{R}'_\flat$, the discontinuity $\mathscr{D}$ starts to accelerate

$$\mathscr{D} = \mathscr{D}_4: \qquad \dot{x}_{\mathscr{D}_4}(t) = v_{\mathscr{R}'_\flat}\left(t, x_{\mathscr{D}_4}(t)\right), \qquad x_{\mathscr{D}_4}(t_M) = x_M. \tag{30}$$

- The discontinuity $\mathscr{D}$ reaches $x = 0$ in P implicitly given by $x_{\mathscr{D}_4}(t_P) = x_P = 0$.

At time $t = t_P$ no vehicles are present in $\mathbb{R}_-$, and the construction of the solution in the left half-plane is concluded. In Figs. 6 and 7, we represent the solution corresponding to

$$p(\rho) = \rho^2, \quad w_1 = 2, \quad w_2 = 10, \quad x_1 = -15, \quad x_2 = -12, \quad t_D = 2, \quad t_H = 8.$$

Notice that we have the following expressions for $\mathscr{D}$ and $\mathscr{C}$:

$$x_{\mathscr{D}}(t) = x_1\, \chi_{[0,t_C]}(t) + x_{\mathscr{D}_2}(t)\, \chi_{]t_C,t_G[}(t) + x_G\, \chi_{[t_G,t_M]}(t) + x_{\mathscr{D}_4}(t)\, \chi_{]t_M,+\infty[}(t),$$

$$x_{\mathscr{C}}(t) = x_2\, \chi_{[0,t_A]}(t) + x_{\mathscr{C}_2}(t)\, \chi_{]t_A,t_F[}(t) + x_E\, \chi_{[t_F,t_I]}(t) + x_{\mathscr{C}_4}(t)\, \chi_{]t_I,+\infty[}(t).$$

In order to compute time t_P, we can exploit the equation

$$\int_{x_{\mathscr{D}_4}(t)}^{0} \rho_{\mathscr{R}'_\flat}(t,y)\, \mathrm{d}y + \int_{t_O}^{t} f_{\mathscr{R}'_\flat}(s,0)\, \mathrm{d}s = p^{-1}(w_1)(x_2 - x_1), \quad t \in [t_O, t_P],$$

to obtain an alternative way to compute t_P given by solving the following equation:

$$t_P: \qquad \int_{t_O}^{t_P} f_{\mathscr{R}'_\flat}(t,0)\, \mathrm{d}t = p^{-1}(w_1)(x_2 - x_1).$$

The above equation allows to compute t_P by solving (29) for times $t \in [t_I, t_L]$ instead of (30) for times $t \in [t_M, t_P]$, that is computationally much more expensive.

4 Locally Constrained PT

In this section we study the Cauchy problem for PT (3), and (4) subject to a point constraint on the density flow (5). More precisely, with the same notations used in the previous sections, we describe the traffic in the *free-flow phase* Ω_{f} with constrained LWR (6) and the traffic in the *congested phase* Ω_{c} with constrained ARZ (23). The coupling is achieved via *phase transitions*, namely, discontinuities that separate two states belonging to different phases and that satisfy the Rankine-Hugoniot conditions.

We point out that in [11, 12, 20, 30], it is assumed that $\Omega_{\mathrm{f}} \cap \Omega_{\mathrm{c}} = \emptyset$, while in [13, 14], it is assumed that $\Omega_{\mathrm{f}} \cap \Omega_{\mathrm{c}} \neq \emptyset$. Moreover, in [13, 14], it is assumed that the flux function vanishes at a maximal density, namely, that the vehicles have (almost) the same length, while in [11, 12, 30], this requirement is not assumed. Here we assume that $\Omega_{\mathrm{f}} \cap \Omega_{\mathrm{c}} \neq \emptyset$ and, in order to ensure the well-posedness of the Cauchy problems, see [20, Remark 2], we also assume that Ω_{f} is characterized by a unique value of the velocity, $V \equiv V_{\max}$. At last, we consider a heterogeneous traffic with vehicles having different lengths. As a consequence

$$\Omega_{\mathrm{f}} = \Omega_{\mathrm{f}}^{-} \cup \Omega_{\mathrm{f}}^{+}, \quad \Omega_{\mathrm{c}} = \left\{ \left(\mathfrak{r}(v, w), v \right) \in \mathbb{R}_+ \times [0, V_{\max}] \colon w \in [W^-, W^+] \right\},$$

where

$$\Omega_{\mathrm{f}}^{-} = [0, \sigma_-) \times \{V_{\max}\}, \qquad \Omega_{\mathrm{f}}^{+} = [\sigma_-, \sigma_+] \times \{V_{\max}\},$$

with $\sigma_\pm = \mathfrak{r}\left(V_{\max}, W^\pm\right)$ and $0 < V_{\max} < W^- < W^+$ are such that

$$V_{\max} < p^{-1}\left(W^- - V_{\max}\right) p'\left(p^{-1}(W^- - V_{\max})\right).$$

Notice that $\Omega_{\mathrm{f}}^{+} = \Omega_{\mathrm{f}} \cap \Omega_{\mathrm{c}}$ is the *metastable phase* and is not empty.

This two-phase approach is motivated by experimental observations, according to which for low densities the flow of vehicles is approximable by a one-dimensional manifold as Ω_{f}, while at high densities, the flow covers a two-dimensional manifold as Ω_{c}; see [20, Figure 1.1] or [14, Figure 3.1].

We introduce the following functions:

$$\begin{aligned}
&\mathtt{w} \colon \Omega \to \left[0, W^+\right], && \mathtt{w}(\rho, v) = \begin{cases} p(\rho) + v & \text{if } (\rho, v) \in \Omega_{\mathrm{c}}, \\ W^- \rho / \sigma_- & \text{if } (\rho, v) \in \Omega_{\mathrm{f}}^{-}, \end{cases} \\
&\mathtt{W} \colon \Omega \to \left[W^-, W^+\right], && \mathtt{W}(\rho, v) = \max\{W^-, \mathtt{w}(\rho, v)\}, \\
&f \colon \Omega \to \mathbb{R}_+, && f(\rho, v) = \rho\, v.
\end{aligned}$$

We consider the Cauchy problem for PT (3), and (4)

$$\begin{array}{ll} \textbf{Free flow} & \textbf{Congested flow} \\ \begin{cases} u{=}(\rho, v) \in \Omega_{\mathrm{f}}, \\ \rho_t + f(\rho, v)_x = 0, \\ v{=}V_{\max}, \end{cases} & \begin{cases} u{=}(\rho, v) \in \Omega_{\mathrm{c}}, \\ \rho_t + f(\rho, v)_x{=}0, \\ [\rho\, \mathtt{w}(\rho, v)]_t + [f(\rho, v)\, \mathtt{w}(\rho, v)]_x = 0, \end{cases} \end{array} \qquad u(0, x){=}u_0(x), \tag{31}$$

subject to a point constraint on the density flow (5)

$$f(\rho, v)(t, 0^{\pm}) \le Q, \tag{32}$$

where $u_0 \in \mathbf{L}^{\infty}(\mathbb{R}; \Omega)$ is the initial datum and Q is the constant maximal density flow allowed at $x = 0$. Clearly, as in [11, 12, 24, 30], the traffic is described by LWR in the free-flow phase and ARZ in the congested phase.

Let $f_{\mathrm{c}}^{\pm} = \sigma_{\pm} V_{\max}$. Introduce $V_Q^{\pm} \in [0, V_{\max}]$ and $W_Q \in [0, W^+]$ defined by the following conditions:

if $Q = f_{\mathrm{c}}^+$:

$$V_Q^+ = V_{\max}, \qquad V_Q^- = V_{\max}, \qquad W_Q = W^+,$$

if $Q \in [f_{\mathrm{c}}^-, f_{\mathrm{c}}^+)$:

$$V_Q^+{=}V_{\max}, \qquad V_Q^- + p\left(\frac{Q}{V_Q^-}\right){=}W^+, \qquad W_Q{=}p\left(\frac{Q}{V_{\max}}\right){+}V_{\max},$$

if $Q \in (0, f_{\mathrm{c}}^-)$:

$$V_Q^+ + p\left(\frac{Q}{V_Q^+}\right) = W^-, \quad V_Q^- + p\left(\frac{Q}{V_Q^-}\right) = W^+, \quad W_Q = \frac{Q}{f_{\mathrm{c}}^-},$$

if $Q = 0$:

$$V_Q^+ = 0, \qquad V_Q^- = 0, \qquad W_Q = 0.$$

For any $Q \in (0, f_{\mathrm{c}}^+)$, let $\Xi_Q : [V_Q^-, V_Q^+] \to [W^-, W^+]$ be given by $\Xi_Q(v) = v + p(Q/v)$. Notice that Ξ_Q is strictly decreasing and strictly convex.

4.1 Existence Result

Before stating the definition of entropy solution to (31), we introduce the family of entropy-entropy flux pairs

$$\mathtt{E}_k(\rho, v){=}\begin{cases} 0 & \text{if } v{\ge}k, \\ \dfrac{\rho}{p^{-1}\left(\mathtt{W}(\rho,v){-}k\right)} - 1 & \text{if } v{<}k, \end{cases} \quad \mathtt{F}_k(\rho, v){=}\begin{cases} 0 & \text{if } v{\ge}k, \\ \dfrac{f(\rho,v)}{p^{-1}\left(\mathtt{W}(\rho,v){-}k\right)} - k & \text{if } v{<}k. \end{cases}$$

Definition 4 We say that $(\rho, v) \in \mathbf{L}^\infty(\mathbb{R}_+; \mathbf{BV}(\mathbb{R}; \Omega)) \cap \mathbf{C}^0\left(\mathbb{R}_+; \mathbf{L}^1_{\mathbf{loc}}(\mathbb{R}; \Omega)\right)$ is a constrained entropy solution to (31), and (32) if the following conditions holds:

(i) (ρ, v) is a weak solution to Cauchy problem (31), i.e., $(\rho, v)(0, x) = (\rho_0, v_0)(x)$ for a.e. $x \in \mathbb{R}$, and for any test function $\phi \in \mathbf{C}^\infty_{\mathbf{c}}((0, \infty) \times \mathbb{R}; \mathbb{R})$, we have

$$\iint_{\mathbb{R}_+ \times \mathbb{R}} \left(\rho\, \phi_t + f(\rho, v)\, \phi_x\right) \mathrm{d}x\, \mathrm{d}t = 0 \tag{33}$$

and if $\phi(\cdot, 0) \equiv 0$, then

$$\iint_{\mathbb{R}_+ \times \mathbb{R}} \left(\rho\, \phi_t + f(\rho, v)\, \phi_x\right) \mathtt{W}(\rho, v)\, \mathrm{d}x\, \mathrm{d}t = 0. \tag{34}$$

(ii) (ρ, v) satisfies constraint (32), namely, $f(\rho, v)(t, 0_\pm) \le Q$ for a.e. $t > 0$ and for any test function $\phi \in \mathbf{C}^\infty_{\mathbf{c}}((0, \infty) \times \mathbb{R}; \mathbb{R}_+)$ such that $\phi(\cdot, 0) \equiv 0$ and constant $k \in [0, V_{\max}]$

$$\iint_{\mathbb{R}_+ \times \mathbb{R}} \left(\mathtt{E}_k(\rho, v)\, \phi_t + \mathtt{Q}_k(\rho, v)\, \phi_x\right) \mathrm{d}x\, \mathrm{d}t \ge 0. \tag{35}$$

In the following proposition, we state which discontinuities are admissible for constrained entropy solutions.

Proposition 3 *If (ρ, v) is a constrained entropy solution of (31), and (32), then:*

- *Any discontinuity $\delta(t)$ of $x \mapsto (\rho, v)(t, x)$ satisfies the first Rankine-Hugoniot jump condition*

$$\Big[\rho\big(t, \delta(t)_+\big) - \rho\big(t, \delta(t)_-\big)\Big]\, \dot\delta(t) = f(\rho, v)\big(t, \delta(t)_+\big) - f(\rho, v)\big(t, \delta(t)_-\big), \tag{36}$$

and if $\delta(t) \neq 0$, then it satisfies also the second Rankine-Hugoniot jump condition

$$\begin{aligned}&\Big[\rho\big(t, \delta(t)_+\big)\, \mathtt{W}(\rho, v)\big(t, \delta(t)_+\big) - \rho\big(t, \delta(t)_-\big)\, \mathtt{W}(\rho, v)\big(t, \delta(t)_-\big)\Big]\, \dot\delta(t)\\ &= f(\rho, v)\big(t, \delta(t)_+\big)\, \mathtt{W}(\rho, v)\big(t, \delta(t)_+\big) - f(\rho, v)\big(t, \delta(t)_-\big)\, \mathtt{W}(\rho, v)\big(t, \delta(t)_-\big).\end{aligned} \tag{37}$$

- *Any discontinuity of (ρ, v) away from the constraint satisfies the Lax entropy inequalities.*
- *Nonclassical discontinuities of (ρ, v) may occur only at the constraint location $x = 0$, and in this case, the density flux at $x = 0$ does not exceed the maximal flux Q allowed by the constraint.*

Remark 2 In (34) and (35), we consider test functions ϕ such that $\phi(\cdot, 0) \equiv 0$. Indeed a constrained entropy solution (ρ, v) to constrained Cauchy problem (31), and (32) does not satisfy in general second Rankine-Hugoniot condition (37) along $x = 0$

$$f(\rho, v)(t, 0_-)\, \mathtt{W}(\rho, v)(t, 0_-) = f(\rho, v)(t, 0_+)\, \mathtt{W}(\rho, v)(t, 0_+) \qquad \text{for a.e. } t > 0.$$

Therefore, even if (ρ, v) takes values in Ω_c, it may not be a weak solution to ARZ (23).

This is in the same spirit of the solutions considered in [12, 24, 28] for traffic through locations with reduced capacity. This choice for the test functions in (34) and (35) does not allow us to better characterize the (density) flux at $x = 0$ associated to nonclassical shocks. In particular, different from what is proved in Sect. 2 for constrained LWR and Sect. 3 for constrained ARZ, we cannot ensure that the flux of the nonclassical shocks of (ρ, v) is equal to Q.

Let the maps $[0, W^+] \ni w \mapsto \hat{u}(w) = (\hat{\rho}(w), \hat{v}(w)) \in \Omega_c$ and $[0, V_{\max}] \ni v \mapsto \check{u}(v) = (\check{\rho}(v), \check{v}(v)) \in \Omega$ be defined in the (v, w) coordinates by

$$\hat{v}(w) = \begin{cases} \Xi_Q^{-1}(w) & \text{if } w > \max\{W^-, W_Q\}, \\ V_Q^+ & \text{if } W_Q < w \le W^-, \\ V & \text{if } w \le W_Q, \end{cases} \qquad \check{v}(v) = \begin{cases} V & \text{if } v > V_Q^+, \\ v & \text{if } v \in [V_Q^-, V_Q^+], \\ V_Q^- & \text{if } v < V_Q^-, \end{cases}$$

$$\hat{w}(w) = \begin{cases} w & \text{if } w > \max\{W^-, W_Q\}, \\ W^- & \text{if } W_Q < w \le W^-, \\ W_Q & \text{if } w \le W_Q, \end{cases} \qquad \check{w}(v) = \begin{cases} W_Q & \text{if } v > V_Q^+, \\ \Xi_Q(v) & \text{if } v \in [V_Q^-, V_Q^+], \\ W^+ & \text{if } v < V_Q^-. \end{cases}$$

Notice that

$$f\big(\hat{u}(w)\big) = f\big(\check{u}(v)\big) = Q.$$

Denote by TV_+ and TV_- are the positive and negative total variations, respectively. For any $u = (\rho, v) \colon \mathbb{R} \to \Omega$, let

$$\hat{\Upsilon}(u) = \mathrm{TV}_+\Big(\hat{v}\big(\mathtt{w}(u)\big); (-\infty, 0)\Big) + \mathrm{TV}_-\Big(\hat{w}\big(\mathtt{w}(u)\big); (-\infty, 0)\Big),$$

$$\check{\Upsilon}(u) = \mathrm{TV}_+\Big(\check{v}(v); (0, \infty)\Big) + \mathrm{TV}_-\Big(\check{w}(v); (0, \infty)\Big).$$

We are now in the position to state the main result of the paper.

Theorem 5 *Let* $(\rho_0, v_0) \in \mathbf{L^1} \cap \mathbf{BV}(\mathbb{R}; \Omega)$ *and* $Q \in [0, f_c^+]$ *satisfy one of the following conditions:*

(i) $Q \in [f_c^-, f_c^+]$;
(ii) $Q \in [0, f_c^-)$ *and* $\hat{\Upsilon}(\rho_0, v_0) + \check{\Upsilon}(\rho_0, v_0)$ *is bounded.*

Then constrained Cauchy problem (31)*, and* (32) *admits a constrained entropy solution* $(\rho, v) \in \mathbf{L}^\infty(\mathbb{R}_+; \mathbf{BV}(\mathbb{R}; \Omega)) \cap \mathbf{C^0}\left(\mathbb{R}_+; \mathbf{L^1_{loc}}(\mathbb{R}; \Omega)\right)$ *and for all* $t, s \in \mathbb{R}_+$

$$\mathrm{TV}\big(u(t)\big) \le C, \quad \|u(t) - u(s)\|_{\mathbf{L^1}} \le L\,|t - s|, \quad \|u(t)\|_{\mathbf{L}^\infty} \le p^{-1}(W^+) + V_{\max},$$

where C *and* L *are constants that depend on* (ρ_0, v_0) *and* Q.

The proof is based on the WFT algorithm; see [10] for the details. Let us just underline that if $Q \in [f_c^-, f_c^+]$, then $w \mapsto \hat{u}(w)$ and $v \mapsto \check{u}(v)$ are Lipschitz continuous, and therefore $\hat{\Upsilon}(\rho_0, v_0) + \hat{\Upsilon}(\rho_0, v_0)$ is bounded if (ρ_0, v_0) has bounded total variation. On the other hand, if $Q < f_c^-$, then $w \mapsto \hat{u}(w)$ and $v \mapsto \check{u}(v)$ are only left-continuous. This motivates the differences between the hypotheses (i) and (ii) of Theorem 5.

4.2 Example

In this section we apply model (31), and (32) to simulate the traffic on a road in the presence of an obstacle, such as a construction site, with capacity Q and placed at $x = 0$; see Fig. 8. More specifically, let $w_2 \in (W^-, W^+]$ be the Lagrangian marker corresponding to vehicles that are initially at rest in $[x_2, 0)$. We place in $[x_1, x_2)$ vehicles with density $\rho_1 \in (0, \sigma_-)$; these vehicles clearly move with speed $V_{\max}$. The resulting initial condition is

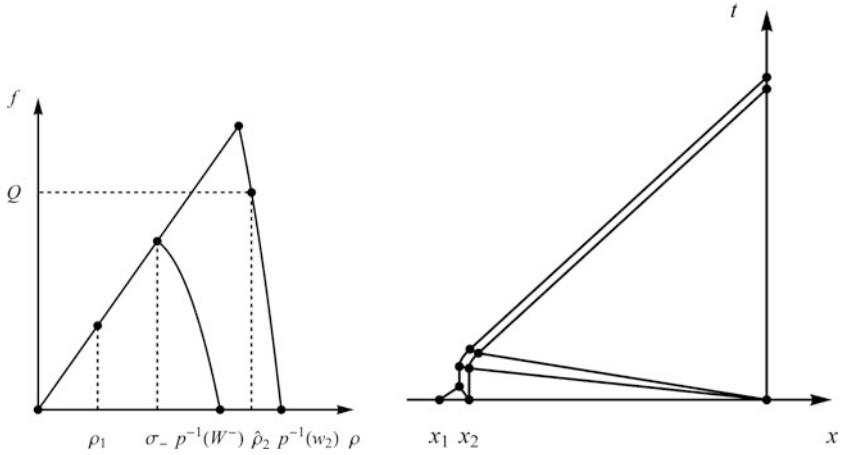

Fig. 8 Left: The fundamental diagrams $\rho \mapsto f(W^- - p(\rho), w_1)$ and $\rho \mapsto f(w_2 - p(\rho), w_2)$. Right: The solution constructed in Sect. 4.2

$$u(0,x) = \begin{cases} u_0 & \text{if } x \in \mathbb{R} \setminus [x_1, 0), \\ u_1 & \text{if } x \in [x_1, x_2), \\ u_2 & \text{if } x \in [x_2, 0) \end{cases}$$

where $u_0 = (0, V_{\max})$, $u_1 = (\rho_1, V_{\max})$ and $u_2 = (p^{-1}(w_2), 0)$. For times sufficiently small, the solution is the juxtaposition of the solutions to three Riemann problems at $(t,x) \in \{0\} \times \{x_1, x_2, 0\}$ that are

$$\mathsf{R}\left[u_0, u_1\right]\left(\frac{x - x_1}{t}\right), \qquad \mathsf{R}\left[u_1, u_2\right]\left(\frac{x - x_2}{t}\right), \qquad \mathsf{R}_Q\left[u_2, u_0\right]\left(\frac{x}{t}\right).$$

More precisely, from $x = x_1$ starts a contact discontinuity from the vacuum state u_0 to u_1, from $x = x_2$ starts a phase transition from u_1 to $(p^{-1}(W^-), 0)$ and a

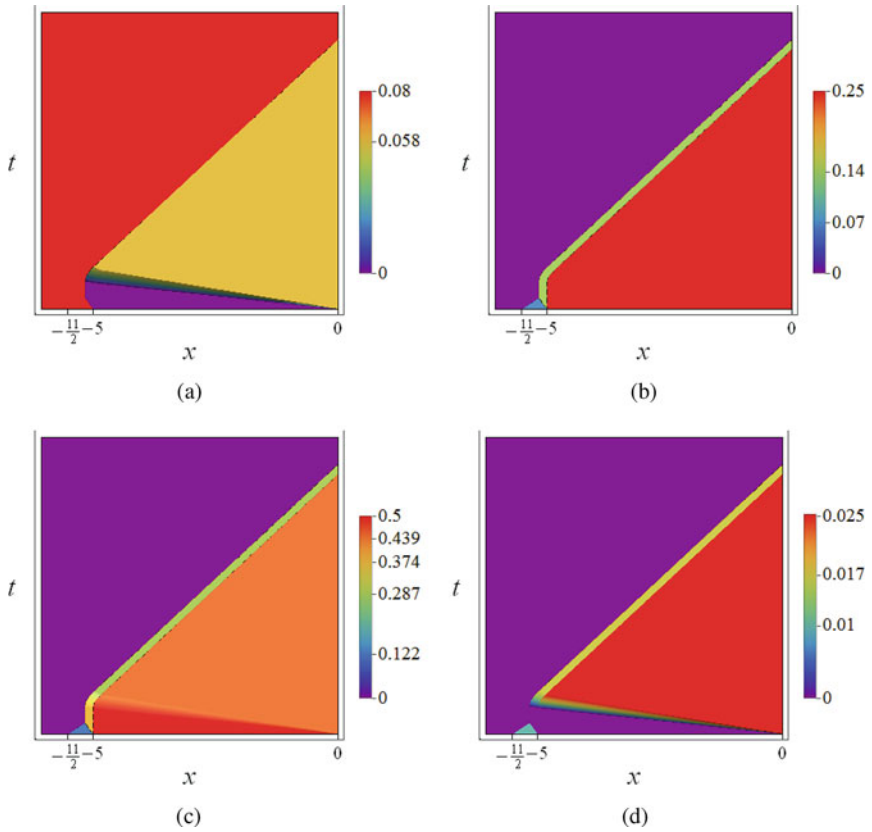

Fig. 9 The solution constructed in Sect. 4.2. (**a**) $(t,x) \mapsto v(t,x)$. (**b**) $(t,x) \mapsto w(t,x)$. (**c**) $(t,x) \mapsto \rho(t,x)$. (**d**) $(t,x) \mapsto f(t,x)$

stationary contact discontinuity from $(p^{-1}(W^-), 0)$ to u_2, and from $x = 0$ starts a rarefaction ranging values from u_2 to $\hat{u}(w_2, Q)$, a (stationary) nonclassical shock from $\hat{u}(w_2, Q)$ to $\check{u}(V_{\max}, Q)$, and a contact discontinuity from $\check{u}(V_{\max}, Q)$ to u_0. The remaining construction of the solution is then similar to that described in Sect. 3.2 for the constrained ARZ. In Fig. 9 we represent the solution corresponding to

$$x_1 = -\frac{11}{2}, \qquad x_2 = -5, \qquad p(\rho) = \rho^2, \qquad V_{\max} = \frac{2}{25},$$
$$W^- = \frac{7}{50}, \qquad w_2 = \frac{1}{4}, \qquad \rho_1 = \frac{\sqrt{6}}{20}, \qquad Q = \frac{7\left(31\sqrt{17} - 15\right)}{31250}.$$

Acknowledgements MDR acknowledges support from Università degli Studi di Ferrara Project 2017 "FIR: Modelli macroscopici per il traffico veicolare o pedonale".

References

1. B. Andreianov, C. Donadello, U. Razafison, J. Y. Rolland, and M. D. Rosini. Solutions of the Aw-Rascle-Zhang system with point constraints. *Networks and Heterogeneous Media*, 11(1):29–47, 2016.
2. B. Andreianov, C. Donadello, U. Razafison, and M. D. Rosini. Riemann problems with non-local point constraints and capacity drop. *Mathematical Biosciences and Engineering*, 12(2):259–278, 2015.
3. B. Andreianov, C. Donadello, U. Razafison, and M. D. Rosini. Qualitative behaviour and numerical approximation of solutions to conservation laws with non-local point constraints on the flux and modeling of crowd dynamics at the bottlenecks. *ESAIM. Mathematical Modelling and Numerical Analysis*, 50(5):1269–1287, 2016.
4. B. Andreianov, C. Donadello, U. Razafison, and M. D. Rosini. Analysis and approximation of one-dimensional scalar conservation laws with general point constraints on the flux. *Journal de Mathématiques Pures et Appliquées*, 2018.
5. B. Andreianov, C. Donadello, and M. D. Rosini. Crowd dynamics and conservation laws with nonlocal constraints and capacity drop. *Mathematical Models and Methods in Applied Sciences*, 24(13):2685–2722, 2014.
6. B. Andreianov, C. Donadello, and M. D. Rosini. A second-order model for vehicular traffics with local point constraints on the flow. *Mathematical Models and Methods in Applied Sciences*, 26(04):751–802, 2016.
7. B. Andreianov, P. Goatin, and N. Seguin. Finite volume schemes for locally constrained conservation laws. *Numerische Mathematik*, 115(4):609–645, 2010.
8. A. Aw and M. Rascle. Resurrection of "Second Order" Models of Traffic Flow. *SIAM Journal on Applied Mathematics*, 60(3):pp. 916–938, 2000.
9. N. Bellomo and C. Dogbe. On the modeling of traffic and crowds: a survey of models, speculations, and perspectives. *SIAM Review*, 53(3):409–463, 2011.
10. M. Benyahia, C. Donadello, N. Dymski, andM. D. Rosini. An existence result for a constrained two-phase transition model with metastable phase for vehicular traffic, 2018. To appear on Nonlinear Differential Equations and Application. Doi:10.1007/s00030-018-0539-1
11. M. Benyahia and M. D. Rosini. Entropy solutions for a traffic model with phase transitions. *Nonlinear Analysis: Theory, Methods & Applications*, 141:167–190, 2016.

12. M. Benyahia and M. D. Rosini. A macroscopic traffic model with phase transitions and local point constraints on the flow. *Networks and Heterogeneous Media*, 12(2):297–317, 2017.
13. S. Blandin, P. Goatin, B. Piccoli, A. Bayen, and D. Work. A general phase transition model for traffic flow on networks. *Procedia - Social and Behavioral Sciences*, 54(Supplement C):302–311, 2012. Proceedings of EWGT2012 - 15th Meeting of the EURO Working Group on Transportation, September 2012, Paris.
14. S. Blandin, D. Work, P. Goatin, B. Piccoli, and A. Bayen. A general phase transition model for vehicular traffic. *SIAM Journal on Applied Mathematics*, 71(1):107–127, 2011.
15. A. Bressan. *Hyperbolic systems of conservation laws*, volume 20 of *Oxford Lecture Series in Mathematics and its Applications*. Oxford University Press, Oxford, 2000. The one-dimensional Cauchy problem.
16. C. Cancès and N. Seguin. Error Estimate for Godunov Approximation of Locally Constrained Conservation Laws. *SIAM Journal on Numerical Analysis*, 50(6):3036–3060, 2012.
17. E. M. Cepolina. Phased evacuation: An optimisation model which takes into account the capacity drop phenomenon in pedestrian flows. *Fire Safety Journal*, 44(4):532–544, 2009.
18. C. Chalons. Numerical approximation of a macroscopic model of pedestrian flows. *SIAM Journal on Scientific Computing*, 29(2):539–555, 2007.
19. C. Chalons, P. Goatin, and N. Seguin. General constrained conservation laws. Application to pedestrian flow modeling. *Networks and Heterogeneous Media*, 8(2):433–463, 2013.
20. R. M. Colombo. Hyperbolic phase transitions in traffic flow. *SIAM Journal on Applied Mathematics*, 63(2):708–721 (electronic), 2002.
21. R. M. Colombo and P. Goatin. A well posed conservation law with a variable unilateral constraint. *Journal of Differential Equations*, 234(2):654–675, 2007.
22. R. M. Colombo, P. Goatin, and M. D. Rosini. On the modelling and management of traffic. *ESAIM: Mathematical Modelling and Numerical Analysis*, 45(05):853–872, 2011.
23. R. M. Colombo and M. D. Rosini. Pedestrian flows and non-classical shocks. *Mathematical Methods in the Applied Sciences*, 28(13):1553–1567, 2005.
24. E. Dal Santo, M. D. Rosini, N. Dymski, and M. Benyahia. General phase transition models for vehicular traffic with point constraints on the flow. *Mathematical Methods in the Applied Sciences*, 40(18):6623–6641, 2017.
25. N. S. Dymski, P. Goatin, and M. D. Rosini. Existence of BV solutions for a non-conservative constrained Aw-Rascle-Zhang model for vehicular traffic. *Journal of Mathematical Analysis and Applications*, 467(2018): 45–66. Doi:10.1016/jjmdd.2018.07.025
26. S. Fan and B. Seibold. Data-fitted first-order traffic models and their second-order generalizations: Comparison by trajectory and sensor data. *Transportation Research Record*, 2391:32–43, 2013.
27. R. E. Ferreira and C. I. Kondo. Glimm method and wave-front tracking for the Aw-Rascle traffic flow model. *Far East Journal of Mathematical Sciences*, 43(2):203–223, 2010.
28. M. Garavello and P. Goatin. The Aw-Rascle traffic model with locally constrained flow. *Journal of Mathematical Analysis and Applications*, 378(2):634–648, 2011.
29. M. Garavello and B. Piccoli. Traffic flow on networks, volume 1 of AIMS Series on Applied Mathematics. *American Institute of Mathematical Sciences (AIMS), Springfield, MO*, 2006.
30. P. Goatin. The Aw-Rascle vehicular traffic flow model with phase transitions. *Mathematical and computer modelling*, 44(3):287–303, 2006.
31. M. Godvik and H. Hanche-Olsen. Existence of solutions for the Aw–Rascle traffic flow model with vacuum. *Journal of Hyperbolic Differential Equations*, 05(01):45–63, 2008.
32. H. Holden and N. H. Risebro. *Front tracking for hyperbolic conservation laws*, volume 152. Springer, 2013.
33. S. N. Kruzhkov. First order quasilinear equations with several independent variables. *Matematicheskii Sbornik*, 81 (123):228–255, 1970.
34. P. D. Lax. Hyperbolic Systems of Conservation Laws II. In P. Sarnak and A. Majda, editors, *Selected Papers Volume I*, pages 233–262. Springer New York, 2005.

35. M. J. Lighthill and G. B. Whitham. On kinematic waves. II. A theory of traffic flow on long crowded roads. *Proceedings of the Royal Society. London. Series A. Mathematical, Physical and Engineering Sciences*, 229:317–345, 1955.
36. T. P. Liu. The Riemann problem for general systems of conservation laws. *Journal of Differential Equations*, 18:218–234, 1975.
37. Y.-G. Lu. Existence of global bounded weak solutions to nonsymmetric systems of Keyfitz-Kranzer type. *Journal of Functional Analysis*, 261(10):2797–2815, 2011.
38. R. Mohan and G. Ramadurai. State-of-the art of macroscopic traffic flow modelling. *International Journal of Advances in Engineering Sciences and Applied Mathematics*, 5(2–3):158–176, 2013.
39. E. Y. Panov. On sequences of measure-valued solutions of a first-order quasilinear equation. *Matematicheskii Sbornik*, 185(2):87–106, 1994.
40. E. Y. Panov. Existence of strong traces for quasi-solutions of multidimensional conservation laws. *Journal of Hyperbolic Differential Equations*, 4(4):729–770, 2007.
41. E. Y. Panov. Generalized solutions of the Cauchy problem for a transport equation with discontinuous coefficients. In *Instability in models connected with fluid flows. II*, volume 7 of *International Mathematical Series (New York)*, pages 23–84. Springer, New York, 2008.
42. B. Piccoli and A. Tosin. Vehicular traffic: A review of continuum mathematical models. In R. A. Meyers, editor, *Mathematics of Complexity and Dynamical Systems*, pages 1748–1770. Springer New York, 2011.
43. P. I. Richards. Shock waves on the highway. *Operations Research*, 4(1):pp. 42–51, 1956.
44. M. D. Rosini. *Macroscopic models for vehicular flows and crowd dynamics: theory and applications*. Understanding Complex Systems. Springer, Heidelberg, 2013.
45. V. V. Rusanov. The calculation of the interaction of non-stationary shock waves with barriers. *Akademija Nauk SSSR. Zhurnal Vychislitel′noi Matematiki i Matematicheskoi Fiziki*, 1:267–279, 1961.
46. F. van Wageningen-Kessels, H. van Lint, K. Vuik, and S. Hoogendoorn. Genealogy of traffic flow models. *EURO Journal on Transportation and Logistics*, pages 1–29, 2014.
47. Walk21-VI, editor. *Understanding capacity drop for designing pedestrian environments*, 2005.
48. H. M. Zhang. A non-equilibrium traffic model devoid of gas-like behavior. *Transportation Research Part B: Methodological*, 36(3):275 – 290, 2002.

Measure-Theoretic Models for Crowd Dynamics

Benedetto Piccoli and Francesco Rossi

Abstract This chapter revises some modeling, analysis, and simulation contributions for crowd dynamics using time-evolving measures. Two key features are strictly related to the use of measures: on one side, this setting permits to generalize both microscopic and macroscopic crowd models. On the other side, it allows an easy description of multi-scale crowd models, e.g., with leaders and followers. The main analytical tool for studying measure evolution is to endow the space of measures with the Wasserstein distance.

This chapter also describes our recent contributions about crowd modeling with time-varying total mass. This requires to use a more flexible metric tool in the space of measures, that we called generalized Wasserstein distance.

1 Introduction

The dynamics of pedestrian crowds can exhibit highly complex phenomena, which stem from the complexity of the cognitive processes behind human actions but also from *self-organization*, emerging from the combination of simple interaction rules. The ubiquity of self-organization of several interacting agents system has been proved in many different fields (see [9, 19, 24, 29, 30, 46]). To model mathematically such complex behaviors, researchers resorted to many different approaches, which encompass different scales. This chapter focuses on a measure-theoretic approach, which allows to combine different scales, taking advantage of different modeling capabilities.

B. Piccoli
Department of Mathematical Sciences, Rutgers University – Camden, Camden, NJ, USA
e-mail: piccoli@camden.rutgers.edu

F. Rossi (✉)
Department of Mathematics "Tullio Levi–Civita", University of Padova, Padua, Italy
e-mail: francesco.rossi@math.unipd.it

L. Gibelli, N. Bellomo (eds.), *Crowd Dynamics, Volume 1*, Modeling and Simulation in Science, Engineering and Technology,
https://doi.org/10.1007/978-3-030-05129-7_6

One of the most famous models at microscopic level is the celebrated social force model, proposed by Helbing and Molnár [27]. The main idea is that the reaction of pedestrians to the environment can be modeled as the effect of forces. The latter are not true physical forces but rather a modeling abstraction to represent the reactions of human as social being and thus are referred to as *social forces*. Such model is mainly based on a desired velocity, depending on the single pedestrian characteristics and goals, and on terms representing interactions among pedestrians and with the environment (such as walls and barriers). Interestingly enough, such model shares many similarities with models proposed, independently, by biologists for animal groups. Moreover, the social force model is similar to the well-known Cucker-Smale alignment model, which has been studied extensively by the applied mathematics community and was first defined to model the dynamics of languages.

As for dilute gases theory, one may pass to the limit in the number of agents (here instead of particles) and achieve mean-field limit equations, usually of Vlasov-Poisson type [12, 23]. Moreover, such equations allow, for nonlocal velocity fields, a well-developed theory for measure solutions and convergence analysis using the Wasserstein distance. The latter, widely used in optimal transport [45], metrizes the weak convergence on compact sets. These facts naturally call to use measures to represent the dynamics of crowds. Moreover, a measure can naturally represent different scales, with Dirac masses corresponding to microscopic components and absolutely continuous measures to macroscopic components.

One can define general nonlinear nonlocal transport equations, which include both the microscopic models as empirical measure solutions and the macroscopic mean-field limits as absolutely continuous solutions. The theory for such equations is strongly based on Wasserstein distances. In particular, Lipschitz conditions w.r.t. the Wasserstein distance for measures and uniform norm for vector fields allow to prove existence and uniqueness of solutions. The same result is not true if one uses the total variation norm, which corresponds to the L^1 distance for functions. The Wasserstein distance also has modeling advantages, as explained in Sect. 2.5.

After revising the theory developed in recent works, we propose a new modeling framework for crowds. The latter is based on the idea of using the mass to represent the social influence of a pedestrian. In other words, a bigger mass would represent a pedestrian with higher effects on the others. We propose a dynamic model where the masses may vary in time. The variation will depend on the mass of the pedestrian under consideration, but also on the interaction with the other pedestrians. We first detail the microscopic model, providing also analytical properties. Natural modeling choices lead to lack of conservation of the mass; thus we resort to the generalized Wasserstein distance, which is defined for measures with different masses. It is possible to define the mean-field limit of these models with time-varying mass. The obtained equations exhibit transport as well as source terms. Using the generalized Wasserstein distance, it is then possible to develop a complete theory for such equations.

To complete the presentation, we include simulation results which show the difference between mass-preserving and mass-varying models for an evacuation problem.

2 Microscopic and Multi-scale Models

The main idea behind the use of measure-theoretic models is the possibility of representing different scales in a unique framework. For this purpose, we will first recall some microscopic models, which provide the basis of ingredients for single pedestrian motion. There is a wealth of mesoscopic and macroscopic models as well: they can be either obtained as mean-field limits of microscopic models or they are based on general principles, such as conservation of mass and balance of momentum. We will not include a review of mesoscopic and macroscopic models and refer the reader to [3, 5–7, 17] for details. Then we introduce the measure-theoretic approach which allows the inclusion of different scales in a unique framework.

2.1 Microscopic: The Social Force Models

The most used microscopic model for pedestrian motion and crowd dynamics is the celebrated social force model first introduced by Helbing and Molnár (see, for instance, [27]). The popularity of the model is mostly due to the fact that it is relatively simple yet capable of capturing various self-organization phenomena observed in crowd dynamics. The work of Helbing and Molnár was inspired by the previous work of Lewin, which considered forces to represent the influence of the environment on social behavior [31]. The main concept behind such approach is the idea that variations in velocity of pedestrians (physically accelerations and decelerations) are caused as reactions to the perceived environment, including the presence of other pedestrians, and can be mimicked by forces. The latter are not real forces but rather the effect of "social" interactions with the environment; this explains the name of the model.

Due to its popularity, many authors contributed to variations of the original model: listing all the proposed model would require too much space; thus we will rather point out the main variations considered. Notice that many effects can be neglected if pedestrians are assumed to be dimensionless points in the space, but more realistically each pedestrian should be modeled according to the space occupied.

Let us start indicating by x_i the position of the i-the pedestrian in a walkable area $\Omega \subset \mathbb{R}^2$. One may consider also the case of $\Omega \subset \mathbb{R}^3$, but this is much less common. Each pedestrian possesses a desired velocity $\bar{v}_i$, which is usually the vector pointing toward the desired destination and having modulus equal to a *comfort* speed. Each pedestrian tends to reach the desired velocity at a given relaxation time τ; thus, a first force is described by:

$$F_i(v_i) = \frac{\bar{v}_i - v_i}{\tau}. \tag{1}$$

Notice that F_i may also depend on the position x_i and time t.

Pedestrians do interact among each other. These interactions may include repulsion effects, when the distance among pedestrians is lower than a desired personal space, and attraction. Both effects can be taken in to account by some attraction-repulsion potential, giving rise to the forces:

$$F_{ij}(x_i, x_j, v_i, v_j) = F_{int}(x_j - x_i, v_j - v_i) = \nabla\Phi(x_j - x_i, v_j - v_i). \tag{2}$$

Notice that terms of this type are very common for models used in other domains, such as animal groups. See also Sect. 2.2.

Then one considers the presence of walls and other obstacles characterizing the environment. The interactions with the environment can be captured by potentials which depend only on the position and speed of the pedestrian, thus giving rise to forces of the type:

$$F_E(x_i, v_i) = \nabla\Psi(x_i, v_i). \tag{3}$$

As mentioned above, many variations have been proposed of the original social force model, including body compression, sliding frictions, other frictions, group forces, and other. While the modeling of the forces F_i, F_{ij}, and F_E appears to be comparable with experimental results, the other terms are usually less easy to tune with data [4].

One of the main assumptions of the social force model is the summability of the effects of the different forces. This is clearly an idealization, that is, most of times the working assumption. Summarizing, given N pedestrians in position x_i and having speed v_i, their dynamics is described by the system of ordinary differential equations:

$$\begin{cases} \dot{x}_i = v_i \\ \dot{v}_i = F_i(v_i) + \sum_j F_{ij}(x_i, x_j, v_i, v_j) + F_E(x_i, v_i). \end{cases} \tag{4}$$

If the functions F_i, F_{ij}, and F_E are Lipschitz continuous, then for every initial condition $x_0 = (x_1(0), \ldots, x_N(0))$, $v_0 = (v_1(0), \ldots, v_N(0))$, there exists a unique solution. The only singularity usually considered occurs when the repulsion component of F_{ij} is unbounded for $x_j - x_i$ tending to 0. This is a well-studied problem in many different fields, for instance, for its application to conflict resolution in aviation [44], robot groups [36], and general mathematical models [11].

Oftentimes researchers include uncertainties by adding stochastic terms. The social force has similarities with various microscopic and kinetic approaches to gas and fluid dynamics, and a wide literature is available, including stochastic models (see, for instance, [13] and references therein). However, to our knowledge, most researchers using the social force model focus on Langevin-type approach for simulations, rather than investigating the mathematically rigorous aspects.

2.1.1 Panic

From a modeling point of view, a lot of attention was devoted to distinguish situations where pedestrians behave normally to those of emergency situations where the rational behavior ceases and other phenomena occur. Many authors refer to "panic" for such situations. The social force model includes panic situations by appropriately modifying the involved forces. Notice that in most panic situation one should include the role played by the mechanics of the pedestrian body; indeed contacts and interactions occur in a fully 3D situation rather than the usual 2D ones. Authors refer to these forces as *body forces*. One of the most known phenomena is the formation of arches at exits that usually slow down or even block the flow through doors or other restricted passages. A full treatment of this situation goes beyond the scope of this paper, and we refer the reader to [17, 33] for details and references. Let us just mention that a wealth of models were proposed for pedestrian motion at nanoscopic level, i.e., considering also the dynamics of the pedestrian body. One of the most celebrated is the Laumond model [2], based on lab experiments. The same problem has been studied also in [14]. See also [22] for a model combining the Laumond and social force model.

2.2 Microscopic: Models for Animal Groups

As mentioned above, a parallel literature was developed for animal group dynamics. Let us just review which are the main ingredients of the models commonly used for animal groups to point out the similarities with social force models and the differences. We notice that such approach was applied to many different species, including fishes, birds, mammals, and others. We refer the reader to [16] for a more extensive discussion.

Microscopic models for animal group dynamics are also based mainly on attraction and repulsion forces. One has to notice that models are either of Newtonian type, i.e., mimicking physical forces as in the social force model, or first order, i.e., prescribing directly the speed of single animals. The modeling explanation of first-order models is based on the fact that animals (but also pedestrians) have high capability of changing their speed quickly in many situations; thus, the control they exert on their motion tends to overcome physical forces. Regarding energy, even if theoretically it is possible to write an energy balance equation, the latter would have to take into account internally stored energy of the animals and thus encompass different time scales and very complex energy processes. A complete debate goes beyond the scope of this paper, but we think that both approaches do have merits. The role of attraction is much better understood and modeled in animal groups with respect to pedestrian: it is based on advantages in foraging, mating, and escaping predators. Also attraction is differentiated between *group attraction*, where

attraction depends and acts only on distances and could enter first-order models, and *alignment*, where attraction acts on velocities and depends on distances, as usual for Newtonian models. Another feature is the fact that the presence of leaders is well discussed in the literature and models may or may not have leader(s). Also in this case, the biological explanations for the presence or absence of leaders appear to be well developed.

In biological literature there are two elements of key importance: the number of interacting members of the group and the shape of interaction zone. Models are classified as metric or topological. The former refers to interaction occurring with all mates present in the interaction zones (thus a variable number). The latter refers to interactions with a fixed number of mates (ordered, for instance, by distance). The interaction zone is usually different depending on the acting force (attraction, repulsion, and alignment) and not isotropic, to reflect the animal body and eyes' positions (or position of other sensing organs).

We notice that most social force models tend to consider all pedestrians to interact with each other. This is not realistic since pedestrians, as animals, tend to interact with closest neighbors or in restricted interaction zones. The assumption of all agents interacting renders the mean-field limit approach easier to manage (see Sect. 3), but formal limits are possible also with topological type models (see [26]).

2.3 Microscopic: Cucker-Smale Model

A special role in the literature is played by the well-known *Cucker-Smale model* (CS) [18] model. Interestingly enough, many authors consider this model a prototype for alignment (thus considered mainly as an animal group model or even aviation model [37]). However, the model was first introduced to study the linguistic dynamics. The CS model has many similarities with the social force ones and was definitely the most studied in the applied mathematics community (see, for instance, [10, 12, 25] and reference therein). The Cucker-Smale model reads:

$$\begin{cases} \dot{x}_i(t) &= v_i(t) \\ \dot{v}_i(t) &= \frac{1}{N}\sum\limits_{j=1}^{N} a(\|x_j(t)-x_i(t)\|)(v_j(t)-v_i(t)), \end{cases} \qquad i=1,\dots,N \quad (5)$$

where $x_i \in \mathbb{R}^d$, $v_i \in \mathbb{R}^d$, and $a \in C^1([0,+\infty))$ is a nonincreasing positive function, called interaction potential or rate of communication. In the original paper, the author set $a(s) = \frac{1}{(1+s^2)^\beta}$, with $\beta > 0$. Notice that the state for each agent is given by the couple (x_i, v_i) and, as in alignment models, the final configuration will promote consensus on the variable v_i.

2.4 Multi-scale Models

We start here by introducing a multi-scale model based on time-evolving measures. The main idea is that a microscopic dynamics as well as a macroscopic one with nonlocal interactions can be included together in a single equation for a measure, which possesses an atomic part (representing the microscopic component) and an absolutely continuous part (representing the macroscopic component).

To deal with the general case, we will consider a measure μ which evolves in time according to a velocity field v. The system is then written as first-order, or single, equation but can easily encompass Newton-type models as we will explain later on. Therefore, the main modeling aspect of the multi-scale model is the velocity field v, which has to account for the various "forces" described above. Once a velocity field is assigned, the evolution equation for a measure $\mu_t = \mu(t)$ is formally written as:

$$\frac{\partial \mu_t}{\partial t} + \nabla \cdot (\mu_t v) = 0, \tag{6}$$

together with an initial condition $\mu(0) = \mu_0$. The equation must be interpreted in weak sense, i.e., for every ϕ smooth with compact support and almost every t we have:

$$\frac{d}{dt} \int_{\mathbb{R}^d} \phi(x)\, d\mu_t(x) = \int_{\mathbb{R}^d} v(t,\, x) \cdot \nabla \phi(x)\, d\mu_t(x),$$

where we assume that the integral on the right-hand side is well defined, which amounts to integrability of v w.r.t. μ_t uniformly in t, and the map $t \to \mu_t$ is continuous for the weak-$*$ topology.

We now discuss possible choices for the velocity field v considering the general situation, i.e., $v = v[\mu]$. As for the social force model, v must take into account a *desired velocity* v^d which depends only on the position x of the pedestrian. Such velocities are usually determined by a final destination and point toward it. If the pedestrian would just follow the integral curves v^d, then she would reach the final destination avoiding obstacles. If other pedestrians are present in the environment, then we assume there is another velocity component called *interaction velocity*, which corresponds to the tendency of avoiding more crowded zones. Clearly, $v^i = v^i[\mu]$ because it depends on the position of other pedestrians, thus on the whole measure μ. The main mathematical question is the expected regularity of v^d and v^i for models reflecting the social force and other approaches. It is natural to assume that v^d is locally Lipschitz and locally bounded; thus trajectories of v^d exist and are unique. This automatically implies existence and uniqueness of weak solutions to (6) (see, for instance, [45]).

The regularity of v^i is more delicate. The main purpose of v^i is to model the attraction-repulsion with other pedestrians. For simplicity we limit to repulsion which acts on areas close to the pedestrian position; thus, it is more problematic for possible presence of singularities. We assume that there exists a kernel function

$\eta : \mathbb{R}^d \to [0, +\infty)$, representing a weighted interaction potential with nearby pedestrians. A possibility is the following: define the center of mass of the crowd w.r.t. η by

$$x^* := \frac{\int_{\mathbb{R}^d} y\, \eta(x-y)\, d\mu(y)}{\int_{\mathbb{R}^d} \eta(x-y)\, d\mu(y)},$$

and set

$$v^i[\mu](x) := (x - x^*) f\left(\int_{\mathbb{R}^d} \eta(x-y)\, d\mu(y)\right). \tag{7}$$

where f is a nondecreasing function. In simple words, the velocity field drives away from the weighted barycenter x^* with strength depending on the crowding. To avoid singularities, we set $v^i[\mu](x) = 0$ when $\int_{\mathbb{R}^d} \eta(x-y)\, d\mu(y) = 0$.

The main question we address now is the well-posedness of the transport equation with nonlocal velocity (6). Notice that $v^i = v^i[\mu]$; therefore, the equation is nonlinear in μ. With this goal, we first introduce the main analytic tool to study such equations, that is, the Wasserstein distance. Then, we recall our main results of existence and uniqueness of solutions to (6). Finally some possible choices of velocities (7) for crowd models are presented, discussing the regularity of the corresponding transport equation.

2.4.1 The Wasserstein Distance

In this section, we briefly recall the definition and the key properties of the Wasserstein distance, referring to [45] for a complete overview. We need first to introduce few concepts of general measure theory.

We denote by $\mathcal{M}$ the set of positive Radon measures with finite mass. If $\mu' \in \mathcal{M}$ is absolutely continuous with respect to $\mu \in \mathcal{M}$, we write $\mu' \ll \mu$. If $\mu' \ll \mu$ and $\mu'(A) \le \mu(A)$ for all Borel sets, we write $\mu' \le \mu$. Given $\mu \in \mathcal{M}$, we denote with $|\mu| := \mu(\mathbb{R}^d)$ its norm (or total mass). More in general, if $\mu = \mu^+ - \mu^-$ is a signed Borel measure, we have $|\mu| := |\mu^+| + |\mu^-|$. Such norm defines a distance in $\mathcal{M}$, that is, $|\mu - \nu|$.

Given two positive measures μ, ν, one can always write in a unique way $\mu = \mu_{ac} + \mu_s$ such that $\mu_{ac} \ll \nu$ and $\mu_s \perp \nu$, i.e., there exists B such that $\mu_s(B) = 0$ and $\nu(\mathbb{R}^d \setminus B) = 0$. This is the Lebesgue decomposition theorem. Then, it exists a unique $f \in L^1(d\nu)$ such that $d\mu_{ac}(x) = f(x)\, d\nu(x)$. Such function is called the Radon-Nikodym derivative of μ with respect to ν. We denote it with $D_\nu \mu$ and we have $|\mu_{ac}| = \int |D_\nu \mu|\, d\nu$. For more details, see, e.g., [21].

Given a Borel map $\gamma : \mathbb{R}^d \to \mathbb{R}^d$, one can consider the following action on a measure $\mu \in \mathcal{M}$, called the *push-forward of measures*:

$$\gamma \# \mu(A) := \mu(\gamma^{-1}(A)).$$

An evident property is that the mass of μ, i.e., $\mu(\mathbb{R}^d)$ is identical to the mass of $\gamma\#\mu$. Then, given two measures μ, ν with the same mass, it is natural to seek for a γ such that $\nu = \gamma\#\mu$, in which case we say that γ sends μ to ν. One can add a cost integrating over the distances covered by the masses moved by γ. More precisely, we define the cost of a map as:

$$I[\gamma] := |\mu|^{-1} \int_{\mathbb{R}^d} |x - \gamma(x)|^p \, d\mu(x).$$

This means that each infinitesimal mass $\delta\mu$ is sent to $\delta\nu$ and that its infinitesimal cost is related to the p-th power of the distance between them. The problem of finding a map γ realizing such minimum is known as the Monge problem and was first formulated in 1791. A minimizing γ exists only for special μ, ν and p. Indeed, there exist simple examples of μ, ν for which a γ sending μ to ν does not exist. For example, the measures $\mu = 2\delta_1$ and $\nu = \delta_0 + \delta_2$ on the real line have the same mass, but there exists no γ with $\nu = \gamma\#\mu$. The main issue is that a map γ cannot separate masses.

One could resort to multifunctions, to send masses to different locations. However, we need to split mass in all possible ways, and this is naturally realized by a probability measure π on the product space $\mathbb{R}^d \times \mathbb{R}^d$, seen as a generalization of a function mapping one measure onto the other. Each infinitesimal mass at a location x is sent to a location y with a probability given by $\pi(x, y)$. Formally, π is "sending" the measure μ onto ν if the following holds:

$$|\mu| \int_{\mathbb{R}^d} d\pi(x, \cdot) = d\mu(x), \qquad |\mu| \int_{\mathbb{R}^d} d\pi(\cdot, y) = d\nu(y). \tag{8}$$

Such a probability measure π is called a *transference plan* between μ and ν, and the set of transference plans between μ and ν is denoted by $\Pi(\mu, \nu)$. The condition (8) is equivalent to ask for all $f, g \in C_c^\infty(\mathbb{R}^d)$ the following equality:

$$|\mu| \int_{\mathbb{R}^d \times \mathbb{R}^d} (f(x) + g(y)) \, d\pi(x, y) = \int_{\mathbb{R}^d} f(x) \, d\mu(x) + \int_{\mathbb{R}^d} g(y) \, d\nu(y).$$

Following the same logic as for maps, one defined the cost of a transference plan π as

$$J[\pi] := \int_{\mathbb{R}^d \times \mathbb{R}^d} |x - y|^p \, d\pi(x, y).$$

The problem of minimizing J over the set $\Pi(\mu, \nu)$ is known as the Monge-Kantorovich problem. The Monge-Kantorovich problem is a generalization of the Monge one: Given a γ, with $\gamma\#\mu = \nu$, a transference plan can be defined by $\pi = (\mathrm{Id} \times \gamma)\#\mu$. In other words, $d\pi(x, y) = \mu(\mathbb{R}^d)^{-1} \, d\mu(x) \delta_{y=\gamma(x)}$. It is easy to check that $J[\mathrm{Id} \times \gamma] = I[\gamma]$. Notice that there always exists a transference plan

between $\mu, \nu \in \mathscr{M}$ with the same mass; indeed one can, e.g., choose $\pi(A \times B) = |\mu|^{-1}\,\mu(A)\nu(B)$, i.e., the mass from μ is split proportionally to the mass of ν.

The Monge-Kantorovich problem can be more generally stated on the space of Radon measures with finite p-moment, that is

$$\mathscr{M}^p := \left\{ \mu \in \mathscr{M} \mid \int |x|^p \, d\mu(x) < \infty \right\}.$$

The minimum realizing the solution to the Monge-Kantorovich problem always exists in such spaces, when μ, ν have the same mass. Such minimum defines a distance on the set of measures of $\mathscr{M}^p$ with a given mass, called the **Wasserstein distance**:

$$W_p(\mu, \nu) = (|\mu| \min_{\pi \in \Pi(\mu,\nu)} J\,[\pi])^{1/p}.$$

The Wasserstein distance metrizes the topology of weak convergence under assumptions of bounds on the p-moments, namely, we have the following:

Proposition 1 *The two following statements are equivalent for* $\mu_i, \mu \in \mathscr{M}^p(\mathbb{R}^d)$*:*

- $\lim_{i\to\infty} W_p(\mu_i, \mu) = 0$*;*
- $\mu_i \rightharpoonup_{n\to\infty} \mu$ *and* $\lim_{R\to\infty} \limsup_i \int_{|x|>R} |x|^p \, d\mu_i(x) = 0$.

We also notice that $W_p(k\mu, k\nu) = k^{1/p} W_p(\mu, \nu)$ for $k \geq 0$, by observing that $\Pi(k\mu, k\nu) = \Pi(\mu, \nu)$ and that $J\,[\pi]$ does not depend on the mass of the measures.

For future use, we recall an important duality property of the Wasserstein distance (for $p = 1$):

$$W_1(\mu, \nu) = \sup \left\{ \int_{\mathbb{R}^d} f \, d(\mu - \nu) \ : f \in \mathrm{Lip}(\mathbb{R}^d, \mathbb{R}),\ Lip(f) \leq 1 \right\}, \qquad (9)$$

where $\mathrm{Lip}(\mathbb{R}^d, \mathbb{R})$ is the space of globally Lipschitz functions and $Lip(f)$ indicates the Lipschitz constant of f. The equality (9) is known as the Kantorovich-Rubinstein duality.

2.4.2 Existence and Uniqueness of Solutions to (6)

In this section, we recall results of existence and uniqueness of solutions to (6). From now on we focus, for simplicity, on the space $\mathscr{P}$ of probability measures (positive Radon measure with mass equal to one) and the subspace $\mathscr{P}_c$ of probability measures with compact support. The key idea is that the correct topology to deal with equations as (6) is the one induced by the Wasserstein distance. More precisely, we will use the classical conditions on each vector field $v[\mu]$ of boundedness and

Lipschitz continuity, while we will ask the map $v[\cdot]$ to be Lipschitz with respect to the Wasserstein distance and the usual C^0 norm on vector fields.

Our main assumptions are the following: The function

$$v\,[\mu] : \begin{cases} \mathscr{P}_c(\mathbb{R}^d) \to C^1(\mathbb{R}^d) \cap L^\infty(\mathbb{R}^d) \\ \mu \quad\quad \mapsto v\,[\mu] \end{cases}$$

satisfies

(H1) $v\,[\mu]$ is uniformly Lipschitz and uniformly bounded, i.e., there exist L, M not depending on μ, such that for all $\mu \in \mathscr{P}_c(\mathbb{R}^d)$, $x, y \in \mathbb{R}^d$,

$$|v\,[\mu]\,(x) - v\,[\mu]\,(y)| \le L|x-y| \qquad |v\,[\mu]\,(x)| \le M.$$

(H2) v is a Lipschitz function, i.e., there exists K such that

$$\|v\,[\mu] - v\,[\nu]\,\|_{C^0} \le K\, W_p(\mu, \nu).$$

Under these assumptions the following holds:

Theorem 1 *Assume that (H1)–(H2) hold true. Then for every $\mu_0 \in \mathscr{P}_c(\mathbb{R}^d)$, there exists a solution to (6). Moreover, given μ, ν, two solutions of (6) in $C([0,T], \mathscr{P}_c(\mathbb{R}^d))$, we have*

$$W_p(\mu_t, \nu_t) \le e^{2t(L+K)} W_p(\mu_0, \nu_0).$$

In particular, if $\mu_0 = \nu_0$, then $\mu_t = \nu_t$ for all $t \in [0,T]$; thus, uniqueness of solutions holds true.

Proof See [38].

2.4.3 Regularity of Interaction Kernels

In view of Theorem 1, to ensure a well-posed theory for crowd dynamics, we need to investigate if velocity models do satisfy assumptions (H1) and (H2). As explained above, the regularity of the component v^d is quite standard; thus, we focus on the component v^i, assuming that it is given in the form (7). We consider two cases: the first is given by $f(x) \equiv 1$, while the second is given by $f(x) = x^\alpha$ with $\alpha \ge 1$. We show that with the first choice the assumptions (H1)–(H2) are not satisfied, while in the second case they are.

We start with the first case, so $f \equiv 1$. If the v^i is nontrivial, i.e., if η is not vanishing everywhere, then the corresponding velocity field $v\,[\mu]$ is not even continuous w.r.t. the Wasserstein distance. We construct a counterexample based on the graphical idea explained in Fig. 1.

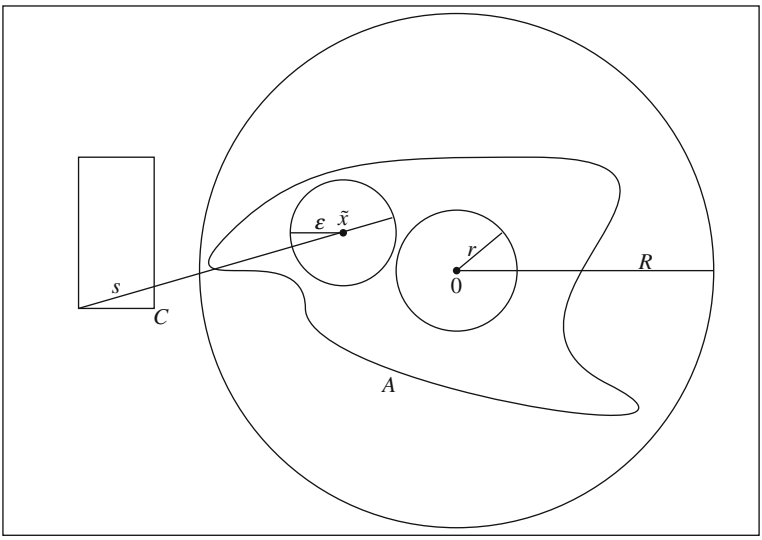

Fig. 1 The velocity field v^i given by (7) is not continuous if $f \equiv 1$

We indicate by $B_s(y)$ the balls centered at y of radius s and by $\overline{B}_s(y)$ its closure. Assume $\text{supp}\,(\eta) \subset B_R(0)$ for $R > 0$. By continuity of η, the set $A := \{\eta > 0\}$ is open. Take $r > 0$ ($r < R$) sufficiently small so that $B_r(0) \subset A$ and there exists $\tilde{x} \in A \backslash \overline{B}_r(0)$. Since A is open and $\overline{B}_r(0)$ closed, there exists ϵ such that $B_\varepsilon(\tilde{x}) \subset A \backslash B_r(0)$. Finally, we let C be a compact set such that $C \cap \overline{B}_r(0) = \emptyset$ and define $s = \sup\{|x - y| \ \text{ s.t. } x \in B_\varepsilon(\tilde{x}),\ y \in C\}$.

We now define a family of measures μ_t that will provide a counterexample to continuity of v^i. Set:

$$\mu_t := \left(t \frac{\chi_{B_\varepsilon(\tilde{x})}}{\mathscr{L}(B_\varepsilon(\tilde{x}))} + (1-t) \frac{\chi_C}{\mathscr{L}(C)} \right) \mathscr{L},$$

where $\mathscr{L}$ is the Lebesgue measure. From $\int_{\mathbb{R}^d} \eta(-y)\, d\mu_0(y) = \frac{1}{\lambda(C)} \int_C 0\, d\mathscr{L}(y) = 0$, we deduce

$$v\,[\mu_0]\,(0) = 0. \tag{10}$$

For $t > 0$, we have $\int_{\mathbb{R}^d} \eta(-y)\, d\mu_t(y) > 0$; hence:

$$|v\,[\mu_t]\,(0)| = \left| \frac{\int_{\mathbb{R}^d} y\eta(-y), d\mu_t(y)}{\int_{\mathbb{R}^d} \eta(-y), d\mu_t(y)} \right| = \left| \frac{\frac{t}{\mathscr{L}(B_\varepsilon(\tilde{x}))} \int_{B_\varepsilon(\tilde{x})} y\eta(-y)\, d\mathscr{L}(y)}{\frac{t}{\mathscr{L}(B_\varepsilon(\tilde{x}))} \int_{B_\varepsilon(\tilde{x})} \eta(-y)\, d\mathscr{L}(y)} \right| \geq$$

$$\geq \frac{\inf\{|y| \ \text{ s.t. } y \in B_\varepsilon(\tilde{x})\} \int_{B_\varepsilon(\tilde{x})} \eta(-y)\, d\mathscr{L}(y)}{\int_{B_\varepsilon(\tilde{x})} \eta(-y)\, d\mathscr{L}(y)} \geq r. \tag{11}$$

From (10) and (11), we have that $v^i[\mu_t]$ is not continuous at $t = 0$. Then assumption (H2) will be violated if we prove that μ_t is continuous at $t = 0$ w.r.t. Wasserstein distance, i.e., if $\lim_{t\to 0} W_p(\mu_0, \mu_t) = 0$. For this, we define $\nu_t := (1-t)\frac{\chi_C}{\mathscr{L}(C)}\mathscr{L}$, then $W_p(\mu_0, \mu_t) = W_p(\mu_0 - \nu_t, \mu_t - \nu_t) = W_p\left(t\frac{\chi_C}{\mathscr{L}(C)}\mathscr{L}, t\frac{\chi_{B_\varepsilon(\tilde{x})}}{\mathscr{L}(B_\varepsilon(\tilde{x}))}\mathscr{L}\right)$. Since all measures are absolutely continuous w.r.t. $\mathscr{L}$, there exists a map γ realizing the Wasserstein distance. Moreover, we can estimate $|x - \gamma(x)| \le s$ and then $W_p(\mu_0, \mu_t) \le st^{1/p}$, proving the continuity of μ_t.

Let us now pass to the case $f(x) = x^\alpha$ with $\alpha \ge 1$. We have the following:

Proposition 2 *Let v^i be defined by (7), where η is a smooth, positive function with bounded support. If $f(x) = x^\alpha$, with $\alpha \ge 1$, then v^i satisfies (H1) and (H2).*

Proof We first prove that (H1) is satisfied. Notice that:

$$\left|\int_{\mathbb{R}^d} \eta(x-y)\, d\mu(y)\right| \le |\eta|_\infty,$$

thus we get $|v[\mu](x)| \le R|\eta|_\infty^\alpha$, assuming $\mathrm{supp}(\eta) \subset B_R(0)$. Moreover, indicating by L the Lipschitz constant of η, it holds:

$$|v[\mu](x) - v[\mu](z)| =\le |\eta|_\infty^{\alpha-1} R \int_{\mathbb{R}^d} |\eta(x-y) - \eta(z-y)|\, d\mu(y) \le$$

$$\le |\eta|_\infty^{\alpha-1} RL|x-z| \int_{\mathbb{R}^d} d\mu(y) = |\eta|_\infty^{\alpha-1} RL|x-z|,$$

thus $v[\mu]$ is bounded and Lipschitz continuous. Similarly, we prove (H2) with the following estimate:

$$|v[\mu](x) - v[\nu](x)| \le |\eta|_\infty^{\alpha-1} \left|\int_{\mathbb{R}^d} (x-y)\eta(x-y)\, d(\mu-\nu)(y)\right|.$$

Since the function $\varphi(y) := (x-y)\eta(x-y)$ is Lipschitz continuous, using the Kantorovich-Rubinstein duality (9), we get

$$\|v[\mu] - v[\nu]\|_{C^0} \le |\eta|_\infty^{\alpha-1} RL W_1(\mu, \nu).$$

2.5 Wasserstein Distance and Total Variation Norm

The Wasserstein distance W_p is a natural distance since it metrizes (over compact sets) the weak* topology as dual of the space $\mathscr{C}_0$ (closure of continuous functions with compact support for the uniform norm). On the other side, one may consider the total norm over signed measures $\|\mu^+ - \mu^-\|_{TV} = \mu^+(\mathbb{R}^d) + \mu^-(\mathbb{R}^d)$ given by the total variation, equal to $\mu(\mathbb{R}^d)$ for positive measures, which corresponds to

strong convergence. It is obvious that mathematically weak convergence is easier to achieve; however, there are also modeling reasons to prefer the Wasserstein distance. In this section we provide a comparison of the two metrics.

First, let us notice that the space $\mathscr{M}$ can be endowed with many different distances (see, e.g., [43]). The total variation norm coincides with the L^1 distance for absolutely continuous measures:

$$\|\mu - \nu\|_{L^1} := \int |\mu(x) - \nu(x)| dx.$$

Assume now that two crowd configurations in the ambient space are represented by the measures $\mu_i = \frac{1}{N}\sum_{j=1}^{N} \delta_{x_j^i}$, $i = 1, 2$, $j = 1, \dots, N$. Then the Wasserstein distance is given by the minimum over all permutations $\sigma : \{1, \dots, N\} \to \{1, \dots, N\}$ of the quantity $\frac{1}{N}\sum_j |x_j^1 - x_{\sigma(j)}^2|$. Indeed, all possible ways to move the mass from μ_1 to μ_2 correspond to the maps between the points x_j^1 and x_j^2, which in turn can be represented by a permutation σ. Consider, for instance, the following situation in $\mathbb{R}$: $\mu_1 = \frac{1}{2}\delta_0 + \frac{1}{2}\delta_1$ and $\mu_2 = \frac{1}{2}\delta_\epsilon + \frac{1}{2}\delta_{1+\epsilon}$. In other words μ_1 is given by two pedestrians in position 0 and 1, while μ_2 by two pedestrians in position ϵ and $1+\epsilon$. The total variation distance verifies $\|\mu_1 - \mu_2\| = 1$, while the Wasserstein distance is $W(\mu_1, \mu_2) = \epsilon$. Clearly, if ϵ is small, the two configurations are close to each other. This is reflected in the Wasserstein distance but not in the total variation one.

Beside the modeling reasons, the Wasserstein distance is preferable also for the uniqueness of solutions to transport equations. For instance, we may replace the assumption (H2) with the following:

(H3) The function $v[\cdot]$ satisfies for some $K > 0$:

$$\|v[\mu] - v[\nu]\|_{C^0} \leq K\|\mu - \nu\|_{TV}.$$

It is possible to define a velocity field v that satisfies assumptions (H1) and (H3) but does guarantee uniqueness of solutions to the Cauchy problem. The idea is depicted in Fig. 2 and is based on lack of uniqueness of the classical example for ordinary differential equations: $\dot{x} = \sqrt{x}$, $x(0) = 0$. We provide a sketch of the proof, referring the reader to [38] for details.

Fix $d = 2$ and define a curve ν_t in the space of probability measures as follows. The squares Q_t^i have sides parallel to coordinate axes of length s_i, share a side, and have the upper ones on the line $y = 1 + t^2$. The measure ν_t is given by:

$$\nu_t := \sum_{i=0}^{\infty} m_i \chi_{Q_t^i} \mathscr{L},$$

where m_i are positive and, as before, $\mathscr{L}$ is the Lebesgue measure. We then define the velocity field by $v[\nu_t] := (0, 2t)$. Choosing $s_i := 4^{-i}$ and $m_i = \frac{1}{2}8^i$, one can prove

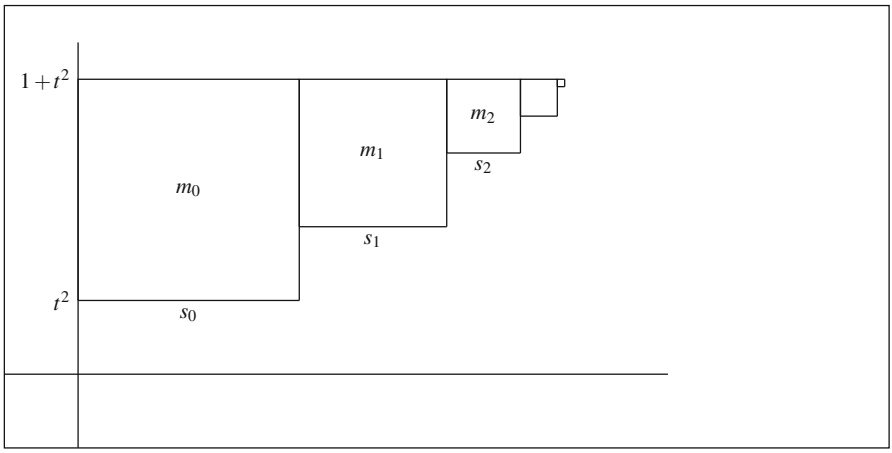

Fig. 2 (H3) does not guarantee uniqueness of the solution

that v satisfies (H3). Moreover, one can define v on the whole $\mathscr{M}$. It is easy to show that the Cauchy problem with initial condition ν_0 has two solutions: $\mu_1(t) \equiv \nu_0$ and $\mu_2(t) = \nu_t$. We can also estimate $W_p(\nu_t, \nu_s) = t^2 - s^2$; thus, v does not satisfy assumption (H2).

3 Mean-Field Limits of Microscopic Models

In this section, we introduce the mean-field limit of microscopic models for crowd dynamics. The goal is to describe the dynamics of the crowd when the number of agents tends to infinity. As a result, the description of each agent is lost, and the crowd is then represented by a spatial density evolving in time.

3.1 Definition of the Mean-Field Limit

In this section, we recall the definition of the mean-field limit. Historically, the mean-field limit has been introduced as the limit of classical and quantum mechanical systems (see, e.g., [34] and references therein). In the case of crowd dynamics, some standard physical interaction laws are not satisfied (e.g., the action-reaction principle). We then use an approach less influenced by the physical intuition, following Neunzert in [35]. Even though his description focuses on ordinary differential equations of the second order, the method presented there can be applied verbatim to first-order systems.

Consider an ordinary differential equation describing the dynamics of N particles in the phase space $\mathbb{R}^d$. In a very general form, it can be written as follows:

$$\dot{x}_i = f_N(x_i; x_1, \dots, x_N), \quad i = 1, \dots, N. \tag{12}$$

Here, we highlight that the expression of the dynamics f_N depends on the number N of particles. Then, one can see (12) as a family of ordinary differential equations indexed by N, each of them describing the dynamics of N particles in the phase space $\mathbb{R}^d$, hence each of them describing a dynamics in the space $\mathbb{R}^{dN}$.

Assume now that each f_N satisfies some properties ensuring existence, uniqueness, and well-posedness of solutions to (12), e.g., the classical Lipschitz condition. Then, for each N and an initial data $X_N^0 = (x_1^0, \dots, x_N^0)$, there exists a unique trajectory $X_N(t) = (x_1(t), \dots, x_N(t))$.

The goal of mean-field limit is to describe the limit of the trajectories of such systems when N tends to infinity. The first difficulty is that each trajectory, indexed by N, lives in a different space, that is, $\mathbb{R}^{dN}$. One then needs to add the following key hypothesis: particles x_i are *identical* or indistinguishable. As a consequence, an exchange of the particle x_i with x_j induces no change in the dynamics of the whole system, in the following sense: the trajectories of these two particles are exchanged, and the trajectories of the other particles are kept. Clearly, this requirement strongly restricts the set of possible dynamics f_N. The most classical expressions are of the form

$$f_N(x_i; x_1, \dots, x_N) = f^0(x_i) + \frac{1}{N} \sum_{j=1}^{N} f^1(x_j - x_i). \tag{13}$$

Under such hypothesis of indistinguishability, one can then replace the trajectory $X_N(t)$ with its description in terms of measures, by introducing the *empirical measure*. Given $X_N(t) = (x_1(t), \dots, x_N(t))$, define the corresponding empirical measure as

$$\mu_N(t) := \frac{1}{N} \sum_{i=1}^{N} \delta_{x_i(t)}.$$

Then, all trajectories μ_N now evolve in the same space $\mathscr{P}(\mathbb{R}^d)$ of probability measures defined on the phase space $\mathbb{R}^d$ that does not depend on N anymore. Moreover, the space $\mathscr{P}(\mathbb{R}^d)$ is naturally endowed with the topology of the weak convergence of measures, that is

$$\mu^i \rightharpoonup_{i\to\infty} \mu^* \quad \Leftrightarrow \quad \lim_{i\to\infty} \int f \, d\mu^i = \int f \, d\mu^* \quad \text{for all} \quad f \in C_c^\infty(\mathbb{R}^d).$$

In the space $\mathscr{P}(\mathbb{R}^d)$, one can define dynamical systems too. For simplicity, we focus on the case that we will use most in the following: a Cauchy problem for measure with dynamics given by a transport equation, that is

$$\begin{cases} \partial_t \mu + \nabla \cdot (V[\mu]\mu) = 0, \\ \mu(0) = \mu^0. \end{cases} \tag{14}$$

Assume to have properties on V ensuring existence and uniqueness of solutions to (14), such as (H1)–(H2) in Sect. 2.4.2. Denote with $\mu(t)$ the corresponding unique solution. In a more abstract setting, one can simply consider to have a functional (e.g., a semigroup) that to each initial state μ^0 associates a unique trajectory $\mu(t)$.

We are now ready to define the mean-field limit. We say that (14) is the mean-field limit of (12) if the following property holds:

$$\mu_N(0) \rightharpoonup_{N\to\infty} \mu(0) \qquad \Rightarrow \qquad \mu_N(t) \rightharpoonup_{N\to\infty} \mu(t) \quad \text{for all } t \geq 0. \tag{15}$$

A particular but relevant case for mean-field limits is the following. Assume to have a measure dynamics of the form (14) with the following property:

(MF-N): When the initial data μ^0 is an empirical probability measure μ_N^0 associated to an initial data X_N^0 of N particles, then the dynamics (14) rewrites as the ordinary differential equation (12).

Hence, given an initial data X_N^0 with N particles, the trajectory of (14) with initial data μ_N^0 coincides with the empirical measure associated to the solution for (12) with initial data X_N. This property is somehow stronger than (15) for empirical measures, since it requires identity of trajectories for each N, and not only convergence for $N \to \infty$. Nevertheless, such property is often naturally imposed in crowd models with arbitrary N agents, e.g., by choosing dynamics of the form (13). Instead, some relevant physical models do not satisfy such property (see, e.g., [34, Sec. 1.5]).

Clearly, condition **(MF-N)** makes sense for empirical measures only. We then need to add a condition for all other measures to ensure that (14) is the mean-field limit of (12). The most natural one is to require the following continuity condition:

(C): The solution $\mu(t)$ to (14) is continuous with respect to the initial data μ^0.

Such property is somehow natural in crowd models that are written in terms of (14), since they are always approximated models of a crowd with a large but finite number of agents. Hence, continuous dependence is necessary to ensure that the behavior of the approximated model is sufficiently close to the real dynamics.

We now prove that (14) is the mean-field limit of (12), under the hypotheses **(MF-N)-(C)**. Indeed, recall that the set of empirical probability measures is dense in $\mathscr{P}(\mathbb{R}^d)$ endowed with the topology of weak convergence. Then, take any initial data $\mu(0)$ and a sequence of empirical measures $\mu_N(0) \rightharpoonup_{N\to\infty} \mu(0)$ that exists by density. Observe now that, by **(MF-N)**, in this specific case $\mu_N(t)$ is both the empirical measure associated to the solution to (12), as in the definition (15) of mean-field limit, and the unique solution to (14). Then, (15) holds, since it is the continuity property **(C)** for the measure dynamics (14).

It is clear that proving (15) can be easier if there exists a metric that metrizes the weak topology of measures. This is the case of the Wasserstein distance (Sect. 2.4.1), under some restrictive hypotheses that usually hold for crowd models.

For crowd modeling, trajectories usually have a uniformly bounded support, e.g., when the initial measure has bounded support and velocities are bounded. Then, in our setting, Proposition 1 ensures that convergence in Wasserstein distance is equivalent to weak convergence of measures. Hence, we can restate (15) in terms of the Wasserstein distance: the dynamics (14) is the mean-field limit of (12) if the following property holds:

$$\lim_{N\to\infty} W_p(\mu_N(0), \mu(0)) = 0 \quad \Rightarrow \quad \lim_{N\to\infty} W_p(\mu_N(t), \mu(t)) = 0 \quad \text{for all } \ t \geq 0.$$

It is important to observe that such statement is a rewriting of (15) in the space $\mathscr{P}_p(\mathbb{R}^d)$ only. In particular, we will see in the following Sect. 5 that the original definition (15) of mean-field limit makes sense also for models with varying mass, while the Wasserstein distance between two measures with different masses is undefined.

3.2 The Mean-Field Limit of the Helbing-Molnár Model

In this section, we derive the mean-field limit of the Helbing-Molnár model of social forces recalled in Sect. 2.1. The idea is to follow the method described in Sect. 3.1: we first write a partial differential equation of the form (14) satisfying the property **(C)** of continuity with respect to the initial data. We then prove that the original Helbing-Molnár model (4) satisfies the property **(MF-N)**, i.e., it is the rewriting of the partial differential equation when the initial data is an empirical measure.

We start by writing the measure $\mu = \mu(t, x, v)$, that is, a time-varying probability measure in the space $\mathscr{P}(\mathbb{R}^d \times \mathbb{R}^d)$, i.e., in the space of probability measures on the space of configurations (x, v) in the space $\mathbb{R}^d$. For the Helbing-Molnár model, one usually has $d = 2$ or 3, as recalled above.

We then write the partial differential equation for the mean-field limit of the Helbing-Molnár model, that is

$$\begin{cases} \partial_t \mu + \nabla \cdot (V_{HM}[\mu]\mu) = 0, \\ \mu(0) = \mu^0. \end{cases} \tag{16}$$

where the vector field for the Helbing-Molnár model is

$$V_{HM}[\mu](x, v) := \begin{pmatrix} v \\ F_i(v) + (F_{int} \star \mu)(x, v) + F_e(x, v) \end{pmatrix} \tag{17}$$

Here, the functions F_i, F_{int}, F_e are defined in (1)–(2)–(3), respectively. We already observed that such functions are chosen to be globally Lipschitz, to ensure existence and uniqueness of the solutions to the ordinary differential equation (4) of the Helbing-Molnár model for all times. We now prove that the vector field (17) satisfy the hypotheses (H1)–(H2) of Theorem 1. More precisely, we will prove that V_{HM} can be modified outside a sufficiently large compact set so as to have the same solutions to (16) and to satisfy (H1)–(H2).

It is clear that the three functions $(x, v) \to v$, F_i and F_e are Lipschitz with respect to (x, v). Moreover, they are independent on μ. We now need to study the term $F_{int} \star \mu$, for which it holds

$$
\begin{aligned}
&|F_{int} \star \mu(x, v) - F_{int} \star \mu(y, w)| \leq \\
&\int_{\mathbb{R}^{2d}} |F_{int}(x - \alpha, v - \beta) - F_{int}(y - \alpha, w - \beta)| \, d\mu(\alpha, \beta) \leq \\
&\int_{\mathbb{R}^{2d}} L \, |(x - \alpha, v - \beta) - (y - \alpha, w - \beta)| \, d\mu(\alpha, \beta) = L|(x, v) - (y, w)|,
\end{aligned}
$$

where L is the Lipschitz constant of F_{int}. Moreover, it also holds

$$
\begin{aligned}
&|F_{int} \star \mu(x, v) - F_{int} \star \nu(x, v)| = \\
&\left| \int_{\mathbb{R}^{2d}} F_{int}(x - \alpha, v - \beta) d(\mu(\alpha, \beta) - \nu(\alpha, \beta)) \right| \leq L W_1(\mu, \nu),
\end{aligned}
$$

where we used the Kantorovich-Rubinstein duality formula (9). Then, V satisfies the first condition of (H1), as well as (H2) with $p = 1$.

We are now left to prove that V also satisfies the second condition of (H1), i.e., uniform boundedness. This is clearly false, e.g., since $(x, v) \to v$ is an unbounded function. Nevertheless, observe that V being uniformly Lipschitz implies that V has sublinear growth, in the following sense: there exists $C > 0$ such that $\text{supp}(\mu) \subset B_R(0)$ implies $V([\mu]) \leq C(1 + R)$. Indeed, observe that the following conditions hold:

- $(x, v) \in \text{supp}(\mu) \subset B_R(0)$ implies $|v| \leq R$;
- $|F_i(v)| \leq L|v| + |F_i(0)| \leq LR + |F_i(0)|$;
- $|F_e(x, v)| \leq L|(x, v)| + |F_e(0, 0)| \leq LR + |F_e(0, 0)|$.

To prove boundedness of $F_{int} \star \mu$, observe that it holds

$$
\begin{aligned}
|F_{int} \star \mu(x, v)| \leq |F_{int} \star \mu(x, v) - F_{int} \star \delta_0(x, v)| + |F_{int} \star \delta_0(x, v) - F_{int} \star \delta_0(0, 0)| + \\
|F_{int} \star \delta_0(0, 0)| \leq L W_1(\mu, \delta_0) + L|(x, v)| + |F_{int} \star \delta_0(0, 0)| \leq \\
2LR + |F_{int}(0, 0)|.
\end{aligned}
$$

Here we used the fact that for a measure μ satisfying $\text{supp}(\mu) \subset B_R(0)$, we have $W_1(\mu, \delta_0) \leq R$, since transportation plans all have rays with length smaller than

R. Then, choosing $C := 2\max\{1+4L, F_i(0)+F_e(0,0)+|F_{int}(0,0)|\}$, one has sublinear growth of the vector field V, independent on the measure μ. Similar to classical techniques for ODEs, this implies that, when $\mathrm{supp}(\mu_0) \in \mathscr{P}(B_R(0))$, then $\mathrm{supp}(\mu(t,\cdot,\cdot)) \in \mathscr{P}(B_{S(t)}(0))$ with $S(t) = e^{Ct}(1+R)-1$.

Let us now consider an initial compact set $K \subset \mathbb{R}^d \times \mathbb{R}^d$ and a time $T > 0$. When $\mathrm{supp}(\mu_0) \in K \subset B_R(0)$ for some R, then the solution satisfies $\mathrm{supp}(\mu(t,\cdot,\cdot)) \in B_{S(T)}(0)$ for all $t \in [0,T]$. Choose now $V'[\mu](x,v)$ coinciding with V_{HM} for $\mu \in \mathscr{P}(B_{S(T)}(0))$ and $(x,v) \in B_{S(T)}(0)$, being bounded, Lipschitz with respect to (x,v) and μ outside of it: then, V' satisfies both conditions of (H1), as well as (H2). Moreover, solutions of (16) with $\mu_0 \in \mathscr{P}(K)$ coincide with the ones where V_{HM} is replaced by V'. Then, we have existence and uniqueness of solutions to (16) when $\mu_0 \in \mathscr{P}(K)$. Since K is an arbitrary compact set, we have existence and uniqueness of solutions to (16) for any μ_0 with compact support. Moreover, continuity with respect to the initial data (i.e., condition **(C)**) is satisfied too.

We are now left to prove that **(MF-N)** is satisfied. A direct rewriting of (16) with $\mu_0 = \frac{1}{N}\sum_{i=1}^N \delta_{x_i}$ shows that it coincides with (4). Then, both conditions **(C)-(MF-N)** are satisfied; hence (16) is the mean-field limit of the Helbing-Molnár model (4).

Remark 1 A relevant particular case of the Helbing-Molnár model is given by the Cucker-Smale model for alignment that we introduced in Sect. 2.3. There, the functions F_i, F_e in (4) are identically zero, while the interaction term $F_{ij}(x_i,x_j,v_i,v_j)$ is given by $a(\|x_j-x_i\|)(v_j-v_i)$.

Then, it is clear that, by choosing

$$F_{int}(x,v) = -a(|x|)v,$$

the measure evolution (16) is the mean-field limit of the Cucker-Smale model (5). This result was already obtained with different techniques in [25]. A classical rewriting, splitting the differential operator in the (x,v) variables, is

$$\partial_t \mu + \langle v, \nabla_x \mu\rangle + \mathrm{div}_v\left((F_{int} \star \mu)\,\mu\right) = 0.$$

4 Microscopic Models with Varying Mass

In this section, we introduce some microscopic models in which each agent has a mass that varies in time. In crowd models, the mass of an agent may represent his influence with respect to the rest of the crowds, such as leadership, reputation, or persuasion.

The key difficulty for these models, strongly correlated to the goal of building mean-field limits for them, is that we do not aim to label agents in different classes (such as leaders vs followers, eventually switching from one to another; see [1, 8, 20]), but to keep a form of homogeneity for them.

In this section, we describe a model of N agents, each of them represented by its position x_i in the phase space and its mass m_i. The dynamics for the crowd is given in the following form:

$$\begin{cases} \dot{x}_i = V_0(x_i) + \sum_{j=1}^N m_j V_1(x_j - x_i), \\ \dot{m}_i = m_i(S_0(x_i) + \sum_{j=1}^N m_j S_1(x_j - x_i)), \end{cases} \qquad i = 1, \dots, N. \tag{18}$$

All the functions V_0, V_1, S_0, S_1 are required to be uniformly bounded and uniformly Lipschitz with respect to their variables, to ensure existence and uniqueness of the solution to the associated Cauchy problem. Moreover, we also require $V_1(0) = S_1(0) = 0$.

We highlight some key properties of the model (18). The first is that, in the first equation, the term m_j is the weight of the interaction term $V_1(x_j - x_i)$. In this sense, the mass m_j plays the role of the influence of the j-th particle onto the i-th one.

The second, crucial property, is that one can replace the i-th particle with position-mass (x_i, m_i) with two (or more) new particles $(y_1, n_1), (y_2, n_2)$ that lie in the same position ($y_1 = y_2 = x_i$) and whose total mass coincides with the initial one ($n_1 + n_2 = m_i$). Indeed, consider on one side the trajectories of the N-particles system $((x_1, m_1), \dots, (x_i, m_i), \dots, (x_N, m_N))$ satisfying (18) and starting from an initial data $((x_1^0, m_1^0), \dots, (x_i^0, m_i^0), , \dots, (x_N^0, m_N^0))$. On the other side, consider the trajectories of the $N + 1$-particles system

$$((\tilde{x}_1, \tilde{m}_1), \dots, (\tilde{x}_{i-1}, \tilde{m}_{i-1}), (y_1, n_1), (y_2, n_2), (\tilde{x}_{i+1}, \tilde{m}_{i+1}), \dots, (\tilde{x}_N, \tilde{m}_N))$$

satisfying (18) and starting from an initial data

$$((\tilde{x}_1^0, \tilde{m}_1^0), \dots, (\tilde{x}_{i-1}^0, \tilde{m}_{i-1}^0), (y_1^0, n_1^0), (y_2^0, n_2^0), (\tilde{x}_{i+1}^0, \tilde{m}_{i+1}^0), \dots, (\tilde{x}_N^0, \tilde{m}_N^0))$$

with the following properties:

- it holds $x_j^0 = \tilde{x}_j^0$ and $m_j^0 = \tilde{m}_j^0$ for all $j \neq i$;
- it holds $x_i^0 = y_1^0 = y_2^0$ and $m_i^0 = n_1^0 + n_2^0$.

Then, the following identities hold true for all times $t \in \mathbb{R}$:

- the trajectories satisfy $(x_j(t), m_j(t)) = (\tilde{x}_j(t), \tilde{m}_j(t))$ for all $j \neq i$;
- the trajectory of the i-th particle satisfies $x_i(t) = y_1(t) = y_2(t)$, while its mass satisfies $m_i(t) = n_1(t) + n_2(t)$.

The proof follows from a direct computation of the derivatives and from uniqueness of the solution to (18). Such property is instrumental for the mean-field limit. Indeed, one needs to preserve the property of indistinguishability of particles also for time-varying masses.

Observe that the model (18) preserves positivity/negativity of the mass. In our interpretation of the mass as a degree of influence, one might accept the presence of negative influences. Moreover, the presence of negative masses would produce signed measures at the mean-field limit that can be efficiently treated with a generalization of the methods described here (see [41]).

A direct computation also shows that the total mass is not preserved, since $\partial_t(\sum_i m_i) \neq 0$. It is then sufficient to add a correction term in $\dot{m}_i$ to ensure such property, such as the rescaling term

$$-\frac{m_i}{\sum_{k=1}^N m_k}\left(\sum_{k=1}^N m_k\left(S_0(x_k)+\sum_{j=1}^N m_j S_1(x_j-x_k)\right)\right).$$

Also in this case, in our setting there is no general reason to assume a constant total influence, and such constraint is not either necessary for the mean-field limit.

We now present a classical pedestrian evacuation problem: the simulation of the exit of a crowd from a room through a single large door. We compare two models. The first is the classical social force model, where the mass of each agent has a constant value for the whole simulation. In the second case, the mass (modeling influence) exponentially decreases when the agent exits the door. These two approaches model two different known behaviors of pedestrians: in the first, the agent wanders around the exit door (confused, trying to find help, or simply stopping in the proximity of the exit), while in the second he runs toward a far safe place (e.g., meeting point). Our simulations show that the average exit time can be reduced 8% when the second model is implemented. The maximal exit time is even reduced 11% in the second model.

Following the first-order model by Piccoli-Tosin [42], inspired by the Helbing-Molnár model, we describe the behavior of a single agent as follows. His velocity is the sum of two terms: first a desired velocity, which in our case is a unitary vector pointing to the exit, and second, a term of repulsion to other agents, to model the tendency of avoiding overcrowded areas. In our simulation, the agent computes the barycenter of the mass of agents in a ball of radius 2 around himself and then moves in the opposite direction of such barycenter.

In Fig. 3 (left), we show three different times of the simulation with no variation of the mass: the initial random configuration of 200 agents, then an intermediate time $T = 6$ in which clusters appear, and finally time $T = 16.4$ in which the last agent exits the room. The average exit time is 8.075 s.

In Fig. 3 (right), we show the simulation in which the mass decreases exponentially when an agent exits the door. This is represented by the circle reducing its radius. The initial configuration coincides with the previous case. The simulation is shown at the intermediate time $T = 6$ and then at the time $T = 14.6$ in which the last agent exits the room. The average exit time is 7.415 s.

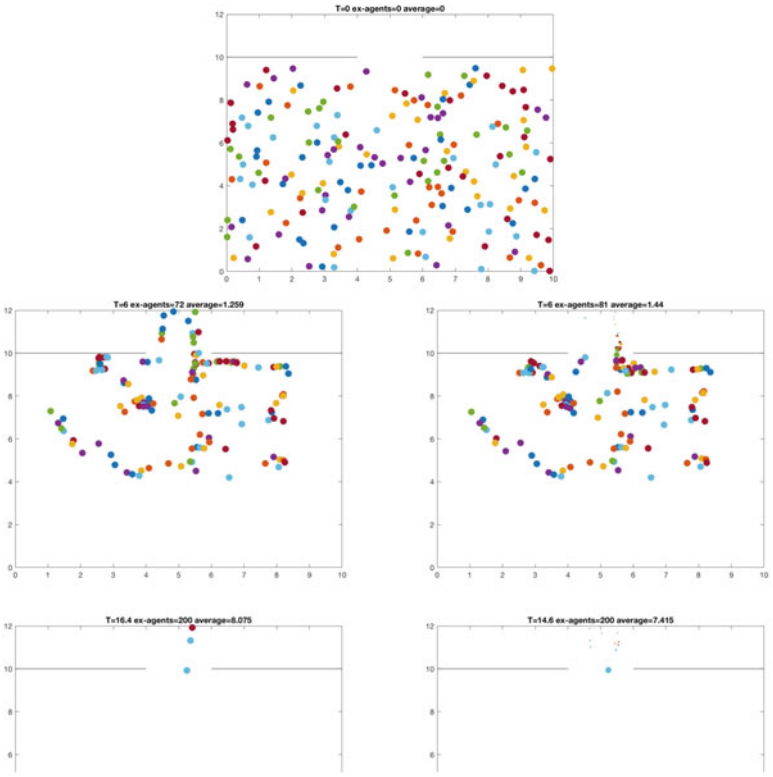

Fig. 3 Evolution of the microscopic model. Left: no mass reduction. Right: mass reduction

5 Measure Dynamics for Mass-Varying Models

In this section, we describe the mean-field limit of microscopic models with varying mass introduced in Sect. 4. With this goal, we first recall the definition of the generalized Wasserstein distance that we introduced in [39, 40]. It will be the main analytical tool for the study of the mean-field limit. We will then write the limit measure dynamics and prove that it is the mean-field limit of the microscopic model. We finally recall main results of well-posedness of the limit PDE.

Other relevant distances between measures of different masses, further generalizing the one presented here, have been recently described (see [15, 28, 32]).

5.1 The Generalized Wasserstein Distance

We recall here the definition of the **generalized Wasserstein distance** $W_p^{a,b}(\mu, \nu)$. We first give a rough description of the idea. Imagine to have three different admissible actions on μ, ν: either add/remove mass to μ or add/remove mass to ν or

transport mass from μ to ν. The three techniques have their cost: add/remove mass has a unitary cost a (in both cases) and transport of mass has the classic Wasserstein cost, multiplied by a fixed constant b. The distance is the minimal cost of a mix of such techniques.

From now on, we denote with $\mathscr{M}$ be the space of Borel measures with finite mass on $\mathbb{R}^d$ and with $\mathscr{M}_c$ its subset of measures with bounded mass and compact support. We now formally define the generalized Wasserstein distance.

Definition 1 Let $a, b \in (0, \infty)$ and $p \geq 1$ be fixed. The **generalized Wasserstein distance** is

$$W_p^{a,b}(\mu, \nu) = \inf_{\tilde{\mu}, \tilde{\nu} \in \mathscr{M}, |\tilde{\mu}| = |\tilde{\nu}|} \left(a|\mu - \tilde{\mu}| + a|\nu - \tilde{\nu}| + bW_p(\tilde{\mu}, \tilde{\nu}) \right).$$

Proposition 3 *The operator $W_p^{a,b}$ is a distance. Moreover, the infimum is always attained.*

We now observe that the generalized Wasserstein distance metrizes the weak convergence of measures, with the additional requirement of tightness.

Theorem 2 *Let μ_n be a sequence of measures in $\mathscr{M}$ and $\mu \in \mathscr{M}$. Then, the two following statements are equivalent:*

- $W_p^{a,b}(\mu_n, \mu) \to 0$;
- $\mu_n \rightharpoonup \mu$ *and μ_n is a tight sequence (i.e., for each $\varepsilon > 0$ there exists a compact set K_ε such that $\mu_n(\mathbb{R}^d \setminus K_\varepsilon) < \varepsilon$ for all n).*

Proof See [39, Thm. 3].

5.2 The Mean-Field Limit for Mass-Varying Models

In this section, we write a measure dynamics with varying mass and prove that it is the mean-field limit of the microscopic model (18) introduced in Sect. 4.

Consider the following dynamics of measures with a transport and a source term:

$$\begin{cases} \partial_t \mu + \nabla \cdot (v[\mu]\, \mu) = h[\mu], \\ \mu_{|_{t=0}} = \mu_0. \end{cases} \tag{19}$$

We assume the following hypotheses about the functions v and s.
(H4) The function

$$v[\mu] : \begin{cases} \mathscr{M} \to C^1(\mathbb{R}^d) \cap L^\infty(\mathbb{R}^d) \\ \mu \mapsto v[\mu] \end{cases}$$

satisfies

- $v[\mu]$ is uniformly Lipschitz and uniformly bounded, i.e., there exist L, M not depending on μ, such that for all $\mu \in \mathscr{M}$ and $x, y \in \mathbb{R}^d$, it holds:

$$|v[\mu](x) - v[\mu](y)| \leq L|x - y| \qquad |v[\mu](x)| \leq M.$$

- v is a Lipschitz function, i.e., there exists N such that

$$\|v[\mu] - v[\nu]\|_{C^0} \leq N W_p^{a,b}(\mu, \nu).$$

(H5) The function

$$h[\mu] : \begin{cases} \mathscr{M} \to \mathscr{M} \\ \mu \mapsto h[\mu] \end{cases}$$

satisfies

- $h[\mu]$ has uniformly bounded mass and support, i.e., there exist P, R such that

$$h[\mu](\mathbb{R}^d) \leq P, \qquad \operatorname{supp}(h[\mu]) \subseteq B_R(0).$$

- h is a Lipschitz function, i.e., there exists Q such that

$$W_p^{a,b}(h[\mu], h[\nu]) \leq Q W_p^{a,b}(\mu, \nu).$$

Under such hypotheses, we proved in [39] the well-posedness of the Cauchy problem (19).

Theorem 3 *Assume that (H4)–(H5) hold true. Then, for each initial measure with finite mass and compact support $\mu_0 \in \mathscr{M}_c$, there exists a solution to (19). Moreover, given μ, ν, two solutions of (19) in $C([0, T], \mathscr{M}_c)$, we have*

$$W_p^{a,b}(\mu_t, \nu_t) \leq e^{2t(L+(|\mu_0|+tP)N+Q)} W_p^{a,b}(\mu_0, \nu_0).$$

In particular, if $\mu_0 = \nu_0$, then $\mu_t = \nu_t$ for all $t \in [0, T]$; thus, uniqueness of solutions holds true.

Proof See [39, Prop. 7 and Thm. 6].

Remark 2 As already stated, the application to pedestrian dynamics also explains the choice of the basic assumptions (H4)–(H5), namely, that we deal with measures with bounded support.

Recall now the definition of mean-field limit given in Sect. 3: given a microscopic model with the associated time-dependent empirical measures $\mu_N(t)$ and the macroscopic model with trajectories $\mu(t)$, it holds

$$\mu_N(0) \rightharpoonup_{N\to\infty} \mu(0) \qquad \Rightarrow \qquad \mu_N(t) \rightharpoonup_{N\to\infty} \mu(t) \quad \text{for all } t \geq 0.$$

In this definition, the fact that both $\mu_N(t)$ and $\mu(t)$ have masses varying in time plays no role. Moreover, we can apply the methods described in Sect. 3 in the particular case of $\mu_N(t)$ already being solutions of the macroscopic model. Then, one has that (19) is the mean-field limit of (18) if the following properties hold:

(MF-N): When the initial data μ^0 is an empirical measure μ_N^0 associated to an initial data $(X_N, M_N)^0$ of N particles, then the dynamics (19) rewrites as the ordinary differential equation (18);

(C): The solution $\mu(t)$ to (19) is continuous with respect to the initial data μ^0.

Property **(C)** holds in general for solutions to (19), according to Theorem 3. Then, we are left to find functionals $V[\mu], h[\mu]$ such that **(MF-N)** holds. It is straightforward to prove that the mean-field limit of (18) is then given by

$$V[\mu] = V_0 + V_1 \star \mu, \qquad h[\mu] = S_0\mu + S_1 \star \mu.$$

We end this section by presenting simulations of the mean-field limit of the two pedestrian models presented in Sect. 4. It describes the dynamics of a pedestrian crowd exiting a room. We refer to details of the dynamics for each agent to the

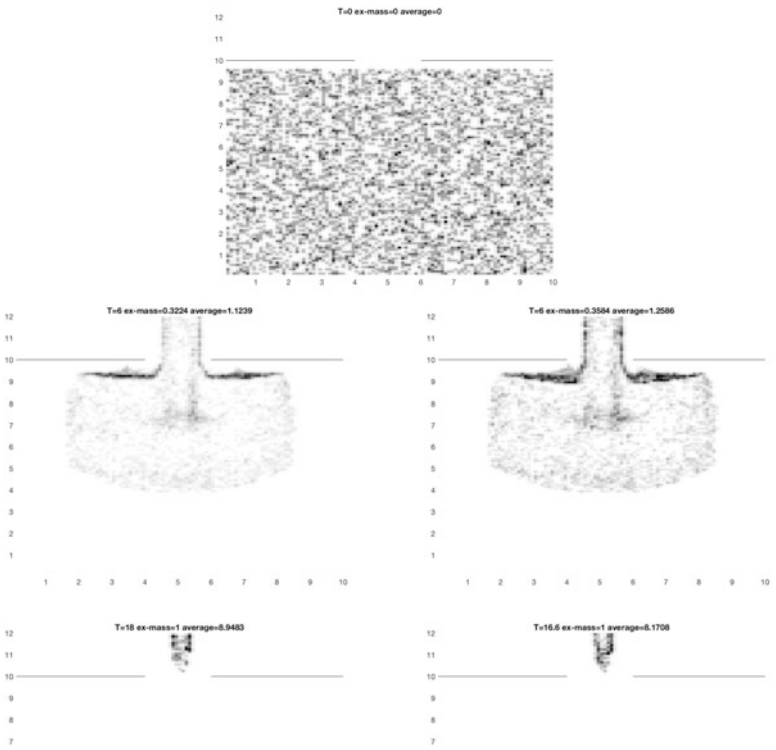

Fig. 4 Evolution of the mean-field model. Left: no mass reduction. Right: mass reduction

previous description. Here, we just recall that the mass (influence) of each agent can be treated in two different ways: either it is constant or it has an exponential decrease when the agent exits the room. Our simulations show that the average exit time can be reduced 8.7% in the second model. The maximal exit time is reduced of 8.1% in the second model.

We now show the dynamics of the mean-field limit of such two possible choices. The mathematical method used to numerically solve the nonlocal equation with or without mass reduction has been introduced and studied in [38, 40, 42]. In Fig. 4, the darker areas represent higher crowd density.

In Fig. 4 (left), we show three different times of the simulation with no variation of the mass: the initial random configuration of agents, then an intermediate time $T = 6$ in which concentration near the exit appears, and finally time $T = 18$ in which the whole crowd exits the room. The average exit time is 8.9 s.

In Fig. 4 (right), we show the simulation in which the mass decreases exponentially when an agent exits the door. The initial configuration coincides with the previous case. The simulation is then shown at two different times $T = 6$ and $T = 16.6$ in which the last agent exits the room. The average exit time is 8.2 s.

References

1. G. Albi, M. Bongini, F. Rossi, and F. Solombrino. Leader formation with mean-field birth and death models. in preparation.
2. G. Arechavaleta, J.-P. Laumond, H. Hicheur, and A. Berthoz. An optimality principle governing human walking. *IEEE Transactions on Robotics*, 24:5–14, 2008.
3. N. Bellomo and A. Bellouquid. On the modeling of crowd dynamics: Looking at the beautiful shapes of swarms. *Networks and Heterogeneous Media*, 6:383–399, 2011.
4. N. Bellomo, D. Clarke, L. Gibelli, P. Townsend, and B. Vreugdenhil. Human behaviours in evacuation crowd dynamics: From modelling to big data toward crisis management. *Physics of Life Reviews*, 18:1–21, 2016.
5. N. Bellomo, B. Piccoli, and A. Tosin. Modeling crowd dynamics from a complex system viewpoint. *Mathematical models and methods in applied sciences*, 22(supp02):1230004, 2012.
6. N. Bellomo and C. Dogbe. On the modeling of traffic and crowds: a survey of models, speculations, and perspectives. *SIAM Rev.*, 53(3):409–463, 2011.
7. N. Bellomo and L. Gibelli. Toward a mathematical theory of behavioral-social dynamics for pedestrian crowds. *Mathematical Models and Methods in Applied Sciences*, 25(13):2417–2437, 2015.
8. M. Bongini, M. Fornasier, F. Rossi, and F. Solombrino. Mean-Field Pontryagin Maximum Principle. *Journal of Optimization Theory and Applications*, 175(1):1–38, 2017.
9. S. Camazine, J. Deneubourg, N. Franks, J. Sneyd, G. Theraulaz, and E. Bonabeau. Self organization in biological systems. *Princeton University Press*, 2003.
10. M. Caponigro, B. Piccoli, F. Rossi, and E. Trélat. Mean-field sparse Jurdjevic-Quinn control. *M3AS: Math. Models Meth. Appl. Sc.*, 27(7):1223–1253, 2017.
11. J. A. Carrillo, M. Di Francesco, A. Figalli, T. Laurent, and D. Slepčev. Global-in-time weak measure solutions and finite-time aggregation for nonlocal interaction equations. *Duke Math. J.*, 156(2):229–271, 02 2011.

12. J. A. Carrillo, M. Fornasier, G. Toscani, and F. Vecil. *Mathematical Modeling of Collective Behavior in Socio-Economic and Life Sciences*, chapter Particle, kinetic, and hydrodynamic models of swarming, pages 297–336. Birkhäuser Boston, Boston, 2010.
13. C. Cercignani, R. Illner, and M. Pulvirenti. *The mathematical theory of dilute gases*, volume 106 of *Applied Mathematical Sciences*. Springer-Verlag, New York, 1994.
14. Y. Chitour, F. Jean, and P. Mason. Optimal control models of goal-oriented human locomotion. *SIAM Journal on Control and Optimization*, 50(1):147–170, 2012.
15. L. Chizat, G. Peyré, B. Schmitzer, and F.-X. Vialard. An interpolating distance between optimal transport and Fisher–Rao metrics. *Foundations of Computational Mathematics*, 18(1):1–44, 2018.
16. E. Cristiani, P. Frasca, and B. Piccoli. Effects of anisotropic interactions on the structure of animal groups. *Journal of mathematical biology*, 62(4):569–588, 2011.
17. E. Cristiani, B. Piccoli, and A. Tosin. Multiscale modeling of granular flows with application to crowd dynamics. *Multiscale Model. Simul.*, 9(1):155–182, 2011.
18. F. Cucker and S. Smale. Emergent behavior in flocks. *IEEE Trans. Automat. Control*, 52(5):852–862, 2007.
19. G. Di Marzo Serugendo, M.-P. Gleizes, and A. Karageorgos. Self-organization in multi-agent systems. *The Knowledge Engineering Review*, 20(2):165–189, 2005.
20. B. Düring, P. Markowich, J.-F. Pietschmann, and M.-T. Wolfram. Boltzmann and Fokker–Planck equations modelling opinion formation in the presence of strong leaders. In *Proceedings of the Royal Society of London A: Mathematical, Physical and Engineering Sciences*, page rspa20090239. The Royal Society, 2009.
21. L. C. Evans and R. F. Gariepy. *Measure theory and fine properties of functions*. CRC press, 1991.
22. F. Farina, D. Fontanelli, A. Garulli, A. Giannitrapani, and D. Prattichizzo. When Helbing meets Laumond: The Headed Social Force Model. In *2016 IEEE 55th Conference on Decision and Control (CDC)*, pages 3548–3553, Dec 2016.
23. I. Giardina. Collective behavior in animal groups: theoretical models and empirical studies. *Human Frontier Science Program Journal*, (205–219), 2008.
24. P. Glensdorf and I. Prigozhin. *Thermodynamic Theory of Structure, Stability and Fluctuations*. Wiley Interscience, 1971.
25. S.-Y. Ha and E. Tadmor. From particle to kinetic and hydrodynamic descriptions of flocking. *Kinetic & Related Models*, 1(3):415–435, 2008.
26. J. Haskovec. Flocking dynamics and mean-field limit in the Cucker–Smale-type model with topological interactions. *Physica D: Nonlinear Phenomena*, 261:42–51, 2013.
27. D. Helbing and P. Molnár. Social force model for pedestrian dynamics. *Physical Review E*, 51(5):4282–4286, 1995.
28. S. Kondratyev, L. Monsaingeon, and D. Vorotnikov. A new optimal transport distance on the space of finite Radon measures. *Adv. Differential Equations*, 21(11-12):1117–1164, 2016.
29. P. Krugman. *The Self Organizing Economy*. Blackwell Publisher, 1995.
30. J. Lehn. Supramolecular chemistry—scope and perspectives molecules, supermolecules, and molecular devices (nobel lecture). *Angewandte Chemie International Edition in English*, 27(1):89–112, 1988.
31. K. Lewin. *Field Theory in Social Science*. Harper & Brothers, 1951.
32. M. Liero, A. Mielke, and G. Savaré. Optimal transport in competition with reaction: the Hellinger-Kantorovich distance and geodesic curves. *SIAM J. Math. Anal.*, 48(4):2869–2911, 2016.
33. B. Maury and J. Venel. A discrete contact model for crowd motion. *ESAIM: Mathematical Modelling and Numerical Analysis*, 45(1):145–168, 2011.
34. A. Muntean, J. Rademacher, and A. Zagaris. *Macroscopic and large scale phenomena: coarse graining, mean field limits and ergodicity*. Springer, 2016.
35. H. Neunzert. An introduction to the nonlinear Boltzmann-Vlasov equation. In C. Cercignani, editor, *Kinetic Theories and the Boltzmann Equation*, pages 60–110, Berlin, Heidelberg, 1984. Springer Berlin Heidelberg.

36. L. Pallottino, V. Scordio, E. Frazzoli, and A. Bicchi. Decentralized cooperative policy for conflict resolution in multivehicle systems. *IEEE Transactions on Robotics*, 23(6):1170–1183, 1998.
37. L. Perea, P. Elosegui, and G. Gómez. Extension of the Cucker-Smale Control Law to Space Flight Formations. *Journal of Guidance, Control, and Dynamics*, 32:527–537, 2009.
38. B. Piccoli and F. Rossi. Transport equation with nonlocal velocity in Wasserstein spaces: convergence of numerical schemes. *Acta Appl. Math.*, 124:73–105, 2013.
39. B. Piccoli and F. Rossi. Generalized Wasserstein distance and its application to transport equations with source. *Arch. Ration. Mech. Anal.*, 211(1):335–358, 2014.
40. B. Piccoli and F. Rossi. On properties of the generalized Wasserstein distance. *Arch. Ration. Mech. Anal.*, 222(3):1339–1365, 2016.
41. B. Piccoli, F. Rossi, and M. Tournus. A norm for signed measures. Application to non local transport equation with source term. preprint, hal-01665244, Dec 2017.
42. B. Piccoli and A. Tosin. Time-evolving measures and macroscopic modeling of pedestrian flow. *Archive for Rational Mechanics and Analysis*, 199(3):707–738, 2011.
43. S. T. Rachev. *Probability metrics and the stability of stochastic models*, volume 269. John Wiley & Son Ltd, 1991.
44. C. Tomlin, G. Pappas, and S. Sastry. Conflict resolution for air traffic management: A study in multiagent hybrid systems. *IEEE Transactions on automatic control*, 43(4):509–521, 1998.
45. C. Villani. *Topics in optimal transportation*, volume 58 of *Graduate Studies in Mathematics*. American Mathematical Society, Providence, RI, 2003.
46. N. Wiener. *The Mathematics of Self-Organising Systems. Recent Developments in Information and Decision Processes*. Macmillan, 1962.

Numerical Methods for Mean-Field and Moment Models for Pedestrian Flow

Raul Borsche, Axel Klar, and Florian Schneider

Abstract Pedestrian flow modelling has attracted the interest of a large number of scientists from different research fields, as well as planners and designers. While planning the architecture of buildings, one might be interested in the pedestrian flow around their intended design so that shops, entrances, corridors, emergency exits and seating can be placed at the best locations. Pedestrian models are helpful in improving efficiency and safety in public places such as airport terminals, train stations, theatres and shopping malls. They are not only used as a tool for understanding pedestrian dynamics at public places but also support transportation planners or managers to design timetables.

1 Introduction

Pedestrian flow modelling has attracted the interest of a large number of scientists from different research fields, as well as planners and designers. While planning the architecture of buildings, one might be interested in the pedestrian flow around their intended design so that shops, entrances, corridors, emergency exits and seating can be placed at the best locations. Pedestrian models are helpful in improving efficiency and safety in public places such as airport terminals, train stations, theatres and shopping malls. They are not only used as a tool for understanding pedestrian dynamics at public places but also support transportation planners or managers to design timetables.

A large number of models for pedestrian flow have appeared on different levels of description in recent years. Microscopic (individual-based) level models building on Newton-type equations as well as vision-based or cellular automata and agent-based models have been developed (see Refs. [21, 34, 35, 50, 53, 56, 64]). Hydrodynamic

R. Borsche · A. Klar · F. Schneider (✉)
TU Kaiserslautern, Kaiserslautern, Germany
e-mail: borsche@mathematik.uni-kl.de; klar@mathematik.uni-kl.de; schneider@mathematik.uni-kl.de

L. Gibelli, N. Bellomo (eds.), *Crowd Dynamics, Volume 1*, Modeling and Simulation in Science, Engineering and Technology,
https://doi.org/10.1007/978-3-030-05129-7_7

pedestrian flow involving equations for density and mean velocity of the flow is derived in Refs. [5, 32]. Modelling of pedestrian flow with scalar conservation laws coupled to the solution of the eikonal equation has been presented and investigated in Refs. [1, 27, 36, 37]. Pros and cons of these models have been discussed in various reviews; we refer to [3–5] for a detailed discussion of the different approaches.

The modelling of pedestrian behaviour in a real-world environment is a complex problem. For example, a majority of the people in a crowd is moving in groups, and social interactions can greatly influence the movement of the crowd. Most of the models mentioned above treat pedestrians as individual agents and neglect the group dynamics among them. The influence of group dynamics on the behaviour of pedestrians and the differences between people walking in groups or alone have been presented in several recent works. We refer to [40, 44, 53], where experimental studies as well as numerical experiments are presented.

In this review, we describe a procedure used for interacting particle systems, for example, in the description of coherent motion of animal groups such as schools of fish, flocks of birds or swarms of insects (see Ref. [12, 13, 30, 52]). We start from a classical microscopic social force model for pedestrians [35] and extend it with an optimal path computation as, for example, in Ref. [37]. Thus, additionally to the local interaction between pedestrians, a non-local term including a global knowledge of the physical setting is introduced. These equations are approximated using a scaling assumption (see Ref. [12]) and a mean-field equation with a convolution term derived from the local interaction in the microscopic model. Although this procedure is classical, it is different to the kinetic equations obtained, for example, in Refs. [5, 7, 33], where classical Boltzmann terms are used for the modelling on the kinetic level. Models on the microscopic level with constant speed are discussed as well. We refer to Ref. [21] for a model hierarchy based on a microscopic constant speed model and a mean-field approach for the so-called heuristic behavioural individual-based model.

Determining the balance equation for density and momentum for the mean-field model and closing the equations with a suitable closure distribution leads to macroscopic equations for the density and mean velocity; compare Ref. [12] for the case of swarming models. The hydrodynamic equations obtained here still contain a non-local interaction term due to the derivation from the mean-field equations with non-local interaction terms. Finally, a quasi-static approximation of the momentum equation yields scalar limit equations with a non-local term and an eikonal equation as in Refs. [17–19] and [37, 38]. Additionally, we consider the case of fixed absolute values of the velocities, which means, in this case, all pedestrians are supposed to have the same fixed speed.

For the numerical simulations, we use meshfree particle methods and finite-volume methods on the different level of the model hierarchy.

In case of the macroscopic equations, particle methods are based on a Lagrangian formulation of these equations. We describe a method which can be viewed as a numerical transition between a discrete-element-type method (DEM) for microscopic interacting particle systems and a meshfree particle method for macroscopic equations. For related approaches we refer to [66]. In macroscopic mean-field

models, an interaction term appears, which is derived from the microscopic interaction term. Usually, this term has the form of a convolution integral. The particle method approximates these convolution integrals in an appropriate way. Using a microscopically large number of macroscopic grid particles, the method is essentially equivalent to the microscopic approach. In contrast, for a small number of grid particles, compared to the interaction or smoothing radius R, one obtains a method which is consistent with the associated limit equation. For intermediate regimes one obtains with this procedure additional correction terms. One purpose of the numerical simulations based on particle methods is to numerically investigate the transition between situations where the number of pedestrians varies from small to large.

The second purpose of the numerical investigations is to compare the different models with each other. In particular, we concentrate on hyperbolic approximations of the constant speed models, namely, the maximum-entropy M_1 model [46] and its linearization, the P_1 model. These are classical approximation, e.g. in radiation transport equations (see [10, 29, 57] and references therein). Especially the maximum-entropy model performs well in many situations (see, e.g. [41]). Moreover, scalar, Hughes-type models [37] are considered. All these models are implemented using finite-volume schemes for the macroscopic and mean-field models and a Monte Carlo approach for the microscopic equation. We compare these models for different settings and a large range of parameters with particular consideration of the dependence of the results on the stochastic noise parameter.

In the following part of the review, we extend the mathematical models and include multigroup behaviour and the impact of group dynamics, addressing in particular larger groups in a pedestrian crowd, into the general set-up using a multiphase approach. The dependence of the solutions on the level of attraction between the group members is investigated and discussed. As a general result, we observe an increase in evacuation time by increasing the attraction between the group members.

Finally, we develop and investigate a coupling procedure to couple pedestrian and traffic flow simulations and describe the interaction of the two types of flows. We restrict ourselves to coupling scalar macroscopic models via their flux functions. The traffic density on the one hand influences the pedestrian velocity. On the other hand, the fundamental diagram for traffic is influenced by the pedestrian density. The numerical methods are based on a first-order approach and use a straightforward splitting method.

This review is based on material from the papers [9, 26, 43, 48, 51]. It is organized in the following way. In Sect. 2, the model hierarchy is presented. The section contains a description of microscopic, mean-field, hydrodynamic and scalar limit equations. Section 3 contains a description of the numerical method used for the simulation of our test cases of the following section. We shortly describe finite-volume and particle methods for the equations considered in Sect. 2. Section 4 contains the numerical results for a variety of different test cases and a comparison of the different models. In Sect. 5 a hierarchy of multigroup pedestrian models is presented. A comparison of the solutions of the equations is presented for different

parameters together with a comparison of the associated evacuation times. In Sect. 6 macroscopic traffic flow model on a network is coupled to the pedestrian flow model. The section contains a description of the coupling procedure and shows numerical results. Section 7 contains the conclusions.

2 Pedestrian Flow Models

2.1 A Microscopic Social Force Model with Optimal Path Computation

We consider as in [26] a microscopic social force model for pedestrian flow including an optimal path computation. It is developed by coupling the classical social force models [32, 35] with an optimal path computation as in the Hughes approach to pedestrian flow (see Ref. [37]). Moreover, an Ornstein-Uhlenbeck-type stochastic process is added. We obtain a two-dimensional interacting particle system with locations $x_i \in \mathbb{R}^2$, $i = 1, \dots, N$ and velocity $v_i \in \mathbb{R}^2$. The equations of motion are

$$\begin{cases} dx_i = v_i dt, \\ dv_i = \sum_{i \neq j} F(x_i - x_j)dt + G(x_i, v_i, \rho_i^N)dt - \frac{A^2}{2} v_i dt + A dW_t^{(i)}, \end{cases} \tag{1}$$

where $W_t^{(i)}$ are independent Brownian motions in $\mathbb{R}^2$ and $A \geq 0$ is a constant.

The desired velocity and direction acceleration is given by

$$G(x, v, \rho) = \frac{1}{T}\left(-V(\rho)\frac{\nabla \Phi(x)}{\|\nabla \Phi(x)\|} - v\right), \tag{2}$$

where ρ is given by a regularized version of the empirical measure

$$\rho^N(x) = \frac{1}{N}\sum_{j=1}^{N} \delta_S(x - x_j),$$

and $\rho_i^N = \rho^N(x_i)$. Here δ_S is a smoothed version of the δ-distribution around 0 with

$$\int \delta_S(x)dx = 1,$$

which we define later. Φ is given by the solution of the eikonal equation

$$V(\rho^N(x))\|\nabla\Phi\| - 1 = 0.$$

V is a density-dependent velocity function, $V : [0, 1] \to [0, V_{\max}]$.

T denotes a reaction time, which might depend also on the density ρ. The interaction force is given by

$$F(x) = -\nabla_x U(\|x\|),$$

where U is an interaction potential given, for example, by

$$U = U_R = C_R\,(R - \|x\|)^2\,, \tag{3}$$

for $\|x\| < R$ and 0 otherwise. C_R is chosen such that

$$\int U(x)dx = D > 0.$$

Here R denotes the radius of interaction of the pedestrians. The above potential is a purely repelling potential. For extensions, see Sect. 5. This force can be complemented by dissipative forces; compare, e.g. Ref. [35].

Boundary conditions for system (1) are realized using nonmoving boundary particles with the same interaction force as for the interior particles. The boundary conditions for the eikonal equation, i.e. boundary conditions for Φ, are chosen as

$$\Phi(x) = 0,\ x \in \partial\Omega_D \quad \text{and} \quad \Phi(x) = \infty,\ x \in \partial\Omega \setminus \partial\Omega_D,$$

where Ω_D denotes the desired location of the pedestrians.

Remark 1 A model with constant speed, i.e. with constant norm of the velocities, might be a more appropriate way to describe the actual movement of pedestrians; compare [21]. It is easily constructed in the following way. We define $v = c\tau$ with $\tau = (\cos(\alpha), \sin(\alpha)) \in S^1$ and assume that $c > 0$ is constant. Then using $d\tau = \tau^{\perp} d\alpha$, we obtain the equations

$$\begin{cases} dx_i = c\tau_i\,dt, \\ cd\alpha_i = \displaystyle\sum_{i\neq j} \tau_i^{\perp} \cdot F(x_i - x_j)dt - \frac{V(\rho_i^N)}{T\|\nabla\Phi(x_i)\|}\tau_i^{\perp} \cdot \nabla\Phi(x_i)dt + A\,dW_t^{(i)}, \end{cases} \tag{4}$$

where $W_t^{(i)}$ are independent Brownian motions in $\mathbb{R}$. Compare Refs. [13, 23] for constant speed models in a biological context. In this model the direction of the pedestrians is changed according to the projection of the direction given by the gradient of the potential ϕ determined from the eikonal equation and the projection of the interaction force onto the orthogonal direction of the motion. An individual-based model with constant speed and the inclusion of a desired direction into an interaction potential can be found in Ref. [21].

Remark 2 Finite size effects with a minimal radius around a pedestrian could be included using interaction potentials with a singularity. Other variants are given by an elliptical interaction force [34] or by a force including the human vision cone [21].

Remark 3 In the definition of the acceleration towards the desired direction, the speed with which the pedestrians are moving depends on the density around a pedestrian. In certain situations this could lead to non-physical effects, for example, if the pedestrian is approached from behind. A determination of the density including a such a vision cone could be used here at the expense of a more complicated model.

Remark 4 A further remark on the above microscopic model concerns the role of the interactions between the pedestrians. Interactions are not only modelled by the interaction potential U but also by the Hughes-type term (2). The motivation for the present way of modelling is a distinction between a short-scale interaction of the pedestrians in direct encounter (described by the interaction potential U) and a reaction of the pedestrian on the global density ρ via the solution of the eikonal equation as in the Hughes approach. In the present model, as in the Hughes model, a knowledge of the density in the whole domain is assumed for this second kind of interaction. This could be changed to certain subregions of the computational domain by restricting the solution of the eikonal equation to these regions.

2.2 Mean Field and Macroscopic Limits

Using the so-called 'weak coupling scaling' assumption [58], one rescales the interaction potential with the factor $\frac{1}{N}$ where N denotes the total number of particles. Neglecting the stochastic force, our scaled microscopic model reads

$$\begin{cases} \dfrac{dx_i}{dt} = v_i, \\ \dfrac{dv_i}{dt} = \dfrac{1}{N} \displaystyle\sum_{i \neq j} F(x_i - x_j) + G(x_i, v_i, \rho_i^N). \end{cases} \tag{5}$$

For N tending to infinity, one can derive the associated mean-field equation in the limit of a large number of particles [11, 12, 58]

$$\partial_t f + v \cdot \nabla_x f + Sf = 0 \tag{6}$$

with force term

$$Sf = \nabla_v \cdot (G(x, v, \delta_S \star \rho(x)) f(x, v)) + \nabla_v \cdot (F \star \rho(x) f(x, v)),$$

where

$$F \star \rho\,(x) = \int F(x-y)\rho(y)dy, \quad \rho(x,t) := \int f(x,v,t)dv.$$

Adding the stochastic force gives an additional diffusion term on the right hand side, i.e.

$$\partial_t f + v \cdot \nabla_x f + Sf = Lf \tag{7}$$

with

$$Lf = \frac{A^2}{2}\nabla_v \cdot (vf + \nabla_v f)\,.$$

Remark 5 In case of constant speed c, the mean-field equation reads

$$\partial_t f + c\tau \cdot \nabla_x f + S_\alpha f = L_\alpha f \tag{8}$$

with force term

$$S_\alpha f = -\partial_\alpha \left(\frac{V(\delta_S \star \rho(x))}{cT} \tau^\perp \cdot \frac{\nabla \Phi(x)}{\|\nabla \Phi(x)\|} f \right) + \frac{1}{c}\partial_\alpha \left(\tau^\perp \cdot F \star \rho f \right)$$

and diffusion term

$$L_\alpha f = \frac{A^2}{2c^2}\partial_{\alpha\alpha} f.$$

Moreover, we define the momentum by

$$\rho u(x,t) := \int v f(x,v,t)dv.$$

Let us mention that the rigorous passage from microscopic particle systems towards the kinetic mean-field equation as $N \to \infty$ has been treated, for example, in Ref. [11] or Ref. [58] for the deterministic and stochastic cases.

Hydrodynamic limits for similar equations have been derived in Refs. [12, 16]. We consider the mean-field equation (7) and derive different limit equations. Integrating against dv and $v\,dv$ gives the continuity equation

$$\partial_t \rho + \nabla_x \cdot (\rho u) = 0 \tag{9}$$

and the momentum equation

$$\partial_t u + u \cdot \nabla_x u + \frac{1}{\rho}\nabla_x \int (v-u) \otimes (v-u) f(x,v) dv \tag{10}$$
$$= \frac{1}{\rho} \int G(x, v, \delta_S \star \rho) f(x,v) dv + F \star \rho - A^2 u.$$

Considering an equation without diffusion, i.e. neglecting fluctuations by setting $A = 0$, a suitable moment closure approach could be to use a monokinetic closure

$$f \sim \rho(x)\delta(v - u(x)).$$

This has been used, for example, in [12]. It will yield a suitable approximation of the kinetic solution in case the kinetic distribution function is peaked around its mean value. One obtains

$$\partial_t u + (u \cdot \nabla_x)u = G(x, u, \delta_S \star \rho) + F \star \rho \tag{11}$$

with

$$G(x, u, \rho) = \frac{1}{T}\left(-V(\rho(x))\frac{\nabla \Phi(x)}{\|\nabla \Phi(x)\|} - u\right).$$

This is coupled to

$$V(\delta_S \star \rho(x))\|\nabla \Phi(x)\| = 1. \tag{12}$$

Using other functions to close the equation with $A \neq 0$ results in equations including a pressure term. One could, for example, use a density-dependent equilibrium distribution with a given finite second moment as closure function. If the second moment is equal to ρ, this leads to

$$\partial_t u + \frac{1}{\rho}\nabla_x \rho = G(x, u, \delta_S \star \rho) + F \star \rho - A^2 u. \tag{13}$$

Further second-order models can be found in Ref. [6].

Remark 6 For the model with constant speed considered in Remark 1, the balance equations read, after integrating the mean-field equation,

$$\partial_t \rho + \nabla_x \cdot (\rho u) = 0, \tag{14}$$

where $\rho = \int_0^{2\pi} f d\alpha$ and $u = c\int_0^{2\pi} \tau f d\alpha$. Integrating the mean-field equation against $c\tau d\tau$, one obtains

$$\partial_t(\rho u) + \nabla_x \cdot P + \frac{V(\delta_S \star \rho)}{T\|\nabla\phi\|} \int \tau^\perp \nabla\phi \cdot \tau^\perp f d\alpha$$
$$- \int \tau^\perp F \star \rho \cdot \tau^\perp f d\alpha = -\frac{A^2}{2c^2}\rho u$$

with

$$P = c^2 \int \tau \otimes \tau f d\alpha.$$

Using $\tau^\perp \otimes \tau^\perp = I - \tau \otimes \tau$, this simplifies to

$$\partial_t(\rho u) + \nabla_x \cdot P + \left(\rho I - \frac{1}{c^2}P\right)\left(\frac{V(\delta_S \star \rho)}{T\|\nabla\phi\|}\nabla\phi - F \star \rho\right) = -\frac{A^2}{2c^2}\rho u.$$

Considering again the case $A = 0$ and using the monokinetic closure $f \sim \rho\delta(\tau - u)$, one obtains

$$\partial_t u + (u \cdot \nabla_x)u + \left(I - \frac{1}{c^2}u \otimes u\right)\left(\frac{V(\rho)}{T\|\nabla\phi\|}\nabla\phi - F \star \rho\right) = 0.$$

Using for the case $A \neq 0$ a constant function $f \sim \frac{\rho}{2\pi}$ as closure gives

$$\partial_t u + \frac{1}{2\rho}\nabla_x \rho + \frac{1}{2}\left(\frac{V(\delta_S \star \rho)}{T\|\nabla\phi\|}\nabla\phi - F \star \rho\right) = -\frac{A^2}{2c^2}u. \tag{15}$$

In the case of constant speed, there are other classical choices for a closure function if $A \neq 0$, for example, a so-called maximum-entropy closure using a von Mises-Fisher distribution

$$f = a \exp(b \cdot \tau)$$

as closure function, where a and b are determined from ρ and u by the moment conditions on f. We refer to Refs. [20, 46] for the classical case of radiative transfer.

This yields

$$P = \rho D(u)$$

with

$$\rho = < a \exp(b \cdot \tau) >, \quad \rho u = c < a\tau \exp(b \cdot \tau) >,$$

$$u = u(b) = c\frac{<\tau \exp(b\cdot\tau)>}{<\exp(b\cdot\tau)>}, \quad D = D(u(b)) = c^2\frac{<\tau\otimes\tau \exp(b\cdot\tau)>}{<\exp(b\cdot\tau)>}.$$

D and u can be written explicitly as functions of b:

$$u = c\frac{I_1(|b|)}{|b|I_0(|b|)}b, \quad |u| = c\frac{I_1(|b|)}{I_0(|b|)},$$
$$D = c^2(1-\chi)\,\mathrm{Id} + c^2\frac{(2\chi-1)}{|b|^2}b\otimes b,$$
$$\chi = \frac{1}{2\pi\rho}\int\left(\tau\cdot\frac{b}{|b|}\right)^2 a\exp(b\cdot\tau)d\alpha = \frac{1}{2}\left(1+\frac{I_2(|b|)}{I_0(|b|)}\right),$$

where I_ν is the ν-th modified Bessel function of the first kind. One inverts the relation between $|u|$ and $|b|$ which can be proven to define a bijection. Then, one uses $|b|\,(|u|)$ in the definition of $\chi(|b|)$ to obtain $D(u)$. Together one obtains the model

$$\partial_t(\rho u) + \nabla_x\cdot(D(u)\rho) + \left(I - \frac{1}{c^2}D(u)\right)\left(\frac{V(\delta_S\star\rho)}{T\|\nabla\Phi\|}\nabla\phi - F\star\rho\right)\rho = -\frac{A^2}{2c^2}\rho u. \tag{16}$$

We note that for small u one obtains $D(u)\sim\frac{c^2}{2}I$. Using this in (16), one obtains again Eq. (15). Finally, we remark that similar closures for more sophisticated pedestrian flow models have been used in Ref. [21].

2.3 Scalar Macroscopic Models

In the following we reduce the hydrodynamic description deriving scalar models. We assume again an interaction potential depending only on x and neglect the dissipative forces. Starting from the hydrodynamic momentum equation (13), we neglect time changes in this equation and obtain an equation for u, which is then used to close the continuity equation. This procedure gives

$$\frac{1}{\rho}\nabla_x\rho + V(\delta_S\star\rho)\frac{\nabla\Phi(x)}{\|\nabla\Phi(x)\|} - TF\star\rho = -(1+A^2T)u.$$

The resulting scalar equation for ρ is, after rescaling time with $1/(1+A^2T)$,

$$\partial_t\rho - \nabla_x\left(V(\delta_S\star\rho(x))\frac{\nabla\Phi(x)}{\|\nabla\Phi(x)\|}\rho\right) + \nabla_x\left(T(F\star\rho)\rho\right) = T\Delta_x\rho. \tag{17}$$

Remark 7 For the model with constant speed, the same procedure gives a trivial velocity for the hydrodynamic model derived from the monokinetic closure. We thus use the constant closure function and obtain from the quasi-stationary momentum equation

$$\frac{1}{\rho}\nabla_x\rho + \frac{1}{2}\left(\frac{V(\delta_S\star\rho)}{T\|\nabla\phi\|}\nabla\phi - F\star\rho\right) = -\frac{A^2}{c^2}u. \tag{18}$$

Plugging this into the continuity equation, we obtain, after rescaling the time with $c^2/(TA^2)$,

$$\partial_t \rho - \nabla_x \left(V(\delta_S \star \rho(x)) \frac{\nabla \Phi(x)}{\|\nabla \Phi(x)\|} \rho \right) + \nabla_x \left(T(F \star \rho)\rho \right) = c^2 T \Delta_x \rho. \quad (19)$$

This is the same equation as before up to a scaling of the diffusion term.

Remark 8 To derive an associated local equation, we write the force F as a gradient field with $F = -\nabla U$. Assuming that we are in a dense situation, we approximate the potential U by

$$U(y) \sim D\delta(y)$$

where the constant $D > 0$ is given by

$$D = \int U(y) dy.$$

The symmetry of the convolution

$$\int \nabla_x U(x-y)\rho(y)dy = -\int \nabla_y U(x-y)\rho(y)dy = \int U(x-y)\nabla_y \rho dy$$

and the above localization gives

$$F \star \rho = -\int U(x-y)\nabla_y \rho dy \sim -D\nabla_x \rho.$$

Neglecting inertia effects and assuming additionally $\delta_S \to \delta$, we obtain

$$\partial_t \rho - \nabla_x (V(\rho(x)) \frac{\nabla \Phi(x)}{\|\nabla \Phi(x)\|} \rho) = DT \nabla_x (\rho \nabla \rho). \quad (20)$$

This is combined with the eikonal equation

$$V(\rho(x))\|\nabla \Phi(x)\| = 1. \quad (21)$$

Thus, we have obtained a diffusive version of the Hughes equation (see Ref. [37]).

Remark 9 We note that (19) is similar to an equation considered in Refs. [17, 18]. There the equation

$$\partial_t \rho - \nabla_x \left(V(\rho(x)) \frac{\nabla \Phi(x)}{\|\nabla \Phi(x)\|} \rho \right) + \epsilon \nabla_x \left(U(\rho) \frac{\nabla \eta \star \rho}{\sqrt{1 + \|\nabla \eta \star \rho\|^2}} \rho \right) = 0 \quad (22)$$

has been considered, where Φ is the solution of the homogeneous eikonal equation and η is a mollifier. This is equivalent to (19) if η is identified with V and

$$T(\rho) = \frac{\epsilon U(\rho)}{\sqrt{1 + \|\nabla \eta \star \rho\|^2}}.$$

Remark 10 Starting from the hydrodynamic equation (11), a similar procedure as above gives

$$\partial_t u + (u \cdot \nabla_x) u = G(x, u, \rho) - D \nabla_x \rho. \tag{23}$$

We conclude this section by summarizing the models and connections between the models discussed in this review in Fig. 1.

3 Numerical Methods

In this section the numerical methods used in Sect. 4 are discussed. We use a particle method for Eqs. (11) and (23) and the scalar versions (17) and (20). A classical finite-volume method is applied for the equations derived from the constant speed model (15), (16), (19) and their localized versions.

3.1 Macroscopic Flow Simulation Using Finite-Volume Methods

The HLL scheme [63] is used for the approximation of the hydrodynamic two-equation models. The scalar equations are approximated using the FORCE scheme (see again [63]). For the numerical evaluation of the macroscopic models, we have to consider boundary conditions, which are incorporated by adding additional ghost cells. The boundary of the computational domain Ω is divided into two parts, namely, the desired location (or the exit) $\partial\Omega_D$, where we prescribe outflow boundary conditions, while on $\partial\Omega \setminus \partial\Omega_D$ reflective boundary conditions are prescribed.

To efficiently solve the eikonal equation, we use a fast marching method (see [59]). It is based on two main ideas: use upwind schemes and a fast sorting method. We follow [54] to approximate $\|\nabla_x \Phi\|$ in (12) with an upwind scheme. Then, the solution is systematically constructed by solving downwind slopes (see [59]). We update the eikonal solution in every fifth time step in order to save computation time.

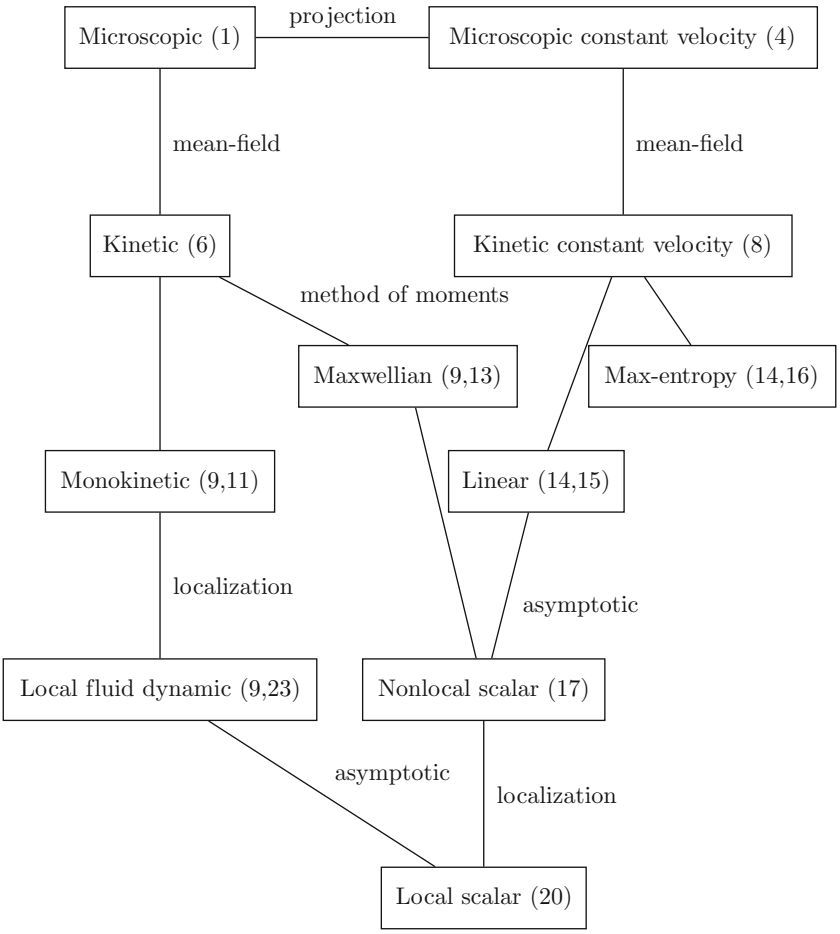

Fig. 1 Hierarchy of models with numbering of equations

3.2 Particle Methods for Macroscopic Equations

In this section, we discuss an alternative approach to the numerical solution of the macroscopic models using a particle method; see, for example, [8, 24, 25, 28, 42, 49, 60]. Mesh-less or particle methods are an appropriate way to solve pedestrian flow problems due to the appearance of situations with complicated geometries, free and moving boundaries and potentially large deformations of the domain of computation, i.e. the region where the density of pedestrians is non-zero. The particle method is based on a Lagrangian formulation of the hydrodynamic equations, compare [61, 62]. Consider, for example, (11). Then the Lagrangian formulation is

$$\frac{dx}{dt} = u$$
$$\frac{d\rho}{dt} = -\rho \nabla_x \cdot u$$
$$\frac{du}{dt} = G(x, u, \delta_S \star \rho) - \nabla_x U \star \rho,$$

where $\frac{d}{dt} = \partial_t + u \cdot \nabla_x$.

To discretize the quantities appearing on the right hand side of the above equations, mesh-free Lagrangian methods use a difference approximation at the particle locations from their surrounding neighbours using suitable weight functions and a least square approximation. For the present computation, we use weight functions w with compact support of radius h, in this way restricting the number of neighbouring particles. The Gaussian weight functions are of the form

$$w = w(x; h) = \begin{cases} \exp(-\alpha \frac{|x|^2}{h^2}), & \text{if } \frac{|x|}{h} \leq 1 \\ 0, & \text{else} \end{cases} \tag{24}$$

The radius h is chosen to initially include enough particles for a stable approximation of the equations, which is approximately three times the initial spacing of the particles. To efficiently perform the necessary computations, a particle management has to be implemented, such that particles are added or removed in case the local distribution of the particles becomes too rarefied or too dense, respectively. See [60] for details of the implementation.

The simplest way to evaluate the integral over the interaction potential is to use a straightforward 'microscopic' integration rule using an approximation of the local area (of the Voronoi cell V_j) around a particle at x_j, i.e. we use

$$F \star \rho(x_i) \sim \sum_{j=1, j\neq i}^{N} \rho_j |V_j| F(x_i - x_j). \tag{25}$$

This works fine for a well-resolved situation with a sufficiently large number of gridpoints. The resulting system of ODEs is then solved by a suitable low-order Runge-Kutta time discretization method. The above considerations show that if the number of macroscopic gridpoints is approximately equal to the (large) number of microscopic particles, then the macroscopic computations are essentially equivalent to a microscopic solution.

Boundary conditions are realized by using fixed boundary particles with a suitable interaction potential. We note that the time step of the computation has to be adapted to the strength of the boundary potential in order to obtain a stable method.

3.3 A Multi-scale Particle Method Based on the Mean-Field Approximation

A situation as described above with a number of macroscopic gridpoints approximately equal to the number of pedestrians does not require a special algorithm including any mean-field or macroscopic considerations. However, if the number of microscopic particles is very large, that does not mean that the number of macroscopic grid particles in the particle method has to be increased in the same way, since the grid particles only play the role of discretization points. The key point of the method for Eq. (11) (compare [42]) is to approximate the convolution integrals appearing in the above equations not by a simple Riemann sum, which would essentially lead to a microscopic computation, but by a higher-order approximation of the functions on the respective Voronoi cells (compare again [42]). This approach yields an accurate method for the limiting macroscopic equations (23) in the localized macroscopic limit, where the interaction radius R goes to 0 and U and δ_S are suitable approximations of the δ distribution, even if the number of macroscopic grid particles is still small compared to the number of pedestrians (microscopic particles).

In certain situations, this approach allows to use a much smaller amount of particles compared to the classical particle method. Correspondingly, the numerical effort, which is essentially determined by the number of particles in the computation, is thus reduced considerably. We refer to [42] for a thorough discussion of this issue and of the multi-scale numerical algorithm.

We note that our particle method for the hydrodynamic equations ranges from a 'nearly microscopic' solver to a purely macroscopic solver depending on the ratio of grid particles involved in the computation and the number of microscopic particles.

4 Numerical Results

4.1 Numerical Transition from Microscopic to Macroscopic Description

We investigate the non-local (11) and localized (23) hydrodynamic systems using the particle method. For further details on the method, see [42, 43]. We consider a configuration defined in Ref. [47]; compare also [26]. Pedestrians are initialized on the left of the domain $(x, y) \in [0, 100] \times [0, 50]$ and evacuated towards the exits on the right, $y \in [5, 20] \cup [30, 45]$. As initial value we choose

$$\rho(x) = \begin{cases} 1 & \text{if } x \in [0, 30] \times [0, 50], \\ 0 & \text{else.} \end{cases}$$

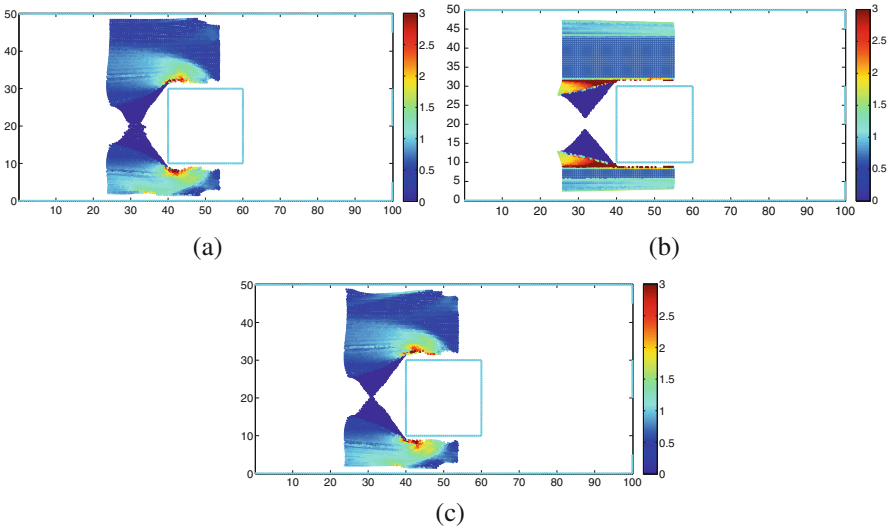

Fig. 2 Density plot determined from local limit equation (23) and non-local equations (11) with microscopic and multi-scale approximation at time $t = 12.5$ for $\Delta x = 0.5$, $R = 0.2$. (**a**) Localized. (**b**) Microscopic. (**c**) Multi-scale

In the centre of the computational domain, an obstacle is located at $[40, 60] \times [10, 30]$. For the eikonal equation, we use $\phi = 0$ on the two exits and $\phi = \infty$ on all walls, including the obstacle, as boundary conditions.

We choose the velocity V as $V(\rho(x)) = v_{\max}\left(1 - \frac{\rho(x)}{\rho_{\max}}\right)$ if $\rho < \rho_{\max}$ and 0 else, where the maximal velocity is $v_{\max} = 2$ and the maximal density $\rho_{\max} = 10$. We vary the initial average distance Δx between grid points from 0.15 to 1, i.e. the number of grid particles varies between 1440 and 61,800. Moreover, we choose the following parameter: $\gamma = 500, \alpha = 1000$. The interaction potential $U = U_R$ is chosen as in (3).

First we consider an underresolved situation with relatively small value $R = 0.2$ and $\Delta x = 0.5$, i.e. a number of particles of approximately $N = 5650$. In Fig. 2 we plot the solution of the localized and the non-local equation using the multi-scale method and the microscopic integration rule. In this case the solution computed via the multi-scale method and the one computed from the localized equation coincide well, whereas the microscopic method deviates strongly. In Fig. 3 we show a comparison of solutions obtained from the microscopic integration rule with decreasing discretization sizes, i.e. increasing number of particles.

Figure 4 considers a well-resolved case with $\Delta x = 0.2$ and $R = 0.4$. In this case we observe a good coincidence of the microscopic and multi-scale approximations (Fig. 5).

Finally, we show the error and the CPU times of the microscopic and the multi-scale method for different numbers of grid particles in Table 1 and Fig. 6. The errors are determined along the line with $y = 37$ and $x \in [25, 55]$. The relative $\mathscr{L}^2$-errors

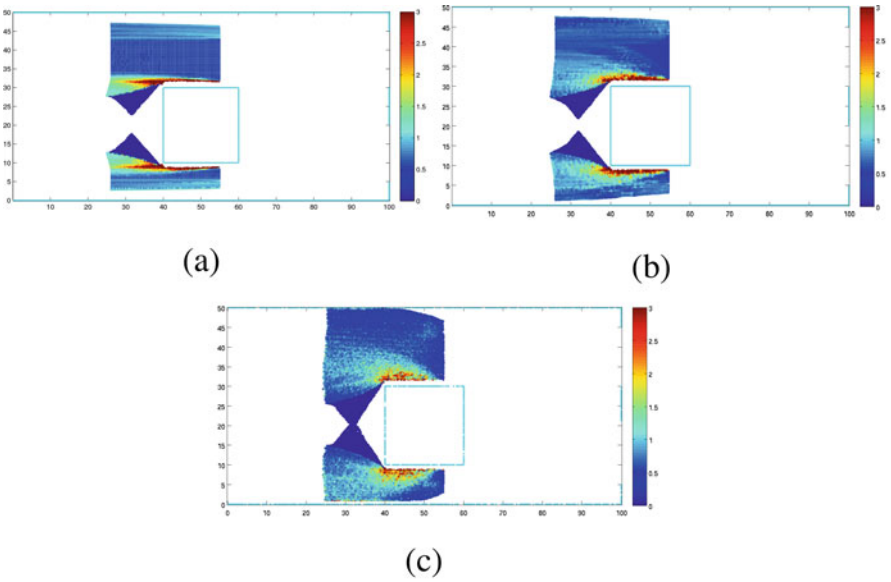

Fig. 3 Density plot determined from non-local equations (11) with microscopic approximation at time $t = 12.5$ for (**a**) $\Delta x = 0.4$, (**b**) $\Delta x = 0.3$ and (**c**) $\Delta x = 0.2$ for $R = 0.2$

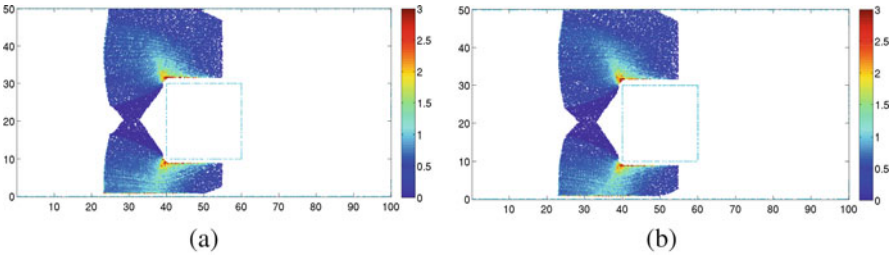

Fig. 4 Density plot determined from local limit equation (23) and non-local equations (11) with microscopic and multi-scale approximation at $t = 12,5$ for $\Delta x = 0.2$ and $R = 0.4$. (**a**) Microscopic. (**b**) Multi-scale

are given as well as the computation times in minutes. The reference solution is computed by using a spacing of $\Delta x = 0.15$ and approximately 62,000 particles. For this fine resolved case, the difference (relative $\mathscr{L}^2$-error) between microscopic integration and multi-scale solution is approximately equal to 10^{-2}. Looking at Table 1 and the multi-scale error with 1400 particles and the microscopic integration error with 35,200 particles, one observes a gain in computation time by more than an order of magnitude.

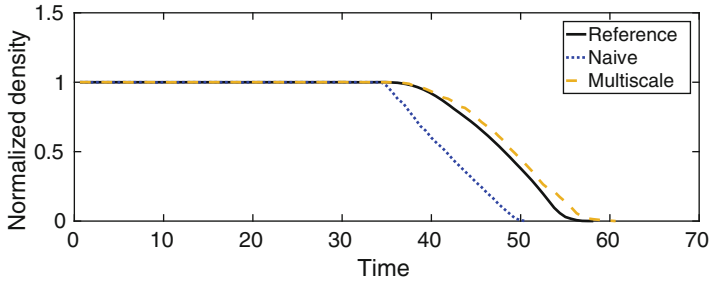

Fig. 5 Time development of the normalized total mass in the computational domain determined from the hydrodynamic pedestrian model (11) using microscopic and multi-scale approximation for fixed interaction radius $R = 0.2$ and coarse initial spacing $\Delta x = 1$ with $N = 1400$ grid particles. The reference solution is shown for comparison

Table 1 Comparison of CPU times between microscopic and multi-scale simulations of the hydrodynamic 2D equations. The error analysis is performed at time 12.5

Initial spacing	# particles	Micro error	Multi-scale error	CPU time
1	1400	0.54	0.14	8 min
0.5	5700	0.36	0.18	23 min
0.35	11,500	0.48	0.22	52 min
0.2	35,200	0.16	0.14	223 min

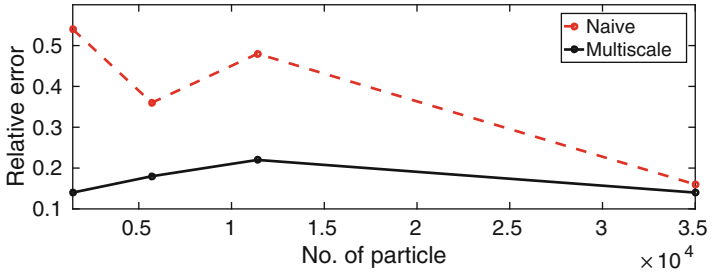

Fig. 6 Error plot for microscopic and multi-scale simulations

4.2 Numerical Comparison of Macroscopic Equations

In this section we present a series of numerical experiments for the constant speed microscopic (4), mesoscopic (8), hydrodynamic (15), (16) and scalar (19) models. For further details see [51]. Different situations are studied numerically using the finite-volume algorithm described above. We note that we compute the eikonal equation only in every sixth time step for all models. For the simulation of the microscopic model, we choose the number of pedestrians as $N = 60{,}000$. For all examples below, we use the same type of initial condition, namely, a Maxwellian in $\mathbb{R}^2$ with a covariance matrix $\sigma = \mathrm{diag}(\sigma_1, \sigma_2) \in \mathbb{R}^{2\times 2}$ and mean value $\mu \in \mathbb{R}^2$. The α variable is uniformly distributed.

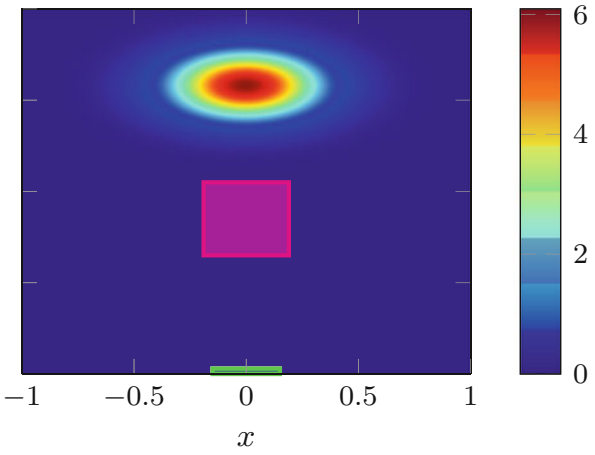

Fig. 7 Obstacle: initial density at $t = 0$

Test case 1: obstacle First we consider pedestrians who have to circumvent an obstacle to reach their destination. We choose the domain $\Omega = [-1, 1] \times [-1, 1]$, the destination $\partial\Omega_D = [-0.15, 0.15] \times \{0\}$ and the obstacle $\Omega_{\text{Obstacle}} = [-0.19, 0.19] \times [-0.35, 0.05]$. The grid size is given as $\Delta x = 0.02$. We use the same velocity function as in the last section, namely, $V(\rho(x)) = v_{\max}\left(1 - \frac{\rho(x)}{\rho_{\max}}\right)$ with $v_{\max}$, where we choose the parameters $\sigma = (0.22, 0.12)$, $\mu = (0, 0.058)$, $v_{\max} = 1.3$, $A = 4$ $T = 1/100$ $R = 1$ $\rho_{\max} = 20$.

Figures 7, 8 and 9 show the evolution of the densities computed with the microscopic model (4) in (a), the mesoscopic model (8) in (b), the nonlinear hydrodynamic model (16) in (c) and the scalar model (19) in (d) at different time steps. In all four models, the pedestrians separate to circumnavigate the obstacle and unite again to reach their destination after passing the obstacle. Despite the fact that all initial densities were positive, the density in the linear hydrodynamic model (15) becomes negative after some time in certain situations, and numerical instabilities arise. This is a well-known observation in radiative transfer; compare, for example, [41] and references therein. Therefore, we do not show the results of the model for this test case. As we can observe in the figures, the differences between the microscopic, mesoscopic and nonlinear hydrodynamic model are negligible compared to the huge difference to the scalar model, resulting from the relatively small value of the diffusion coefficient A.

To compare the behaviour for a larger range of values of A, we investigate the evacuation times for different values of A. The evacuation time is defined as the time instance when at least 94% of the initial density of the pedestrians have left the domain. In Fig. 10 the evacuation times are plotted with respect to the diffusion coefficient A for the microscopic, the mesoscopic, the maximum-entropy and the scalar model. One observes that the evacuation times of the microscopic, mesoscopic and M_1 models coincide very well in contrast to those determined from the scalar model. In particular, large differences can be observed for smaller values

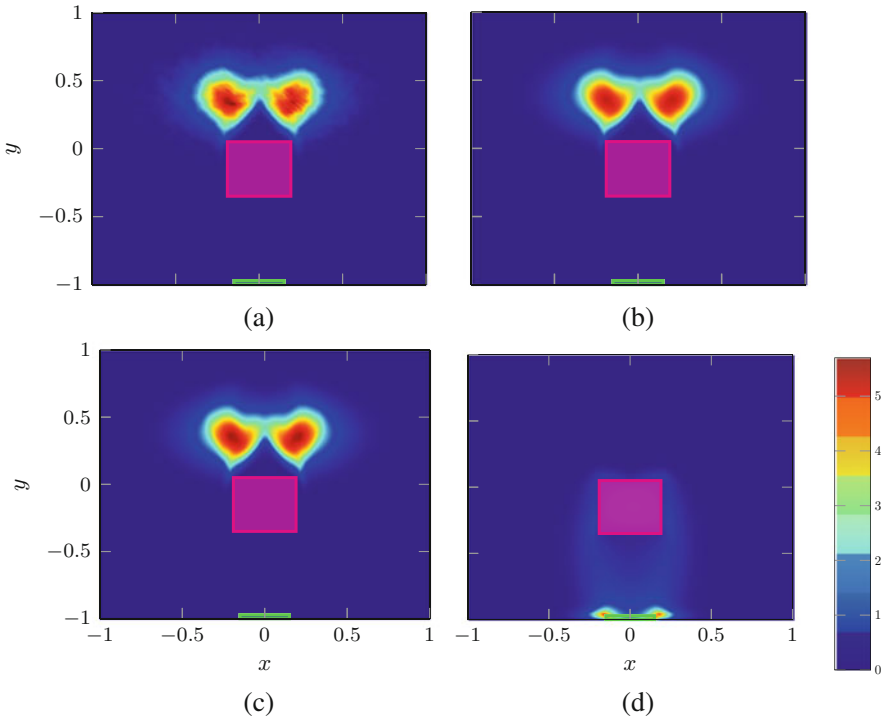

Fig. 8 Obstacle: densities at the point of time $t = 0.18$. (**a**) Micro. (**b**) Mean field. (**c**) M_1. (**d**) Scalar

of A. With increasing A, all the models coincide as expected, which is a result from the derivation of the scalar model and the parameters considered in the present example.

Test-case 2: crosswalks We consider an example where the pedestrians cross a road with two crosswalks and leave the domain through two exits. We choose $\Omega = [-1, 1] \times [-1, 1]$, the two destinations $\partial\Omega_{D1} = [-0.925, -0.675] \times \{0\}$ and $\partial\Omega_{D2} = [0.275, 0.875] \times \{0\}$, the street $S = [-1, 1] \times [-0.07, 0.05]$ and the crosswalks $C_1 = [-0.925, -0.125] \times [-0.07, 0.05]$ and $C_2 = [0.775, 0.875] \times [-0.07, 0.05]$. The grid size is given as $\Delta x = 0.02$, $\sigma = (0.2, 0.08)$, $\mu = (0, 0.6)$, $v_{\max} = 1.3$, $A = 18$, $T = 1/100$, $R = h$, $\rho_{\max} = 20$.

To model cars on the road, we choose the density of the cars as

$$\rho_{cars} = \begin{cases} 0.05 & \text{on the crosswalks,} \\ 18 & \text{on the street,} \\ 0 & \text{else} \end{cases}$$

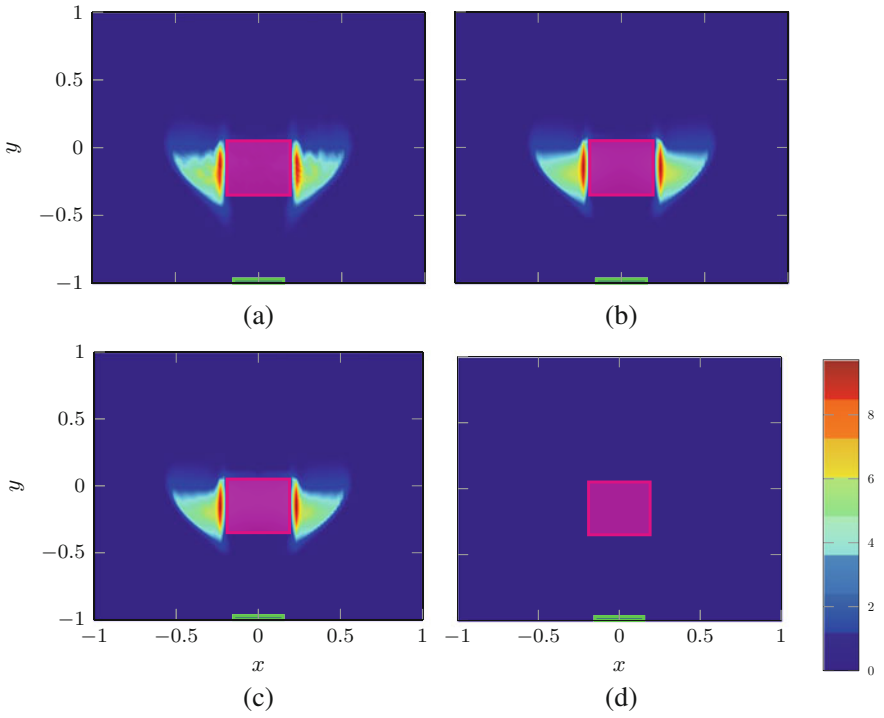

Fig. 9 Obstacle: densities at the point of time $t = 0.63$. (**a**) Micro. (**b**) Mean field. (**c**) M_1. (**d**) Scalar

Moreover, the velocity function is chosen as

$$V(\rho) = v_{\max}\left(1 - \frac{\rho_{\text{cars}}}{\rho_{\max}}\right)\left(1 - \frac{\rho}{\rho_{\max}}\right)$$

for $\rho(x) < \rho_{\max}$ and 0 else.

We show the time evolution of the densities of the microscopic model (4) in (a), the mesoscopic model (8) in (b), the nonlinear hydrodynamic model (16) in (c), the scalar model (19) in (d) and the linear hydrodynamic model 15 in (e) in Figs. 11, 12 and 13.

All models show a similar behaviour for the chosen set of parameters. This is to be expected due to the choice of $A = 18$, since in this case we are near to the diffusive/scalar limit.

In Fig. 14, we present the evacuation time in dependence of the parameter A. Again, for small A the evacuation time determined from the scalar model differs strongly from the microscopic, the mesoscopic and the hydrodynamic one. For large values of A, all simulations give similar results.

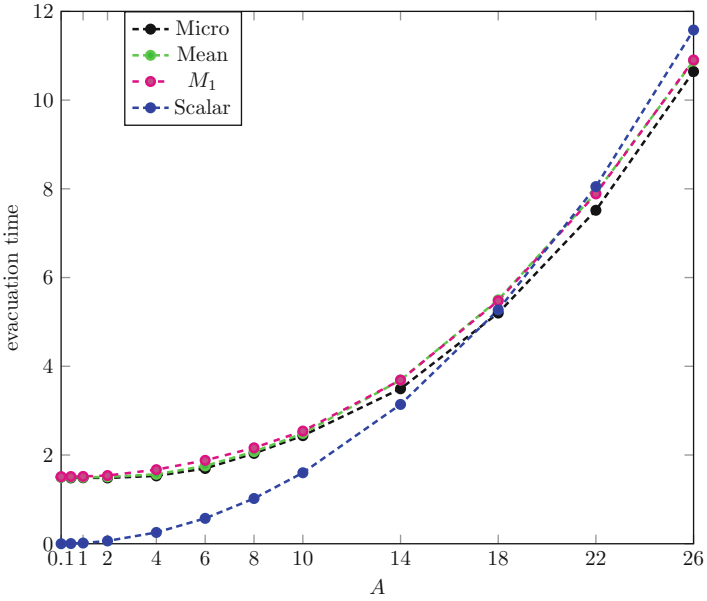

Fig. 10 The evacuation time in dependence of the parameter A for the microscopic, mesoscopic, maximum-entropy and scalar models with $T = 1/100$

Fig. 11 Crosswalks: initial density of microscopic, mesoscopic, scalar and macroscopic models. (**a**) Micro

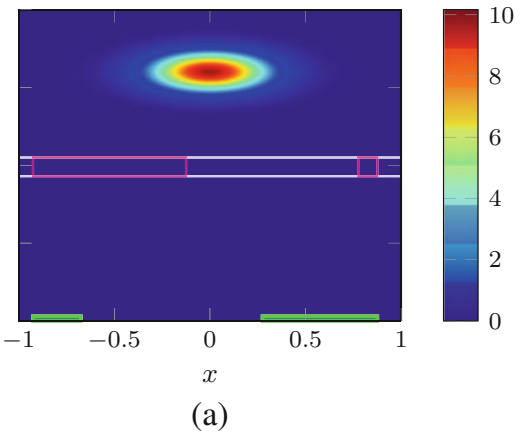

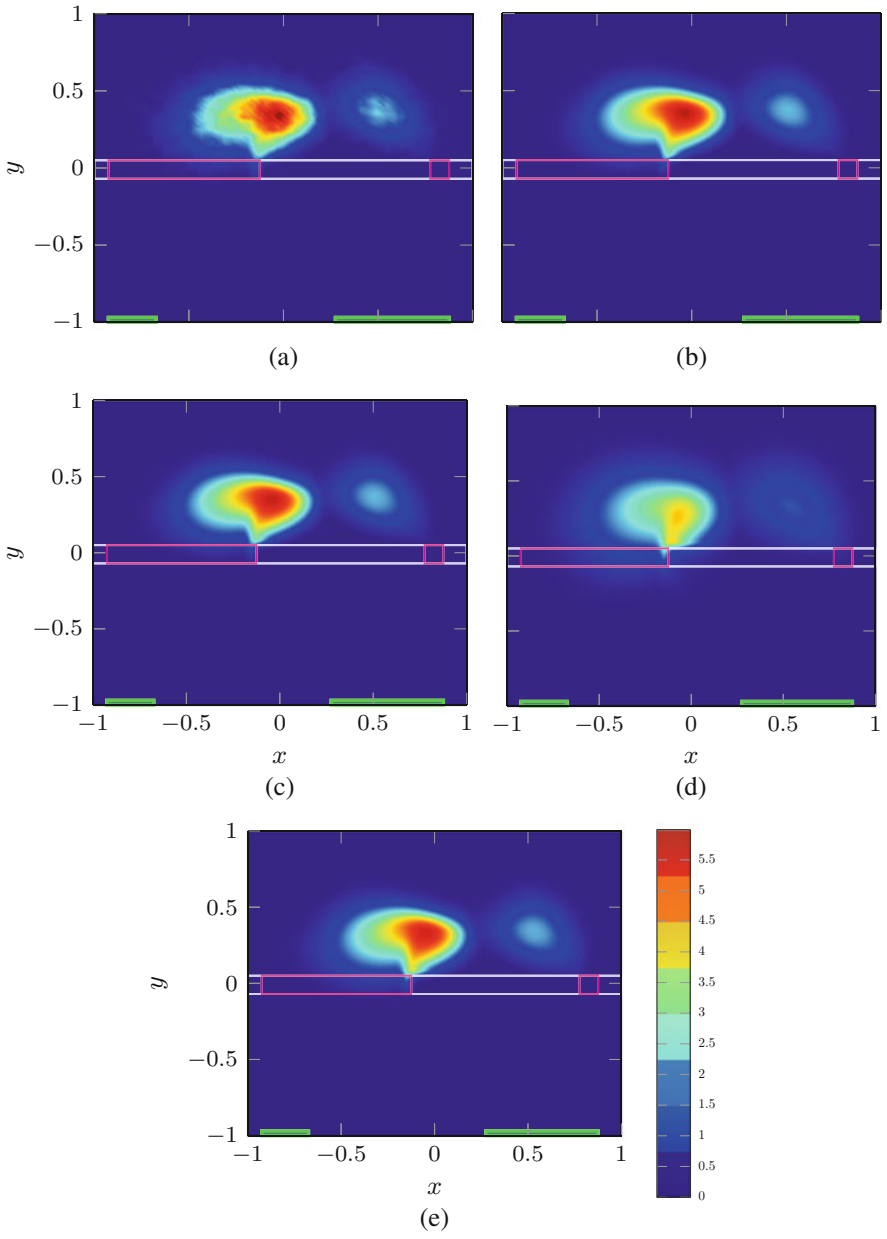

Fig. 12 Crosswalks: densities at the point of time $t = 0.6$. (**a**) Micro. (**b**) Mean field. (**c**) M_1. (**d**) Scalar. (**e**) P_1

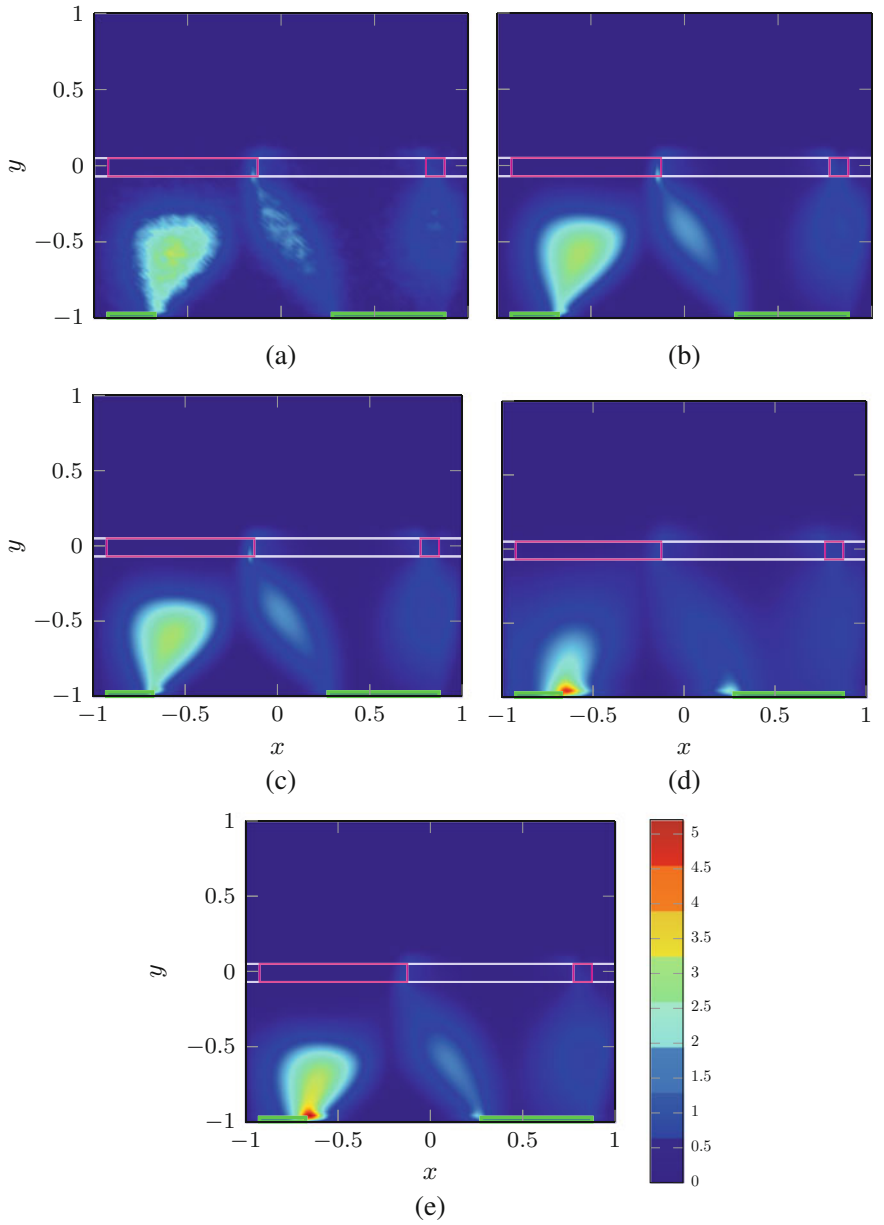

Fig. 13 Crosswalks: densities at the point of time $t = 2.42$. (**a**) Micro. (**b**) Mean field. (**c**) M_1. (**d**) Scalar. (**e**) P_1

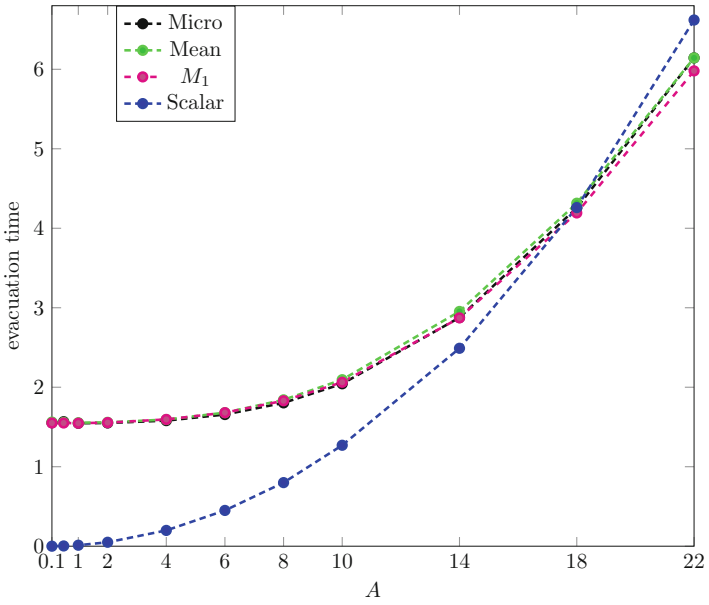

Fig. 14 The evacuation time in dependence of the parameter A for microscopic, mesoscopic, M_1 and scalar models with $T = 1/100$

5 Multigroup Traffic

In this section, we consider a multigroup microscopic model for pedestrian flow using a multigroup microscopic social force model including the solution of the eikonal equation (see [48]). We proceed by deriving multigroup hydrodynamic and scalar models from the microscopic model.

5.1 The Microscopic Multigroup Model

We consider a microscopic social force model for pedestrian flow including an optimal path computation. For references, see for example Refs. [34, 36]. For N pedestrians divided into M groups, we obtain an interacting particle system in two dimensions with locations $x_i^{(k)} \in \mathbb{R}^2$ and velocity $v_i^{(k)} \in \mathbb{R}^2$. Here, the index $i = 1, \ldots N$ is used to number all pedestrians; the index $k = 1, \ldots, M$ denotes the group to which the pedestrian belongs. $S^{(k)}$ denotes the set of all i which are in group k, and N_k denotes the number of pedestrians in group k with $N = \sum_{l=1}^{M} N_l$. The equations of motion are

$$\begin{aligned}\frac{dx_i^{(k)}}{dt} &= v_i^{(k)}\\ \frac{dv_i^{(k)}}{dt} &= -\sum_{l=1}^{M}\sum_{j\in S^{(l)}} \nabla_{x_i} U^{(k,l)}(\mid x_i^{(k)} - x_j^{(l)} \mid) + G^{(k)}(x_i^{(k)}, v_i^{(k)}, \rho^N(x_i^{(k)})),\end{aligned} \tag{26}$$

where $U^{(k,l)}$ is an interaction potential denoting the interaction between members of groups k and l. A common choice is the Morse potential (see [12]),

$$U^{(k,l)}(r) = -C_a e^{-r/l_a} + C_r e^{-r/l_r}. \tag{27}$$

Here, C_a, C_r are attractive and repulsive strengths and l_a, l_r are their respective length scales. These constants depend on the groups k and l under consideration. Similarly, one could use potentials given by polynomial or rational functions. An attractive interaction force acts only between members of the same group. The repulsive force acts between all pedestrians. The acceleration towards the desired direction is given by

$$G^{(k)}(x, v, \rho^N) = \frac{1}{T}\left(-V^{(k)}(\rho^N)\frac{\nabla\Phi^{(k)}(x)}{\|\nabla\Phi^{(k)}(x)\|} - v\right), \tag{28}$$

where ρ^N is given by

$$\rho^N(x) = \frac{1}{N}\sum_{l=1}^{M}\sum_{j\in S^{(l)}} \delta_S(x - x_j^{(l)}).$$

Finally, $\Phi^{(k)}$ is given by the solution of the eikonal equation

$$V^{(k)}(\rho^N(x))\|\nabla\Phi^{(k)}\| - 1 = 0.$$

$V^{(k)}$ is a density-dependent velocity function, $V^{(k)} : \mathbb{R}^+ \longrightarrow \mathbb{R}^+$, and T denotes a reaction time. Moreover, for the different groups, we denote

$$\rho^{N,(l)}(x) = \frac{1}{N}\sum_{j\in S^{(l)}} \delta_S(x - x_j^{(l)}),$$

such that $\rho^N(x) = \sum_{l=1}^{M} \rho^{N,(l)}(x)$.

Remark 11 The parameters in the above formulas, in particular in the definition of the interaction potential (27), give average distances between the particles, consistent with empirical data from social distance theory or proxemics (see [31, 39]).

Remark 12 In [53], an attractive interaction of the members of the group with the 'centre of mass' is postulated. This gives an additional term

$$\nabla_{x_i} U_{CM}^{(k)} \left(|x_i^{(k)} - \frac{1}{N_k} \sum_{j \in S^{(k)}} x_j^{(k)}| \right).$$

The different types of interaction rules will be compared numerically in the following.

5.2 The Multigroup Hydrodynamic Model

Deriving a multigroup mean-field equation and integrating it against dv and vdv, one obtains the continuity equation for group k

$$\partial_t \rho^{(k)} + \nabla_x \cdot (\rho^{(k)} u^{(k)}) = 0 \tag{29}$$

and the second balance equation for group k

$$\partial_t u^{(k)} + (u^{(k)} \cdot \nabla_x) u^{(k)} = \frac{1}{\rho^{(k)}} \int G^{(k)}(x, v, \delta_S \star \rho(x)) f^{(k)} dv \tag{30}$$
$$- \frac{1}{\rho^{(k)}} \int \sum_{l=1}^{M} \left(\nabla_x U^{(k,l)} \star \rho^{(l)} \right) f^{(k)} dv.$$

Using the monokinetic closure function

$$f^{(k)} \sim \rho^{(k)}(x) \delta_{u^{(k)}(x)}(v),$$

we obtain

$$\int G^{(k)}(x, v, \delta_S \star \rho(x)) f^{(k)}(x, v) dv = \int G^{(k)}(x, v, \delta_S \star \rho(x)) \rho^{(k)}(x) \delta_{u^{(k)}(x)}(v) dv$$
$$= \rho^{(k)}(x) G^{(k)}(x, u^{(k)}(x), \delta_S \star \rho(x))$$

and

$$\int \sum_{l=1}^{M} \nabla_x U^{(k,l)} \star \rho^{(l)} f^{(k)}(x, v) dv = \int \sum_{l=1}^{M} \left(\nabla_x U^{(k,l)} \star \rho^{(l)} \right) \rho^{(k)}(x) \delta_{u^{(k)}(x)}(v) dv$$
$$= \rho^{(k)}(x) \sum_{l=1}^{M} \left(\nabla_x U^{(k,l)} \star \rho^{(l)} \right).$$

Thus, Eq. (30) becomes the momentum equation

$$\partial_t u^{(k)} + (u^{(k)} \cdot \nabla_x) u^{(k)} = G^{(k)}(x, u^{(k)}(x), \delta_S \star \rho(x)) - \sum_{l=1}^{M} \left(\nabla_x U^{(k,l)} \star \rho^{(l)} \right) \quad (31)$$

with

$$G^{(k)}(x, u^{(k)}, \delta_S \star \rho(x)) = \frac{1}{T} \left(-V^{(k)}(\delta_S \star \rho(x)) \frac{\nabla \Phi^{(k)}(x)}{\|\nabla \Phi^{(k)}(x)\|} - u^{(k)} \right), \quad (32)$$

for $k = 1, \ldots, M$, coupled to

$$V^{(k)}(\delta_S \star \rho(x)) \|\nabla \Phi^{(k)}(x)\| = 1.$$

5.3 The Multigroup Scalar Model

In this section, we reduce the hydrodynamic description to a scalar models and connect the approach to a multigroup Hughes model. Neglecting time changes and inertia terms in Eq. (32), one obtains

$$G(x, u^{(k)}, \delta_S \star \rho(x)) = \sum_{l=1}^{M} \nabla_x U^{(k,l)} \star \rho^{(l)}.$$

Using Eq. (32), we get

$$u^{(k)} = -\sum_{l=1}^{M} T \nabla_x U^{(k,l)} \star \rho^{(l)} - V^{(k)}(\delta_S \star \rho(x)) \frac{\nabla \Phi^{(k)}(x)}{\|\nabla \Phi^{(k)}(x)\|}.$$

Thus, the resulting scalar equation for $\rho^{(k)}$ is

$$\partial_t \rho^{(k)} + \nabla_x \cdot \left[\rho^{(k)} \left(-\sum_{l=1}^{M} T \nabla_x U^{(k,l)} \star \rho^{(l)} - V^{(k)}(\delta_S \star \rho(x)) \frac{\nabla \Phi^{(k)}(x)}{\|\nabla \Phi^{(k)}(x)\|} \right) \right] = 0, \quad (33)$$

for $k = 1, \ldots, M$.

A further simplification is obtained approximating the potential $U^{(k,l)}$ by a δ distribution, i.e.

$$U^{(k,l)}(y) \sim D^{(k,l)} \delta_0(y)$$

with the constant $D^{(k,l)} > 0$ given by

$$D^{(k,l)} = \int U^{(k,l)}(y)dy.$$

This yields straightforwardly

$$\nabla_x U^{(k,l)} \star \rho^{(l)} = D^{(k,l)} \nabla_x \rho^{(l)}.$$

Using additionally $\delta_S \sim \delta$, Eq. (33) becomes a multigroup version of the Hughes equations

$$\partial_t \rho^{(k)} - \nabla_x \left(V^{(k)}(\rho(x)) \frac{\nabla \Phi^{(k)}(x)}{\|\nabla \Phi^{(k)}(x)\|} \rho^{(k)} \right) = \sum_{l=1}^{M} D^{(k,l)} T \nabla_x \left(\rho^{(k)} \nabla_x \rho^{(l)} \right), \quad (34)$$

where $k = 1, \ldots, M$. This is again combined with the eikonal equation

$$V^{(k)}(\rho(x)) \|\nabla \Phi^{(k)}(x)\| = 1.$$

Remark 13 Using similar arguments one obtains a localized hydrodynamic model.

5.4 Numerical Results

First we consider a multigroup pedestrian model with three groups: The largest group consists of pedestrians interacting with each other with a purely repulsive interaction term as in the single group model. The second and third group consist of pedestrians with an additional attraction between the members of the respective groups. We have chosen the interaction potential (27) with $l_r = 0.5, l_a = 1, C_r = 200$ and $C_a = 50$, while for the first group of pedestrians, we use $C_a = 0$. See Fig. 15 for the location of the groups at $t = 0$. The initial density at the corresponding spots is $\rho = 2$ and zero elsewhere.

We have simulated the multigroup pedestrian flow model with our microscopic and multi-scale algorithms. In Fig. 16, we have plotted the positions of the pedestrians obtained from the microscopic and multi-scale simulations at time $t = 40$ with initial spacing $\Delta x = 1, 0.5$ and 0.25, which approximately corresponds to the number of particles $N = 750, 3000$ and $12{,}000$, respectively. We observe that the structure of the multi-scale solutions is similar to the microscopic solution with $12{,}000$ pedestrian even for a smaller number of grid particles.

For the following investigations on the influence of parameters on the solution, we use $N = 500$ pedestrians, initially located in $[0, 10] \times [0, 50]$ with $\rho = 1$. We consider only two groups. Group 2 with repulsive and attractive interaction terms is initially located in $[0, 10] \times [0, 10]$ and $[0, 10] \times [15, 20]$. Group 1 consists of the remaining initial pedestrians with only repulsive interaction terms.

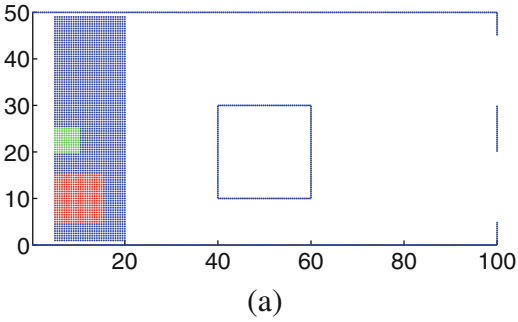

Fig. 15 Initial configuration. Group 1, blue; group 2, red; group 3, green. (**a**) Multigroup pedestrian

5.4.1 Comparison Between Single and Multigroup Pedestrian Flow Models with Weak and Strong Reciprocal Interaction

We use the following parameters for the numerical simulation: $l_r = 2$ and $C_r \in \{100, 200\}$ for the repulsive interaction and $l_a = 4$ and $C_a \in \{0, 10, 50, 70\}$ for the attractive interaction. Single pedestrians are modelled by $C_a = 0$.

Figure 17 shows the corresponding density plots for the time $t = 20$ for the single and multigroup case with $C_a = 70$.

The percentage of grid particles being in the computational domain for single and multigroup hydrodynamic models with different interaction parameters with respect to time is shown in Fig. 18. One observes that the evacuation time is larger in the case of grouped pedestrians. Moreover, choosing the attraction coefficient in the above range, one obtains a monotonic behaviour: the evacuation times increase with increasing attraction.

Comparing Fig. 18a, b, one observes a similar trend for both cases; however, for smaller repulsive interaction, the pedestrians from group 2 become much slower, leading to the plateau observed in Fig. 18b.

5.4.2 Comparison Between Models with Weak and Strong Centre of Mass Attraction

For the numerical simulation, we use a quadratic repulsive interaction potential $U(x) = C(2R - |x|)^2$ with parameters $C = 1000$ and $R = 0.4$. We use as attractive potential $U_{CM}(x) = -C_{CM}|x|^2$, yielding a linear force towards the centre of mass. In Fig. 19 we display five results: the case without centre of mass attraction and the cases with $C_{CM} =\in \{10, 50, 100, 200\}$. Obviously, the centre of mass attraction has a similar influence as the reciprocal interaction in the above subsection. Choosing the parameters in the above range, one obtains again a monotonic behaviour for the evacuation times.

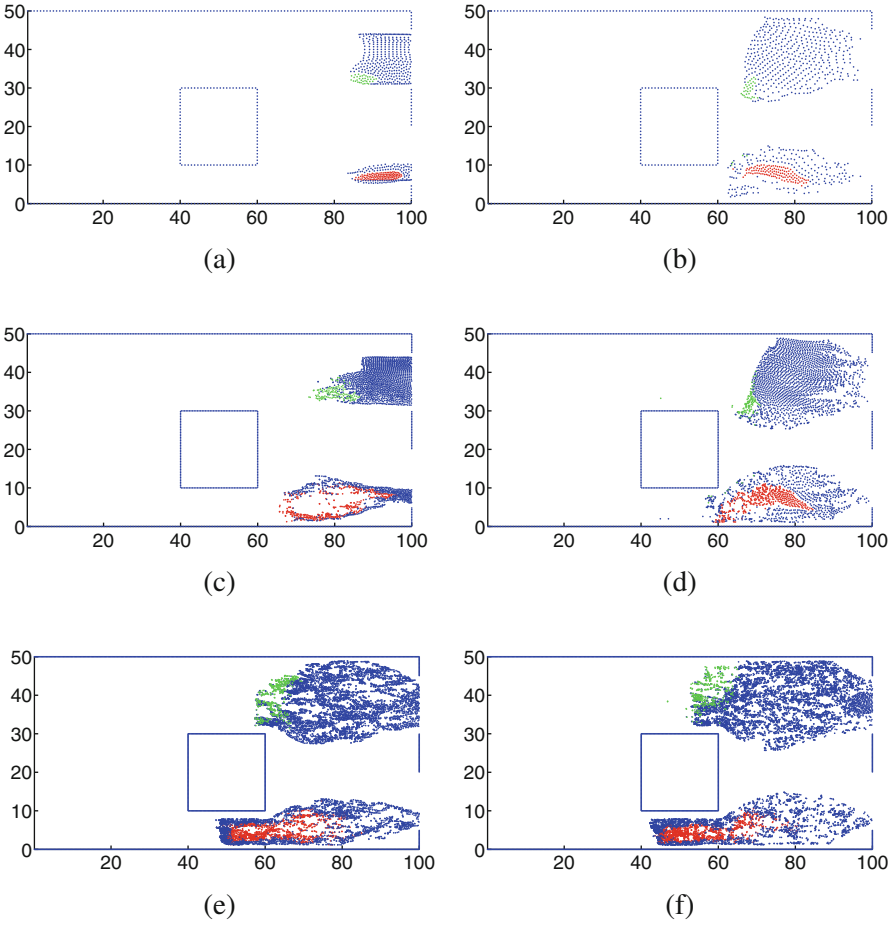

Fig. 16 The position of group and individual pedestrians obtained from microscopic and multiscale approaches at time $t = 40$ for various initial particle spacings Δx. (**a**) $\Delta x = 1$, micro. (**b**) $\Delta x = 1$, multiscale. (**c**) $\Delta x = 0.5$, micro. (**d**) $\Delta x = 0.5$, multiscale. (**e**) $\Delta x = 0.25$, micro. (**f**) $\Delta x = 0.25$, multiscale

5.5 Discussion of Experimental Data

The effect of grouping of pedestrians on evacuation processes, and in particular on the evacuation time, has been considered in a series of recent publications from an experimental point of view, as well as with the help of numerical experiments. We refer to [40, 44] for experimental data in simplified situations. Moussaid et al. [53] discusses the walking speed for groups of different sizes and [15] and [14] use an agent-based model to investigate social groups in pedestrian flow. Larger groups are, for example, considered in [65]. In [45], besides showing results on evacuation times, a comparison and a critical discussion of previous approaches is given.

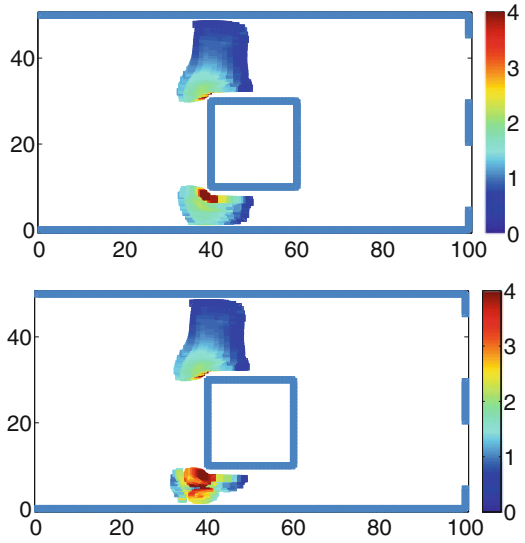

Fig. 17 Density of pedestrians for single (top) and multigroup (bottom) hydrodynamic model at times $t = 20$

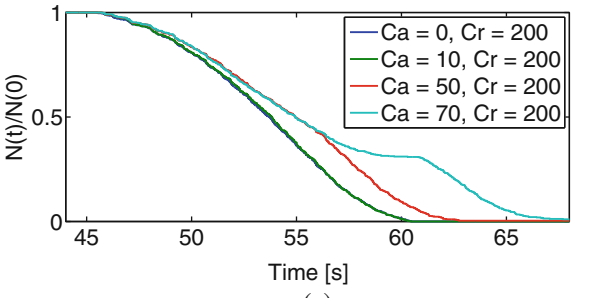

(a)

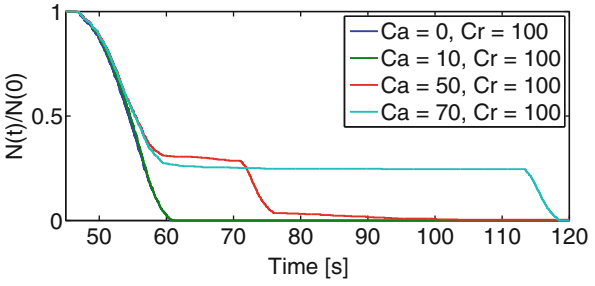

(b)

Fig. 18 Ratio of initial and actual grid particles with respect to time in single and multigroup hydrodynamic model with $C_a = 0, 10, 50, 70$ and $C_r = 100, 200$ for pedestrians in group 2. (**a**) $C_r = 200$. (**b**) $C_r = 100$

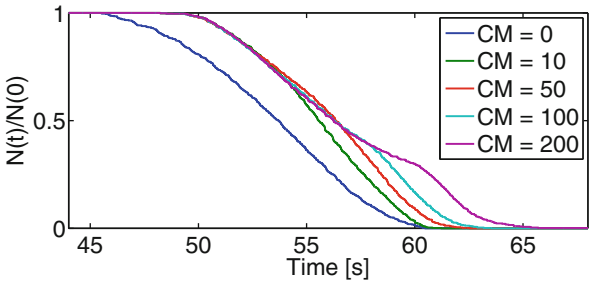

Fig. 19 Ratio of initial and actual grid particles in the computational domain with respect to time for multigroup hydrodynamic model with centre of mass attraction

The experimental results in [44] consider only small groups. Nevertheless, they show an increase in evacuation time for an increase in group size. Similarly, in [40] the authors obtain a longer evacuation time for groups with cooperative behaviour than for individuals. Such a trend can also be seen in [15] and [45]. In particular, in the last two papers, larger groups are shown to have up to 50% longer evacuation times than individuals. This is in accordance with our results giving evacuation times for grouped motion, which are up to 50% longer; compare the results in Fig. 18 for not too large values of C_a.

6 Coupling Pedestrian to Traffic Flow

In this section we investigate models coupling pedestrian movement to traffic flow equations (see [9]).

6.1 The Traffic and Pedestrian Flow Model

For the car traffic flow, we consider the scalar Lighthill-Whitham model. The car density $\rho_C = \rho_C(x,t) \in \mathbb{R}^+, x \in \mathbb{R}, t \in \mathbb{R}^+$ is governed by the equation

$$\partial_t \rho_C + \partial_x(\rho_C V_C) = 0\,.$$

V_C is a velocity function for traffic flow specified later.

For pedestrian flow we consider the classical Hughes model with the pedestrian density $\rho_P = \rho_P(\mathbf{x},t), \mathbf{x} \in \mathbb{R}^2, \rho_P \in \mathbb{R}^+, \Phi : \mathbb{R}^2 \to \mathbb{R}$. The equations are

$$\partial_t \rho_P + \nabla_{\mathbf{x}} \left(\rho_P V_P \frac{\nabla \Phi}{\|\nabla \Phi\|} \right) = 0\,,$$

with V_P specified in the following. Moreover, Φ is determined by the eikonal equation

$$V_P \|\nabla \Phi(\mathbf{x})\| = 1\,. \tag{35}$$

6.2 The Coupling

We denote the influence of the car traffic on pedestrians by a rate function $g_{CtoP}(\rho_C)$ and the influence of pedestrians on the cars by the rate function $g_{PtoC}(\rho_P)$.

Pedestrian to traffic The influence of pedestrians on the traffic flow is modelled via the traffic velocity function

$$V_C = V_C(\rho_C, \rho_P) = g_{PtoC}(\rho_P) V_C^{\max} \left(1 - \frac{\rho_C}{\rho_C^{\max}}\right) ,$$

with the rate of driving g_{PtoC} decreasing with increasing pedestrian density such that g is 1 for $\rho_P = 0$ and g is 0 for $\rho_P = \rho_P^{\max}$. This can be achieved by the function

$$g_{PtoC}(\rho_P) = (1 - \rho_P/\rho_P^{\max})^{n_1}, \quad n_1 \geq 1 . \tag{36}$$

The choice of the parameter n_1 depends on the situation to be considered. In regions where the drivers are more careful, a larger value of n_1 is enforcing a stronger reduction of their speed. In order to evaluate such a function, the 2D pedestrian distributions have to be projected on the 1D traffic space. This can be achieved by suitable operators which depend on the shape of the roads.

Traffic to pedestrian The influence of cars on the flow of the pedestrians is modelled via the pedestrian velocity function

$$V_P(\rho_P, \rho_C) = g_{CtoP}(\rho_C) V_P^{\max} \left(1 - \frac{\rho_P}{\rho_P^{\max}}\right) ,$$

with pedestrian crossing rate $g_{CtoP} \in [0, 1]$. Analogous to the cars, the pedestrians might slow down if many cars are present

$$g_{CtoP}^{(1)}(\rho_C) = \left(1 - \frac{\rho_C}{\rho_C^{\max}}\right)^{n_2}, \quad n_2 \geq 1 . \tag{37}$$

On the other hand, smaller densities imply higher velocities of the cars. This might be even more dangerous for people crossing the roads, e.g. g_{CtoP} can be chosen as

$$g_{CtoP}^{(2)}(\rho_C) = \left(\frac{\rho_C}{\rho_C^{\max}}\right)^{n_2}, \quad n_2 \geq 1 .$$

As a third option, both considerations can be combined. This leads for example to

$$g_{CtoP}^{(3)}(\rho_C) = \left(1 - \left(1 - \frac{\rho_C}{\rho_C^{\max}}\right) \frac{\rho_C}{\rho_C^{\max}}\right)^{n_2}, \quad n_2 \geq 1 .$$

In any case the function g_{CtoP} has to live in the 2D pedestrian domain. Therefore the 1D traffic data is extended to the 2D pedestrian region. This is modelled by the functions, which assign the appropriate space of the road in the 2D domain.

Remark 14 If traffic or pedestrian flow is described by two equations for density ρ and mean velocity u like the Aw-Rascle equations [2], then more sophisticated coupling conditions can be applied. For example, conditions like

$$g_{TtoP}(\rho) = (1 - \rho/\rho_m)(1 - u/u_m)$$

seem to be more appropriate.

6.3 Numerical Methods and Results

For the solution of the 1D conservation law on the network, we use a classical Godunov scheme. The 2D conservation law for pedestrians is solved using the FORCE scheme (see [63]). The eikonal equation is solved by the fast marching method and implemented as discussed in [59]. One way to solve the coupled problem is to use a (first-order) splitting method:

Algorithm (Coupling procedure)

1. Project pedestrian densities onto the network.
2. Compute V_C for every grid point, where g_{PtoC} depends on ρ_P.
3. Evaluate one time step in the traffic network.
4. Project the new traffic densities onto the pedestrian domain.
5. Compute V_P for every grid point, where g_{TtoP} depends on the ρ_P.
6. Solve the eikonal equation (12).
7. Evaluate one time step of the pedestrians with the flux V_P.

To test the convergence of the coupling algorithm, we consider the following example. The computational domain is $[0, 1] \times [0, 1]$ and a single road is given by the line $y = 0.5$. The maximal density and maximal velocity are $\rho_C^{\max} = V_P^{\max} = 1$. The road width is $z = 0.2$. The initial condition for the cars is $\rho_{C,\text{init}}(x) = 0.5$ and the pedestrian initial conditions are

$$\rho_P^0(x, y) = \begin{cases} 0.5, & \text{if} \quad 0.4 \le x \le 0.8 \wedge 0.6 \le y \le 1 \\ 0, & \text{else} . \end{cases}$$

The destination is located at $y = 0$. The coupling functions are chosen as (36) and (37).

Comparison of coupling functions To show how the different coupling functions influence the solution of the coupled problem, we consider an example with two roads with different maximal velocities. We consider a computational domain $[0, 2] \times [0, 2]$ and a traffic network given by the vertices $v_1 = (0, 1)$, $v_2 = (1, 1)$, $v_3 = (1, 2)$. The first edge $e_1 = (v_1, v_2)$ has maximal velocity $V_C^{\max} = 2$ and

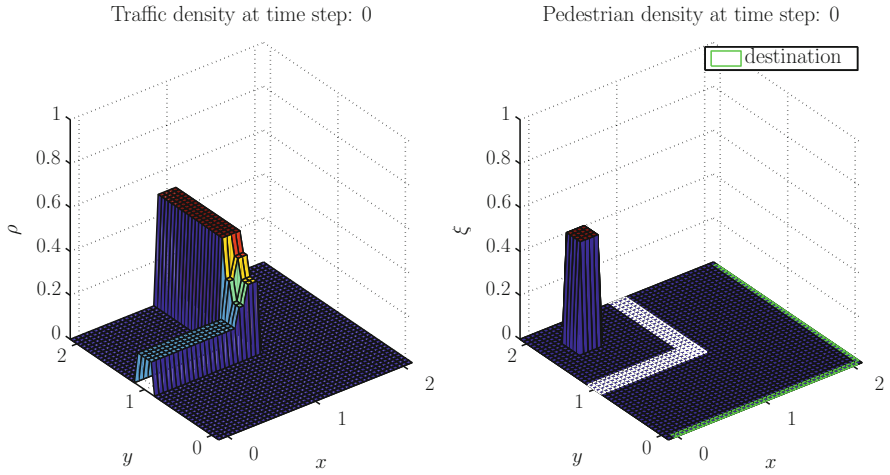

Fig. 20 Initial condition for all test cases

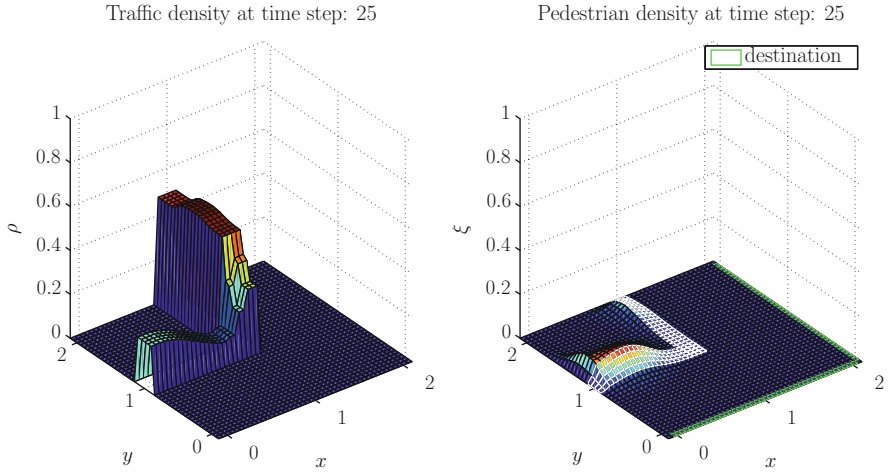

Fig. 21 Test case 1: densities with coupling function $g^{(1)}(\rho)$. Most of the pedestrians choose the first edge to cross the road

$\rho_C^{\max} = 1$. The second edge $e_2 = (v_2, v_3)$ has $V_C^{\max} = \rho_C^{\max} = 1$. The initial conditions on the roads are $\rho_{1,\text{init}}(x) = 0.5 - \sqrt{0.125}$ and $\rho_{2,\text{init}}(x) = 0.5$. The grid size is $h = 0.05$ and $\Delta t = 0.025$. The road width is $z = 0.2$.

The initial condition for the pedestrians is

$$\rho_P^0(x, y) = \begin{cases} 0.5, & \text{if}(x, y) \in [0.2\ 0.4] \times [1.6\ 1.8] \\ 0, & \text{else}\ . \end{cases}$$

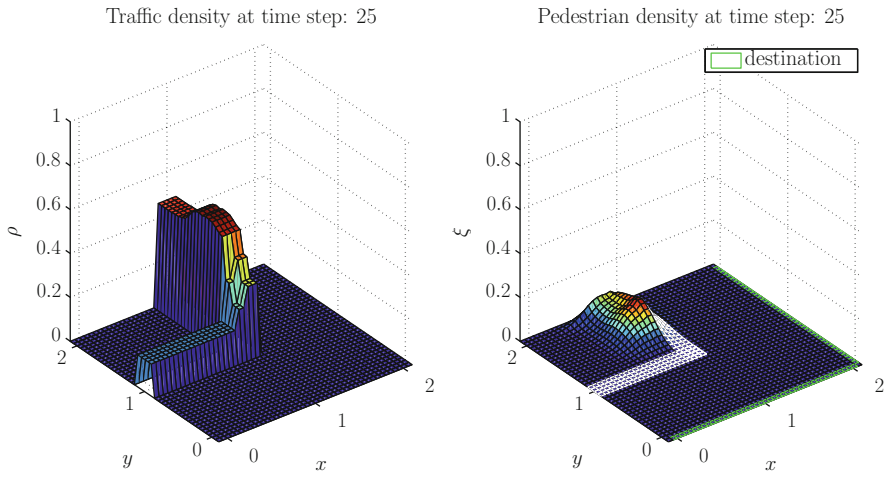

Fig. 22 Test case 2: densities with coupling function $g^{(2)}(\rho)$. Most of the pedestrians choose the second edge to cross the road

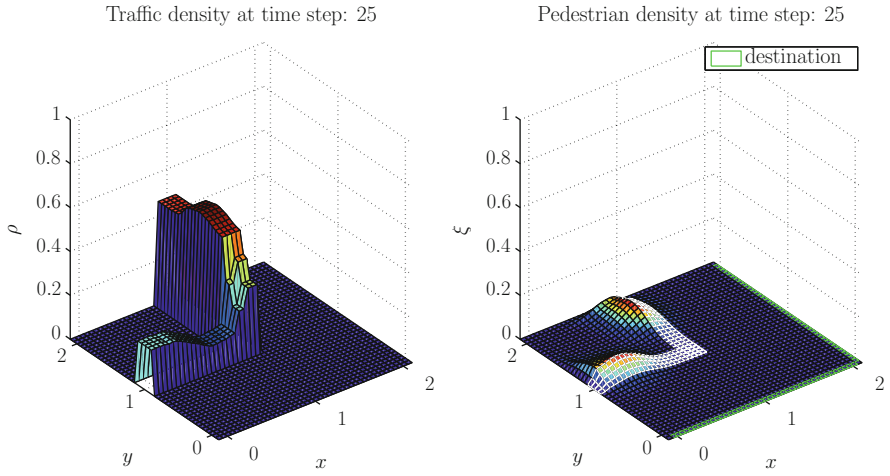

Fig. 23 Test case 3: densities with coupling function $g^{(3)}(\rho)$. One half of the pedestrians takes the first and the other half the second road. It does not matter which road to take since the flux is the same on both roads

The destinations are the lines $y = 0$ and $x = 2$. We consider three test cases, with $n_1 = 4$ and $n_2 = 1$ and $g^{(i)}_{CtoP}$ for $i = 1, 2, 3$. In Figs. 20, 21, 22 and 23, we display the resulting traffic density on the left and the pedestrian density on the right.

In Fig. 21 we observe that most of the pedestrians choose the road with smaller density. In Fig. 22, most of the pedestrians choose the road with smaller maximal velocity but greater density. In Fig. 23 there is no preference since the fluxes are identical on both roads.

Crosswalk In this example we model a crosswalk. The computational domain is $[0, 3] \times [0, 3]$ and the road is located at $y = 1.5$ with width 0.2. The domain of the crosswalk is given by $[1.3, 1.7] \times [1.4, 1.6]$.

To model the crosswalk, we choose the following coupling function:

$$g^{(1)}_{CtoP}(\rho_C) = \begin{cases} \left(1 - \frac{\rho_C}{\rho_C^{\max}}\right) & \text{on the crosswalk,} \\ \left(1 - \frac{\rho_C}{\rho_C^{\max}}\right)^5 & \text{else .} \end{cases}$$

The maximal density and maximal velocity are $\rho_C^{\max} = V_C^{\max} = 1$ on every edge. The initial condition for the network is $\rho_{\text{init}}(x) = 0.5$. The grid size is $h = 0.1$ and $\Delta t = 0.1$. The initial condition for the pedestrians is

$$\rho_P^0(x, y) = \begin{cases} 0.5, & \text{if} \quad (x, y) \in [0.1\ 0.6] \times [2.4\ 2.9] \\ 0, & \text{else .} \end{cases}$$

The destination is the line $y = 0$ from $x = 0$ until $x = 1$. The coupling function g_{PtoC} is chosen as in (36) with $n_1 = 4$.

In Figs. 24, 25 and 26, the traffic density is displayed on the left and the pedestrian density on the right.

The pedestrians can identify the crosswalk as region to pass the road, and the presence of the cars justifies a deviation from the straight line to the destination. When the people start to enter the road, the cars have to stop and a jam forms.

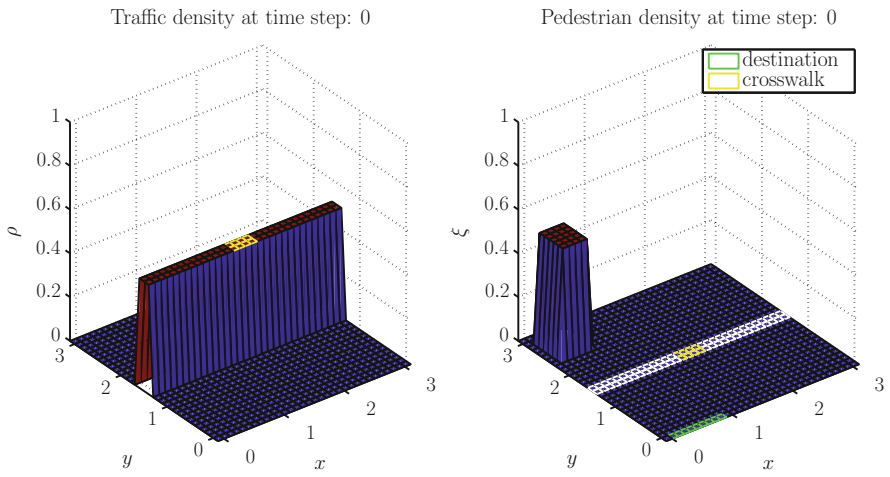

Fig. 24 Crosswalk at time step 0: initial condition of the crosswalk

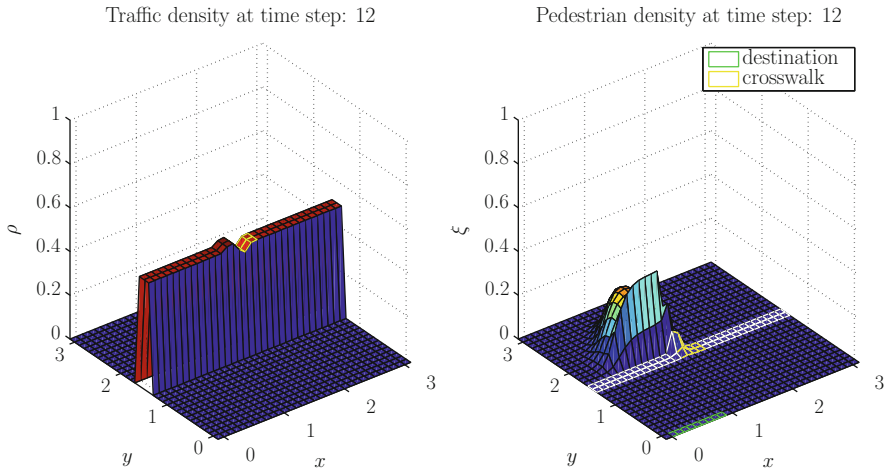

Fig. 25 Crosswalk at time step 12: pedestrians enter the road on the crosswalk. Hence, the car density is higher in front of and lower behind the crosswalk

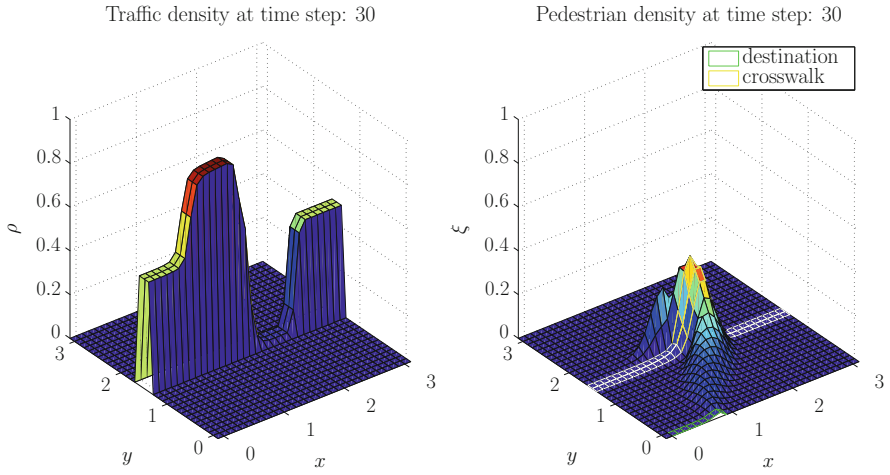

Fig. 26 Crosswalk at time step 30: a congestion arises in front of the crosswalk due to the huge number of pedestrians walking over the street. The first pedestrians reach the destination

7 Conclusions and Outlook

In this review we have presented model hierarchies for pedestrian flow simulations. They range from microscopic social force model coupled to an eikonal equation to Hughes-type scalar conservation laws. These hierarchies have been investigated numerically using finite-volume and Lagrangian particle methods. The particle method has been extended to a multi-scale version working uniformly for a large

range of interaction parameters R. Moreover, the different models have been compared with each other and the underlying microscopic solution showing large differences, in particular for smaller values of stochasticity. Additionally, we have presented a multigroup approach which has been investigated for various test cases with different behavioural models. Finally, we have developed a coupled model for pedestrian and traffic flow modelling the influence of car traffic on pedestrian motion and vice versa.

Looking at the numerical results, one observes that using a numerical method, which is able to work uniformly during the transition from a microscopic or non-local description of the problem to a description based on localized equations, saves for certain physical situation a considerable amount of computational time compared to a fully microscopic solver. Second, concerning the behaviour of the different models, one observes, for example, for the macroscopic models the following. In certain situations, for example, for small values of the noise parameter, simple scalar approximations, like the Hughes model, do not necessarily give appropriate results. In such a case, higher-order models like nonlinear maximum-entropy models are more suited to yield an accurate approximation of fully microscopic or kinetic solution. Finally including a multigroup ansatz into the models leads to experimentally observed longer evacuation times compared to a single group approach.

Future research directions may include the consideration of more complex situations like complex geometries or more sophisticated interaction models (compare [22, 55]). Moreover, a more detailed identification procedure for the physical parameters in the above models is necessary. Finally, from the point of view of applications, the investigation of global or feedback optimization for the models presented here would be of high interest.

Acknowledgements This work is supported by the German Research Foundation, DFG grant KL 1105/20-1, and by the DAAD PhD programme MIC.

References

1. D. Amadoria, M. Di Francesco, The one-dimensional Hughes model for pedestrian flow: Riemann-type solutions, Acta Mathematica Scientia, 32 (2012) 259–280.
2. A. Aw and M. Rascle, Resurrection of second order models of traffic flow, SIAM J. Appl. Math., 60 (2000), pp. 916–938.
3. N. Bellomo, C. Dogbe, On the Modeling of Traffic and Crowds: A Survey of Models, Speculations, and Perspectives, SIAM Review 53 (2011) 409–463.
4. N. Bellomo, A. Bellouquid, On the modeling of crowd dynamics: Looking at the beautiful shapes of swarms, Netw. Heterog. Media, 6 (2011) 383–99.
5. N. Bellomo, A. Bellouquid, D. Knopoff, From the microscale to collective crowd dynamics, SIAM J. Multiscale Model. Simul. 11 (2013) 943–963.
6. N. Bellomo, C. Dogbe, On the modelling crowd dynamics from scaling to hyperbolic macroscopic models, Math. Models Methods Appl. Sci. 18 (2008) 1317–1345.

7. N. Bellomo, B. Piccoli, A. Tosin, Modeling crowd dynamics from a complex system viewpoint, Math. Models Methods Appl. Sci. 22 (2012) 1230004.
8. T. Belytschko, Y. Guo, W. Liu, S.P. Xiao, A unified stability analysis of meshless particle methods, Int. J. Numer. Meth. Engng. 48 (2000) 1359–1400.
9. R. Borsche, A. Klar, S. Kühn, A. Meurer, Coupling traffic flow networks to pedestrian motion, Math. Methods Models Appl. Sci. 24 (2), 359–380, 2014
10. T. Brunner, Forms of approximate radiation transport, SAND2002-1778, Sandia National Laboratory
11. J.A. Cañizo, J.A. Carrillo, J. Rosado, A well-posedness theory in measures for some kinetic models of collective motion, Math. Models Methods Appl. Sci. 21 (2011) 515–539.
12. J.A. Carrillo, M.R. D'Orsogna, V. Panferov, Double milling in self-propelled swarms from kinetic theory, Kinetic and Related Models 2 (2009) 363–378.
13. J. A. Carrillo, A. Klar, S. Martin, S. Tiwari, Self-propelled interacting particle systems with roosting force, Math. Models Methods Appl. Sci. 20 (2010) 1533–1552.
14. L. Cheng, V. Reddy, C. Fookes, and P. K. D. V. Yarlagadda, Impact of passenger group dynamics on an airport evacuation process using an agent-based model, International Conference on Computational Science and Computational Intelligence, Las Vegas, Nevada, USA (2014).
15. M.L. Chu, P. Parigi, K. Law, J.-C. Latombe, Modeling social behaviors in an evacuation simulator, Computer animation and virtual worlds, Comp. Anim. Virtual Worlds 2014; 25:375–384
16. Y.L. Chuang, M.R. D'Orsogna, D. Marthaler, A.L. Bertozzi, L. Chayes, State transitions and the continuum limit for a 2D interacting, self-propelled particle system, Physica D 232 (2007) 33–47.
17. R. Colombo, M. Garavello, M. Lecureux-Mercier, A Class of Non-Local Models for Pedestrian Traffic, Math. Models Methods Appl. Sci. 22 (2012) 1150023.
18. R. Colombo, M. Garavello, M. Lecureux-Mercier, Non-local crowd dynamics, Comptes Rendus Mathmatique 349 (2011) 769–772.
19. R. Colombo, M. Rosini, Pedestrian flows and non-classical shocks, Math. Models Methods Appl. Sci. 28 (2005) 1553–1567.
20. J.F. Coulombel, F. Golse, T. Goudon, Diffusion approximation and entropy based moment closure for kinetic equations, Asymptotic Analysis, 45 (2005) 1–39.
21. P. Degond, C. Appert-Rolland, M. Moussaid, J. Pettre, G. Theraulaz, A hierarchy of heuristic-based models of crowd dynamics, J. Stat. Phys. 152 (2013) 1033–1068.
22. P. Degond, C. Appert-Rolland, J. Pettre, G. Theraulaz, Vision-based macroscopic pedestrian models, Kinetic and Related models, AIMS 6, 4, (2013), 809–839
23. P. Degond, S. Motsch, Continuum limit of self-driven particles with orientation interaction, Math. Models Methods Appl. Sci. 18 (2008) 1193–1215.
24. P. Degond, F.J. Mustieles, Approximation of diffusion equations by deterministic convections of particles, SIAM J. on Scientific and Statistical Computing 11 (1990) 293–310.
25. G.A. Dilts, Moving-least-squares-particle hydrodynamics: I. Consistency and stability, Int. J. Numer. Meth. Engng 44 (1999) 1115–1155.
26. R Etikyala, S Göttlich, A Klar, and S Tiwari. Particle methods for pedestrian flow models: From microscopic to nonlocal continuum models. Mathematical Models and Methods in Applied Sciences, 20(12), 2503–2523, 2014.
27. M. Di Francesco, P.A. Markowich, J.F. Pietschmann, M.T. Wolfram, On the Hughes model for pedestrian flow: The one-dimensional case, J. Differential Equations 250 (2011) 1334–1362.
28. R.A. Gingold, J.J. Monaghan, Smoothed Particle Hydrodynamics: theory and application to non-spherical stars, Mon. Not. Roy. Astron. Soc. 181 (1977) 375–389.
29. M. Frank, H. Hensel, A. Klar, A fast and accurate moment method for the Fokker-Planck equation and applications to electron radiotherapy, SIAM Journal on Applied Mathematics 67, 582–603, 2007
30. S.Y. Ha, E. Tadmor, From particle to kinetic and hydrodynamic descriptions of flocking, Kinetic and Related Models 1 (2008) 415–435.
31. E.T., Hall, The Hidden Dimension. Anchor Books. ISBN 0-385-08476-5, 1966.

32. D. Helbing, Traffic and related self-driven many-particle systems, Rev. Modern Phys. 73 (2001) 1067–1141.
33. D. Helbing, A fluid dynamic model for the movement of pedestrians, Complex Systems 6 (1992) 391–415.
34. D. Helbing, P. Molnar, Social force model for pedestrian dynamics, Phys. Rev. E 51 (1995) 4282–4286.
35. D. Helbing, I.J. Farkas, P. Molnar, T. Vicsek, Simulation of pedestrian crowds in normal and evacuation situations, in: M. Schreckenberg, S.D. Sharma (Eds.), Pedestrian and Evacuation Dynamics, Springer-Verlag (2002) 21–58.
36. R.L. Hughes, A continuum theory for the flow of pedestrians, Transp. Res. Part B: Methodological 36 (6) (2002), pp. 507–535.
37. R.L. Hughes, A continuum theory for the flow of pedestrians, Transp. Res. Part B: Methodological 36 (2002) 507–535.
38. R.L. Hughes, The flow of human crowds, Annu. Rev. Fluid Mech. 35 (2003) 169–182.
39. D.P. Kennedy, J. Gläscher, J.M. Tyszka, R. Adolphs, Personal space regulation by the human amygdala. Nat Neurosci. 12, 1226–1227, 2009.
40. C. v. Krüchten, A. Schadschneider, Empirical study on social groups in pedestrian evacuation dynamics, Physica A 475 (2017) 129–141
41. A. Klar, F. Schneider, O. Tse, Maximum entropy models for stochastic dynamic systems on the sphere and associated Fokker-Planck equations, Kinetic and Related Models (KRM) 7 (3), 509–529, 2014
42. A. Klar, S. Tiwari, A multi-scale meshfree particle method for macroscopic mean field interacting particle models, SIAM Multiscale Mod. Sim. 12, 3, 2014
43. A. Klar, S. Tiwari, A multi-scale particle method for mean field equations: the general case, https://arxiv.org/abs/1705.03324
44. G. Koester, F. Treml, M. Seitz, and W. Klein, Validation of crowd models including social groups. In Ulrich Weidmann, Uwe Kirsch, and Michael Schreckenberg, editors, Pedestrian and Evacuation Dynamics 2012, 1051–1063. Springer International Publishing, 2014.
45. A.E. Kremyzas, Social Group Behavior and Path Planning, Master Thesis, University Utrecht
46. C.D. Levermore, Relating Eddington factors to flux limiters, J. Quant. Spectrosc. Radiat. Transf. 31 (1984) 149–160.
47. H. Ling, S.C. Wong, M. Zhang, C.H. Shu, W.H.K. Lam, Revisiting Hughes dynamic continuum model for pedestrian flow and the development of an efficient solution algorithm, Transp. Res. Part B: Methodological 43 (2009) 127–141.
48. N.K. Mahato, A. Klar, S. Tiwari, Particle methods for multi-group pedestrian flow, Appl. Math. Modeling 53, 447–461, 2018
49. S. Mas-Gallic, P. Raviart, A particle method for first-order symmetric systems, Numerische Mathematik 51 (1987) 323–352.
50. B. Maury, A. Roudneff-Chupin, F. Santambrogio, A macroscopic crowd motion model of the gradient-flow type, Math. Models Methods Appl. Sci. 20 (2010) 1787–1821.
51. L. Müller, A. Meurer, F. Schneider, A. Klar, A numerical investigation of flux-limited approximations for pedestrian dynamics, M3AS 27 (6), 1177–1197, 2017
52. A. Mogilner, L. Edelstein-Keshet, L. Bent, A. Spiros, Mutual interactions, potentials, and individual distance in a social aggregation, J. Math. Biol. 47 (2003) 353–389.
53. M. Moussaid, N. Perozo, S. Garnier, D. Helbing, and G. Theraulaz, Walking Behaviour of Pedestrian Social Groups and Its Impact on Crowd Dynamics, PLoS ONE, 5(4), e10047(2010).
54. S. Osher and J. Sethian, Fronts propagating with curvature-dependent speed: Algorithms based on Hamilton–Jacobi formulations, J. Comput. Phys. 79 (1988) 12–49.
55. J. Ondrej, J. Pettre, A.H. Olivier, S. Donikian, A synthetic-vision based steering approach for crowd simulation, ACM Transactions on Graphics, 29, 4, Article 123 (2010)
56. B. Piccoli, A. Tosin, Pedestrian flows in bounded domains with obstacles, Contin. Mech. Thermodyn. 21 (2009) 85–107.

57. F. Schneider, G. Alldredge, M. Frank, A. Klar, Higher Order Mixed-Moment Approximations for the Fokker–Planck Equation in One Space Dimension, SIAM Journal on Applied Mathematics 74 (4), 1087–1114, 2014
58. H. Spohn, Large scale dynamics of interacting particles. Texts and Monographs in Physics, Springer (1991).
59. J. A. Sethian, Fast Marching Methods, SIAM Review 41 (1999) 199–235.
60. S. Tiwari, J. Kuhnert, Modelling of two-phase flow with surface tension by Finite Point-set method (FPM), J. Comp. Appl. Math. 203 (2007) 376–386.
61. S. Tiwari, J. Kuhnert, Finite pointset method based on the projection method for simulations of the incompressible Navier-Stokes equations, M. Griebel, M. A. Schweitzer (Eds.), Springer LNCSE: Meshfree Methods for Partial Differential Equations, Springer-Verlag 26 (2003) 373–387.
62. S. Tiwari, A. Klar, S. Hardt, A particle-particle hybrid method for kinetic and continuum equations, JCP 228 (2009) 7109–7124.
63. E. Toro, Riemann Solvers and Numerical Methods for Fluid Dynamics: A Practical Introduction (Springer, 2009).
64. A. Treuille, S. Cooper, Z. Popovic, Continuum crowds, in: ACM Transaction on Graphics, Proceedings of SCM SIGGRAPH 25 (2006) 1160–1168.
65. J. Xi, X. Zou, Z. Chen, J. Huang, Multi-pattern of Complex Social Pedestrian Groups Transportation Research Procedia Volume 2, 2014, 60–68
66. H.P. Zhu, A.B. Yu, Averaging method of granular materials, Phys. Rev. E 66 (2002) 021302.

Modelling Interactions Between Active and Passive Agents Moving Through Heterogeneous Environments

Matteo Colangeli, Adrian Muntean, Omar Richardson, and Thi Kim Thoa Thieu

Abstract We study the dynamics of interacting agents from two distinct intermixed populations: one population includes active agents that follow a predetermined velocity field, while the second population contains exclusively passive agents, i.e., agents that have no preferred direction of motion. The orientation of their local velocity is affected by repulsive interactions with the neighboring agents and environment. We present two models that allow for a qualitative analysis of these mixed systems. We show that the residence times of this type of systems containing mixed populations is strongly affected by the interplay between these two populations. After showing our modelling and simulation results, we conclude with a couple of mathematical aspects concerning the well-posedness of our models.

PACS: 02.70.Uu, 07.05.Tp, 05.06.-k.

MSC 2010: 65Z05, 82C80, 91E30.

1 Introduction

Unlike fluid flows, pedestrian flows are rarely uniform. Hence, their motion is difficult to predict accurately. The main source of nonuniformity stems from the fact that pedestrian flows are "thinking flows," i.e., both agent-agent interactions

M. Colangeli
Università degli Studi dell'Aquila, LAquila, Italy
e-mail: matteo.colangeli1@univaq.it

A. Muntean · O. Richardson (✉)
Karlstad University, Karlstad, Sweden
e-mail: adrian.muntean@kau.se; omar.richardson@kau.se

T. K. T. Thieu
Gran Sasso Science Institute, LAquila, Italy
e-mail: thikimthoa.thieu@gssi.it

L. Gibelli, N. Bellomo (eds.), *Crowd Dynamics, Volume 1*, Modeling and Simulation in Science, Engineering and Technology,
https://doi.org/10.1007/978-3-030-05129-7_8

and agent-structure interactions are always active and are much more complex than the standard Van der Waals-like (attraction-repulsion) interactions which govern to a large extent the molecular description of fluids and gases. In this framework, we consider a particular type of nonuniformity. Looking at a heterogeneous environment (e.g., a complex office building), we consider our target pedestrian flow to contain the dynamics of interacting agents from two distinct populations:

- *active agents*, knowing where to go (they are aware of a predetermined optimal velocity field leading toward the exits),
- *passive agents*, randomly exploring the environment (they have no information about the exit routes but base their motion on interaction with other agents).

We are particularly interested in investigating what mechanisms can be responsible for the minimization of the residence time of the pedestrians when an emergency evacuation situation has occurred, for instance, due to the unexpected occurrence of a fire that produces a significant amount of smoke. Our standing assumption is that the use of a purely macroscopic crowd model, which encodes the motion of a uniform flow, is prone to underestimate the residence time and does not properly capture crowd interaction.

In this chapter, we present conceptually different crowd dynamics models that describe the joint evolution of such passive and active agents. One of the models employs systems of nonlinear stochastic differential equations of motion one-way coupled with the diffusive-convective dynamics of the smoke, while another model is a lattice-gas-type approach based on a Monte Carlo stochastic dynamics. Both models give estimates of the residence time of the particles as well as of the local occupancy (local pedestrian densities). When treating such scenarios, the complexity of the work is high. One of the difficulties is handling the agent-structure interaction. Even if all agents have a predetermined path to the exit, agent-agent and agent-structure interactions normally lead to clogging or faster-is-slower effects when the number of agents is sufficiently high, given a certain geometry; see, e.g., [46] and [24]. Another difficulty is to handle the presence of fire, and consequently, of smoke and of the increased discomfort the agents feel. We refer the reader to [38] for one possible way of treating the presence of obstacles and to [39] for hints on how to introduce the fire physics in the evolution equations describing the dynamics of the crowd. In this framework, we focus exclusively on the effect of knowledge of the geometry on the actual dynamics of the agents.

After reviewing a number of relevant related contributions, we proceed with the description of two closely related modelling scenarios where the type of models previously mentioned apply. Then we solve the models numerically and illustrate the typical behavior of the output: positions, residence times, discomfort values, etc. We also discuss a few basic aspects concerning the mathematical well-posedness of one crowd model related to Model 1. We close the chapter with a discussion section where we also include hints toward further potential contributions in this context.

The results reported here should be seen as preliminary. More efforts are currently invested to develop these research directions.

2 Related Contributions

Escape evacuation and social human behavior are closely connected. In an emergency situation, building occupants require information about the surrounding environment and social interactions in order to evacuate successfully. The experiments in [26] can serve as a typical example for the relevance of distinguishing between two groups of occupants: regular users of the building and those less familiar with it.

In the model presented in [10], the building occupants are modelled as agents who decide their evacuation actions on the basis of their infrastructural knowledge and their interactions with the social groups and the neighboring crowd therein. The authors showed that both familiar agents with the geometry building and social influence can dramatically impact on egress performance. As a multi-agent evacuation simulation tool, the ESCAPES system (presented in [44]) describes a realistic spread of knowledge to model two types of different knowledge: exit knowledge together with event knowledge. The conclusions made based on these models are supported by experimental findings such as those reported in [40], where an evacuation was performed and the exit choice of participants was investigated, as well as the effect of the evacuation geometry.

Commonly, agent-based crowd models are based on developing individual trajectories. Yet for dense crowds, additional dynamics come into play. This has been observed in, for instance, [15], where the interaction in dense crowds has been measured and analyzed, obtaining statistics for aggregate dynamics. These *macroscopic* properties have been observed from a theoretical perspective as well in, e.g., [32]. One way to bridge the gap between models for regular and dense crowds is to use representation defined on different spatial scales, giving rise to a so-called multiscale model. In [16], a multiscale model is proposed in terms of a granular flow formulation to display both microscopic and macroscopic crowd behavior. For an investigation of handling contacts in such flows of granular matters applied to crowds, we refer the reader to the work of Maury and co-authors and compare [22]. All these papers assume that the exits are visible. For study cases when the walking environment is not visible due to the lack of light, we refer the reader to [11]. There the main question is whether the grouping of the agents (involving higher coordination costs and information overload) has a chance to favorize a potentially quicker evacuation strategy. From a different perspective, interesting connections to crisis management issues are made in [3] and references cited therein.

We refer the reader to further related contributions on modelling crowd dynamics as reported, for instance, in [2, 28, 34], as well as in [4] and [14].

3 Agent-Based Dynamics (Model 1)

In this section we introduce an agent-based model in a continuous two-dimensional multiple connected region Ω, containing obstacles with a fixed location, a fire that produces smoke, and an exit. Ω represents the environment in which the crowd is present and tries to find the fastest way to the exit, avoiding any obstacles and the fire. The crowd is represented by the two aforementioned groups, active and passive agents. At time $t = 0$, the crowd starts to evacuate from Ω. In the rest of this section, Ω refers to the geometry displayed in Fig. 1.

Active agents have a perfect knowledge of the environment and the locations of the obstacles, but are not aware of the location of the fire prior to experiencing sensory cues. Passive agents have no information on the environment and follow their neighbors to reach the exit. A similar model as the one described below has been presented in [39].

Active and passive agents are seen as members from the sets $X_A = \{a_1, \ldots, a_{N_A}\}$ and $X_B = \{b_1, \ldots, b_{N_B}\}$, respectively. The dynamics governing their motion are described in the following sections.

3.1 Active Agents

The motion of the active agents is governed by a potential field model proposed by Hughes in [27] and adapted in [43]. It functions similarly to a floor field function, its counterpart in lattice models presented in, e.g., [42] and [9]. We modify the potential field model to account for the presence of obstacles and the effects of fire and smoke.

The potential field agrees with the principle of *minimization of effort*, serving as a dynamic generalized distance transform. Let **x** be an arbitrary point selected in Ω.

Fig. 1 Basic geometry for our case study cf. Model 1. Agents are initialized in a random location within the geometry and have to reach the exit (green) while avoiding the obstacles (black)

We introduce a *marginal cost field* $u(\mathbf{x}) > 0$, defined as

$$u(\mathbf{x}) = \alpha + u_{\text{obs}}(\mathbf{x}) + wH(\mathbf{x}).$$

The marginal cost field represents the effort of moving through a certain location and consists of a base level of constant walking effort $\alpha > 0$, information on the geometry and the obstacles u_{obs}, and information on the fire source wH. Here, w takes value 1 if the agent is aware of the location of the fire and 0 otherwise.

Let S be a path going from point $\mathbf{x}_p$ to point $\mathbf{x}_q$. Then the effort of walking on the path S can be expressed as

$$\int_S u(\boldsymbol{\xi})d\boldsymbol{\xi} = \int_S \alpha + u_{\text{obs}}(\boldsymbol{\xi}) + wH(\boldsymbol{\xi})d\boldsymbol{\xi}.$$

At the beginning of the simulation, w is 0 for all agents. When an active agent experiences a significant increase in temperature because of his proximity to the location of the fire, w is set to 1, and S changes, and as a result, the fire is avoided.

Let $G \subset \Omega$ be the set of all inaccessible locations in the geometry (i.e., those parts of Ω covered by obstacles). Then for all $\mathbf{x} \in \Omega$, the geometry information (i.e., the obstacle cost field) can be expressed as

$$u_{\text{obs}}(\mathbf{x}) = \begin{cases} \infty & \text{if } \mathbf{x} \in G, \\ \frac{1}{|d(\mathbf{x},G)|} & \text{if } \mathbf{x} \notin G \text{ and } d(\mathbf{x}, G) \leq r_G, \\ 0 & \text{if } d(\mathbf{x}, G) > r_G, \end{cases} \tag{1}$$

where r_G is a parameter of the order of the size of the agents. The obstacle cost makes sure that obstacle locations are inaccessible, and r_G adds a tiny layer of repulsion around each obstacle to ensure the basic fact that agents do not run into walls.

The preferred path S^* for an agent with location $\mathbf{x}_p$ and motion target $\mathbf{x}_q$ is determined as

$$S^* = \arg\min_S \int_S u(\boldsymbol{\xi})d\boldsymbol{\xi},$$

where we minimize over the set of all possible motion paths S from $\mathbf{x}_p$ to $\mathbf{x}_q$. In this framework, the active agents are aware of all exits, and the optimal path S^* is made available by means of the potential function Φ, a solution to the equation

$$||\nabla \Phi(\mathbf{x})|| = u(\mathbf{x}), \tag{2}$$

where $||\cdot||$ denotes the standard Euclidean norm. Passive agents do not have access to the optimal paths.

Figures 2 and 3 display the potential field and the corresponding paths for our case study. Figures 4 and 5 display the adaption active agents make as soon as they become aware of the fire locations and take an alternative route out.

Let $\mathbf{x}_{a_i}(t)$ denote the position of active agent i at time t. We express their motion within the geometry Ω by

$$\begin{cases} \dfrac{d\mathbf{x}_{a_i}}{dt} & = -v_s(\mathbf{x}_{a_i}, t)\dfrac{\nabla\Phi(\mathbf{x}_{a_i}) - \nabla p(\mathbf{x}_{a_i}, t)}{||\nabla\Phi(\mathbf{x}_{a_i}) - \nabla p(\mathbf{x}_{a_i}, t)||}, \\ \mathbf{x}_{a_i}(0) & = \mathbf{x}_{a_i,0}, \end{cases} \tag{3}$$

where $\mathbf{x}_{a_i,0}$ represents the initial configuration of the active agents and v_s represents a predefined walking speed. In (3), p represents a given discomfort term that

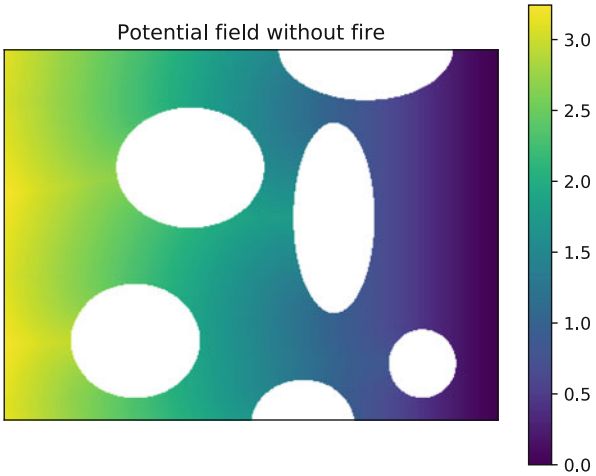

Fig. 2 Potential field Φ for the environment of the case study, not taking any fire into account

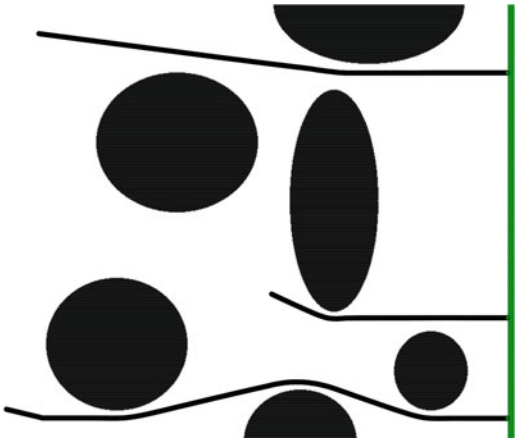

Fig. 3 Paths generated from the potential field in Fig. 2

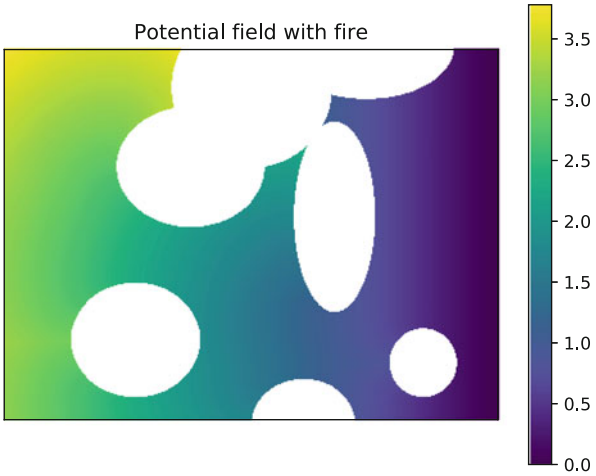

Fig. 4 Potential field Φ for the environment of the case study for agents aware of the fire location

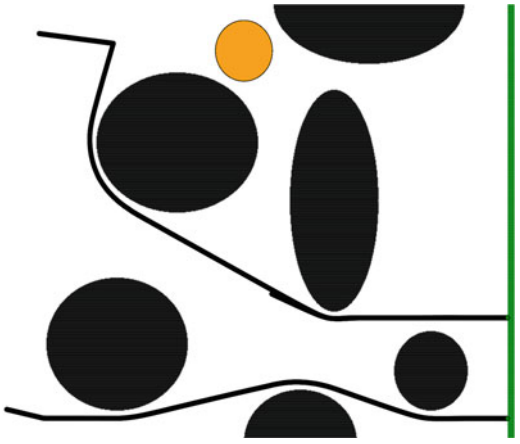

Fig. 5 Paths generated from the potential field in Fig. 4, avoiding the fire

influences agent interactions at the macroscopic scale. The discomfort measures how much agents locally have to deviate from their ideal velocity. We are on purpose vague concerning this macroscopic discomfort. In a follow-up publication, we will tackle a multiscale nonuniform crowd model where p will be part of the solution to a macro-micro flow problem.

3.2 Passive Agents

Since we assume in this context that passive agents are unfamiliar with their environment, it is reasonable to postulate that to obtain information, they rely solely on neighboring agents. This is a modelling assumption which has been confirmed

for, e.g., primates in [33]. This idea has already been applied in other crowd dynamics models (cf., e.g., [25]).

To model this strategy, we choose to apply a Cucker-Smale-like model which averages the velocity of nearby agents (an idea introduced originally in [17]). A Brownian term $\mathbf{B}_i$ is added to this swarming-like model to represent disorienting and chaotic effects which inherently appear while moving through an unknown environment.

We denote the positions and velocities of agent i from population X_B as $\mathbf{x}_{b_i}$ and $\mathbf{v}_{b_i}$ and positions and velocities from member j of the complete set $X_A \cup X_B$ as $\mathbf{x}_j$ and $\mathbf{v}_j$, respectively.

We express the motion of passive agents in the following way:

$$\begin{cases} \frac{d\mathbf{v}_{b_i}}{dt} & = \sum_{j\in X}(\mathbf{v}_j - \mathbf{v}_{b_i})w_{ij} - \nabla H(\mathbf{x}_{b_i}, t) \\ & \quad + \frac{\mathbf{v}_{b_i} - \nabla p}{||\mathbf{v}_{b_i} - \nabla p||}\Upsilon\left(s(\mathbf{x}_{b_i}, t)\right) + \mathbf{B}_i(t), \\ \frac{d\mathbf{x}_{b_i}}{dt} & = \mathbf{v}_{b_i}, \\ \mathbf{v}_{b_i}(0) & = \mathbf{v}_{b_i,0}, \\ \mathbf{x}_{b_i}(0) & = \mathbf{x}_{b_i,0}. \end{cases} \tag{4}$$

In (4), w_{ij} are weight factors, decreasing as a function of distance, defined as

$$w_{ij} \sim \frac{1}{r_s^2}\exp\left(-\frac{|\mathbf{x_i} - \mathbf{x_j}|^2}{r_s^2}\right). \tag{5}$$

In (5), r_s is the sight radius in the agents' location, affected by smoke level $s(\mathbf{x}, t)$ (see Sect. 3.3). It should also be noted that we do not take into account those walls that block the transfer of information between agents, since they are ignored in (5). However, in the simulations described in the next section, the size of the walls generally exceeds the size of the interaction radius. The term $\Upsilon\left(s(\mathbf{x}_{b_i}, t)\right)$ is simply an a priori known normalization factor depending of the smoke level; one can take $\Upsilon\left(s(\mathbf{x}_{b_i}, t)\right) = 1$ just for simplicity. In the context of (5), the gradient in the discomfort level[1] ∇p asymptotically bounds the speed of the passive agents.

Note that, based on (4), passive agents follow a set of coupled second-order differential equations (a social force-like model), while following (3), the active agents are expected to respect a set of coupled first-order differential equations (a social velocity-like model). We believe that the "social inertia" is much higher in the case of passive agents, so we keep the classical Langevin structure of the balance of forces, while for the active agents, we choose an overdamped version.

Another important observation is that in this model, passive agents do not know which of the other agents are active and which are passive themselves; they follow others indiscriminately.

[1] Here, we assume that the discomfort is perceptible, known.

3.3 Smoke Effects

In addition to repelling the agents, the fire produces smoke which propagates in Ω and reduces the visual acuity of the agents. The creation and propagation of the smoke is modelled as a diffusion-dominated reaction-advection-diffusion process.

The smoke density $s(\mathbf{x}, t)$ is assumed to respect the following equation:

$$\begin{cases} \partial_t s = \operatorname{div}(D\nabla s) - \operatorname{div}(\mathbf{v}s) + y_s H(\mathbf{x}) & \text{in } \Omega \setminus G, \\ (-D\nabla s + \mathbf{v}s) \cdot \mathbf{n} = 0 & \text{on } \partial\Omega \cup \partial G, \\ s(\mathbf{x}, 0) = 0 & \text{in } \Omega, \end{cases} \tag{6}$$

where $D > 0$ represents the smoke diffusivity, determined by the environment, $\mathbf{n}$ is the outer normal vector to $\partial\Omega \cup \partial G$, $\mathbf{v}$ is a given drift corresponding to, for instance, ventilation systems or indoor airflow, while $H(\mathbf{x})$ encodes the shape and intensity of the fire, viz.

$$H(\mathbf{x}) = \begin{cases} R & \text{if } |\mathbf{x} - \mathbf{x}_0| < r_0 \\ 0 & \text{otherwise} \end{cases}. \tag{7}$$

In our context, $D > 0$ is the molecular diffusion coefficient for the smoke, and a slight space dependence in D is allowed. At a later stage, maybe eventually also an s-dependence of D can be foreseen, if one would replace (6) by an averaged version where the free motion paths and the geometry are perceived as some sort of "homogenized" porous medium.

Figure 6 illustrates a snapshot of the smoke density for our case study.

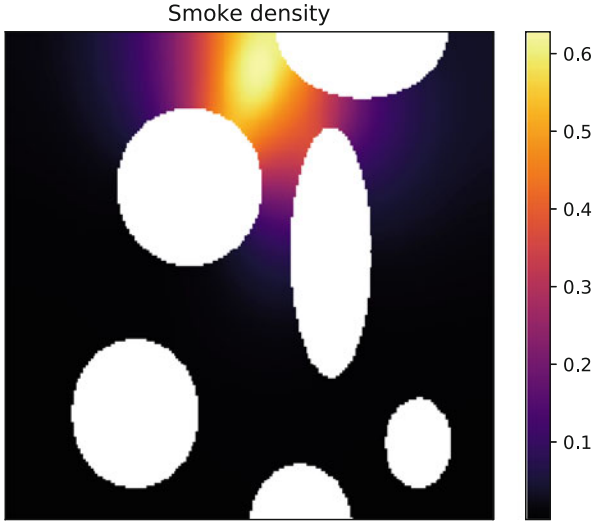

Fig. 6 Smoke density in the environment at $t = 60$

4 Results Model 1: Agent-Based Dynamics

This section contains our numerical results obtained using the agent-based dynamics described in the previous section.

The results are run in crowd simulation prototyping application *Mercurial* [37]. This is an open-source framework developed in Python and Fortran to simulate hybrid crowd representations as the one described in Sect. 3. It provides both agent-based and continuum-level visualizations and supports the design of arbitrary two-dimensional geometries. More details on the structure and implementation of *Mercurial* are found in [38].

Figure 1 shows the geometry of our case study. It has a fairly simple structure to ensure the exit can be reached even without environment knowledge. However, the placement of the obstacles is such that zones of congestion easily occur and paths to the exit will necessarily have to be curved.

The simulation was run twice with 1000 agents, varying the ratio between active and passive agents. The first run (Case 1), of which a snapshot is presented in Fig. 7, contains a total of 800 active agents and 200 passive agents. The second run (Case 2), illustrated with a snapshot in Fig. 8, contains a total of 200 active agents and 800 passive agents.

Figures 9 and 10 illustrate a coherent discomfort field in an ongoing simulation due to a large number of agents with conflicting directions. The corresponding agents configuration (i.e., their spatial distribution) is displayed in Figs. 7 and 8. It is visible that close to the fire, a lot of discomfort is generated. The main cause for this congestion is the conflict between active agents who have identified the location of the fire and want to move in different directions and active agents which

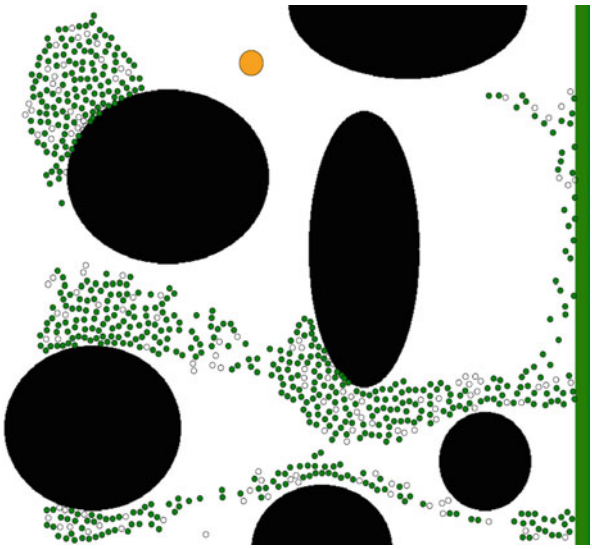

Fig. 7 Snapshot after $t = 17.9$ for a population with 80% active agents. Active agents are displayed as filled circles and passive agents as open circles. The larger circle represents the center of the fire

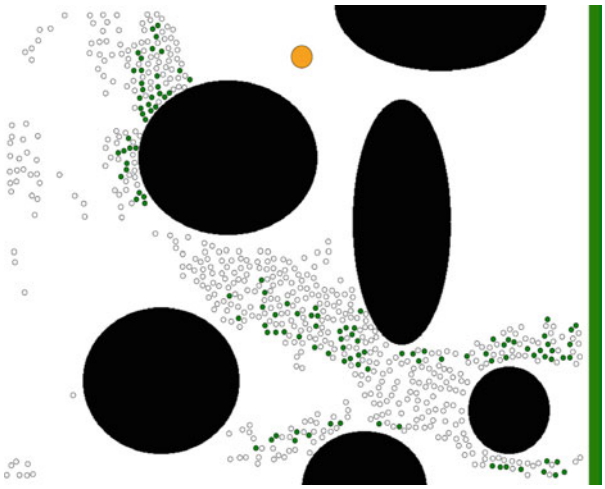

Fig. 8 Snapshot after $t = 37.5$ for a population with 20% active agents. Active agents are displayed as filled circles and passive agents as open circles. The larger circle represents the center of the fire

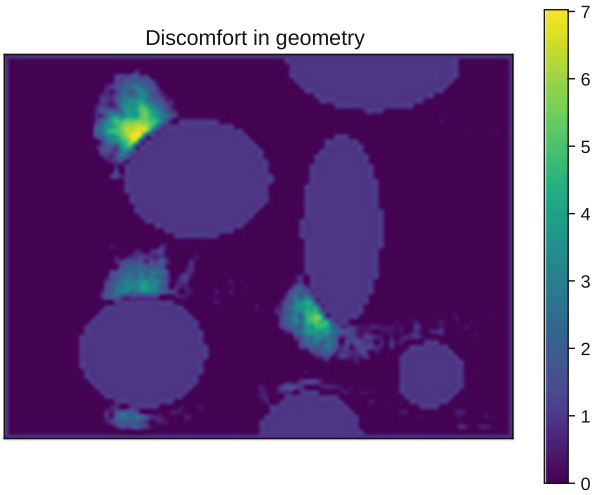

Fig. 9 Discomfort observed in the simulation snapshot of Fig. 7

are still unaware and want to exit the geometry through that particular corridor. This reminisces of the panic zone that occurs in crowd disasters close to the origin of the panic. Notice how this zone is much more present in Case 1 than in Case 2, due to the lack of active agents in Case 2. While the passive agents take a lot longer to reach the exit, their following-dominated behavior amounts to less discomfort in doing so.

It would be interesting to have a partial differential equation describing at least approximately the macroscopic space-time evolution of such discomfort field

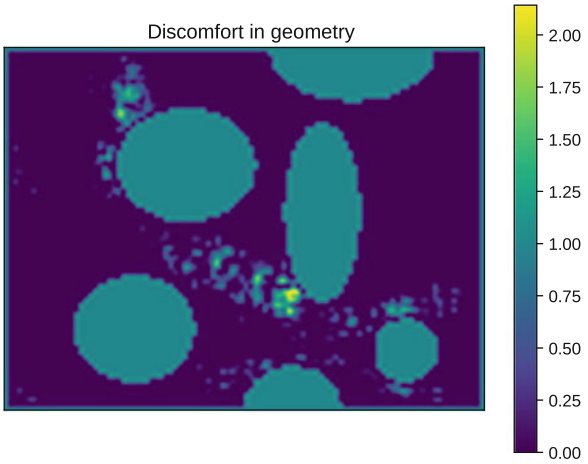

Fig. 10 Discomfort observed in the simulation snapshot of Fig. 8

available. Also, such an object would be very useful from a practical point of view – it would allow a fast detection of zones of high discomfort, which could be helpful in taking management decisions to reduce the potential of risks and accidents.

In Case 1 (Fig. 7), we observe that all agents belong to a collective moving toward the exit, regardless of population. As one would expect, Case 2 (Fig. 8) displays less order than Case 1. Most agents move in smaller groups, either guided by active agents or randomly moving throughout the geometry.

Figures 11 and 12 depict the agents leaving the environment as a function of time. In Fig. 11 we observe three stages: the first stage (from $t = 0$ to $t \approx 100$) corresponds to the group of active agents that exit the geometry without any obstructions, guiding most of the passive agents while doing so. The second stage (from $t \approx 100$ to $t \approx 400$) has virtually no agents that reach the exit; all the remaining agents are trapped in the high discomfort panic-like zone close to the fire. The third stage shows the final active agents have escaped the panic zone, reaching the exit.

Figure 12 displays a similar first stage, but because the discomfort zones are a lot less intensive, there is no pronounced second and third stage. Notice how after the bulk of the active agents have left the geometry, the egress of the passive agents has reduced to a random walk.

These observations are supported by Figs. 13 and 14, where the cumulative discomfort for each location $\mathbf{x}$ in Ω is displayed. Case 1 (Fig. 13) shows significantly higher discomfort both near the fire and where the geometry narrows itself. Case 2 (Fig. 14) shows a much higher usage of the space in the geometry, i.e., agents walking in locations that do not belong to any shortest path. However, the high discomfort zones are an order of magnitude lower than in Case 1, due to the "flexibility" of passive agents.

Concluding, simulations support the following observations. Differences in environment knowledge can have a significant impact on several aspects on the

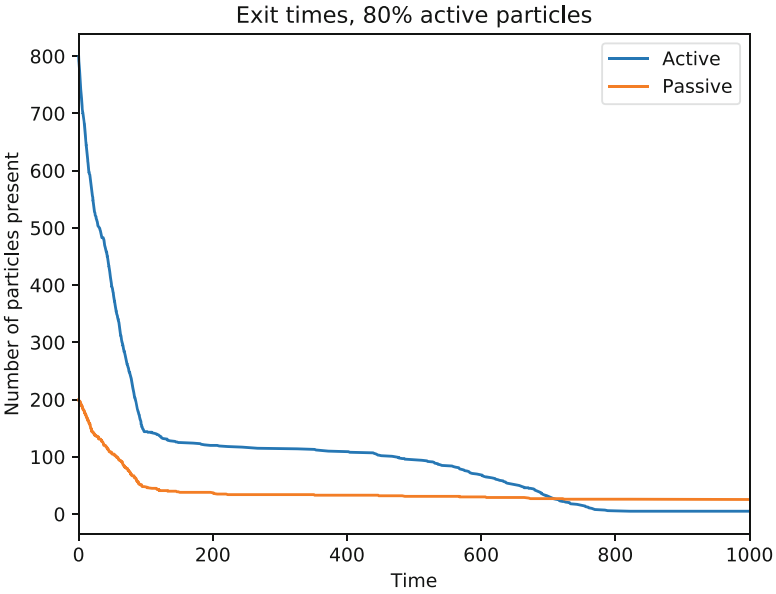

Fig. 11 Agent exit times in Case 1

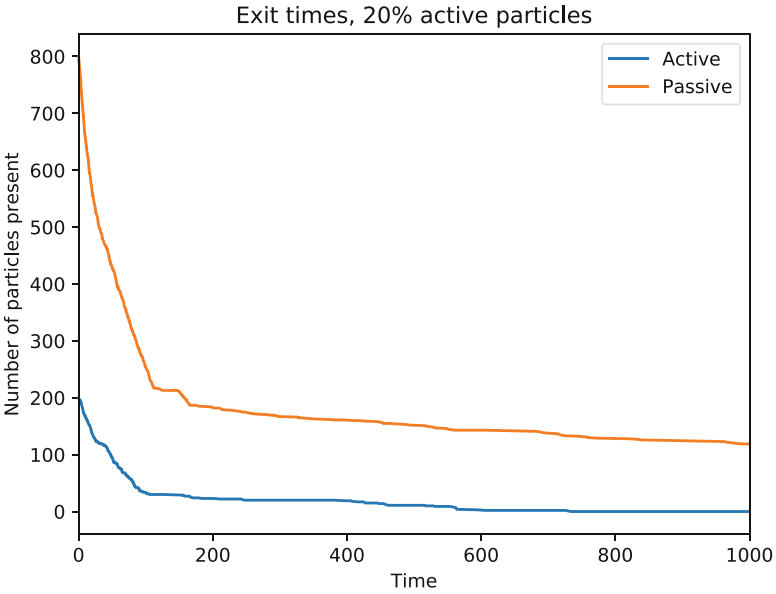

Fig. 12 Agent exit times in Case 2

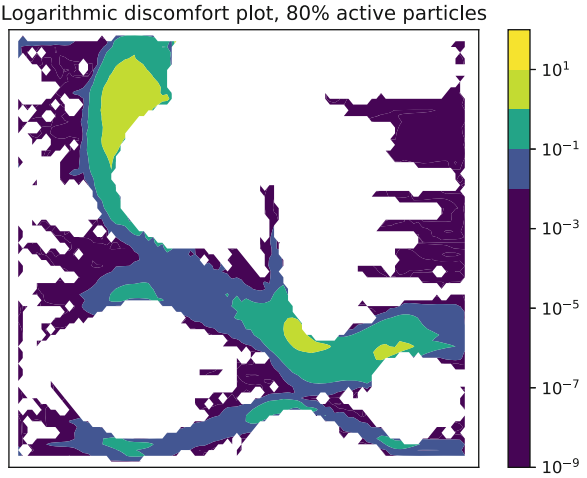

Fig. 13 Logarithmic heat map of discomfort zones that developed in the scenario with 80% active agents. White regions indicate no experienced discomfort

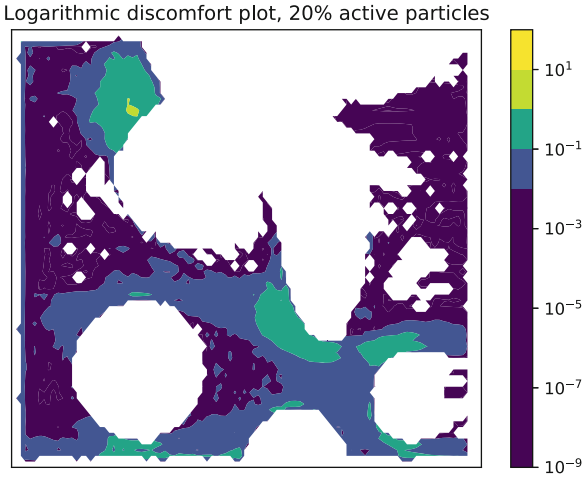

Fig. 14 Logarithmic heat map of discomfort zones that developed in the scenario with 20% active agents. White regions indicate no experienced discomfort

dynamics of crowds in, e.g., evacuations. While it is true that additional knowledge decreases evacuation time, the autonomy of active agents can cause problems when their information turns out to be incorrect. When steering passive agents, it is significantly more difficult to maintain order in the evacuation, but the fact that they can be guided can relieve discomfort and reduce congestion.

5 Lattice Gas Dynamics (Model 2)

The second model we shall consider is a simple exclusion process (SEP) [30] on a $2D$ rectangular lattice $\Lambda = \{1, \ldots, L_x\} \times \{1, \ldots, L_y\}$. Recall that two sites are said to be *nearest neighbors* if their Euclidean distance is one. A pair of nearest

neighboring sites is called a *bond*. Following the basic tenets of the SEP dynamics, each particle attempts a jump to one of its nearest neighbors, provided that the target site is empty. The waiting time between two consecutive jump attempts is an exponentially distributed random variable.

We assume that particles may leave the system only through a small set of lattice sites $\mathscr{D} = \{(x, y) \in \Lambda : y = L_y \ , \ x \in [x_{ex}, x_{ex} + w_{ex}]\}$, located on the upper horizontal row, called the "exit door" (of width w_{ex}). A particle departing from a site located within the exit door and hopping upward is annihilated. Note that particles can only leave the system through the door: no inward flux of particles is considered in this model. The aim of our numerical investigation is, indeed, to shed light on the characteristic time scales associated with the particle evacuation from the system. To complete the description of the geometry of the model, as in Sect. 3, we call G the set of all inaccessible sites on the lattice (representing, e.g., obstacles, cf. Fig. 15). Finally, we call the "exit strip" the set of lattice sites with horizontal coordinate $x \in [x_{ex}, x_{ex} + w_{ex}]$.

As in the case of Model 1, we distinguish between two species of particles, namely, *aware* (or active) particles and *unaware* (or passive) particles. For simplicity, we shall refer to them as particles "A" and "U" in this section. While particles U perform a symmetric simple exclusion dynamics on the lattice, particles A are subjected to both a horizontal and a vertical drift, denoted below as ϵ_x and ϵ_y, that enhance the rates at which these particles hop toward the exit door.

The microscopic dynamics is defined as follows. Call $\eta^{(U)}(w)$ and $\eta^{(A)}(w)$ the occupation number on the site $w = (x, y)$ of the two species U and A. Moreover, let $z = (x_2, y_2)$ be a nearest neighbor site of w, such that $w, z \in \Lambda \setminus G$. Then, we define the hopping *rate* of the species U from w to z (no matter if the jump occurs along a horizontal or a vertical bond) as:

$$c^{(U)}(w, z) = \eta^{(U)}(w) \left[1 - \eta^{(U)}(z) - \eta^{(A)}(z)\right] \ . \tag{8}$$

To define the corresponding hopping rate for the species A, we need to distinguish between vertical and horizontal bonds. For the vertical bonds, we set:

$$c^{(A)}(w, z) = \begin{cases} (1 + \epsilon_y)\eta^{(A)}(w) \left[1 - \eta^{(A)}(z) - \eta^{(U)}(z)\right] & \text{if} y_2 > y \ , \\ \\ 0 & \text{if} y_2 < y \ . \end{cases} \tag{9}$$

for upward or downward jumps, respectively. The hopping rate in Eq. (9) mimics the tendency of the species A to move upward, i.e., toward the exit door, thus preventing any redundant vertical motion in the opposite direction. Note, also, that the presence of the drift ϵ_y in Eq. (9) makes the rate of an upward jump larger than the unitary rate characterizing the dynamics of the species U in Eq. (8). For the horizontal bonds, we shall first consider the case in which the departure site is not located inside the exit strip. In this case we set:

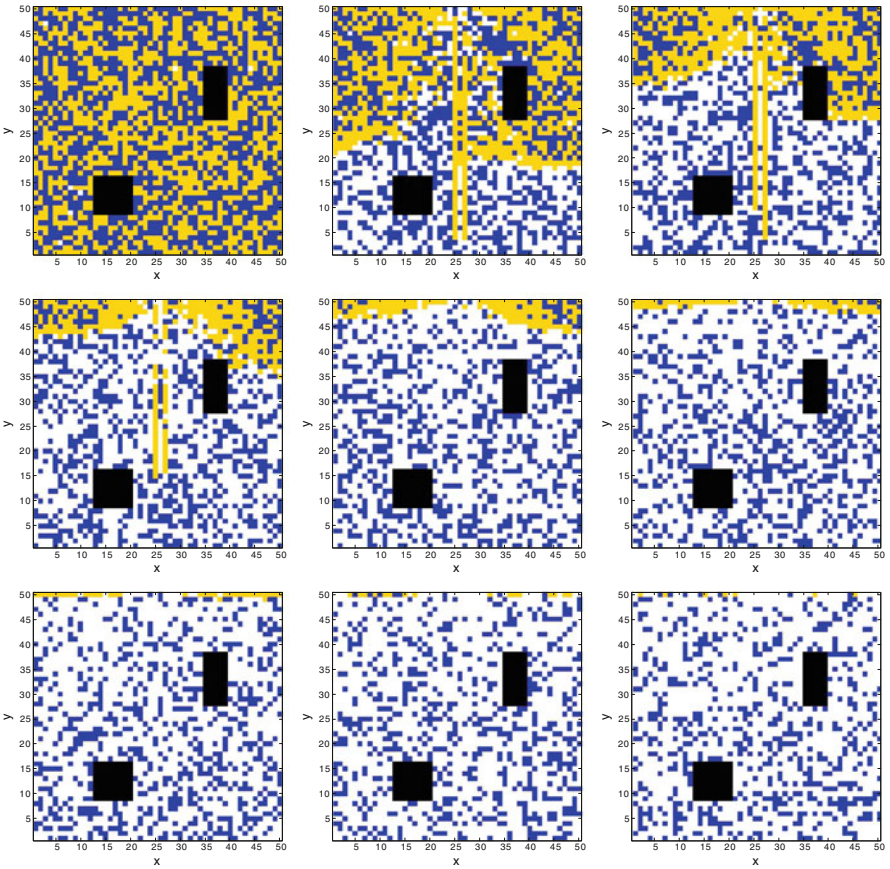

Fig. 15 Microscopic configurations of the lattice model sampled at different times (time increases from top to bottom, left to right). The configurations were obtained from Kinetic Monte Carlo simulations performed on a $2D$ square lattice Λ with $L_x = L_y = 50$. The yellow pixels correspond to particles of the species A, the blue pixels to particles of the species U, the white pixels represent empty spots on the lattice, whereas the black pixels denote the fixed obstacles (inaccessible sites). The width of the exit door, located at the center of the first horizontal row, is set equal to $w_{ex} = 2$. The horizontal and vertical drifts are set equal to $\epsilon_x = \epsilon_y = 0.1$. The initial configuration (top left panel) sees an equal number of particles of the species A and U on the lattice, and the two species together occupy a fraction 98.5% of all the accessible lattice sites

$$c^{(A)}(w,z) = \begin{cases} (1+\epsilon_x)\eta^{(A)}(w)\left[1-\eta^{(A)}(z)-\eta^{(U)}(z)\right] & \text{if } (x_2-x)(x_{ex}-x) > 0\,, \\ \eta^{(A)}(w)\left[1-\eta^{(A)}(z)-\eta^{(U)}(z)\right] & \text{if } (x_2-x)(x_{ex}-x) < 0\,. \end{cases} \tag{10}$$

The presence of a horizontal drift ϵ_x, in Eq. (10), indicates that particles A move preferably in the direction that enables them to reach the exit strip. Instead, if the departure site is inside the exit strip, we set:

$$c^{(A)}(w,z) = 0 \quad \text{if } x \in [x_{ex}, x_{ex} + w_{ex}] \,, \tag{11}$$

namely, particles A avoid wandering randomly along the horizontal direction inside the exit strip: they just patiently wait for their turn to move upward and ultimately evacuate the system. This causes the formation of queues along the vertical direction that are observed in numerical simulations, cf. Fig. 15.

All rates associated with bonds joining a site $w \in \Lambda \setminus G$ with a site $z \in G$ are set to 0. Finally, the rates c_{ex} related to upward jump from a departure site $w \in \mathscr{D}$ are defined as:

$$c_{ex}(w) = \eta^{(U)}(w)(1 - \eta^{(A)}(w)) + (1 + \epsilon_y)\eta^{(A)}(w)(1 - \eta^{(U)}(w)) \,. \tag{12}$$

The evacuation of particles from the lattice can be tracked by measuring, for each species, the number of particles $N(t)$ as a function of time. Then, for a given species, the average particle current J at time t is defined as:

$$J(t) = \frac{N(0) - N(t)}{t} \,. \tag{13}$$

6 Results Model 2: Lattice Gas Dynamics

This section contains our numerical results for the Model 2, obtained by running Monte Carlo simulations. In particular, we implemented the Kinetic Monte Carlo (KMC) method [31], which is suited to describe transient processes, in which physical time plays a decisive role in the microscopic evolution [7, 45].

The model has been simulated as follows: first, a number τ is picked up at random with exponential distribution of parameter λ, given by the sum of the rates defined in Sect. 5, associated with each lattice bond [12, 13]; time is then updated to $t + \tau$; a bond is chosen with probability equal to the corresponding rate divided by λ; finally, a particle hops from the occupied site to the empty site of the chosen bond.

The results of the KMC simulations are shown in Figs. 15 and 16. In Fig. 15 we present the microscopic configurations of the particles A and U at different times, from the initial configuration (top left panel) up to a final time in which the evacuation of particles A is almost completed (bottom right panel, corresponding to some 3×10^6 time steps of the dynamics).

In the left panel of Fig. 16, we show the total number of particles A and U as functions of time, for different values of the parameters w_{ex}, ϵ_x, and ϵ_y. Clearly, a larger width of the exit door favors the evacuation of both particles A and U. The left panel of Fig. 16 highlights an interesting effect related to the drift parameters: an increase of ϵ_x and ϵ_y enhances the evacuation rate of the particles A, but has also an effect on the evacuation of particles U. Indeed, these have access to a larger number of empty sites on the lattice, as a result of the increased evacuation of particles A. Finally, in the right panel of Fig. 16, we show the behavior of the particle current,

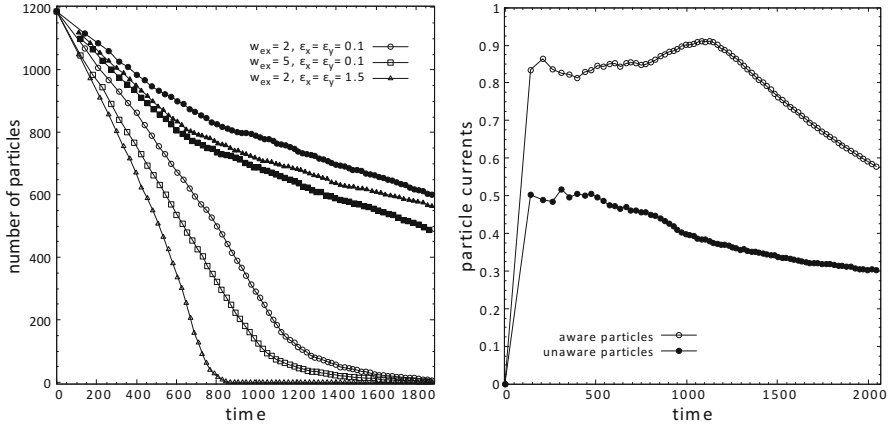

Fig. 16 *Left panel:* Behavior of the number of particles of the species A (empty symbols) and B (filled symbols) vs. time, with $L_x = L_y = 50$, and for different values of the exit width w_{ex} and of the drift terms ϵ_x and ϵ_y. *Right panel:* behavior of the current vs. time for the two species A and U with $L_x = L_y = 50$, $w_{ex} = 2$, and $\epsilon_x = \epsilon_y = 0.1$

defined in (13), for the two species A and U as a function of time, for fixed values of the parameters w_{ex}, ϵ_x, and ϵ_y. The higher evacuation rate observed for the particles A stems directly from the definition of the rates given in Sect. 5.

7 Mathematical Aspects of Social Dynamics in Mixed Populations

In this section, we discuss the solvability of a social dynamics model of mixed populations, resembling an overdamped version of Model 1. Note that Model 2 is well-posed by construction. Here, interesting questions would be pointing toward the rigorous derivation of the corresponding hydrodynamic limit equations [19] and/or the numerical evaluation of non-equilibrium collective effects (e.g., the inclusion of a reaction mechanism within the microscopic dynamics, allowing particles to switch from one species to the other, or the presence of long-range interactions between particles), but these aspects are not in our focus for the moment.

This section contains a couple of technical preliminaries needed to state the evolution problem in a functional analytic framework. We use standard methods to handle the well-posedness of a coupled set of SDEs for the agents dynamics, also linked to a linear parabolic equation describing the motion of the smoke.

Fig. 17 Basic geometry for our case study cf. Model 1. Obstacles are colored black, while the exit is colored green

7.1 Technical Preliminaries, Notation, and Assumptions

7.1.1 Geometry

We consider a two-dimensional domain, which we refer to as $\tilde{\Omega}$. This domain presents the geometry of the evacuation scenario. In addition, as a building geometry, parts of the domain are filled with obstacles (G_1 and G_2) denoted by $G := G_1 \cup G_2$ and the fire denoted by $\tilde{F}$. Moreover, the domain has exits denoted by E. Let $\Omega := \tilde{\Omega} \backslash (G \cup E \cup \tilde{F}) \subset \mathbb{R}^d$ for $d = 2$ and $\partial\Omega$ be C^2 or at least satisfying the exterior sphere condition. A typical example of such Ω is depicted in Fig. 17.

7.1.2 Function Spaces

In this section, we employ a number of Sobolev spaces; see, e.g., [1, 20] for details on their definition and properties.

The space $H^m(\Omega)$, $m \in \mathbb{N}$, is endowed with the norm

$$\|v\|^2_{H^m(\Omega)} := \sum_{|\alpha| \leq m} \int_\Omega |D^\alpha v|^2 dx \text{ for all } v \in H^m(\Omega),$$

while for the space $W^{m,\infty}(\Omega)$, we consider the norm

$$\|v\|_{m,\infty}(\Omega) := \sum_{|\alpha| \leq m} \operatorname{ess\ sup}_\Omega |D^\alpha v| \text{ for all } v \in W^{m,\infty}(\Omega), m \in \mathbb{N}.$$

Our analysis of the stochastic differential equations (SDEs) describing the evolution of our populations follows the line of reasoning from [23] and [18] (the compactness method of SPDEs and martingale solutions). We refer to [21] and [36] for the basic concepts and usual notations.

Let $\mathbf{x}_t$ be a continuous-time stochastic process. We define the family of laws

$$\left\{ Q(\mathbf{x}_t^n);\, t \geq 0, n \geq 1 \right\}. \tag{14}$$

This is a family of probability distribution of $\mathbf{x}_t^n$.

Recall the classical Ascoli-Arzelà theorem:
A family of functions $F \subset C([0,T];\mathbb{R}^d)$ is relatively compact (in uniformly topology) if

i. for every $t \in [0,T]$, the set $\{f(t);\, f \in F\}$ is bounded.
ii. for every $\varepsilon > 0$ and $t, s \in [0,T]$, there is $\delta > 0$ such that

$$|f(t) - f(s)| \leq \varepsilon, \tag{15}$$

whenever $|t-s| \leq \delta$ for all $f \subset F$.

We introduce the definition of Hölder seminorms, for $f : [0,T] \to \mathbb{R}^d$ as

$$[f]_\alpha = \sup_{t \neq s} \frac{|f(t) - f(s)|}{|t-s|}, \tag{16}$$

and the supremum norm as

$$\|f\|_\infty = \sup_{t \in [0,T]} |f(t)|. \tag{17}$$

Using Ascoli-Arzelà theorem, starting from the facts:

i′. there is $M_1 > 0$ such that $\|f\|_\infty \leq M_1$ for all $f \in F$.
ii′. for some $\alpha \in (0,1)$, there is an $M_2 > 0$ such that $[f]_{C^\alpha} \leq M_2$ for all $f \in F$,

we infer that the set

$$K_{M_1 M_2} = \left\{ f \in C([0,T];\mathbb{R}^d);\, \|f\|_\infty \leq M_1, [f]_{C^\alpha} \leq M_2 \right\} \tag{18}$$

is relatively compact in $C([0,T];\mathbb{R}^d)$.

For $\alpha \in (0,1)$, $T > 0$ and $p > 1$, the space $W^{\alpha,p}(0,T;\mathbb{R}^d)$ is defined as the set of all $f \in L^p(0,T;\mathbb{R}^d)$ such that

$$[f]_{W^{\alpha,p}} := \int_0^T \int_0^T \frac{|f(t) - f(s)|^p}{|t-s|^{1+\alpha p}} dt ds < \infty.$$

This space is endowed with the norm

$$\|f\|_{W^{\alpha,p}} = \|f\|_{L^p} + [f]_{W^{\alpha,p}}.$$

Moreover, we know that if $\alpha p > 1$, then

$$W^{\alpha,p}(0,T;\mathbb{R}^d) \subset C^{\gamma}([0,T];\mathbb{R}^d) \quad \text{for } (\alpha p - \gamma) > 1$$

and $[f]_{C^{\gamma}} \leq C_{\gamma,\alpha,p}\|f\|_{W^{\alpha,p}}$. Relying on the Ascoli-Arzelà theorem, we have the following situation:

ii''. for some $\alpha \in (0,1)$ and $p > 1$ with $\alpha p > 1$, there is $M_2 > 0$ such that $[f]_{W^{\alpha,p}} \leq M_2$ for all $f \in F$.

If i' and ii'' hold, then the set

$$K'_{M_1 M_2} = \left\{ f \in C([0,T];\mathbb{R}^d);\ \|f\|_{\infty} \leq M_1, [f]_{W^{\alpha,p}} \leq M_2 \right\} \tag{19}$$

is relatively compact in $C([0,T];\mathbb{R}^d)$, if $\alpha p > 1$.

7.1.3 Hypotheses

In this framework, we require the following assumptions:

(A_1) $\phi \in C^2(\Omega)$ (see also Sect. 7.3.1).
(A_2) $p_{\max} = N|\Omega| < \infty$ (bounded maximal discomfort).
(A_3) The smoke matrix diffusion coefficient $D = \mathbf{D}(x) \in W^{m,\infty}(\Omega)$ satisfies the uniform ellipticity condition, i.e., there exists positive constants $\underline{\theta}, \overline{\theta}$ such that

$$\underline{\theta}|\xi|^2 \leq \mathbf{D}(x)\xi_i\xi_j \leq \overline{\theta}|\xi|^2 \text{ for any } \xi \in \Omega.$$

(A_4) The smoke interface exchange coefficient on the boundary of our domain $\lambda := \Lambda(x) \in W^{m,\infty}(\partial\Omega)$ is such that there exist positive constants $\underline{\gamma}, \overline{\gamma}$ satisfying

$$-\underline{\gamma}|\xi|^2 < \lambda(x)\xi_i\xi_j \leq \overline{\gamma}|\xi|^2 \text{ for any } \xi \in \partial\Omega.$$

Changing the functional framework will naturally lead to a reconsideration of these assumptions.

7.1.4 First-Order Social Agents Dynamics

We focus on the interaction between two groups of pedestrians, one familiar (active agents) and one unfamiliar (passive agents, visitors) with the geometry. To keep the

presentation simple, we decide to tackle here the case when both active and passive agents follow a first-order dynamics (overdamped Langevin equations). To this end, we modify the dynamics of the passive agents, deviating this way from Model 1.

Let $\mathbf{x}_{a_i}$ denote the position of the agent i from group A at time t. The crowd dynamics in group A is expressed by the first-order differential equation encoding optimal environment knowledge within the domain Ω, viz.

$$\begin{cases} \frac{d\mathbf{x}_{a_i}(t)}{dt} = -\Upsilon(s(\mathbf{x}_{a_i}, t)) \left(\frac{\nabla\phi(\mathbf{x}_{a_i})}{\|\nabla\phi(\mathbf{x}_{a_i})\|} \right) (p_{\max} - p(\mathbf{x}_{a_i}, t)), \\ \mathbf{x}_{a_i}(0) = \mathbf{x}_{a_i,0}, \end{cases} \tag{20}$$

where $p_{\max}$ is a discomfort threshold proportional to the overall population size, say $p_{\max} = N|\Omega|$, with $N := N_A + N_B$ and $p(\mathbf{x}, t)$ is the local discomfort (realization of social pressure) so that

$$p(\mathbf{x}, t) = \int_{\Omega \cap B(\mathbf{x}, \tilde{\delta})} \sum_{j=1}^{N} \delta(z - \mathbf{x}_{c_j}(t)) dz. \tag{21}$$

In (21), δ is the Dirac (point) measure, and $B(\mathbf{x}, \tilde{\delta})$ is a ball center $\mathbf{x}$ with small enough radius $\tilde{\delta}$ such that $\tilde{\delta} > 0$. Hence, the discomfort $p(\mathbf{x}, t)$ represents a finite measure on the bounded set $\Omega \cap B(\mathbf{x}, \tilde{\delta})$. In addition, we assume the following structural relation between the smoke extinction and the walking speed:

$$\Upsilon(s(\mathbf{x}, t)) = -as(\mathbf{x}, t) + b,$$

where a, b are given positive numbers. Note that every member of this group wants to follow the motion path explicitly given by $\nabla\phi$ (with ϕ the potential function solving the eikonal equation), which minimizes the distance between particle positions $\mathbf{x}_{a_i}$ and the exit location E.

As mentioned before, concerning the second population, since the agents do not know the geometry, they must rely on the information from their neighbor. The unfamiliarity with the local environment is expressed here by means of a Brownian motion term B_i. Moreover, the passive agents like to stay away the fire – for this to happen, we use a repulsion term pinpointing to the location of the fire source ∇H_ϵ. Hence, the dynamics is described as a stochastic differential equation as follows:

$$\begin{cases} \frac{d\mathbf{x}_{b_k}(t)}{dt} = \sum_{j=1}^{N} \frac{(\mathbf{x}_{c_j} - \mathbf{x}_{b_k})}{\|\mathbf{x}_{c_j} - \mathbf{x}_{b_k}\|} w(\hat{\delta}, s(\mathbf{x}_{b_k}, t)) - \nabla H_\epsilon(\mathbf{x}_{b_k}, t) + \tilde{D} B_k(t), \\ \mathbf{x}_{b_k}(0) = \mathbf{x}_{b_k,0}. \end{cases} \tag{22}$$

Here $\tilde{D}$ is the constant diffusion coefficient matrix, while $\hat{\delta} \sim \|\mathbf{x}_{c_j} - \mathbf{x}_{b_k}\|$, and w is a weight factor decreasing as a function of distance. They are defined as

$$w(x, y) \sim \frac{1}{r_s^2} \exp\left(-\frac{(x - y)^2}{r_s^2} \right). \tag{23}$$

In (23), r_s is the sight radius in the evacuees location. Since H is in general not differentiable everywhere (cf., e.g., (50)), in order to be able to take the gradient of H, we consider from the start a mollified H, say H_ϵ. Furthermore, note that $\tilde{D}$ can in principle also depend on the space position. This way the random effects can be skipped in the regions where the geometry is not available for walking. It is worth noting that we have many ways to express how the active agents sense the fire. We choose here to introduce the fire location as a region to be avoided and impose it in the definition domain of the eikonal equation. It is worth comparing this model for the evolution of the passive agents and the one prescribed in Model 1. Notice here the following important aspects: not only the dynamics is overdamped, but also the expression of the social velocity is slightly adapted to avoid an implicit definition.

7.2 Well-Posedness

Our evolution system consists of an ODE (20) coupled to an SDE (22). Therefore, due to the randomness incorporated in the SDE (22), the ODE becomes an SDE after coupling. So, we can consider (20) and (22) as a SDE system. Note that this system is one-way coupled with the reaction-diffusion-drift equation describing the smoke evolution.

For convenience, we rephrase the solution to the system (20) and (22) in terms of the vector $\mathbf{x}_t^n$ such that

$$\mathbf{x}_t^n = (\mathbf{x}_{a_i}^n(t), \mathbf{x}_{b_k}^n(t)), \tag{24}$$

$$F_1(\mathbf{x}_t^n, t) := -\Upsilon(s(\mathbf{x}_{a_i}^n, t)) \frac{\nabla\phi(\mathbf{x}_{a_i}^n)}{\|\nabla\phi(\mathbf{x}_{a_i}^n)\|} (p_{\max} - p(\mathbf{x}_{a_i}^n, t)), \tag{25}$$

$$F_2(\mathbf{x}_t^n, t) := \sum_{j=1}^{N} \frac{(\mathbf{x}_{c_j}^n - \mathbf{x}_{b_k}^n)}{\|\mathbf{x}_{c_j}^n - \mathbf{x}_{b_k}^n\|} w(\hat{\delta}, s(\mathbf{x}_{b_k}^n, t)) - \nabla H_\epsilon(\mathbf{x}_{b_k}^n, t). \tag{26}$$

Furthermore, we set

$$b_n(\mathbf{x}_t^n, t) := \begin{bmatrix} F_1(\mathbf{x}_t^n, t) \\ F_2(\mathbf{x}_t^n, t) \end{bmatrix} \text{ and } \tilde{\sigma} := \begin{bmatrix} \tilde{0} \\ \tilde{D} \end{bmatrix}, \tag{27}$$

with

$$\tilde{0} := \begin{bmatrix} 0 & 0 \\ 0 & 0 \end{bmatrix} \quad \text{and } \tilde{D} := \begin{bmatrix} D_{11} & D_{12} \\ D_{21} & D_{22} \end{bmatrix} \tag{28}$$

and initial datum

$$\mathbf{x}_0^n := \begin{bmatrix} \mathbf{x}_{a_i,0}^n \\ \mathbf{x}_{b_k,0}^n \end{bmatrix}. \tag{29}$$

In this section, we use the compactness method for proving the existence of solutions; we follow the arguments by G. Da Prato and J. Zabczyk (2014) (cf. [18], Section 8.3) and a result of F. Flandoli (1995) (cf. [23]) for martingale solutions. The starting point of this argument is based on considering a sequence $\{\mathbf{x}_t^n\}$ of solutions of the following stochastic differential equation:

$$\begin{cases} d\mathbf{x}_t^n = b_n(\mathbf{x}_t^n, t)dt + \tilde{\sigma}\, dB_t \\ \mathbf{x}_0^n = \mathbf{x}_0^n \end{cases} \tag{30}$$

To ensure the applicability of the compactness argument, we need the following structural assumptions:

(A_5) b_n be a consequence of continuous functions and uniformly Lipschitz in x.
(A_6) b_n be equibounded $\|b_n\|_\infty \leq C$.

It is not difficult to see that in our case, Assumptions (A_4) and (A_5) are fulfilled. By $s \in C([0, T]; C^1(\Omega))$ from Remark 1, we have $\tilde{v}_s$ Lipschitz in x. Moreover, by Assumption (A_1), we obtain $\nabla\phi$ is Lipschitz for $x \in \Omega$. On the other hand, the term $p_{\max} - p(\mathbf{x}_{a_i}, t)$ is a finite measure on bounded sets – it is automatically Lipschitz. These considerations lead to the fact that F_1 is Lipschitz in $x \in \Omega$. In addition, by (A_2) together with taking H_ϵ (as a mollified H) implies that ∇H_ϵ is uniformly Lipschitz in $x \in \Omega$. By the formula (23), the weight factors are Lipschitz in $x \in \Omega$. Thus, F_2 inherits the Lipschitz property. Clearly, from these arguments, we obtain not only that F_1 and F_2 are Lipschitz but also that these functions are equibounded $\|F_1\|_\infty \leq C$ and $\|F_2\|_\infty \leq C$. Hence, we have b_n satisfying both assumptions (A_4) and (A_5).

The compactness argument proceeds as follows. We begin with solutions $\mathbf{x}_t^n$, $n \in \mathbb{N}$ of the system (20) and (22), describing in (30). The construction of these solutions can be investigated on a probability space $(\Omega, \mathscr{F}, P)$ with a filtration $\{\mathscr{F}_t\}$ and a Brownian motion $B(t)$. Next, let Q^n be the laws of $\mathbf{x}_t^n$ which is defined cf. (14). Then, by using Prokhorov's theorem, we show that the sequence of laws $\{Q^n(\mathbf{x}_t^n)\}$ is weakly convergent to $Q(\mathbf{x}_t)$ in $C([0, T]; \mathbb{R}^d)$. Then, by using the "Skorohod representation theorem," the weak convergence is in a new probability space with a new stochastic process, for a new filtration. This leads to some arguments for weak convergence results of two stochastic processes in two different probability spaces that we need to use to obtain the existence of our SDE system. Finally, we prove the uniqueness of solutions to our system.

Let us start with handling the tightness of the laws $\{Q^n\}$ through the following lemma.

Lemma 1 *Assume (A_4) and (A_5) hold. The family of $\{Q^n\}$ is tight in $C([0, T]; \mathbb{R}^d)$*

Proof In order to prove the tightness, let us recall the following compact sets $K_{M,P}$ (as in the preliminaries Sect. 7.1):

$$K_{M_1 M_2} = \left\{ f \in C([0, T]; \mathbb{R}^d);\ \|f\|_\infty \leq M_1, [f]_{C^\alpha} \leq M_2 \right\}$$

Now, we will show that for a given $\varepsilon > 0$, there are $M_1, M_2 > 0$ such that

$$P(\mathbf{x}^n_\cdot \in K^c_{M_1 M_2}) < \varepsilon, \text{ for all } n \in \mathbb{N}.$$

This means that

$$P(\|\mathbf{x}^n_\cdot\|_\infty > M_1 \text{ or } [\mathbf{x}^n_\cdot]_{C^\alpha} > M_2) < \varepsilon.$$

A sufficient condition is

$$P(\|\mathbf{x}^n_\cdot\|_\infty > M_1) < \frac{\varepsilon}{2} \text{ and } P([\mathbf{x}^n_\cdot]_{C^\alpha} > M_2) < \frac{\varepsilon}{2}. \tag{31}$$

Now, we consider the first one $P(\|\mathbf{x}^n_\cdot\|_\infty > M_1) < \frac{\varepsilon}{2}$. Using Markov's inequality (cf. [29], Corollary 5.1), we get

$$P(\|\mathbf{x}^n_\cdot\|_\infty > M_1) \leq \frac{1}{M_1} E\left[\sup_{t\in[0,T]} \left|\mathbf{x}^n_t\right|\right],$$

but

$$\sup_{t\in[0,T]} \left|\mathbf{x}^n_t\right| = \sup_{t\in[0,T]} \left\{ \left| \mathbf{x}^n_{a_i,0} + \int_0^t F_1(\mathbf{x}^n_y, y)dy \right|, \right.$$
$$\left. \left| \mathbf{x}^n_{b_k,0} + \int_0^t F_2(\mathbf{x}^n_y, y)dy + \int_0^t \tilde{\sigma}\, dB_y \right| \right\}.$$

We estimate

$$\sup_{t\in[0,T]} \left|\mathbf{x}^n_t\right| \leq \sup_{t\in[0,T]} \left\{ |\mathbf{x}^n_{a_i,0}| + \left| \int_0^t F_1(\mathbf{x}^n_y, y)dy \right|, |\mathbf{x}^n_{b_k,0}| \right.$$
$$\left. + \left| \int_0^t F_2(\mathbf{x}^n_y, y)dy \right| + \left| \int_0^t \tilde{\sigma}\, dB_y \right| \right\}$$

Since F_1, F_2 bounded, then we have

$$\int_0^T \left| F_1(\mathbf{x}^n_y, y) \right| dy = \int_0^T \left| -\Upsilon(s(\mathbf{x}^n_{a_i}, y)) \left(\frac{\nabla\phi(\mathbf{x}^n_{a_i})}{\|\nabla\phi(\mathbf{x}^n_{a_i})\|} \right) (p_{\max} - p(\mathbf{x}^n_{a_i}, y)) \right| dy \leq C,$$

$$\int_0^T \left| F_2(\mathbf{x}^n_y, y) \right| dy = \int_0^T \left| \sum_{j=1}^N \frac{(\mathbf{x}^n_{c_j} - \mathbf{x}^n_{b_k})}{\|\mathbf{x}^n_{c_j} - \mathbf{x}^n_{b_k}\|} w(\hat{\delta}, s(\mathbf{x}^n_{b_k}, y)) - \nabla H_\epsilon(\mathbf{x}^n_{b_k}, y) \right| dy \leq C.$$

Taking the expectation, we have the following estimate:

$$E\left[\sup_{t\in[0,T]}|\mathbf{x}_t^n|\right]\leq C.$$

Hence, for $\varepsilon>0$, we can choose $M_1>0$ such that $P(\|\mathbf{x}_\cdot^n\|_\infty>M_1)<\frac{\varepsilon}{2}$.

From now on, we consider the second inequality in (31). This reads

$$P([\mathbf{x}_\cdot^n]_{C^\alpha}>M_2)=P\left(\sup_{t\neq r}\frac{|\mathbf{x}_t^n-\mathbf{x}_t^r|}{|t-r|}>M_2\right)\leq\frac{\varepsilon}{2}.$$

Let us introduce another class of compact sets now in the Sobolev space $W^{\alpha,p}(0,T;\mathbb{R}^d)$ (which for suitable exponents lies in $C^\gamma([0,T],\mathbb{R}^d)$). Additionally, we recall the relatively compact sets $K'_{M_1M_2}$ in (19) such that

$$K'_{M_1M_2}=\left\{f\in C([0,T];\mathbb{R}^d);\,\|f\|_\infty\leq M_1,\,[f]_{W^{\alpha,p}}\leq M_2\right\}.$$

A sufficient condition for $K'_{M_1M_2}$ to be relatively compact in the underlying space is $\alpha p>1$. Having this in mind, we wish to prove that there exist $\alpha\in(0,1)$ and $p>1$ with $\alpha p>1$ together with the property: given $\varepsilon>0$, there is $M_2>0$ such that

$$P([\mathbf{x}_\cdot^n]_{W^{\alpha,p}}>M_2)<\frac{\varepsilon}{2},$$

for every $n\in\mathbb{N}$.

Using Markov's inequality, we obtain

$$\begin{aligned}P([\mathbf{x}_\cdot^n]_{W^{\alpha,p}}>M_2)&\leq\frac{1}{M_2}E\left[\int_0^T\int_0^T\frac{|\mathbf{x}_t^n-\mathbf{x}_r^n|^p}{|t-r|^{1+\alpha p}}dtdr\right]\\&=\frac{C}{M_2}\int_0^T\int_0^T\frac{E\left[|\mathbf{x}_t^n-\mathbf{x}_r^n|^p\right]}{|t-r|^{1+\alpha p}}dtdr.\end{aligned}$$

For $t\geq r$, we have

$$\mathbf{x}_t^n-\mathbf{x}_r^n=\begin{pmatrix}\int_r^t F_1(\mathbf{x}_y^n,y)dy\\ \int_r^t F_2(\mathbf{x}_y^n,y)dy\end{pmatrix}+\begin{pmatrix}0\\ \int_r^t\tilde{\sigma}\,dB_y\end{pmatrix}.$$

Let us introduce some further notation. For a vector $u=(u_1,u_2)$, we set $|u|:=|u_1|+|u_2|$. At this moment, we consider the following expression:

$$|\mathbf{x}_t^n-\mathbf{x}_r^n|=\left|\int_r^t F_1(\mathbf{x}_y^n,y)dy\right|+\left|\int_r^t F_2(\mathbf{x}_y^n,y)dy+\int_r^t\tilde{\sigma}\,dB_y\right|.\qquad(32)$$

Taking the modulus up to the power $p > 1$, (32) reads

$$\begin{aligned}|\mathbf{x}_t^n - \mathbf{x}_r^n|^p &= \left(\left|\int_r^t F_1(\mathbf{x}_y^n, y)dy\right| + \left|\int_r^t F_2(\mathbf{x}_y^n, y)dy + \int_r^t \tilde{\sigma} dB_y\right|\right)^p \\ &\leq \left|\int_r^t F_1(\mathbf{x}_y^n, y)dy\right|^p + \left|\int_r^t F_2(\mathbf{x}_y^n, y)dy\right|^p + \left|\int_r^t \tilde{\sigma} dB_y\right|^p \\ &\leq \int_r^t \left|F_1(\mathbf{x}_y^n, y)\right|^p dy + \int_r^t \left|F_2(\mathbf{x}_y^n, y)\right|^p dy + \left|\int_r^t \tilde{\sigma} dB_y\right|^p \\ &\leq C(t-r)^p + \left|\int_r^t \tilde{\sigma} dB_y\right|^p. \end{aligned} \tag{33}$$

Taking the expectation on (33), we obtain the following estimate:

$$E[|\mathbf{x}_t^n - \mathbf{x}_r^n|^p] \leq C(t-r)^p + E\left[\left|\int_r^t \tilde{\sigma} dB_y\right|^p\right]. \tag{34}$$

Now, we consider the second term of the right-hand side of (34). By using the Burkholder-Davis-Gundy inequality (cf. [18], Hypothesis 6.4), we obtain

$$E\left[\left|\int_r^t \tilde{\sigma} dB_y\right|^p\right] \leq CE\left[\left(\int_r^t dy\right)^{p/2}\right] \leq C(t-r)^{p/2}. \tag{35}$$

Combining (34) and (35), we have the upper bound

$$E[|\mathbf{x}_t^n - \mathbf{x}_r^n|^p] \leq C(t-r)^{p/2}.$$

On the other hand, the integral

$$\int_0^T \int_0^T \frac{1}{|t-r|^{1+(\alpha-\frac{1}{2})p}} dtdr$$

is finite if $\alpha < \frac{1}{2}$. Consequently, we can pick $\alpha < \frac{1}{2}$. Taking now $p > 2$ together with the constraint $\alpha p > 1$, we can find $M_2 > 0$ such that

$$P\left([\mathbf{x}_\cdot^n]_{W^{\alpha,p}} > M_2\right) < \frac{\varepsilon}{2}.$$

This complete the proof of this lemma.

Theorem 1 *Assume* (A_1) *and* (A_2) *hold. There exists a solution to SDE system* (20) *and* (22) *that governs the microscopic dynamics.*

Proof From Lemma 1, we have obtained that the sequence $\{Q^n\}$ is tight in $C([0,T];\mathbb{R}^d)$. Applying the Prokhorov's Theorem (cf. [6], Theorem 5.1), there are subsequences $\{Q^{n_k}\}$ which converge weakly. For simplicity of the notation, we denote these subsequences by $\{Q^n\}$. This means that we have $\{Q^n\}$ converges weakly to some probability measure Q on Borel sets in $C([0,T];\mathbb{R}^d)$.

Since we have that $Q(\mathbf{x}_t^n)$ converges weakly to $Q(\mathbf{x}_t)$, by using the "Skorohod Representation Theorem" (cf. [18], Theorem 2.4), there exists a probability space $(\tilde{\Omega}, \tilde{\mathscr{F}}, \tilde{P})$ with the filtration $\{\tilde{\mathscr{F}}_t\}$ and $\tilde{\mathbf{x}}_t^n, \tilde{\mathbf{x}}_t$ belong to $C([0,T];\mathbb{R}^d)$ with $n \in \mathbb{N}$, such that $Q(\tilde{\mathbf{x}}) = Q(\mathbf{x})$, $Q(\tilde{\mathbf{x}}_t^n) = Q(\mathbf{x}_t^n)$ with $n \in \mathbb{N}$, and $\tilde{\mathbf{x}}_t^n \to \tilde{\mathbf{x}}_t$ as $n \to \infty$, $\tilde{P}-$a.s.

By using this argument, we get that $\tilde{\mathbf{x}}_t^n$ converges to $\tilde{\mathbf{x}}_t$ a.s. in the uniform topology on compacts sets, and then $\tilde{\mathbf{x}}_t^n$ converges in probability toward $\tilde{\mathbf{x}}_t$. It leads to

$$\int_r^t \tilde{b}_n(\tilde{\mathbf{x}}_y^n, y)dy \to \int_r^t \tilde{b}(\tilde{\mathbf{x}}_y, y)dy$$

in probability. To prove that these new processes satisfy the SDEs, we rely on an argument of Bensoussan cf. [5]. Essentially, we need to check that the pair $(\tilde{\mathbf{x}}_\cdot^n, \tilde{B}_\cdot)$ satisfies the following equation:

$$\tilde{\mathbf{x}}_t^n = \tilde{\mathbf{x}}_0^n + \int_0^t b_n(\tilde{\mathbf{x}}_y^n, y)dy + \int_0^t \tilde{\sigma} d\tilde{B}_y. \tag{36}$$

Let us call

$$\tilde{\mathscr{M}}_t^n := \tilde{\mathbf{x}}_t^n - \tilde{\mathbf{x}}_0^n - \int_0^t b_n(\tilde{\mathbf{x}}_y^n, y)dy - \int_0^t \tilde{\sigma} d\tilde{B}_y.$$

To prove (36), we define the following equation:

$$\mathscr{M}_t^n := \mathbf{x}_t^n - \mathbf{x}_0^n - \int_0^t b_n(\mathbf{x}_y^n, y)dy - \int_0^t \tilde{\sigma} dB_y.$$

Clearly, this definition implies $\mathscr{M}_t^n = 0 \quad P$ a.s. . Hence, we have $E\left[\frac{\mathscr{M}_t^n}{\mathscr{M}_t^n+1}\right] = 0$. Now, we want to check that

$$\tilde{E}\left[\frac{\tilde{\mathscr{M}}_t^n}{\tilde{\mathscr{M}}_t^n + 1}\right] = 0. \tag{37}$$

Consider the fact that

$$\frac{\mathscr{M}_t^n}{\mathscr{M}_t^n + 1} = \phi^n(\mathbf{x}_\cdot^n, B_\cdot) \quad \text{and} \quad \frac{\tilde{\mathscr{M}}_t^n}{\tilde{\mathscr{M}}_t^n + 1} = \phi^n(\tilde{\mathbf{x}}_\cdot^n, \tilde{B}_\cdot),$$

where ϕ^n belong to $\mathscr{B}(E)$ which is the Borel sets of E with $E := C([0,T];\mathbb{R}^d)$. We note that

$$\tilde{E}\left[\frac{\tilde{\mathscr{M}}_t^n}{\tilde{\mathscr{M}}_t^n+1}\right] = \tilde{E}[\phi^n(\tilde{\mathbf{x}}_\cdot^n, \tilde{B}_\cdot)] = \int_{\mathscr{B}(E)} \phi^n dQ^n = E[\phi^n(\mathbf{x}_\cdot^n, B_\cdot)] = E\left[\frac{M_t^n}{\mathscr{M}_t^n+1}\right].$$

Thus, (37) holds. This implies $\tilde{\mathscr{M}}_t^n = 0 \quad \tilde{P}$ a.s. Therefore, the new process, posed in the new probability space, satisfies the SDE. □

Proposition 1 *The solution of SDE system* (20) *and* (22) *is unique.*

Proof Assume that we have two distinct solutions $\mathbf{x}_1$ and $\mathbf{x}_2$ belonging to $C([0,T];\mathbb{R}^d)$ with continuous sample paths almost surely. Then it also holds

$$\mathbf{x}_1(t) - \mathbf{x}_2(t) = \int_0^t (b(\mathbf{x}_1, y) - b(\mathbf{x}_2, y))dy,$$

and hence,

$$E(|\mathbf{x}_1(t) - \mathbf{x}_2(t)|) \le E\left(\left|\int_0^t b(\mathbf{x}_1(y), y) - b(\mathbf{x}_2(y), y)dy\right|\right). \tag{38}$$

For a detailed check, we consider

$$E\begin{pmatrix} |\int_0^t F_1(\mathbf{x}_1(y), y) - F_1(\mathbf{x}_2(y), y)dy| \\ |\int_0^t F_2(\mathbf{x}_1(y), y) - F_2(\mathbf{x}_2(y), y)dy| \end{pmatrix}. \tag{39}$$

Since the terms of F_1 is Lipschitz, the first line of (39) reads

$$\begin{aligned}
&\left|\int_0^t F_1(\mathbf{x}_1(y), y) - F_1(\mathbf{x}_2(y), y)dy\right| \\
&= \left|\int_0^t \left(- \Upsilon(s(\mathbf{x}_{a_i}^1(y), y)) \left(\frac{\nabla\phi(\mathbf{x}_{a_i}^1(y))}{\|\nabla\phi(\mathbf{x}_{a_i}^1(y))\|}\right)(p_{\max} - p(\mathbf{x}_{a_i}^1(y), y))\right.\right. \\
&\quad \left.\left. + \Upsilon(s(\mathbf{x}_{a_i}^2(y), y)) \left(\frac{\nabla\phi(\mathbf{x}_{a_i}^2(y))}{\|\nabla\phi(\mathbf{x}_{a_i}^2(y))\|}\right)(p_{\max} - p(\mathbf{x}_{a_i}^2(y), y))\right)dy\right| \\
&\le C\int_0^t |\mathbf{x}_{a_i}^2(y) - \mathbf{x}_{a_i}^1(y)|dy.
\end{aligned} \tag{40}$$

By the same argument, the second line of (39) becomes

$$\left| \int_0^t F_2(\mathbf{x}_1(y), y) - F_2(\mathbf{x}_2(y), y) dy \right| =$$

$$\left| \int_0^t \left(\sum_{j=1}^{N} \frac{(\mathbf{x}^1_{c_j} - \mathbf{x}^1_{b_k})}{\|\mathbf{x}^1_{c_j} - \mathbf{x}^1_{b_k}\|} w(\hat{\delta}, s(\mathbf{x}^1_{b_k}, y)) - \nabla H_\epsilon(\mathbf{x}^1_{b_k}, y) \right.\right.$$

$$\left.\left. - \sum_{j=1}^{N} \frac{(\mathbf{x}^2_{c_j} - \mathbf{x}^2_{b_k})}{\|\mathbf{x}^2_{c_j} - \mathbf{x}^2_{b_k}\|} w(\hat{\delta}, s(\mathbf{x}^2_{b_k}, y)) + \nabla H_\epsilon(\mathbf{x}^2_{b_k}, y) \right) dy \right| =$$

$$\left| \int_0^t \sum_{j=1}^{N_A} \frac{\mathbf{x}^1_{a_j} - \mathbf{x}^1_{b_k}}{\|\mathbf{x}^1_{a_j} - \mathbf{x}^1_{b_k}\|} w(\hat{\delta}, s(\mathbf{x}^1_{b_k}, y)) - \sum_{j=1}^{N_A} \frac{\mathbf{x}^2_{a_j} - \mathbf{x}^2_{b_k}}{\|\mathbf{x}^2_{a_j} - \mathbf{x}^2_{b_k}\|} w(\hat{\delta}, s(\mathbf{x}^2_{b_k}, y)) \right.$$

$$+ \sum_{j=1}^{N_B} \frac{\mathbf{x}^1_{b_j} - \mathbf{x}^1_{b_k}}{\|\mathbf{x}^1_{b_j} - \mathbf{x}^1_{b_k}\|} w(\hat{\delta}, s(\mathbf{x}^1_{b_k}, y)) - \sum_{j=1}^{N_B} \frac{\mathbf{x}^2_{b_j} - \mathbf{x}^2_{b_k}}{\|\mathbf{x}^2_{b_j} - \mathbf{x}^2_{b_k}\|} w(\hat{\delta}, s(\mathbf{x}^2_{b_k}, y))$$

$$\left. \nabla H_\epsilon(\mathbf{x}^2_{b_k}, y) - \nabla H_\epsilon(\mathbf{x}^1_{b_k}, y) dy \right|$$

$$= \left| \int_0^t (A_1 + A_2 + A_3) dy \right|, \tag{41}$$

where

$$A_1 := \sum_{j=1}^{N_A} \frac{\mathbf{x}^1_{a_j} - \mathbf{x}^1_{b_k}}{\|\mathbf{x}^1_{a_j} - \mathbf{x}^1_{b_k}\|} w(\hat{\delta}, s(\mathbf{x}^1_{b_k}, y)) - \sum_{j=1}^{N_A} \frac{\mathbf{x}^2_{a_j} - \mathbf{x}^2_{b_k}}{\|\mathbf{x}^2_{a_j} - \mathbf{x}^2_{b_k}\|} w(\hat{\delta}, s(\mathbf{x}^2_{b_k}, y)),$$

$$A_2 := \sum_{j=1}^{N_B} \frac{\mathbf{x}^1_{b_j} - \mathbf{x}^1_{b_k}}{\|\mathbf{x}^1_{b_j} - \mathbf{x}^1_{b_k}\|} w(\hat{\delta}, s(\mathbf{x}^1_{b_k}, y)) - \sum_{j=1}^{N_B} \frac{\mathbf{x}^2_{b_j} - \mathbf{x}^2_{b_k}}{\|\mathbf{x}^2_{b_j} - \mathbf{x}^2_{b_k}\|} w(\hat{\delta}, s(\mathbf{x}^2_{b_k}, y)),$$

$$A_3 := \nabla H_\epsilon(\mathbf{x}^2_{b_k}, y) - \nabla H_\epsilon(\mathbf{x}^1_{b_k}, y).$$

By the Lipschitz property of the weight factors, the term $\left| \int_0^t A_1 dy \right|$ reads

$$\begin{aligned}
\left|\int_0^t A_1 dy\right| &= \left|\int_0^t \sum_{j=1}^{N_A} \frac{\mathbf{x}^1_{a_j} - \mathbf{x}^1_{b_k}}{\|\mathbf{x}^1_{a_j} - \mathbf{x}^1_{b_k}\|} w(\hat{\delta}, s(\mathbf{x}^1_{b_k}, y)) - \sum_{j=1}^{N_A} \frac{\mathbf{x}^1_{a_j} - \mathbf{x}^1_{b_k}}{\|\mathbf{x}^1_{a_j} - \mathbf{x}^1_{b_k}\|} w(\hat{\delta}, s(\mathbf{x}^2_{b_k}, y))\right. \\
&\quad \left. + \sum_{j=1}^{N_A} \frac{\mathbf{x}^1_{a_j} - \mathbf{x}^1_{b_k}}{\|\mathbf{x}^1_{a_j} - \mathbf{x}^1_{b_k}\|} w(\hat{\delta}, s(\mathbf{x}^2_{b_k}, y)) - \sum_{j=1}^{N_A} \frac{\mathbf{x}^2_{a_j} - \mathbf{x}^2_{b_k}}{\|\mathbf{x}^2_{a_j} - \mathbf{x}^2_{b_k}\|} w(\hat{\delta}, s(\mathbf{x}^2_{b_k}, y)) dy\right| \\
&= \left|\int_0^t \sum_{j=1}^{N_A} \frac{\mathbf{x}^1_{a_j} - \mathbf{x}^1_{b_k}}{\|\mathbf{x}^1_{a_j} - \mathbf{x}^1_{b_k}\|} \left(w(\hat{\delta}, s(\mathbf{x}^1_{b_k}, y)) - w(\hat{\delta}, s(\mathbf{x}^2_{b_k}, y))\right)\right. \\
&\quad \left. + \sum_{j=1}^{N_A} \left(\frac{\mathbf{x}^1_{a_j} - \mathbf{x}^1_{b_k}}{\|\mathbf{x}^1_{a_j} - \mathbf{x}^1_{b_k}\|} - \frac{\mathbf{x}^2_{a_j} - \mathbf{x}^2_{b_k}}{\|\mathbf{x}^2_{a_j} - \mathbf{x}^2_{b_k}\|}\right) w(\hat{\delta}, s(\mathbf{x}^2_{b_k}, y)) dy\right| \\
&\leq C_1 \int_0^t \left|\mathbf{x}^1_{b_k}(y) - \mathbf{x}^2_{b_k}(y)\right| dy + C_2 \int_0^t \left(\left|\mathbf{x}^1_{a_j}(y) - \mathbf{x}^2_{a_j}(y)\right| \right. \\
&\quad \left. + \left|\mathbf{x}^1_{b_k}(y) - \mathbf{x}^2_{b_k}(y)\right| \right) dy. \qquad (42)
\end{aligned}$$

In (42), C_1, C_2 are constants with C_2 defined as

$$C_2 := \max\left\{\frac{1}{\|\mathbf{x}^1_{a_j} - \mathbf{x}^1_{b_k}\|}, \frac{1}{\|\mathbf{x}^2_{a_j} - \mathbf{x}^2_{b_k}\|}\right\}.$$

Thus, (42) can be written as

$$\left|\int_0^t A_1 dy\right| \leq C \int_0^t \left|\mathbf{x}^1_{a_i}(y) - \mathbf{x}^2_{a_i}(y)\right| + \left|\mathbf{x}^1_{b_k}(y) - \mathbf{x}^2_{b_k}(y)\right| dy. \qquad (43)$$

By the same argument, we consider $\left|\int_0^t A_2 dy\right|$, then we obtain

$$\begin{aligned}
\left|\int_0^t A_2 dy\right| &\leq C \int_0^t \left|\mathbf{x}^1_{b_j}(y) - \mathbf{x}^2_{b_j}(y)\right| + \left|\mathbf{x}^1_{b_k}(y) - \mathbf{x}^2_{b_k}(y)\right| dy \\
&\leq C \int_0^t \left|\mathbf{x}^1_{b_k}(y) - \mathbf{x}^2_{b_k}(y)\right| dy. \qquad (44)
\end{aligned}$$

Now, using the Lipschitz property of ∇H_ε, we estimate the last term $\left|\int_0^t A_3 dy\right|$ by

$$\left|\int_0^t A_3 dy\right| \leq C \int_0^t \left|\mathbf{x}^1_{b_k}(y) - \mathbf{x}^2_{b_k}(y)\right| dy. \qquad (45)$$

Combining (43), (44), and (45) gives

$$\left|\int_0^t (A_1 + A_2 + A_3)dy\right| \leq C \int_0^t \left|\mathbf{x}_{a_i}^1(y) - \mathbf{x}_{a_i}^2(y)\right| + \left|\mathbf{x}_{b_k}^1(y) - \mathbf{x}_{b_k}^2(y)\right| dy.$$

Therefore, from (40), (41), together with taking expectation, we obtain

$$\begin{aligned} &E\begin{pmatrix} |\int_0^t F_1(\mathbf{x}_1(y), y) - F_1(\mathbf{x}_2(y), y)dy| \\ |\int_0^t F_2(\mathbf{x}_1(y), y) - F_2(\mathbf{x}_2(y), y)dy| \end{pmatrix} \\ &\leq C\begin{pmatrix} \int_0^t |\mathbf{x}_{a_i}^1(y) - \mathbf{x}_{a_i}^2(y)|dy \\ \int_0^t \left|\mathbf{x}_{a_i}^1(y) - \mathbf{x}_{a_i}^2(y)\right| + \left|\mathbf{x}_{b_k}^1(y) - \mathbf{x}_{b_k}^2(y)\right| dy \end{pmatrix} \end{aligned}$$

From (38), we get the following estimate:

$$\begin{pmatrix} E\left(\left|\mathbf{x}_{a_i}^1 - \mathbf{x}_{a_i}^2\right|\right) \\ E\left(\left|\mathbf{x}_{b_k}^1 - \mathbf{x}_{b_k}^2\right|\right) \end{pmatrix} \leq C\begin{pmatrix} \int_0^t |\mathbf{x}_{a_i}^1(y) - \mathbf{x}_{a_i}^2(y)|dy \\ \int_0^t \left|\mathbf{x}_{a_i}^1(y) - \mathbf{x}_{a_i}^2(y)\right| + \left|\mathbf{x}_{b_k}^1(y) - \mathbf{x}_{b_k}^2(y)\right| dy \end{pmatrix}$$

Thanks to the Grönwall lemma, we obtain

$$\begin{pmatrix} E\left(\left|\mathbf{x}_{a_i}^1 - \mathbf{x}_{a_i}^2\right|\right) \\ E\left(\left|\mathbf{x}_{b_k}^1 - \mathbf{x}_{b_k}^2\right|\right) \end{pmatrix} = \begin{pmatrix} 0 \\ 0 \end{pmatrix}$$

This implies that $\mathbf{x}_1(t) = \mathbf{x}_2(t)$ almost surely that

$$P\left(\sup_{t\in[0,T]} |\mathbf{x}_1(t) - \mathbf{x}_2(t)| = 0\right) = 1.$$

□

7.3 *Background Results*

This section contains a few remarks about the regularity of the agents' paths as well as of the concentration of smoke. These results are fairly standard; we add them here for the sake of completeness of our arguments.

7.3.1 A Regularized Eikonal Equation

In this section, we regularize the eikonal equation introduced for Model 1; see (2). This is often referred to as a " viscous" eikonal equation.

For $\varepsilon > 0$, we introduce the following semilinear viscous problem approximating as $\varepsilon \to 0$ our eikonal equation:

Find $\phi_\varepsilon \in C(\overline{\Omega}) \cap C^2(\Omega)$ satisfying

$$\begin{cases} -\varepsilon \Delta \phi_\varepsilon + |\nabla \phi_\varepsilon|^2 = f^2 & \text{in } \Omega, \\ \phi_\varepsilon(x) = 0 & \text{at } \partial\Omega \cup \partial G, \\ \nabla \phi_\varepsilon \cdot \mathbf{n} = g & \text{at } E, \end{cases} \tag{46}$$

With suitable assumptions on f, g, Ω, this problem with mixed Dirichlet-Neumann boundary conditions can be shown to be well-posed; see, e.g., Theorem 2.1, p.10, in [41] for the case of the Dirichlet problem. Note also that it is sometimes convenient to transform this semilinear PDE via

$$w_a := \exp(-\varepsilon^{-1}\phi_\varepsilon) - 1, \tag{47}$$

where $a = \frac{1}{\varepsilon}$. Then w_a becomes a solution of the following linear PDE with mixed Dirichlet-Robin boundary conditions:

$$\begin{cases} -\Delta w_a + f^2 a^2 w_a + a^2 = 0 & \text{in } \Omega, \\ w_a = 0 & \text{at } \partial\Omega \cup \partial G, \\ \nabla w_a \cdot \mathbf{n} = \tilde{g}(w_a) & \text{at } E, \end{cases} \tag{48}$$

where $\tilde{g}(w_a) = -\varepsilon^{-1}(w_a + 1)g$.

7.3.2 Higher Regularity Estimates for the Smoke Concentration

We introduce the evolution of fire throughout a diffusion-dominated convection process. The production and spreading of smoke, with the smoke density $s(\mathbf{x}, t)$, are described as the following diffusion-drift-reaction equation:

$$\begin{cases} \partial_t s + \text{ div } (-D\nabla s + \mathbf{v}_d s) = y_s H(\mathbf{x}, t) & \text{in } \Omega \times (0, T], \\ (-D\nabla s + \mathbf{v}_d s) \cdot \mathbf{n} = 0 & \text{on } \partial\Omega \cup \partial G \times (0, T], \\ (-D\nabla s + \mathbf{v}_d s) \cdot \mathbf{n} = \lambda s & \text{at } \partial E \times (0, T], \\ s(x, 0) = s_0 & \text{in } \Omega \times \{t = 0\}, \end{cases} \tag{49}$$

where D is the smoke diffusive coefficient, $\mathbf{v}_d$ is a given drift corresponding (e.g., wind's velocity,...), and y_s is a smoke production coefficient, while H represents the shape and intensity of the fire. The center of the fire location is denoted by $\mathbf{x}_0$ with radius r_0. H reads

$$H(\mathbf{x},t)=\begin{cases}R(\mathbf{x},t) & \text{if } |\mathbf{x}-\mathbf{x}_0|<r_0,\\ 0 & \text{otherwise},\end{cases} \tag{50}$$

where $R(\mathbf{x},t)$ is defined by

$$R(\mathbf{x},t)=c(t)\exp\left(-\kappa\frac{|\mathbf{x}-\mathbf{x}_0|}{L}\right).$$

Here, κ is the convection heat transfer constant coefficient, $c(t)$ is a constant function depending on t, L is the typical length of a stationary temperature distribution within the geometry, and λ is an interface exchange smoke coefficient. For convenience, in order to take the gradient of H, we consider H_ϵ a suitable mollification of H. In our case, from now on, we consider the coefficient y_s as a constant c_y and put $f(x,t):=c_yH_\epsilon(x,t)$, then (49) becomes

$$\begin{cases}\partial_t s+\ \text{div}\,(-D\nabla s+\mathbf{v}_d s)=f(\mathbf{x},t) & \text{in } \Omega\times(0,T],\\ (-D\nabla s+\mathbf{v}_d s)\cdot\mathbf{n}=0 & \text{on } \partial\Omega\cup\partial G\times(0,T],\\ (-D\nabla s+\mathbf{v}_d s)\cdot\mathbf{n}=\lambda s & \text{at } \partial E\times(0,T],\\ s(\mathbf{x},0)=s_0 & \text{in } \Omega\times\{t=0\},\end{cases} \tag{51}$$

In order to have a well-posed dynamics of pedestrians model, we need the solution of (51) to belong to $C([0,T];C^1(\Omega))$. Since the pedestrian dynamics system couple one way with the smoke equation, the solution s of (51) should be Lipschitz to guarantee the well-posedness of the system. In the next part, we adapt the approach in [35] to get a short proof of increased parabolic regularity for a bounded domain Ω in $\mathbb{R}^d$. Moreover, from now on, we assume the boundaries $\partial\Omega\cup\partial G$ and ∂E are C^2 (or, at least, they satisfy the exterior sphere condition).

Theorem 2 (Lower-order regularity) *Assume Assumptions* (A_3), (A_4) *to hold. Suppose* $f\in H^1(\Omega)$ *and* $\mathbf{v}_d\in W^{1,\infty}(\Omega)$. *Then, for any* $T>0$, $t\in(0,T]$, *there exists a unique*

$$s\in C([0,T];H^1(\Omega))\text{ and }s'\in L^2(0,T;H^{-1}(\Omega))$$

that solves (51). *Furthermore, the following a priori estimates hold:*

$$\sup_{t\in[0,T]}\|s\|^2_{L^2(\Omega)}\le C_T\left(\|s_0\|^2_{L^2(\Omega)}+\|f\|^2_{L^2(\Omega)}\right)\text{ and }\|\nabla s\|^2_{L^2(\Omega)}\le\frac{C_T}{t}\left(\|s_0\|^2_{L^2(\Omega)}+\|f\|^2_{H^1(\Omega)}\right).$$

Proof We adapt the arguments from [35] to our setting and split the proof into fourth steps:

- Step 1: *Galerkin approximation*
  Firstly, we assume that the functions $w_k = w_k(x)(k \in \mathbb{N})$ are smooth and that

$$\{w_k\}_{k=1}^{\infty} \text{ is an orthonormal basis of } H^1(\Omega). \tag{52}$$

  We are looking for an approximation of (51) in the form

$$s_m(t) := \sum_{k=1}^{m} d_n^k(t) w_k, \tag{53}$$

  where the coefficients d_m^k satisfy the following system:

$$\begin{cases} \langle s_m', w_k \rangle_{L^2(\Omega)} + \langle D\nabla s_m, \nabla w_k \rangle_{L^2(\Omega)} - \langle \mathbf{v}_d s_m, \nabla w_k \rangle_{L^2(\Omega)} \\ +\langle \lambda s_m, w_k \rangle_{L^2(\partial E)} = \langle f, w_k \rangle_{L^2(\Omega)}, \\ s_m(0) = s_{0m} \text{ with } k = 1 \dots m, \end{cases} \tag{54}$$

  where

$$s_{0m} = \sum_{k=1}^{m} c_m^k w_k \to s_0 \tag{55}$$

  strongly in $L^2(\Omega)$.
- Step 2: *A priori estimates*
  The goal of this step is to obtain some useful a priori estimates. Multiplying (54) by $d_m^k(t)$, taking the summation for $k \in \{1, \dots, m\}$. Then recalling (53), using Green's formula together with the mixed boundary condition, we arrive at

$$\frac{1}{2}\frac{d}{dt}\|s_m(t)\|_{L^2(\Omega)}^2 + \int_{\Omega} \nabla s_m \cdot D\nabla s_m dx + \int_{\partial E} \lambda s_m^2 d\sigma(E) = \int_{\Omega} s_m \mathbf{v}_d \cdot \nabla s_m dx + \int_{\Omega} f s_m dx. \tag{56}$$

  Thanks to Cauchy-Schwarz's inequality ε for an $\varepsilon > 0$, we have

$$\frac{1}{2}\frac{d}{dt}\|s_m(t)\|_{L^2(\Omega)}^2 + \int_{\Omega} \nabla s_m \cdot D\nabla s_m dx + \int_{\partial E} \lambda s_m^2 d\sigma(E) \le +\|\mathbf{v}_d\|_{1,\infty}\Big(\varepsilon\|s_m\|_{L^2(\Omega)}^2 + \frac{1}{\varepsilon}\|\nabla s_m\|_{L^2(\Omega)}^2\Big) + \frac{1}{2}\left(\|f\|_{L^2(\Omega)}^2 + \|s_m\|_{L^2(\Omega)}^2\right).$$

Next, by using the ellipticity property of the diffusion coefficient D and the assumption on the interface exchange coefficient, we obtain

$$\frac{1}{2}\frac{d}{dt}\|s_m(t)\|^2_{L^2(\Omega)} \leq -\underline{\theta}\|\nabla s_m\|^2_{L^2(\Omega)} + \underline{\gamma}\|s_m\|^2_{L^2(\partial E)} + \|\mathbf{v}_d\|_{1,\infty}\left(\frac{1}{\varepsilon}\|s_m\|^2_{L^2(\Omega)} + \varepsilon\|\nabla s_m\|^2_{L^2(\Omega)}\right) + \frac{1}{2}\left(\|f\|^2_{L^2(\Omega)} + \|s_m\|^2_{L^2(\Omega)}\right). \tag{57}$$

By the trace inequality applied to $\|s_m\|^2_{L^2(\partial E)}$, (57) reads

$$\frac{1}{2}\frac{d}{dt}\|s_m(t)\|^2_{L^2(\Omega)} \leq -\underline{\theta}\|\nabla s_m\|^2_{L^2(\Omega)} + C(\underline{\gamma})\|s_m\|^2_{H^1(\Omega)} + \|\mathbf{v}_d\|_{1,\infty}\left(\frac{1}{\varepsilon}\|s_m\|^2_{L^2(\Omega)} + \varepsilon\|\nabla s_m\|^2_{L^2(\Omega)}\right) + \frac{1}{2}\left(\|f\|^2_{L^2(\Omega)} + \|s_m\|^2_{L^2(\Omega)}\right).$$

By choosing $\varepsilon = \underline{\theta}(2\|\mathbf{v}_d\|_{1,\infty})^{-1}$, we get the following estimate:

$$\frac{1}{2}\frac{d}{dt}\|s_m(t)\|^2_{L^2(\Omega)} \leq C\left(\|f\|^2_{L^2(\Omega)} + \|s_m\|^2_{H^1(\Omega)}\right) + \left(C(\underline{\gamma}) - \frac{\underline{\theta}}{2}\right)\|\nabla s_m\|^2_{L^2(\Omega)}. \tag{58}$$

Multiplying with $\varphi = \partial_x s_m$ (51) differentiated with respect to x, we obtain after integrating by part that

$$\frac{1}{2}\frac{d}{dt}\|\partial_x s_m\|^2_{L^2(\Omega)} + \int_\Omega \nabla\partial_x s_m \cdot D\nabla\partial_x s_m dx + \int_\Omega \nabla\partial_x s_m \cdot \partial_x D\nabla s_m dx - \int_\Omega \nabla\partial_x s_m \cdot \mathbf{v}_d\partial_x s_m dx - \int_\Omega \nabla\partial_x s_m \cdot \partial_x\mathbf{v}_d s_m dx + \int_{\partial E}\lambda|\partial_x s_m|^2 d\sigma(E) + \int_{\partial E}\partial_x(\lambda s_m)\partial_x s_m d\sigma(E) = \int_\Omega \partial_x f\partial_x s_m dx.$$

This leads to

$$\frac{1}{2}\frac{d}{dt}\|\partial_x s_m\|^2_{L^2(\Omega)} = -\int_\Omega \nabla\partial_x s_m \cdot D\nabla\partial_x s_m dx - \int_\Omega \nabla\partial_x s_m \cdot \partial_x D\nabla s_m dx + \int_\Omega \nabla\partial_x s_m \cdot \mathbf{v}_d\partial_x s_m dx + \int_\Omega \nabla\partial_x s_n \cdot \partial_x\mathbf{v}_d s_m dx - \int_{\partial E}\lambda|\partial_x s_m|^2 d\sigma(E) - \int_{\partial E}\partial_x(\lambda s_m)\partial_x s_m d\sigma(E) + \int_\Omega \partial_x f\partial_x s_m dx. \tag{59}$$

Using the assumptions on D and λ as well as Cauchy-Schwarz' inequality for the right-hand side of (59), we obtain the following estimate:

$$\begin{aligned}\frac{1}{2}\frac{d}{dt}\|\partial_x s_m\|^2_{L^2(\Omega)} \leq & -\underline{\theta}\|\nabla\partial_x s_m\|^2_{L^2(\Omega)} + \|D\|_{W^{1,\infty}}\left(\varepsilon_1\|\nabla\partial_x s_m\|^2_{L^2(\Omega)}\right.\\ &\left.+\frac{1}{\varepsilon_1}\|\nabla s_m\|^2_{L^2(\Omega)}\right) + |\mathbf{v}_d|\left(\varepsilon_{2'}\|\nabla\partial_x s\|^2_{L^2(\Omega)} + \frac{1}{\varepsilon_{2'}}\|\partial_x s\|^2_{L^2(\Omega)}\right)\\ &+\|\mathbf{v}_d\|_{1,\infty}\left(\varepsilon_2\|\nabla\partial_x s\|^2_{L^2(\Omega)} + \frac{1}{\varepsilon_2}\|s\|^2_{L^2(\Omega)}\right) + \underline{\gamma}\|\partial_x s_m\|^2_{L^2(\partial E)}\\ &+\|\lambda\|_{1,\infty}\|\partial_x s_m\|^2_{L^2(\partial E)} + \frac{1}{2}\left(\|\partial_x f\|^2_{L^2(\Omega)} + \|\partial_x s_m\|^2_{L^2(\Omega)}\right).\end{aligned}$$

By choosing $\varepsilon_1 = \underline{\theta}(4\|D\|_{1,\infty})^{-1}$, $\varepsilon_{2'} = \underline{\theta}(8C)^{-1}$, $\varepsilon_2 = \underline{\theta}(8\|\mathbf{v}_d\|_{1,\infty})^{-1}$ together with the use of the trace inequality to handle the boundary terms, we arrive at

$$\begin{aligned}\frac{1}{2}\frac{d}{dt}\|\partial_x s_m\|^2_{L^2(\Omega)} &\leq -\frac{\underline{\theta}}{2}\|\nabla\partial_x s_m\|^2_{L^2(\Omega)} + C\|\nabla s_m\|^2_{L^2(\Omega)} + C\|\partial_x s_m\|^2_{L^2(\Omega)}\\ &\quad + C\|s_m\|^2_{L^2(\Omega)} + C(\underline{\gamma})\left(\|\partial_x s_m\|^2_{L^2(\Omega)} + \|\nabla\partial_x s_m\|^2_{L^2(\Omega)}\right)\\ &\quad + \frac{1}{2}\left(\|\partial_x f\|^2_{L^2(\Omega)} + \|\partial_x s_m\|^2_{L^2(\Omega)}\right)\\ &\leq \left(-\frac{\underline{\theta}}{2} + C(\underline{\gamma})\right)\|\nabla\partial_x s_m\|^2_{L^2(\Omega)}\\ &\quad + C\left(\|\nabla s_m\|^2_{L^2(\Omega)} + \|\partial_x s_m\|^2_{L^2(\Omega)} + \|s_m\|^2_{L^2(\Omega)}\right). \qquad (60)\end{aligned}$$

Taking the summation over all first-order derivatives, we have

$$\frac{1}{2}\frac{d}{dt}\|\nabla s_m\|^2_{L^2(\Omega)} \leq \left(C(\underline{\gamma}) - \frac{\underline{\theta}}{2}\right)\|\nabla^2 s_m\|^2_{L^2(\Omega)} + C\left(\|s_m\|^2_{H^1(\Omega)} + \|f\|^2_{H^1(\Omega)}\right).$$

Let us introduce a linear expansion in t as follows:

$$\zeta_1(t) = \|s_m\|^2_{L^2(\Omega)} + \frac{C(\underline{\theta},\underline{\gamma})t}{2}\|\nabla s_m\|^2_{L^2(\Omega)}. \qquad (61)$$

Taking the derivative of (61) with respect to t, we obtain

$$\zeta_1'(t) = \frac{d}{dt}\|s_m\|^2_{L^2(\Omega)} + \frac{C(\underline{\theta},\underline{\gamma})}{2}\|\nabla s_m\|^2_{L^2(\Omega)} + \frac{C(\underline{\theta},\underline{\gamma})t}{2}\frac{d}{dt}\|\nabla s_m\|^2_{L^2(\Omega)}.$$

Combining (58) and (60), we are led to the following estimate:

$$\zeta'(t) \le 2C\left(\|f\|^2_{L^2(\Omega)} + \|s_m\|^2_{H^1(\Omega)}\right) - 2\left(C(\underline{\gamma}) - \frac{\underline{\theta}}{2}\right)\|\nabla s_m\|^2_{L^2(\Omega)} + \frac{C(\underline{\theta},\underline{\gamma})}{2}\|\nabla s_m\|^2_{L^2(\Omega)} + \frac{C(\underline{\theta},\underline{\gamma})t}{2}\Bigg[\left(C(\underline{\gamma}) - \frac{\underline{\theta}}{2}\right)\|\nabla^2 s_m\|^2_{L^2(\Omega)} + C\left(\|s_m\|^2_{H^1(\Omega)} + \|f\|^2_{H^1(\Omega)}\right)\Bigg].$$

Choosing $\underline{\theta}$, $\underline{\gamma}$ such that $-\frac{\underline{\theta}}{2} + C(\underline{\gamma}) < 0$ and put $-\frac{\underline{\theta}}{2} + C(\underline{\gamma}) =: -C(\underline{\theta},\underline{\gamma})$, we obtain

$$\zeta'(t) \le C_T\left(\|f\|^2_{H^1(\Omega)} + \zeta(t)\right) \text{ for a.e. } t \in (0,T). \tag{62}$$

Applying Grönwall's inequality to (62), we have the following estimate:

$$\zeta(t) \le C_T\left(\zeta(0) + \|f\|^2_{H^1(\Omega)}\right) = C_T\left(\|s_0\|^2_{L^2(\Omega)} + \|f\|^2_{H^1(\Omega)}\right). \tag{63}$$

Combining (61) and (63) gives

$$\|s_m(t)\|^2_{L^2(\Omega)} \le C_T\left(\|s_0\|^2_{L^2(\Omega)} + \|f\|^2_{H^1(\Omega)}\right) \tag{64}$$

and

$$\|\nabla s_m\|^2_{L^2(\Omega)} \le \frac{C_T}{Ct}\left(\|s_0\|^2_{L^2(\Omega)} + \|f\|^2_{H^1(\Omega)}\right). \tag{65}$$

The estimates (64) and (65) imply that s_m is a bounded sequence in $H^1(\Omega)$ and a.e $t \in (0,T)$.

- Step 3: *Passage to the limit* $m \to \infty$
  Using the a priori estimates (64) and (65), we obtain the following inequality:

$$\int_0^T \frac{1}{2}\frac{d}{dt}\|s_m(t)\|^2_{L^2(\Omega)}dt + \int_0^T \|\nabla s_m\|^2_{L^2(\Omega)}dt \le C_T\int_0^T\left(\|f\|^2_{H^1(\Omega)} + \|s_0\|^2_{L^2(\Omega)}\right).$$

This implies that (s_m) is a bounded sequence in $L^2(0,T;H^1(\Omega))$.
On the other hand, in order to use Aubin-Lions's lemma, we additionally need to prove $s'_m \in L^2(0,T;H^{-1}(\Omega))$. Take an arbitrary $v \in H^1(\Omega)$, with $\|v\|_{H^1(\Omega)} \le$

1. We can deduce for a.e. $0 < t < T$ that

$$\langle s'_m, v\rangle_{L^2(\Omega)} = \langle f, v\rangle_{L^2(\Omega)} + \langle \mathbf{v}_d s_m, \nabla v\rangle_{L^2(\Omega)} - \langle D\nabla s_m, \nabla v\rangle_{L^2(\Omega)} - \langle \lambda s_m, v\rangle_{L^2(\partial E)}.$$

Then, we get

$$|\langle s'_m, v\rangle| \leq C\|s_m\|_{H^1(\Omega)} + C\|f\|_{L^2(\Omega)}. \tag{66}$$

for $\|v\|_{W^{1,2}(\Omega)} \leq 1$. Moreover, (66) implies that

$$\|s'_m\|_{H^{-1}(\Omega)} \leq C\left(\|s_m\|_{H^1(\Omega)} + \|f\|_{L^2(\Omega)}\right). \tag{67}$$

Integrating (67) on $(0, T)$, we obtain the following estimate:

$$\int_0^T \|s'_m\|^2_{H^{-1}(\Omega)} dt \leq C\int_0^T \|s_m\|_{H^1(\Omega)} + \|f\|_{L^2(\Omega)} dt \leq C\left(\|s_0\|^2_{L^2(\Omega)} + \|f\|_{L^2(0,T;L^2(\Omega))}\right). \tag{68}$$

Thus, $s'_m \in L^2(0, T; H^{-1}(\Omega))$. Therefore, we conclude that

$$\begin{cases} s_m \rightharpoonup s \text{ weakly in } L^2(0, T; H^1(\Omega)), \\ s'_m \rightharpoonup s' \text{ weakly in } L^2(0, T; H^{-1}(\Omega)). \end{cases}$$

Relying on Aubin-Lions lemma in [8] with $p, q = 2$,

$$E_0 = H^1(\Omega), \quad E = L^2(\Omega), \quad E_1 = H^{-1}(\Omega)$$

together with Rellich theorem (cf. [20], Section 5.7, Theorem 1) for the compactness embedding $H^1(\Omega) \subset L^2(\Omega)$, we have that the sequence $\{s_m\}$ is relatively compact in $L^2(0, T; L^2(\Omega))$ in the strong topology. This sequence is also weakly relatively compact in $L^2(0, T; H^1(\Omega))$ and weakly star relatively compact in $C([0, T]; L^2(\Omega))$. Hence, there exists a subsequence s_{m_k} (just for simplicity of notation, let us denote it by s_m) which converges to a function s belonging to $L^2(0, T; H^1(\Omega))$ and $C([0, T]; L^2(\Omega))$. Therefore, we can conclude that there exists a solution $s \in L^2(0, T; H^1(\Omega)) \cup C([0, T]; L^2(\Omega))$ satisfying (51).

- Step 4: *Uniqueness of solutions*
  Assume that (51) admits 2 solutions s_1 and s_2 belonging to $L^2(0, T; H^1(\Omega)) \cup C([0, T]; L^2(\Omega))$. Denote $w = s_1 - s_2$. Then (51) becomes

$$\begin{cases} \partial_t w + \text{ div } (-D\nabla w + \mathbf{v}_d w) = 0 & \text{in } \Omega \times (0,T], \\ (-D\nabla w + \mathbf{v}_d w)\cdot \mathbf{n} = 0 & \text{on } \partial\Omega \cup \partial G \times (0,T], \\ (-D\nabla w + \mathbf{v}_d w)\cdot \mathbf{n} = \lambda w & \text{at } \partial E \times (0,T], \\ w(t=0) = 0 & \text{in } \Omega \times \{t=0\}, \end{cases}$$

Recalling (54), we note that

$$\frac{1}{2}\frac{d}{dt}\int_\Omega w^2 dx + \int_\Omega D|\nabla w|^2 dx + \int_{\partial E} \lambda w^2 d\sigma(E) = \int_\Omega w\mathbf{v}_d \cdot \nabla w dx,$$

which leads to

$$\frac{d}{dt}\left(\|w\|^2_{L^2(\Omega)}\right) + \overline{\theta}\|\nabla w\|^2_{L^2(\Omega)} + \overline{\gamma}\|w\|^2_{L^2(\partial E)} \le C\|w\|^2_{L^2(\Omega)}.$$

This also implies

$$\frac{d}{dt}\left(\|w\|^2_{L^2(\Omega)}\right) \le C\|w\|^2_{L^2(\Omega)}. \tag{69}$$

Integrating (69) on $(0,T)$, gives

$$\|w\|^2_{L^2(\Omega)} \le \|w(0)\|^2_{L^2(\Omega)} + C\int_0^t \|w\|^2_{L^2(\Omega)}.$$

Grönwall's lemma ensure

$$\|w\|^2_{L^2(\Omega)} \le \|w(0)\|^2_{L^2(\Omega)}(1 + Cte^{Ct}),$$

which for $w(0) = 0$, gives $\|w\|_{L^2(\Omega)} = 0$. So, $w = 0$ a.e. in Ω and everywhere in $[0,T]$, which ensures the desired uniqueness.

Now, let us show that $s \in C([0,T]; H^1(\Omega))$. We consider $w_r(t) = s(t+r) - s(t)$; then $w_r(t)$ satisfies (51) with $f = 0$, $w(0) = s_0 - s(r)$, and $\lambda s(t+r) - \lambda s(t) = \lambda w_r(t)$. By using a similar argument, we obtain

$$\|w_r(t)\|^2_{L^2(\Omega)} + \frac{C(\underline{\theta},\underline{\gamma})t}{2}\|\nabla w_r(t)\|^2_{L^2(\Omega)} \le C_T\left(\|s_0 - s(r)\|^2_{L^2(\Omega)}\right).$$

Since we have $s \in C([0,T]; L^2(\Omega))$, then $\lim_{r\to\infty}\|s(t+r) - s(t)\| = 0$ and $\lim_{r\to\infty}\|\nabla s(t+r) - \nabla s(t)\| = 0$ for $t > 0$. Therefore, we obtain $s \in C([0,T]; H^1(\Omega))$.

□

Theorem 3 (High-order regularity) *Assume* (A_3), (A_4) *to hold. Suppose* $f \in H^m(\Omega)$ *and* $\mathbf{v}_d \in W^{m,\infty}(\Omega)$ *for every* $m \in \mathbb{N}$, *and* $s_0 \in L^2(\Omega)$. *Then, for any* $T > 0$, $t \in [0,T]$, *the solution of* (51) *satisfies the following estimate:*

$$\|\nabla^k s\|^2_{L^2(\Omega)} \leq \frac{C_T}{t^k}\left(\|s_0\|^2_{L^2(\Omega)} + \|f\|^2_{H^k(\Omega)}\right) \text{ for } k = 0, 1, \ldots, m.$$

Proof We use the method of induction on $m \in \mathbb{N}$, using the fact that we have done the first case $m = 1$ mathematically in Theorem 2. We define the gradient of a function s as follows:

$$\|\nabla^k s\|^2_{L^2(\Omega)} := \sum_{|\alpha|\leq k} \|\partial_x^\alpha s\|^2_{L^2(\Omega)}.$$

Now, taking the $k-$order derivative with respect to x for $k \in \mathbb{N}$ which is denoted by ∂_x^α of (51), multiplying by $\partial_x^\alpha s$ and integrating the results by parts together with using Green's theorem for the equation, we obtain

$$\frac{1}{2}\frac{d}{dt}\|\partial_x^\alpha s(t)\|^2_{L^2(\Omega)} + \int_\Omega \nabla\partial_x^\alpha s \cdot \sum_{j=0}^{k} \sum_{|\beta|=j,\beta+\gamma=\alpha} \binom{\alpha}{\beta} \partial_x^\beta D\nabla\partial_x^\gamma s dx$$

$$- \int_\Omega \nabla\partial_x^\alpha s \cdot \sum_{j=0}^{k} \sum_{|\beta|=j,\beta+\gamma=\alpha} \binom{\alpha}{\beta} \partial_x^\beta \mathbf{v}_d \partial_x^\gamma s dx + \int_{\partial E} \partial_x^\alpha s \lambda \partial_x^\alpha s d\sigma(E)$$

$$+ \int_{\partial E} \partial_x^\alpha(\lambda s) \cdot \partial_x^\alpha s d\sigma(E) = \int_\Omega \partial_x^\alpha f \partial_x^\alpha s dx,$$

and thus

$$\frac{1}{2}\frac{d}{dt}\|\partial_x^\alpha s(t)\|^2_{L^2(\Omega)} = -\int_\Omega \nabla\partial_x^\alpha s \cdot \sum_{j=0}^{k} \sum_{|\beta|=j,\beta+\gamma=\alpha} \binom{\alpha}{\beta} \partial_x^\beta D\nabla\partial_x^\gamma s dx$$

$$+ \int_\Omega \nabla\partial_x^\alpha s \cdot \sum_{j=0}^{k} \sum_{|\beta|=j,\beta+\gamma=\alpha} \binom{\alpha}{\beta} \partial_x^\beta \mathbf{v}_d \partial_x^\gamma s dx - \int_{\partial E} \partial_x^\alpha s \lambda \partial_x^\alpha s d\sigma(E)$$

$$- \int_{\partial E} \partial_x^\alpha(\lambda s) \cdot \partial_x^\alpha s d\sigma(E) + \int_\Omega \partial_x^\alpha f \partial_x^\alpha s dx. \tag{70}$$

Denote

$$A := -\int_\Omega \nabla\partial_x^\alpha s \cdot \sum_{j=0}^{k} \sum_{|\beta|=j,\beta+\gamma=\alpha} \binom{\alpha}{\beta} \partial_x^\beta D\nabla\partial_x^\gamma s dx$$

$$= -\int_\Omega \nabla\partial_x^\alpha s \cdot D\nabla\partial_x^\alpha s dx - \int_\Omega \nabla\partial_x^\alpha s \cdot \sum_{j=1}^{k} \sum_{|\beta|=j,\beta+\gamma=\alpha} \binom{\alpha}{\beta} \partial_x^\beta D\nabla\partial_x^\gamma s dx.$$

We can estimate $|A|$ from above:

$$|A| \leq -\underline{\theta}\|\nabla\partial_x^\alpha s\|^2_{L^2(\Omega)} + C\|D\|_{1,\infty}\left(\varepsilon_1\|\nabla\partial_x^\alpha s\|^2_{L^2(\Omega)} + \frac{1}{\varepsilon_1}\|s\|^2_{H^{k-1}(\Omega)}\right)$$
$$\leq \frac{-\underline{\theta}}{2}\|\nabla\partial_x^\alpha s\|^2_{L^2(\Omega)} + C\|s\|^2_{H^{k-1}(\Omega)}, \quad (71)$$

where we choose $\varepsilon_1 = \underline{\theta}(4C\|D\|_{m,\infty})^{-1}$. Set

$$B := \int_\Omega \nabla\partial_x^\alpha s \cdot \sum_{j=0}^{k}\sum_{|\beta|=j,\beta+\gamma=\alpha}\binom{\alpha}{\beta}\partial_x^\beta \mathbf{v}_d\partial_x^\gamma s dx,$$

and obtain the upper bound

$$|B| \leq C\|\mathbf{v}_d\|_{m,\infty}\left(\varepsilon_2\|\nabla\partial_x^\alpha s\|^2_{L^2(\Omega)} + \frac{1}{\varepsilon_2}\|\partial_x^\alpha s\|^2_{H^{k-1}(\Omega)}\right). \quad (72)$$

Now, let us label the third and fourth terms in the right-hand side of (70) as follows:

$$\tilde{C} := -\int_{\partial E}\partial_x^\alpha s\lambda\partial_x^\alpha s d\sigma(E) - \int_{\partial E}\partial_x^\alpha(\lambda s)\cdot\partial_x^\alpha s d\sigma(E).$$

Using the assumptions on λ together with applying Cauchy's inequality, trace inequality for $\tilde{C}$, we have the following estimate:

$$\tilde{C} \leq \underline{\gamma}\|\partial_x^\alpha s\|^2_{L^2(\partial E)} + \|\lambda\|_{m,\infty}\|\partial_x^\alpha s\|^2_{L^2(\partial E)} \leq C(\underline{\gamma})\left(\|\nabla\partial_x^\alpha s\|^2_{L^2(\Omega)} + \|\partial_x^\alpha s\|^2_{L^2(\Omega)}\right). \quad (73)$$

Finally, we estimate the last term of (70), by using Cauchy's inequality, we obtain

$$\int_\Omega \partial_x^\alpha f\partial_x^\alpha s dx \leq \frac{1}{2}\left(\|\partial_x^\alpha f\|^2_{L^2(\Omega)} + \|\partial_x^\alpha s\|^2_{L^2(\Omega)}\right). \quad (74)$$

Combining (71), (72), (73), and (74) and choosing $\varepsilon_2 = \underline{\theta}(4C\|\mathbf{v}_d\|_{1,\infty})^{-1}$, we have the following estimate:

$$\frac{1}{2}\frac{d}{dt}\|\partial_x^\alpha s(t)\|^2_{L^2(\Omega)} \leq \frac{-\underline{\theta}}{2}\|\nabla\partial_x^\alpha s\|^2_{L^2(\Omega)} + C\|s\|^2_{H^{k-1}(\Omega)} + C\|\partial_x^\alpha s\|^2_{H^{k-1}(\Omega)}$$
$$+C(\underline{\gamma})\|\nabla\partial_x^\alpha s\|^2_{L^2(\Omega)} + \|f\|^2_{H^k(\Omega)}.$$

Now, summing all of first-order derivatives, we obtain

$$\frac{1}{2}\frac{d}{dt}\|\nabla^k s(t)\|^2_{L^2(\Omega)} \leq \left(C(\underline{\gamma}) - \frac{\underline{\theta}}{2}\right)\|\nabla^{k+1} s\|^2_{L^2(\Omega)} + C\left(\|f\|^2_{H^k(\Omega)} + \|s\|^2_{H^k(\Omega)}\right). \tag{75}$$

Now, we aim to find $s \in C([0,T], H^{m-1}(\Omega))$ using the induction hypothesis under the assumptions $f \in H^{m-1}(\Omega)$ and $D, \lambda, \mathbf{v}_d \in W^{m,\infty}(0,T;\Omega)$. Using the same argument as in the case $m = 1$, we define

$$\zeta_2(t) := \sum_{k=1}^{n} \frac{(C(\underline{\theta},\underline{\gamma})t)^k}{2^k k!}\|\nabla^k s\|^2_{L^2(\Omega)}. \tag{76}$$

Taking the derivative of (76) with respect to t, we obtain

$$\begin{aligned}\zeta_2'(t) &= \sum_{k=1}^{m} \frac{(C(\underline{\theta},\underline{\gamma}))^k t^{k-1}}{2^k(k-1)!}\|\nabla^k s\|^2_{L^2(\Omega)} + \sum_{k=0}^{m} \frac{(C(\underline{\theta},\underline{\gamma}))^k}{2^k k!}\frac{d}{dt}\|\nabla^k s\|^2_{L^2(\Omega)} \\ &:= G_1 + G_2.\end{aligned}$$

$$\begin{aligned}G_2 &\leq \sum_{k=0}^{m} \frac{(C(\underline{\theta},\underline{\gamma})t)^k}{2^k k!}\left(-C(\underline{\theta},\underline{\gamma})\|\nabla^{k+1} s\|^2_{L^2(\Omega)} + C\left(\|f\|^2_{H^k(\Omega)} + \|s\|^2_{H^k(\Omega)}\right)\right) \\ &= -2\sum_{k=0}^{m} \frac{(C(\underline{\theta},\underline{\gamma}))^{k+1} t^k}{2^{k+1}k!}\|\nabla^{k+1} s\|^2_{L^2(\Omega)} \\ &+ C\sum_{k=0}^{m} \frac{(C(\underline{\theta},\underline{\gamma}))^k}{2^k k!}\left(\|f\|^2_{H^k(\Omega)} + \|s\|^2_{H^k(\Omega)}\right) \\ &\leq -2G_1 - \frac{2(C(\underline{\theta},\underline{\gamma}))^{m+1} t^m}{2^{m+1}m!}\|\nabla^{m+1} s\|^2_{L^2(\Omega)} \\ &+ C\sum_{k=0}^{m} \frac{(C(\underline{\theta},\underline{\gamma}))^k}{2^k k!}\left(\|f\|^2_{H^k(\Omega)} + \|s\|^2_{H^k(\Omega)}\right).\end{aligned} \tag{77}$$

On the other hand, the induction hypothesis gives the following inequality:

$$\|s\|^2_{H^{k-1}(\Omega)} \leq \frac{C_T}{t^{k-1}}\left(\|f\|^2_{H^{k-1}(\Omega)} + \|s_0\|^2_{L^2(\Omega)}\right). \tag{78}$$

Combining (77) and (78), we obtain

$$\begin{aligned}
\zeta_2'(t) &\le C \sum_{k=0}^{m} \frac{(C(\underline{\theta}, \underline{\gamma}))^k}{2^k k!} \left(\|f\|^2_{H^k(\Omega)} + \|s\|^2_{H^k(\Omega)} \right) \\
&\le C_T \left(\|f\|^2_{H^m(\Omega)} + \sum_{k=0}^{m} \frac{(C(\underline{\theta}, \underline{\gamma})t)^k}{2^k k!} \left[\|\nabla^k s\|^2_{L^2(\Omega)} + \|s\|^2_{H^{k-1}(\Omega)} \right] \right) \\
&\le C_T \left(\|f\|^2_{H^m(\Omega)} + \zeta_2(t) + \sum_{k=0}^{m} \frac{(C(\underline{\theta}, \underline{\gamma})t)^k}{2^k k!} \frac{C_T}{t^{k-1}} \left[\|f\|^2_{H^{k-1}(\Omega)} + \|s_0\|^2_{L^2(\Omega)} \right] \right) \\
&\le C_T \left(\|f\|^2_{H^m(\Omega)} + \|s_0\|^2_{L^2(\Omega)} + \zeta_2(t) \right).
\end{aligned}$$

Grönwall's inequality yields

$$\zeta_2(t) \le C_T \left(\|f\|^2_{H^m(\Omega)} + \|s_0\|^2_{L^2(\Omega)} + \zeta_2(0) \right) \le C_T \left(\|f\|^2_{H^m(\Omega)} + \|s_0\|^2_{L^2(\Omega)} \right).$$

The bound on $\zeta_2(t)$ gives the following estimate:

$$\|\nabla^m s\|^2_{L^2(\Omega)} \le \frac{C_T}{(C(\underline{\theta}, \underline{\gamma})t)^m},$$

which completes the induction proof. □

Remark 1 From Theorem 3, for $m = 3$, $\Omega \subset \mathbb{R}^d$ with $d = 2$, there exists a unique solution $s \in C([0, T]; C^1(\Omega))$ and $s' \in L^2(0, T; H^{-1}(\Omega))$ that solves (51).

By the same arguments as in Theorem 2, this also implies that $s \in C([0, T]; H^m(\Omega))$. In our model, we consider our domain in $\Omega \subset \mathbb{R}^d$ with $d = 2$. Moreover, assume Ω satisfies the strong locally Lipschitz condition (cf. [1], Theorem 4.12), taking $m = 3$, hence $H^3(\Omega)$ compact embedding into $C^1(\Omega)$, i.e., $H^3(\Omega) \subset C^1(\Omega)$. As a conclusion, we obtain $s \in C([0, T]; C^1(\Omega))$. This property ensures that the smoke concentration s is Lipschitz with respect to the space variable – a fact needed to handle the well-posedness of our SDEs.

8 Discussion

In this chapter, we presented various models aimed at modelling crowds of mixed populations (active and passive) moving inside heterogeneous environments.

Based on our numerical experiments, we observed the impact of passive agents on the residence times of the population and conclude that the lack of environment knowledge can have a substantial impact on the evacuation. Additionally, we notice

that the size of the obstacles and doors has a significant influence on the overall dynamics.

While the presence of passive agents increases the evacuation time, we speculate that by manipulating the spatial distribution of active particles, it is possible to optimize the residence time of the passive agents. We plan to investigate these aspects in a forthcoming publication.

From a mathematical point of view, the situation becomes a lot more challenging when there is a feedback mechanism between the agent-based dynamics and the environment (fire, smoke, geometry). Formulating this relationship mathematically would allow for an optimization approach, potentially in a multiscale setting. The main advantage of such a mathematical framework would be to contribute to an intelligent design of building interiors and to provide a basis for smart evacuation signaling systems.

References

1. Adams, R.A., Fournier, J.J.: Sobolev Spaces, vol. 140. Academic Press (2003)
2. Anh, N.T.N., Daniel, Z.J., Du, N.H., Drogoul, A., An, V.D.: A hybrid macro-micro pedestrians evacuation model to speed up simulation in road networks. In: International Conference on Autonomous Agents and Multiagent Systems, pp. 371–383. Springer (2011)
3. Bellomo, N., Clarke, D., Gibelli, L., Townsend, P., Vreugdenhil, B.: Human behaviours in evacuation crowd dynamics: from modelling to big data toward crisis management. Physics of Life Reviews **18**, 1–21 (2016)
4. Bellomo, N., Gibelli, L.: Toward a mathematical theory of behavioral-social dynamics for pedestrian crowds. Mathematical Models and Methods in Applied Sciences **25**(13), 2417–2437 (2015)
5. Bensoussan, A.: Stochastic Navier-Stokes equations. Acta Applicandae Mathematica **38**(3), 267–304 (1995)
6. Billingsley, P., Dudley, R., et al.: Convergence of probability measures. Bulletin of the American Mathematical Society **77**(1), 25–27 (1971)
7. Bortz, A., Kalos, M., Lebowitz, J.: A new algorithm for Monte Carlo simulation of Ising spin systems. Journal of Computational Physics **17**(1), 10–18 (1975)
8. Boyer, F., Fabrie, P.: Mathematical tools for the study of the incompressible Navier-Stokes equations and related models, vol. 183. Springer Science & Business Media (2012)
9. Cao, S., Song, W., Liu, X., Mu, N.: Simulation of pedestrian evacuation in a room under fire emergency. Proceeding Engineering **71**, 403–409 (2014)
10. Chu, M.L., Parigi, P., Law, K., Latombe, J.C.: Modeling social behaviors in an evacuation simulator. Computer Animation and Virtual Worlds **25**(3–4), 373–382 (2014)
11. Ciallella, A., Cirillo, E.N.M., Curşeu, P.L., Muntean, A.: Free to move or trapped in your group: Mathematical modeling of information overload and coordination in crowded populations. Mathematical Models and Methods in Applied Sciences M3AS (2018)
12. Cirillo, E.N.M., Colangeli, M.: Stationary uphill currents in locally perturbed zero-range processes. Phys. Rev. E **96**, 052,137 (2017)
13. Cirillo, E.N.M., Colangeli, M., Muntean, A.: Blockage-induced condensation controlled by a local reaction. Phys. Rev. E **94**, 042,116 (2016)
14. Colombo, R.M., Lorenz, T., Pogodaev, N.I.: On the modeling of moving populations through set evolution equations. Discrete & Continuous Dynamical Systems - A **35**(1), 73–98 (2015)

15. Corbetta, A., Bruno, L., Muntean, A., Toschi, F.: High statistics measurements of pedestrian dynamics. Transportation Research Procedia **2**, 96–104 (2014)
16. Cristiani, E., Piccoli, B., Tosin, A.: Multiscale modeling of granular flows with application to crowd dynamics. Multiscale Modeling & Simulation **9**(1), 155–182 (2011)
17. Cucker, F., Smale, S.: Emergent behavior in flocks. IEEE Transactions on automatic control **52**(5), 852–862 (2007)
18. Da Prato, G., Zabczyk, J.: Stochastic Equations in Infinite Dimensions. Cambridge University Press (2014)
19. De Masi, A., Presutti, E.: Mathematical Methods for Hydrodynamic Limits. Lecture notes in mathematics. Springer-Verlag (1991)
20. Evans, L.: Partial Differential Equations, vol. 19. American Mathematical Society (2010)
21. Evans, L.: An Introduction to Stochastic Differential Equations, vol. 82. American Mathematical Soc. (2012)
22. Faure, S., Maury, B.: Crowd motion from the granular standpoint. Mathematical Models and Methods in Applied Sciences **25**(03), 463–493 (2015)
23. Flandoli, F., Gatarek, D.: Martingale and stationary solutions for stochastic Navier-Stokes equations. Probability Theory and Related Fields **102**(3), 367–391 (1995)
24. Garcimartín, A., Pastor, J., Ferrer, L., Ramos, J., Martín-Gómez, C., Zuriguel, I.: Flow and clogging of a sheep herd passing through a bottleneck. Physical Review E **91**(2), 022,808 (2015)
25. Helbing, D., Farkas, I., Vicsek, T.: Simulating dynamical features of escape panic. Nature **407**(6803), 487 (2000)
26. Horiuchi, S., Murozaki, Y., Hukugo, A.: A case study of fire and evacuation in a multi-purpose office building, Osaka, Japan. Fire Safety Science **1**, 523–532 (1986)
27. Hughes, R.: A continuum theory for the flow of pedestrians. Transportation Research Part B: Methodological **36**(6), 507–535 (2002)
28. Hung, N.M., Vinh, H.T., Jean-Charles, R.: Modeling and simulation of fire evacuation in public buildings. Advances in Computer Science: an International Journal **4**(6), 1–7 (2015)
29. Jacod, J., Protter, P.: Probability Essentials. Springer Science & Business Media (2004)
30. Kipnis, C., Landim, C.: Scaling Limits of Interacting Particle Systems. Grundlehren der mathematischen Wissenschaften. Springer Berlin Heidelberg (1998)
31. Landau, D., Binder, K.: A Guide to Monte Carlo Simulations in Statistical Physics. Cambridge University Press, New York, NY, USA (2005)
32. Majmudar, T.S., Sperl, M., Luding, S., Behringer, R.P.: Jamming transition in granular systems. Phys. Rev. Lett. **98**, 058,001 (2007)
33. Meunier, H., Leca, J.B., Deneubourg, J.L., Petit, O.: Group movement decisions in capuchin monkeys: the utility of an experimental study and a mathematical model to explore the relationship between individual and collective behaviours. Behaviour **143**(12), 1511–1527 (2006)
34. Nguyen, M.H., Ho, T.V., Zucker, J.D.: Integration of smoke effect and blind evacuation strategy (sebes) within fire evacuation simulation. Simulation Modelling Practice and Theory **36**, 44–59 (2013)
35. Pankavich, S., Michalowski, N.: A short proof of increased parabolic regularity. Electronic Journal of Differential Equations **205** (2005)
36. Pavliotis, G.A.: Stochastic Processes and Applications: Diffusion Processes, the Fokker-Planck and Langevin Equations, vol. 60. Springer (2014)
37. Richardson, O.: Mercurial. https://github.com/0mar/mercurial (2015). Python framework for building, running and post-processing crowd simulations
38. Richardson, O.: Large-scale multiscale particle models in inhomogeneuous domains: Modelling and implementation. Master's thesis, Technische Universiteit Eindhoven (2016)
39. Richardson, O., Jalba, A., A, M.: Effects of environment knowledge in evacuation scenarios involving fire and smoke - a multiscale modelling and simulation approach. ArXiv e-prints (2017). URL https://arxiv.org/pdf/1709.07786.pdf

40. Ronchi, E., Fridolf, F., Frantzich, H., Nilsson, D., Walter, A.L., Modig, H.: A tunnel evacuation experiment on movement speed and exit choice in smoke. Fire Safety Journal (2017)
41. Schieborn, D.: Viscosity Solutions of Hamilton-Jacobi Equations of Eikonal Type on Ramified Spaces. Ph.D. thesis, University Tübingen (2006)
42. Tan, L., Hu, M., Lin, H.: Agent-based simulation of building evacuation: Combining human behavior with predictable spatial accessibility in a fire emergency. Information Sciences **295**, 53–66 (2015)
43. Treuille, A., Cooper, S., Popovic, Z.: Continuum crowds. ACM Trans. Graph. **25**(3), 1160–1168 (2006)
44. Tsai, J., Fridman, N., Bowring, E., Brown, M., Epstein, S., Kaminka, G., Marsella, S., Ogden, A., Rika, I., Sheel, A., et al.: Escapes: evacuation simulation with children, authorities, parents, emotions, and social comparison. In: The 10th International Conference on Autonomous Agents and Multiagent Systems-Volume 2, pp. 457–464. International Foundation for Autonomous Agents and Multiagent Systems (2011)
45. Voter, A.F.: Introduction to the Kinetic Monte Carlo Method. In: K.E. Sickafus, E.A. Kotomin, B.P. Uberuaga (eds.) Radiation Effects in Solids, pp. 1–23. Springer Netherlands, Dordrecht (2007)
46. Zuriguel, I., Parisi, D.R., Hidalgo, R.C., et al.: Clogging transition of many-particle systems flowing through bottlenecks. Scientific reports **4**, 7324 (2014)

Pedestrian Models Based on Rational Behaviour

Rafael Bailo, José A. Carrillo, and Pierre Degond

Abstract Following the paradigm set by attraction-repulsion-alignment schemes, a myriad of individual-based models have been proposed to calculate the evolution of abstract agents. While the emergent features of many agent systems have been described astonishingly well with force-based models, this is not the case for pedestrians. Many of the classical schemes have failed to capture the fine detail of crowd dynamics, and it is unlikely that a purely mechanical model will succeed. As a response to the mechanistic literature, we will consider a model for pedestrian dynamics that attempts to reproduce the rational behaviour of individual agents through the means of anticipation. Each pedestrian undergoes a two-step time evolution based on a perception stage and a decision stage. We will discuss the validity of this game theoretical-based model in regimes with varying degrees of congestion, ultimately presenting a correction to the mechanistic model in order to achieve realistic high-density dynamics.

1 Introduction

The behaviour of humans moving in crowds was studied early on from the engineering perspective [23, 28, 62]. These works were based on the observation of crowds, either directly or through photographs and film, and ultimately aimed to provide planning guidelines and construction directives such as [70, 71]. These studies have always had an economic concern, but most importantly a safety outlook, as a good understanding of crowd dynamics can help prevent the injuries and deaths which derive from the confluence of inordinate numbers of people in places that are not prepared for such occupancy [32, 33], for instance, as a result of a popular sporting event [26] or a concert [48]. A review of incidents of this type can be found in [61].

R. Bailo (✉) · J. A. Carrillo · P. Degond
Department of Mathematics, Imperial College London, London, UK
e-mail: r.bailo@imperial.ac.uk; carrillo@imperial.ac.uk; p.degond@imperial.ac.uk

L. Gibelli, N. Bellomo (eds.), *Crowd Dynamics, Volume 1*, Modeling and Simulation in Science, Engineering and Technology,
https://doi.org/10.1007/978-3-030-05129-7_9

The walking behaviour of humans is extremely complex and not easy to capture in models. The observed phenomena in crowds is often unintuitive, for instance, small obstacles in the way of an exit can serve to stabilise the flow and make traffic more efficient [32]; when it comes to emergencies, it is found that evacuation is safer and more efficient at lower speeds [33].

Extensive experimental work in the area has focused in numerous aspects of the dynamics of pedestrians, such as the behaviour of agents around bottlenecks [18, 19, 50], intersections [32], in counterflows [49], following behaviours [51], cluster formation [56], the effects of fatigue [55] and the empirical relation between crowd density and walking speed [67] (known as the fundamental diagram). These studies have led to some understanding of the emergent features, those that arise not from the actions of any particular individual but rather as a result of the interactions of the collective. Stop-and-go waves [35], lane formation [37, 57] (somewhat a human counterpart to flocking [64]), the crowding behaviour around bottlenecks [18, 33] and the fluid-like properties (shockwaves, turbulence) displayed by extremely dense crowds [34, 35] are just some examples of the rich and subtle properties of the dynamics. Some of these features have been successfully reproduced in models, for instance, lane formation in [36, 58]. Some, such as the fundamental diagram [75], have evaded many modelling attempts and are still the subject of avid debate despite substantial experimental work in the area [1, 47], often requiring studies specific to particular configurations such as single direction flow [45, 67], behaviour around bottlenecks [49] and assessment of the *level of service* [60, 63].

Pedestrians were early on modelled from a macroscopic perspective [39, 40, 53, 54], where only the features of the crowd as a whole (such as the pedestrian density, the flow through a corridor or the emergence of consensus [11]) are of interest. Some of these models are prescribed directly [43, 44, 46], and some derived from the kinetic point of view [4, 21, 30]. An overview can be found in [5, 6]. Such models have been successful in providing an understanding of the large-scale behaviour, but provide no insight into the behaviour of individuals. The relation between the microscopic dynamics and the macroscopic scale in general is an active area of research. In humans, local effects have only been added to macroscopic models in some cases [13].

Many individual-based models have also been developed. A recent review can be found in [7]. These models are often based on alignment and force principles which follow in the reductionist philosophies of the social field [52] and the social forces [24], which gave rise to models such as [36]. These microscopic models sometimes concern agents in the more abstract sense [9]. Often they deal with simple 'animals', whether in general [22, 64, 65] or with a specific animal in mind [68, 69]. Sometimes they involve alignment processes [15, 16], and phase transitions were detected early on in works such as [73]. These abstractions serve to study the natural emergence of self-organisation [14, 27] and swarming [12] as well as the methods to induce such feature when they do not occur spontaneously [8, 10]. Furthermore, many agent

models have been developed specifically for pedestrians: early force models [29, 36] and subsequent improvements [2, 59], models exploring self-organisation [31, 38, 51] as well as evacuation models [33].

While the force-based models are ubiquitous and relatively successful, there is a limit to what behaviours they can capture. Humans and their motion are not completely described by simple mechanistic models, as they fail to incorporate our rational behaviour. Not only are we capable of estimating the position and velocities of moving obstacles [17], but we are able to assess the danger they pose to us [74]. The literature in biology, psychology and neuroscience points to the existence of specialised neural mechanisms in the retina and the brain that enable pedestrians to detect potential obstacles and to assess the time until the collision with said obstacles occurs [42, 66]. Those heuristics are then used by the agents to make quick, close-to-optimal adjustments to their trajectories in order to avoid possible collisions [3, 25].

This work will discuss a model that attempts to replicate said rationality in order to realistically simulate the dynamics of pedestrians. Based on the principles of [58] and the formulation of [20], the model fundamentally consists of a two-step evolution process: the first step involves the evaluation of heuristics of the environment and their use to estimate the proximity and dangerousness of encounters; the second concerns the decision-making process of each agent, which will involve an optimisation game in order to remain in motion towards a target while avoiding potential collisions. Section 2 introduces the model in its original formulation, as well as a number of implementation alternatives. Section 3 develops improvements and variations aimed to generalise the model to multiple situations and density regimes. Section 4 concludes the presentation of the model in a final assessment and presents the outlook of this work.

2 A Model with Rational Behaviour

The pedestrian model of [20, 58] simulates the rational decision-making involved in the steering behaviour of agents. This model is an attempt to capture the complexity behind the steering behaviour of pedestrians. Collision avoidance on humans is an intricate conscious process, and any attempts to reproduce it through a purely mechanical set of rules can only achieve limited success.

The following section presents the formulation of the model as well as some implementation details. The model is conceptually fractioned into two steps: a *perception stage* and a *decision stage*. The perception stage comprises the use of visual stimuli to inform pedestrians of their environment, the surrounding obstacles (moving or not) and any potential collision. The decision stage encompasses the mechanisms through which each agent judges available paths and resolves to move in a specific direction.

2.1 Perception Stage

The perception stage is the first step towards collision avoidance in the model. Pedestrians in this stage derive *heuristics* about their environment based on the position and velocity of visible obstacles (objects or other pedestrians). The heuristics are first examined for encounters between only two agents. Afterwards, *global* heuristics are considered.

2.1.1 Pairwise Encounters

We shall first study a binary encounter, consisting of two pedestrians i and j which happen to approach each other as they move towards their targets. We assume that agent i is aware of his own *position* x_i and *velocity* v_i and can also perceive j's x_j and v_j accurately. This knowledge shall be used to derive *heuristics* that will inform the decision making in the next section.

Throughout the text we will use the terms *collision*, *interaction* and *encounter* interchangeably. All of these refer to a situation where two pedestrians approach enough to enter each other's *personal space*; as a result they might be at risk of colliding, and the interaction must be resolved.

If the velocities of the agents are momentarily constant, their distance as a function of time can be expressed as:

$$d_{i,j}^2(t) = \left\| x_j + v_j t - x_i - v_i t \right\|^2, \tag{1}$$

$$= \left\| v_j - v_i \right\|^2 \left(t + \frac{\left(x_j - x_i\right) \cdot \left(v_j - v_i\right)}{\left\| v_j - v_i \right\|^2} \right)^2 + \left\| x_j - x_i \right\|^2 - \frac{\left(\left(x_j - x_i\right) \cdot \left(v_j - v_i\right)\right)^2}{\left\| v_j - v_i \right\|^2}. \tag{2}$$

The *time to interaction of i and j*, $\tau_{i,j}$, is the time that minimises $d_{i,j}$. This can be found by inspection of (2), namely:

$$\tau_{i,j} = \underset{t \in \mathbb{R}}{\arg\min} \left\{ d_{i,j} \right\} = -\frac{\left(x_j - x_i\right) \cdot \left(v_j - v_i\right)}{\left\| v_j - v_i \right\|^2}. \tag{3}$$

Note that this time may be negative if the pedestrians are moving away from each other, i.e. $\left(x_j - x_i\right) \cdot \left(v_j - v_i\right) > 0$; see Fig. 2.

Further useful quantities can be derived from $\tau_{i,j}$; see Fig. 1. The *point of closest approach of i to j*, $p_{i,j}$, is the point along the trajectory of i where the agents will be closest:

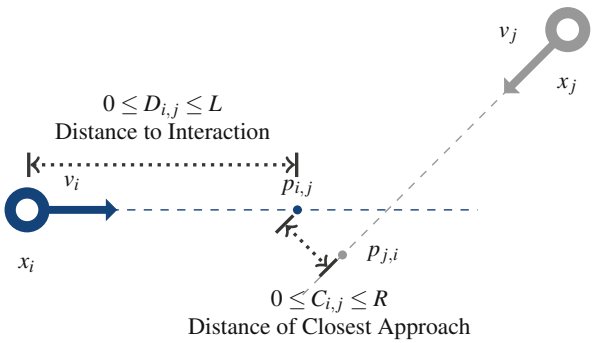

Fig. 1 Dissection of a binary pedestrian encounter. Agent i extrapolates his and j's trajectories assuming their respective velocities will remain constant. This allows the estimation of *distance of closest approach* $C_{i,j}$ as well as the *distance to interaction* $D_{i,j}$

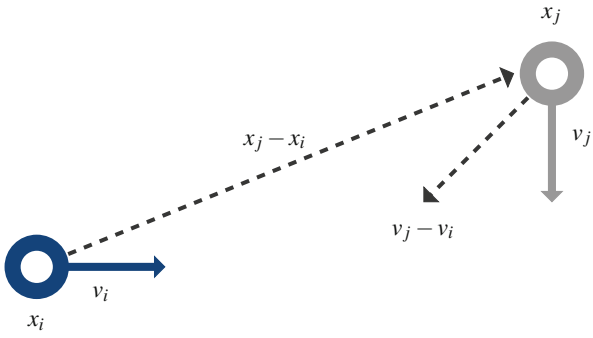

Fig. 2 Approaching pedestrians. Agent i only considers j if they are approaching, i.e. if $(x_j - x_i) \cdot (v_j - v_i) < 0$

$$\left\| p_{i,j} - p_{j,i} \right\| = \min_{t \in \mathbb{R}} \left\| x_i(t) - x_j(t) \right\| \quad \text{and} \quad p_{i,j} = x_i + v_i \tau_{i,j}. \tag{4}$$

The *distance to interaction of i with j*, $D_{i,j}$, is the distance of i to $p_{i,j}$, that is:

$$D_{i,j} = \left\| p_{i,j} - x_i \right\| = \tau_{i,j} \left\| v_i \right\| = -\frac{(x_j - x_i) \cdot (v_j - v_i)}{\left\| v_j - v_i \right\|^2} \left\| v_i \right\|. \tag{5}$$

Last but not least, the *distance of closest approach of i and j*, $C_{i,j}$:

$$C_{i,j} = \left\| p_{i,j} - p_{j,i} \right\| = \left(\left\| x_j - x_i \right\|^2 - \frac{\left((x_j - x_i) \cdot (v_j - v_i) \right)^2}{\left\| v_j - v_i \right\|^2} \right)^{\frac{1}{2}}. \tag{6}$$

It is worth noting that $\tau_{i,j}$ and $C_{i,j}$ are symmetric for i and j.

2.1.2 Assumptions on the Heuristics

We will make a number of assumptions about the quantities derived above which will dictate what encounters can be considered by pedestrians:

1. $\tau_{i,j} > 0$ and $D_{i,j} > 0$. From its definition on (3), it is clear that $\tau_{i,j}$ will be a negative number whenever $\left(x_j - x_i\right) \cdot \left(v_j - v_i\right) > 0$. Geometrically, the inner product is positive whenever pedestrians i and j are moving away from each other; see Fig. 2. As such, we can limit our consideration to positive values of $\tau_{i,j}$ (and by extension $D_{i,j}$), since pedestrians that are separating will simply ignore each other because there is no potential collision.
2. $D_{i,j} < L$. The bound on the distance to interaction reflects the fact that i does not react to obstacles beyond a certain distance. L can be thought of as a *visual horizon* for pedestrians that limits their interactions. The encounters will be ignored unless they are sufficiently close.
3. $C_{i,j} < R$. In the same vein, the bound on the distance of closest approach points to the fact that i does not account for obstacles that will never be close by. R is a measure of the *personal space* of the agents. Unless this space is invaded, there is no reaction.
4. Only visible pedestrians are considered. An agent i cannot consider j for collision avoidance without seeing them since all the heuristics are derived from optical stimuli. Pedestrian j is visible from i's point of view whenever:

$$\frac{\left(x_j - x_i\right) \cdot v_i}{\left\|x_j - x_i\right\| \left\|v_i\right\|} > \cos(\vartheta/2), \tag{7}$$

for agents with a *horizontal field of view* ϑ. In humans, $\vartheta = 7\pi/6$ [72].

2.1.3 Global Encounters

While the pairwise encounters of Sect. 2.1.1 are the typical interaction between pedestrians in situations of low agent concentration, more complex configurations are expected in the higher density regimes. A characterisation of arrangements involving more than two pedestrians is required.

The pairwise heuristics presented above can be combined to render *global heuristics* describing more intricate encounters. In order to do so, we will assume that pedestrians react first to whichever interaction is closest. Given two potential collisions, the agent will avoid the nearer one first, and then deal with the further one if necessary.

Bearing in mind the order of interactions, it is straightforward to define the *global distance to interaction for* i, D_i:

$$D_i = \min_j \left\{D_{i,j}\right\} \quad \text{forsuitable}\, j. \tag{8}$$

Admissible agents j for the minimisation are the *agents perceived by* i, i.e. those satisfying the assumptions from Sect. 2.1.2 together with i. The definition of the *global distance of closest approach for* i, C_i follows immediately as a consequence of this choice:

$$C_i = C_{i,j} \quad \text{for } j \text{ that minimises (8).} \tag{9}$$

Both of these global heuristics will be used to inform the pedestrian during his choice of direction on the next phase.

2.2 Decision Stage

The decision stage is the second and last step towards collision avoidance in the model. Following the obtention of global heuristics during the previous phase, pedestrians must now employ said heuristics in order to decide how to alter their trajectory.

In deciding on a new path, it is helpful to portray the heuristics of each pedestrian as functions of their velocity. Each of the quantities is transformed into a map by allowing v_i to become a variable: $D_{i,j}(v)$ and $C_{i,j}(v)$. In [20] pedestrians are assumed to have a uniform speed s, and thus the heuristics are purely functions of the *direction* ω.

Each agent can use the perceived overall heuristics to inform their choice of velocity. The decision obeys two antagonist interests: navigation towards a target and obstacle avoidance. Pedestrians will maintain their *target velocity* v_i^* consisting of their *comfort speed* s_i^* and their *target direction* ω_i^* whenever possible. They will only deviate from this velocity when a collision is about to occur. Agents will then consider directions within their field of view and make a choice that resolves the collisions while deviating minimally from the target (Fig. 3).

2.2.1 The Decision Potential

The task of finding a suitable direction can be cast as a game-theoretical problem involving the minimisation of a cost. We formulate this task through the *decision potential* or *decision function* $\Phi_i(v)$. This function must reflect the wishes and tendencies of the agents: to move according to a navigation goal and to resolve

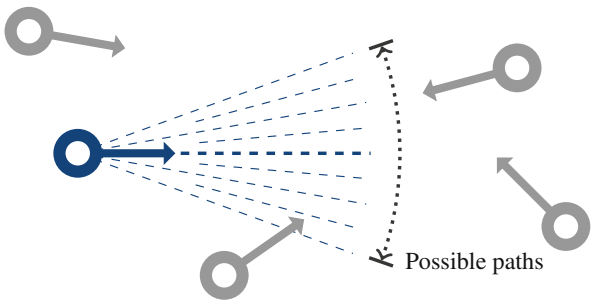

Fig. 3 A pedestrian considers possible paths. They intend to remain in motion towards the target but must avoid colliding with other agents. Both of these goals must be considered in deciding on a new direction

potential collisions. Suitable velocities, which are clear of interactions and oriented towards the target, will yield low values of Φ_i. Less suitable velocities, either incurring collisions or leading away from the target, will have higher costs.

Each pedestrian will choose the optimal velocity according to the decision potential and evolve through an interval of time Δt before making a new choice. This minimisation reflects the decision-making of pedestrians, who strive to always move towards their target while avoiding collisions with a minimal amount of steering.

Letting u_i^n be the minimiser at the n-th step, the evolution of each agent will be written as a difference equation:

$$x_i^{n+1} = x_i^n + u_i^n \Delta t, \qquad u_i^n = \arg\min_v \Phi_i^n(v). \tag{10}$$

2.2.2 A Choice of Potential

The formulation of [20] proposes the decision function:

$$\Phi_i(v) = \frac{k}{2} \left\| D_i v - L v_i^* \right\|^2, \tag{11}$$

where k is a positive constant and v_i^* is the *target velocity* of agent i.

The workings of each individual tendency are reflected on the potential. Φ penalises deviations of v from v_i^* (moving away from the target) as well as deviations of D_i from L (potential collisions). In the absence of other pedestrians $D_i \equiv L$ and thus $\Phi_i(v) \equiv kL^2 \left\| v - v_i^* \right\|^2 / 2$, a convex cost with unique minimum $v = v_i^*$.

2.3 A Gradient-Based Formulation

The model as presented thus far is computationally costly; numerically solving two minimisation problems per pedestrian per step is not practical. Furthermore the choice of time step can be problematic: $\Delta t < D_i / \|v_i\|$ is required in order to successfully resolve collisions, but too small a step can result on the velocity of an agent varying erratically when interacting with a large number of pedestrians in a dense setting.

An alternative is to formulate the decision-making process in terms of the gradient of the decision function through the differential equation:

$$\frac{\mathrm{d}x_i}{\mathrm{d}t} = v_i, \qquad \frac{\mathrm{d}v_i}{\mathrm{d}t} = -\nabla_v \Phi_i(v_i). \tag{12}$$

While (12) is governed by similar principles to those of the optimisation model, it yields a continuous dynamic that accounts for a decision-making process similar to that of (10) but lets agents gradually shift towards suitable velocities by descending the gradient of Φ.

2.3.1 Optimality Versus Efficiency

The gradient scheme (12) provides an efficient alternative to the optimisation formulation, as the numerical computation of $\nabla\Phi$ once per agent per time step is inexpensive when compared with the performance of any optimisation scheme that may be used to approximate the global minimiser.

The optimisation scheme (10) remains the preferable method for simulations involving a small number of agents and low densities, as it guarantees the optimal choice of velocity for all agents. Gradient descent may simply not reach the global minimum that would be found otherwise, as it may stall upon reaching a local minimum. However, in high-density regimes, the decision potential becomes volatile, as the increased interaction rate rapidly changes the cost of each velocity; local minima are unlikely to persist. Furthermore, the global minimum may change abruptly and repeatedly, which would result in rapid switching of agent directions. A gradient method appears more suitable, as simply shifting away from high-cost velocities might be sufficient for collision avoidance.

2.4 Summary of the General Model

Consider N pedestrians, where agent i has position x_i, velocity v_i, and target velocity v_i^*. The dynamics will be given by the solution to either (10):

$$x_i^{n+1} = x_i^n + u_i^n \Delta t, \qquad u_i^n = \arg\min_v \Phi_i^n(v), \tag{13}$$

or (12), namely:

$$\frac{\mathrm{d}x_i}{\mathrm{d}t} = v_i, \qquad \frac{\mathrm{d}v_i}{\mathrm{d}t} = -\nabla_v \Phi_i(v_i). \tag{14}$$

The evaluation of the decision potential Φ is as follows:

1. For each pair of agents i and j, compute the heuristics $D_{i,j}$ and $C_{i,j}$ as defined in (5) and (6):

$$D_{i,j} = -\frac{(x_j - x_i)\cdot(v_j - v_i)}{\|v_j - v_i\|^2}\|v_i\|, \tag{15}$$

$$C_{i,j} = \left(\left\| x_j - x_i \right\|^2 - \frac{\left(\left(x_j - x_i \right) \cdot \left(v_j - v_i \right) \right)^2}{\left\| v_j - v_i \right\|^2} \right)^{\frac{1}{2}}. \tag{16}$$

2. Decide whether i will take j into account using the conditions from Sect. 2.1.2:

$$D_{i,j} < L, \tag{17}$$

$$C_{i,j} < R, \tag{18}$$

$$\left(x_j - x_i \right) \cdot \left(v_j - v_i \right) < 0, \tag{19}$$

$$\cos(\vartheta/2) < \frac{\left(x_j - x_i \right) \cdot v_i}{\left\| x_j - x_i \right\| \left\| v_i \right\|}. \tag{20}$$

3. Obtain overall heuristics D_i and C_i as defined in (8) and (9):

$$D_i = D_{i,j^*}, \qquad C_i = C_{i,j^*}, \qquad j^* = \arg\min_j \left\{ D_{i,j} \right\}. \tag{21}$$

4. Use the global heuristics to construct the cost function Φ_i as defined in (11).

3 Towards a High-Density Model

The model of [20] is explicitly formulated for low pedestrian densities, where all agents have a uniform, constant speed. Moving at such a speed is simply infeasible in more congested regimes, as agents will be required to slow down or even stop completely in order to avoid collisions. Even groups where all the agents move in the same direction will show a reduction on speed whenever the intra-crowd density is beyond some thresholds [75].

This section presents a study of the original formulation, followed by a series of variations of the model that aim to extend its validity to pedestrians with variable speeds and scenarios of higher densities.

3.1 A Frontal Collision

A natural range of validity for the model can be obtained by considering a frontal encounter of two pedestrians and studying the corresponding decision function under the framework of (10). For simplicity, we choose:

$$x_i = (-d, 0), \qquad x_j = (d, 0), \tag{22}$$

$$v_i = (s, 0), \qquad v_j = (-s, 0),$$

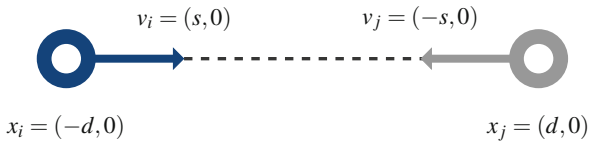

Fig. 4 Study of a frontal collision. Agents i and j are placed in a simple arrangement, at a distance $2d$ and approaching in a straight line, each with speed s. The possible velocities for i are parametrised as $v = s\,(\cos\theta, \sin\theta)$

for given distance d and speed s (Fig. 4). Considering a test velocity for agent i, $v = s\,(\cos\theta, \sin\theta)$, and ignoring variations on the speed as per the original formulation, it can be readily verified:

$$\tau_{i,j}(v) = \frac{d}{s}, \qquad D_{i,j}(v) = d, \qquad C_{i,j}(v) = \sqrt{2d^2(1-\cos\theta)}. \tag{23}$$

$D_i(v)$ is thus equal to d if i perceives j and equal to L otherwise. The decision function reduces to:

$$\Phi_i(v) = \begin{cases} ks^2\left(\dfrac{L^2+d^2}{2} - Ld\cos\theta\right) & \text{if } i \text{ perceives } j, \\ ks^2L^2(1-\cos\theta) & \text{otherwise.} \end{cases} \tag{24}$$

If we assume $d < L$, then the perception of j by i is conditioned solely by $C_i < R$, which yields:

$$|\theta| < \theta^* := \arccos\left(1 - \frac{R^2}{2d^2}\right). \tag{25}$$

Each segment of Φ now has clear minima: the perception section, where θ verifies (25), has its minimum at $\theta = 0$ and takes the value $\Phi(0) = ks^2(L-d)^2/2$; the remaining section has its minima at the boundary of the two regions, $|\theta| = \theta^*$, where $\Phi(\theta^*) = ks^2L^2R^2/2d^2$.

In order for the collision to be successfully resolved, the central minimum must not be selected in (10). The wrong choice is made whenever $\Phi(0) < \Phi(\theta^*)$, and this criterion can be used to ascertain validity:

$$\Phi(0) < \Phi\left(\theta^*\right) \qquad \Longleftrightarrow \qquad d^2(L-d)^2 < L^2R^2, \tag{26}$$

since $k > 0$, $s > 0$.

Given that L and R are constants, the resulting polynomial of d, $p(d) := d^2(L-d)^2$, encodes the fate of the interaction. In order to navigate the collision successfully, the condition of (26), rewritten as $p(d) < L^2R^2$, must be violated at

some point as the agents i and j approach. Recall $D_{i,j} = d$; if the condition is met for large d (say, $d = L$) and continues to hold as $d \to 0$, the agents will collide.

The polynomial $p(d)$ is a monic quartic with double roots at $d = 0$ and $d = L$. Naturally, this suggests a single maximum at $d = L/2$, with $p(L/2) = L^4/2^4$. This extremum must exceed L^2R^2; otherwise (26) is valid for all $d \in (0, L)$, and a collision occurs. Simplifying:

$$p\left(\frac{L}{2}\right) < L^2R^2 \qquad \Longleftrightarrow \qquad L < 4R. \tag{27}$$

The comparison yields $L < 4R$ as a sufficient condition for the model to fail by means of the interaction minimum ($\theta = 0$) becoming the global minimum, resulting in a collision (see Fig. 5). Equation (27) amounts to a natural scale of the model, which is only valid in regimes where $L \gg R$, i.e. the visual horizon is much larger than the personal space of the agents. A large horizon is a characteristic of low-density scenarios, which justifies the original choice of prescribing the model for such regimes and constant speeds. Denser scenarios typically show $L \sim R$, as agents can only consider nearby interactions, which takes the model outside its region of validity.

3.2 Grading by Collision Severity

Following the analysis of the original model, and considering the natural scale found in Sect. 3.1, we aim to extend this model to higher-density regimes where the criterion $L \leq 4R$ might be met.

A straightforward solution to the model choosing the erroneous central minimum is simply removing the minimum altogether. Notice that, while both global heuristics D_i and C_i are used to discern what pedestrians need to be considered by i for collision avoidance, only D_i appears explicitly on the potential. Recall that C_i is a measure of the severity of an interaction, ranging from 0 for a full collision to R for no interaction at all. Thus penalising deviations of C_i from R on top of the existing penalisations in (11) will result in a higher cost at points of full collision, namely, the troubling point $\theta = 0$. We propose:

$$\Phi_{C,i}(v) = \frac{k}{2R^2} \left\| D_i C_i v - LRv_i^* \right\|^2. \tag{28}$$

Figure 6 shows the analogous of Fig. 5 for the new cost Φ_C. Figure 7 shows the result of a numerical simulation of the frontal collision under Φ_C.

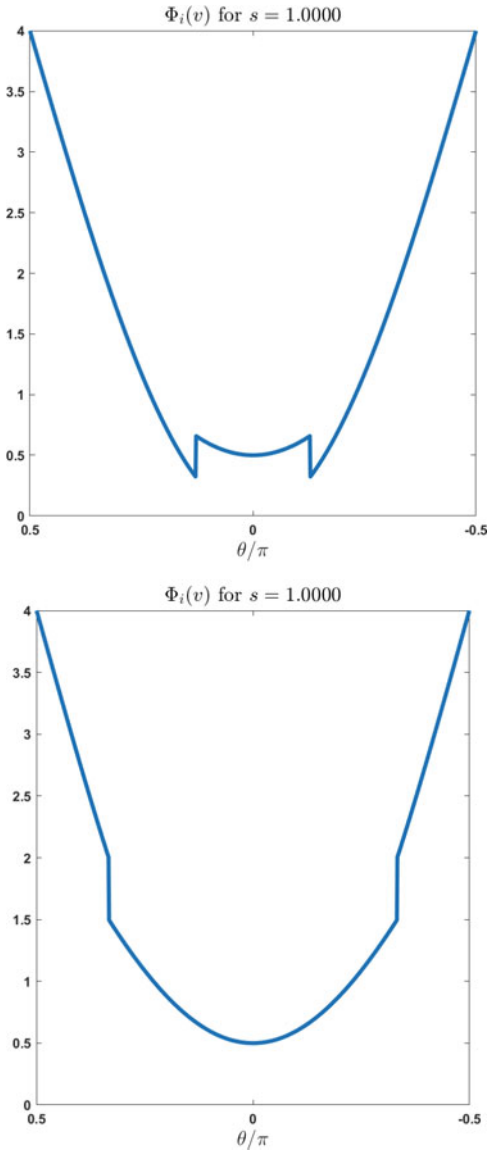

Fig. 5 Comparison of Φ_i for the frontal collision. $d = 1.0, s = 1.0, k = 1.0$. **Top:** $L = 2.0, R = 0.4$. The global minima correctly fall to either side of the region of interaction. **Bottom:** $L = 2.0, R = 1.0$. The global minimum appears at $\theta = 0$, leading to a collision

3.3 Modelling Variable Speeds

To continue the generalisation of the model towards high-density regimes, we must allow for variations on the speed of pedestrians. Unfortunately the decision functions Φ and Φ_C have an unintended side effect on the choice of speeds.

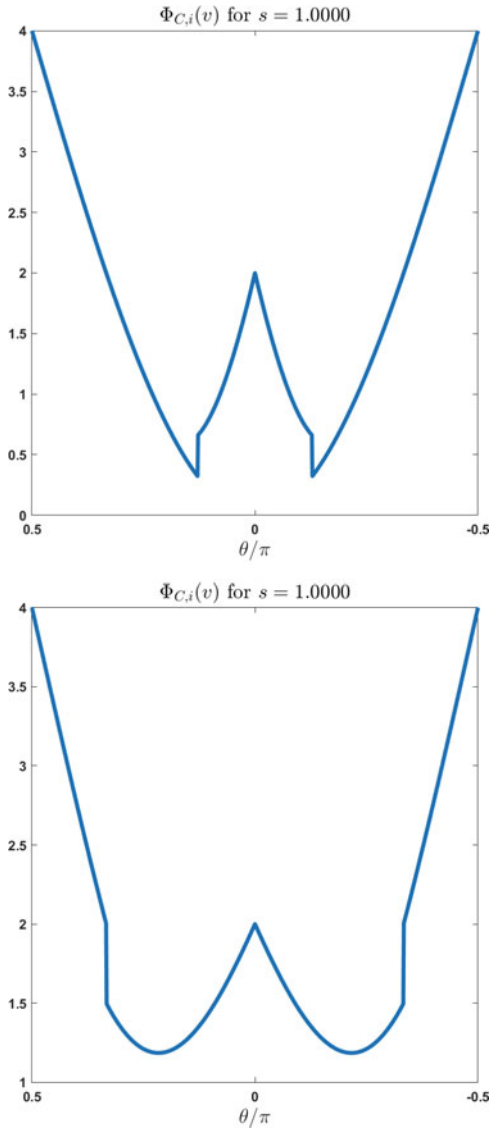

Fig. 6 Comparison of $\Phi_{C,i}$ for the frontal collision. $d = 1.0, s = 1.0, k = 1.0$. Contrary to Fig. 5, both sets of parameters yield correct shapes. In particular, the central minima have disappeared. **Top:** $L = 2.0, R = 0.4$. **Bottom:** $L = 2.0, R = 1.0$

Recall that both functions involve penalisations whenever the distance to interaction D_i is less than L. In the case of the frontal encounter discussed above, under the gradient formulation, accelerating towards j guarantees an increase of D_i (and therefore a decrease of the cost), as the collision will occur closer to j. Hence, under the models discussed thus far, pedestrians navigating frontal collisions will accelerate towards rather than away from each other if the speed is allowed to vary. See Figs. 8 and 9 for a visualisation of the cost.

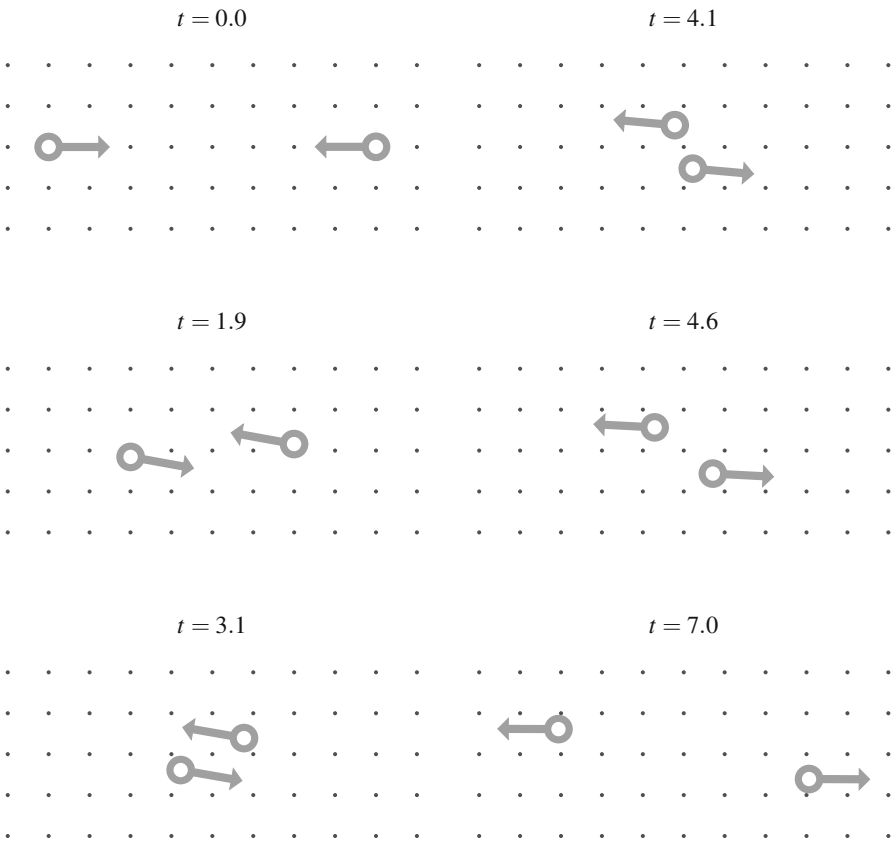

Fig. 7 Frontal collision—Φ_C decision potential. Simulation of the frontal collision described in Sect. 3.1 under the decision function Φ_C using the gradient formulation. The two agents can be seen reacting to each other from a distance, steering to avoid the collision before recovering their desired direction. $L = 2.0, R = 1.0$. Interactive simulations available online at rafaelbailo.com/rationalbehaviour/

Such peculiar acceleration suggests controlling the speed of pedestrians directly on the cost to avoid huge fluctuations away from the comfort speed s_i^*. We propose:

$$\begin{aligned}\Phi_{S,i}(v) &= \Phi_{C,i}(v) + \frac{\tilde{k}}{2}\left(\|v\|^2 - \left\|v_i^*\right\|^2\right)^2, \\ &= \frac{k}{2R^2}\left\|D_i C_i v - LRv_i^*\right\|^2 + \frac{\tilde{k}}{2}\left(\|v\|^2 - \left\|v_i^*\right\|^2\right)^2.\end{aligned} \tag{29}$$

Figure 10 shows the modified decision potential. The minima can now be seen close to the target speed and away from the boundary.

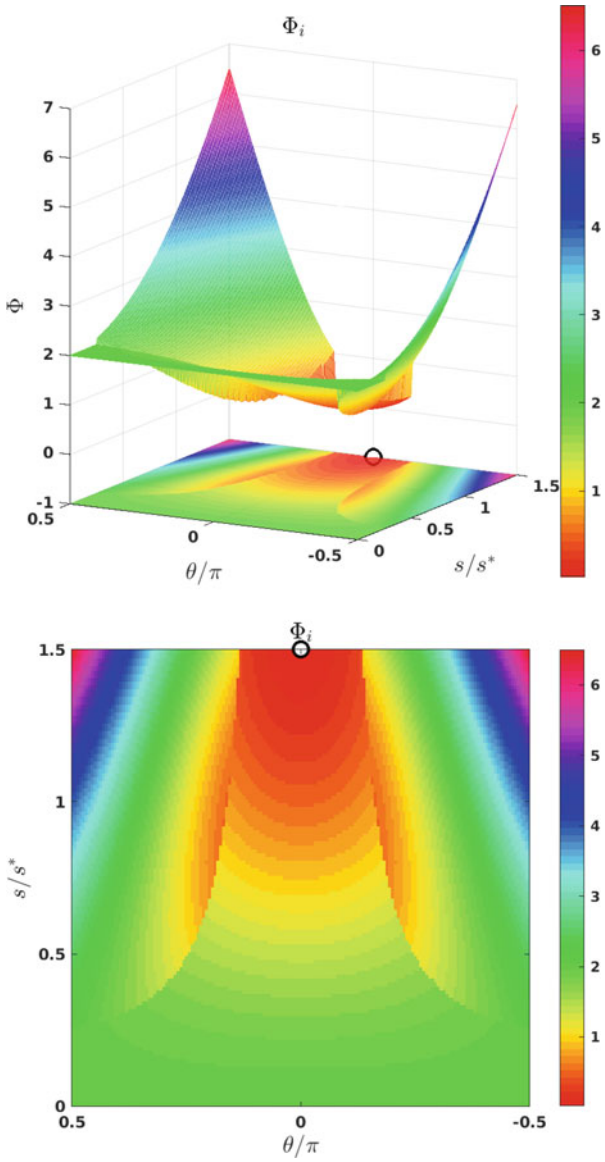

Fig. 8 Φ_i as a function of s and θ for the frontal collision. $d = 1.0, k = 1.0, L = 2.0, R = 0.4$. Observe the marked global minimum on the boundary $s = 1.5s^*$; agent i will accelerate forward, in a direction close to the collision

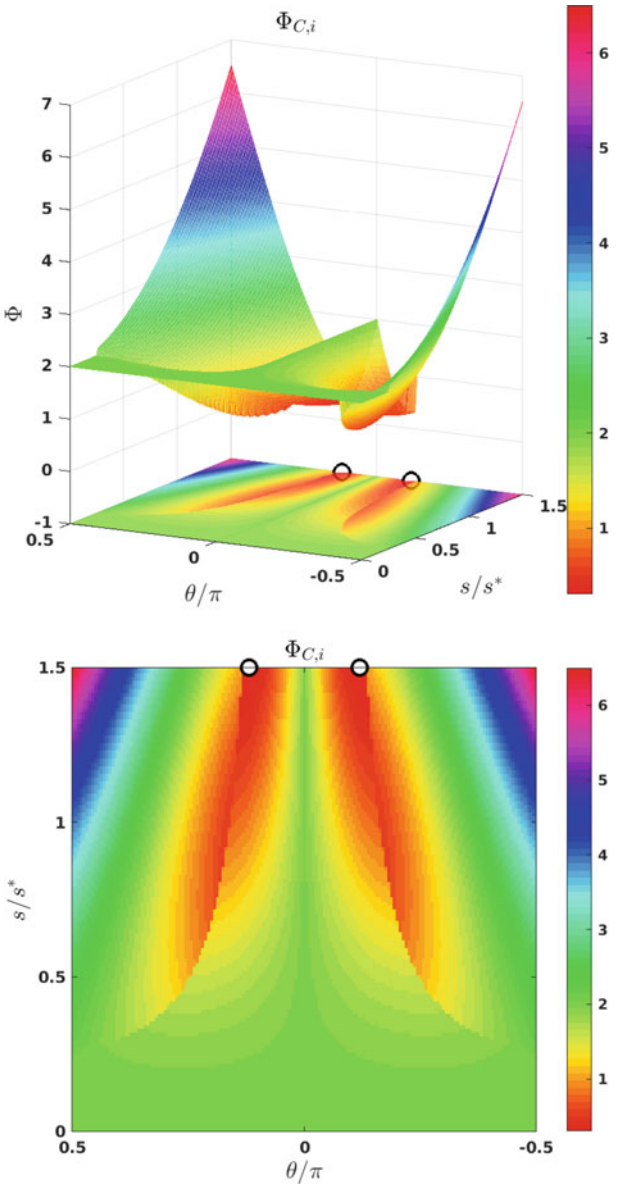

Fig. 9 $\Phi_{C,i}$ as a function of s and θ for the frontal collision. $d = 1.0$, $k = 1.0$, $L = 2.0$, $R = 0.4$. Again the global minima lie on the boundary $s = 1.5s^*$, leading to forward acceleration

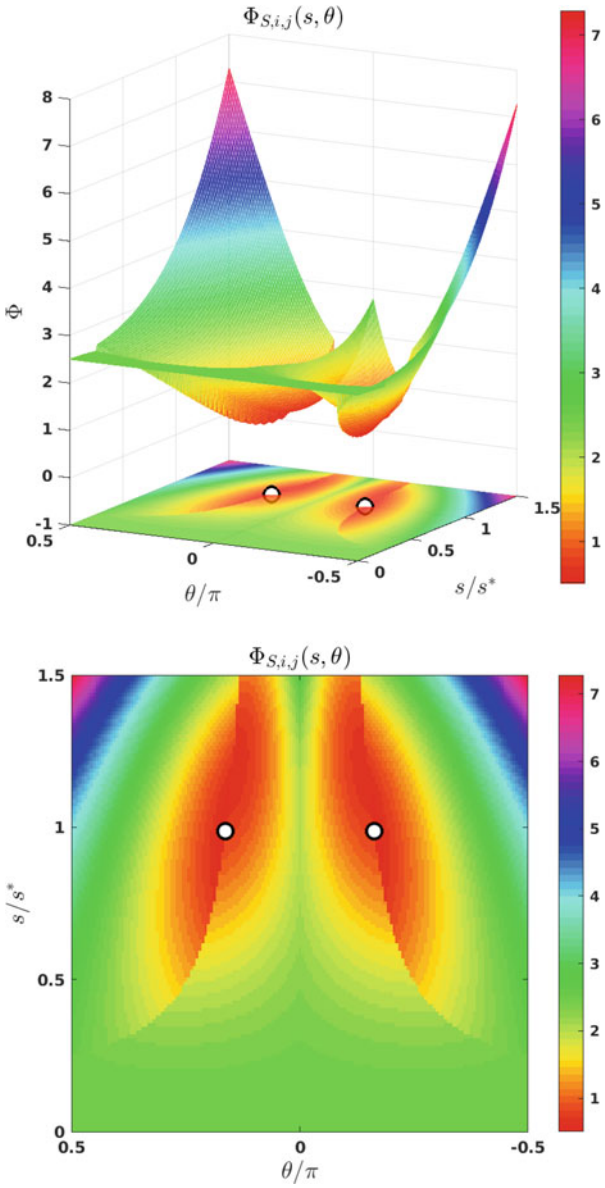

Fig. 10 $\Phi_{S,i}$ as a function of s and θ for the frontal collision. $d = 1.0$, $k = 1.0$, $L = 2.0$, $R = 0.4$. Observe the marked minima have shifted away from the boundary and now sit close to $s = s^*$

3.4 Environmental Coercion

The modified decision potential from (29), Φ_S, satisfactorily reflects the steering behaviour of pedestrians. As was discussed in Sect. 2, this decision function encodes the game-theoretical nature of human collision avoidance, where agents resolve potential collisions while attempting to remain in motion towards their target. This potential has been generalised to situations beyond the original scope (discussed in Sect. 3.1), allowing pedestrians to resolve collisions in high-density regimes where not every agent is able to constantly move at their desired speed.

The models as discussed thus far are only concerned with the rational avoidance of collisions by agents. However, we are yet to account for external factors that may influence the dynamics in high-density regimes. The constrains of these scenarios will be included in the gradient formulation through an additional term, the *environmental coercion* ϵ_i:

$$\frac{\mathrm{d}x_i}{\mathrm{d}t} = v_i, \qquad \frac{\mathrm{d}v_i}{\mathrm{d}t} = -\nabla_v \Phi_{S,i}\left(v_i\right) + \epsilon_i. \tag{30}$$

Observe the dychotomy of the *decision potential* $\Phi_{S,i}$ and the *environmental coercion* ϵ_i. As discussed, the decision function is the principal driver of the pedestrian dynamics. The goals, strategy and overall rationality of human motion are encoded through a game of *anticipation* and *optimisation*. The predictive nature of the potential is made explicit through the dependence on v; the decision-making is always based on the predicted *future* state of the agents. Meanwhile, the environmental factor can be thought of as a higher-order correction to the model. This additional component must never dominate the dynamics and will only become significant as the pedestrian density becomes high. The term is only allowed a dependency on *present* state of the agents, as it is solely a constraint due to the current density and not a rational decision process.

3.4.1 Repulsion as Anticipation

A typical feature of high-density regimes is distance-keeping: pedestrians, particularly when in motion, maintain a safe distance away from all other agents, whether a collision is imminent or not. This amounts to a probabilistic form of collision prevention; in avoiding close proximity, the agents are decreasing the likelihood of a collision due to a sudden change in direction by a neighbour.

The avoidance can be modelled through the introduction of an agent-to-agent force. The environmental coercion of (30) can be defined as a soft repulsion term:

$$\epsilon_{f,i}\left(x_i\right) := \sum_{j \neq i} f\left(\left\|x_j - x_i\right\|\right) \frac{x_j - x_i}{\left\|x_j - x_i\right\|}. \tag{31}$$

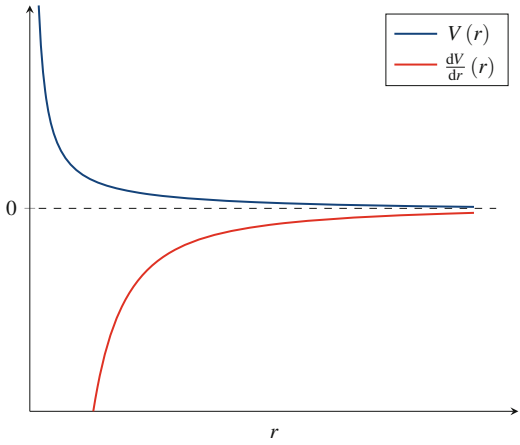

Fig. 11 Plot of the radial potential V and its derivative $f(r) := \frac{dV}{dr}(r)$

An intuitive choice is to set f as the derivative of a radial potential, for instance:

$$f(r) := \frac{dV}{dr}(r), \qquad V(r) = D\frac{\exp\{-ar^2\}}{r^p}, \tag{32}$$

where a, D and p are positive constants; see Fig. 11.

It is important to ensure the repulsion does not dominate the dynamics, as the collision avoidance mechanism is sufficient in most cases. For instance, the frontal collision of Sect. 3.1 can and will be resolved by steering through the choice of a suitable decision function such as (28) or (29); the forces should play no role here. The function f should decay rapidly to prevent middle to long distance effects, and it should be weighted by a suitably small coefficient in order to avoid sudden changes in the direction of pedestrians. Only agents that remain under close proximity during an interval of time longer than timescale of the typical collision ought to be noticeably affected by the repulsion effects.

Since the typical high-density scenario involves a large number of agents moving through a narrow geometry, it may be useful to add a similar repulsion term between each agent and the surrounding walls. Without such a term, the forces within the crowd will push agents near the boundary against the walls. This repulsion will be of a similar intensity as the agent-to-agent force, but it is imperative that it only acts on agents that approach the wall. Agents standing near a wall or moving parallel to it should experience no repulsion.

Figure 12 shows the result of the numerical simulation of a large crowd incorporating the repulsion effects.

3.4.2 Friction and the Fundamental Diagram

Another relevant behaviour in the dynamics of pedestrians is the inability to walk at full comfort speed within large crowds, even if everyone in the crowd is moving with

the same velocity. The term *fundamental diagram* refers to the empirical relation between crowd density and crowd speed. It has been observed that while pedestrians move at their comfort speed when moving in low densities, their movement is

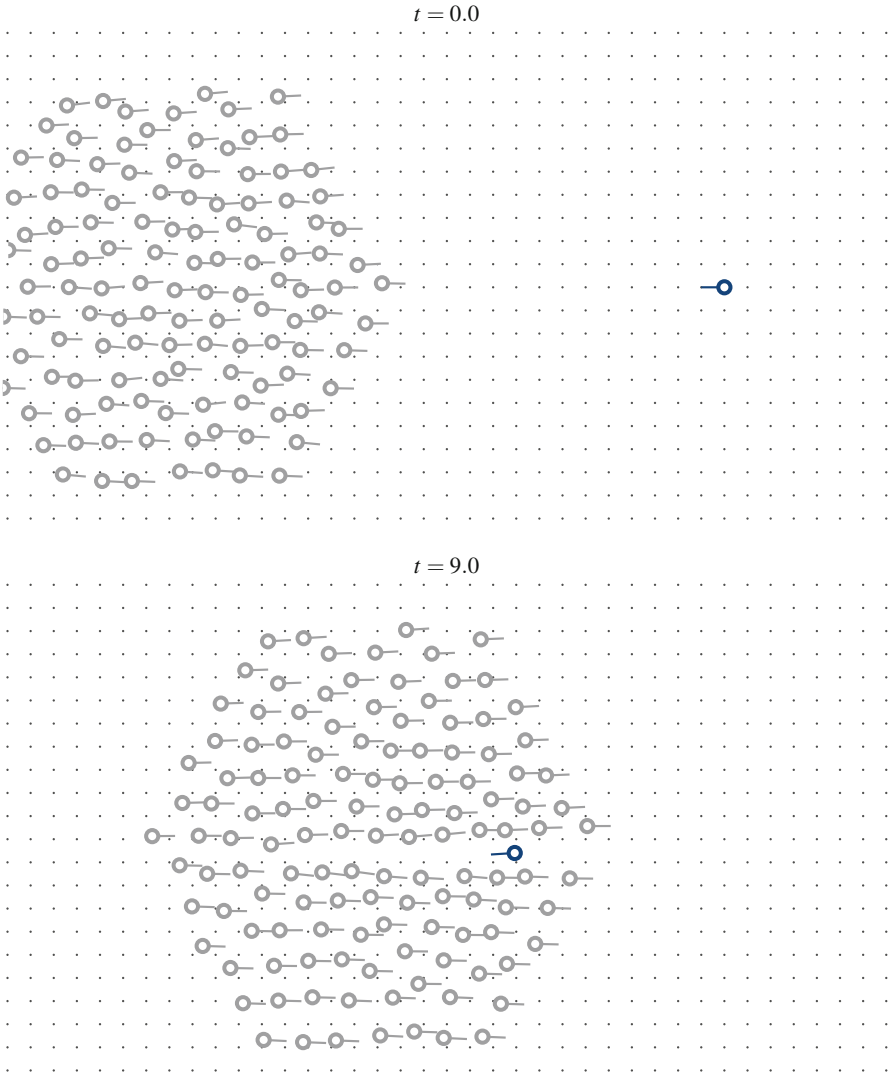

Fig. 12 Large crowd—repulsion effects. Simulation of a large crowd with an incoming collision incorporating the repulsion effects of (31) using the gradient formulation. Agents at the front of the crowd steer to avoid the collision. After resolving the interaction, the repulsion effect causes the agents to reclaim the space that has been created on the trail of the agent, progressively returning to a homogeneous configuration. Interactive simulations available online at rafaelbailo.com/rationalbehaviour/

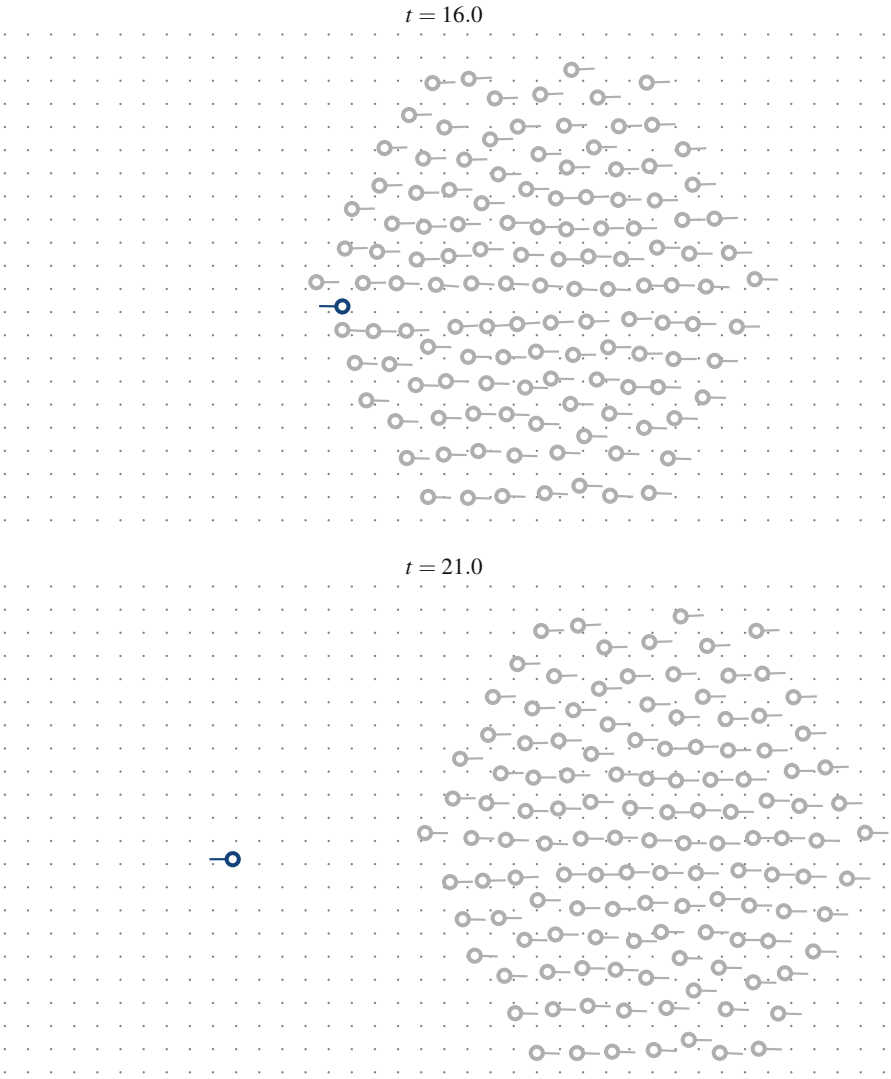

Fig. 12 (continued)

impaired by higher densities and their average speed is reduced; upon reaching a certain threshold the crowd is brought to a standstill.

This speed-density coupling can be thought of a frictional force whose intensity depends on the local density of agents. Here, the *local density* ρ_i is the density perceived by agent i, which is in turn a function of the number of agents within i's cone of vision. Given the *number of agents perceived by* i, N_i, the *average area occupied by a pedestrian* A_p and the *area of the cone of vision* A_c, the local density is simply aproximated by the ratio:

$$\rho_i \simeq N_i \frac{A_p}{A_c}\,, \tag{33}$$

see Fig. 13 for further insights.

The simplest frictional force can then be written as

$$\epsilon_{\mu,i}\left(x_i, v_i\right) := -\,\mu\left(\rho_i\right) v_i\,. \tag{34}$$

The overall environmental coercion, a combination of the repulsion (f) and the friction (μ) terms, becomes:

$$\begin{aligned}\epsilon_i\left(x_i, v_i\right) :=& \epsilon_{f,i}\left(x_i\right) + \epsilon_{\mu,i}\left(x_i, v_i\right) \\ =& \sum_{j\neq i} f\left(\left\|x_j - x_i\right\|\right) \frac{x_j - x_i}{\left\|x_j - x_i\right\|} - \mu\left(\rho_i\right) v_i\,.\end{aligned} \tag{35}$$

One basic possibility for the friction is $\mu(\rho) \propto \rho_{\max}/\left(\rho_{\max} - \rho\right)$, for a *stopping density* $\rho_{\max}$; see Fig. 14.

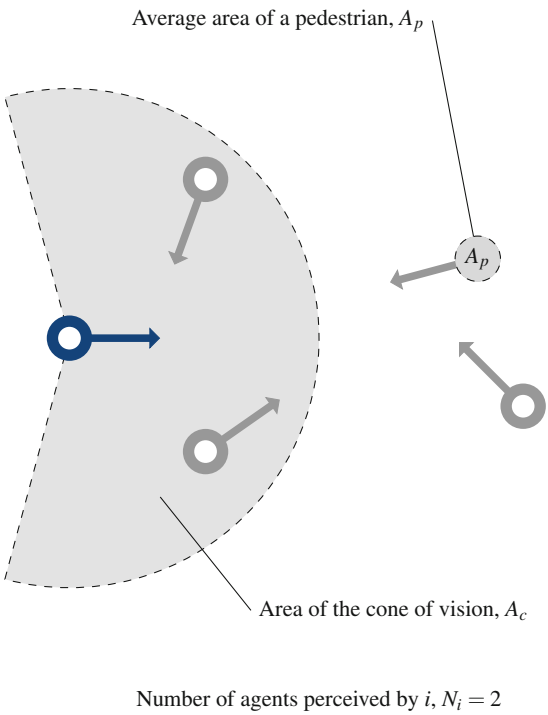

Fig. 13 The cone of vision. Detail of the average area of a pedestrian A_p and the area of the cone of vision A_c. Observe that only two other agents fall within the cone of vision, $N_i = 2$

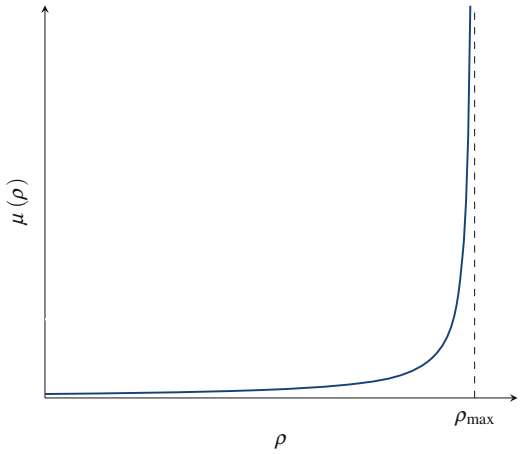

Fig. 14 Plot of the intensity of the frictional effect as a function of ρ, for a stopping density $\rho_{\max}$. $\mu(\rho) \propto \rho_{\max}/(\rho_{\max} - \rho)$

As in the case of the repulsion effects in Sect. 3.4.1, it is crucial that the friction term only dominates the dynamics in scenarios where the agent density is high. Fast, small fluctuations of the density when resolving interactions should not result in variations of the speed, as it is known that pedestrians would rather steer than deviate from their comfort speed when avoiding collisions. The effects of the new friction must only become apparent when the concentration of agents makes it impossible to avoid collisions while cruising at comfort speed.

Figure 15 shows the result of the numerical simulation of a large crowd incorporating the frictional effects.

3.5 Summary of the Modified Gradient Model

Consider N pedestrians, where agent i has position x_i, velocity v_i, and target velocity v_i^*. The dynamics will be given by the solution to (30), namely:

$$\frac{\mathrm{d}x_i}{\mathrm{d}t} = v_i, \qquad \frac{\mathrm{d}v_i}{\mathrm{d}t} = -\nabla_v \Phi_{S_i}(v_i) + \epsilon_i. \tag{36}$$

The evaluation of the *decision potential* Φ_S is as follows:

1. For each pair of agents i and j, compute the heuristics $D_{i,j}$ and $C_{i,j}$ as defined in (5) and (6):

$$D_{i,j} = -\frac{\left(x_j - x_i\right) \cdot \left(v_j - v_i\right)}{\left\| v_j - v_i \right\|^2} \left\| v_i \right\|, \tag{37}$$

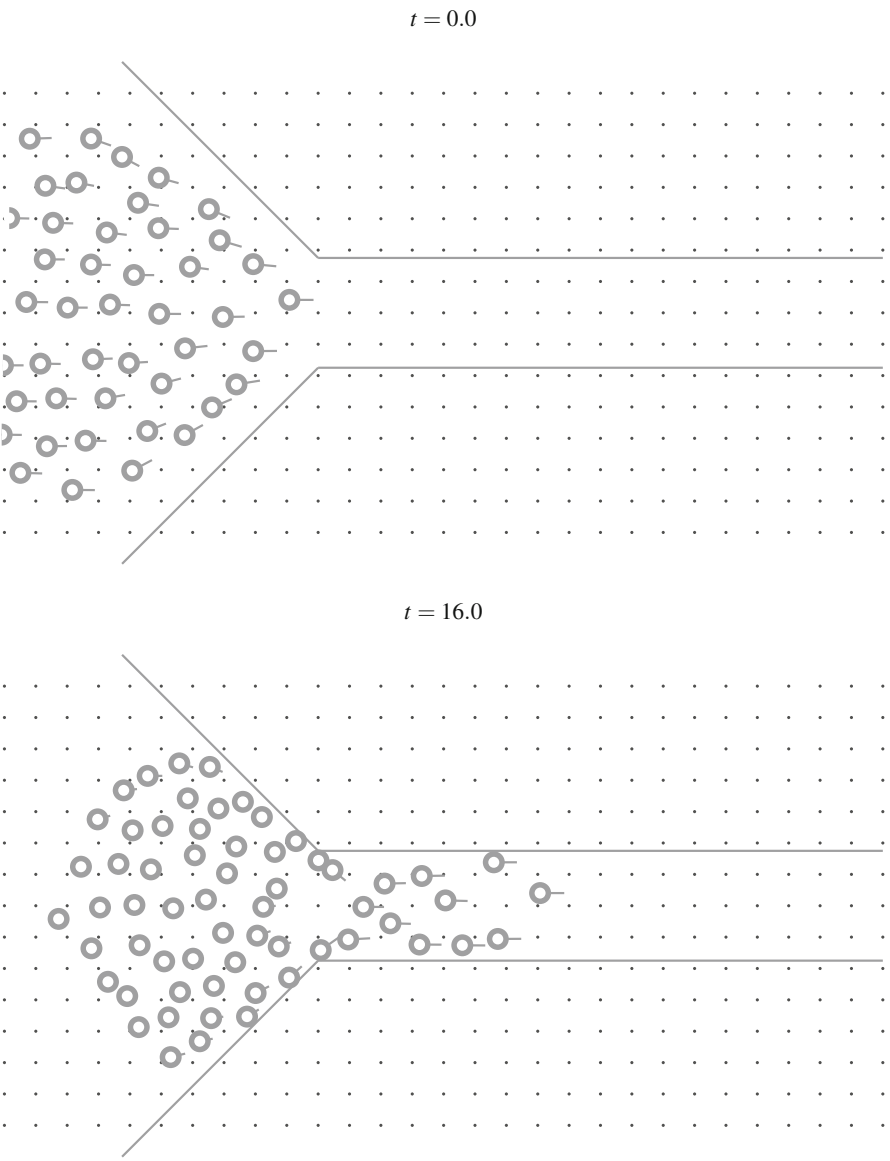

Fig. 15 Bottleneck—frictional effects. Simulation of a large crowd navigating a bottleneck incorporating the frictional effects of (34) using the gradient formulation. Agents at the front of the crowd are able to enter the corridor unobstructed. As people begin to occupy the corridor, the entrance quickly becomes crowded. Pedestrians waiting to enter are brought to a complete standstill until the density in front of them decreases. Interactive simulations available online at rafaelbailo.com/rationalbehaviour/

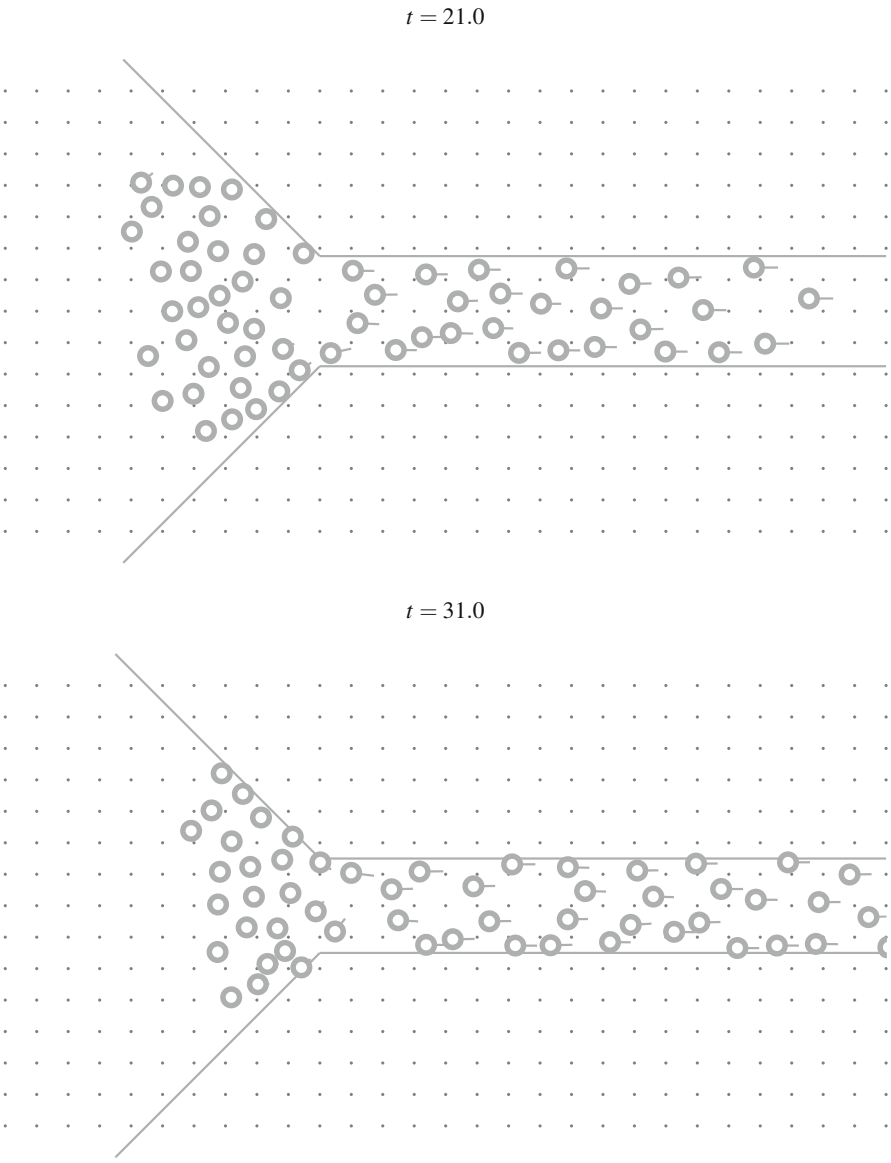

Fig. 15 (continued)

$$C_{i,j} = \left(\left\| x_j - x_i \right\|^2 - \frac{\left(\left(x_j - x_i \right) \cdot \left(v_j - v_i \right) \right)^2}{\left\| v_j - v_i \right\|^2} \right)^{\frac{1}{2}}. \tag{38}$$

2. Decide whether i will take j into account using the conditions from Sect. 2.1.2:

$$D_{i,j} < L, \tag{39}$$

$$C_{i,j} < R, \tag{40}$$

$$\left(x_j - x_i \right) \cdot \left(v_j - v_i \right) < 0, \tag{41}$$

$$\cos(\vartheta/2) < \frac{\left(x_j - x_i \right) \cdot v_i}{\left\| x_j - x_i \right\| \left\| v_i \right\|}. \tag{42}$$

3. Obtain overall heuristics D_i and C_i as defined in (8) and (9):

$$D_i = D_{i,j^*}, \qquad C_i = C_{i,j^*}, \qquad j^* = \arg\min_j \left\{ D_{i,j} \right\}. \tag{43}$$

4. Use the global heuristics to construct the cost function Φ_S as defined in (29).

The computation of the *environmental coercion* consists of two parts:

1. The *distance keeping* term, as defined in (31):

$$\epsilon_{f,i}\left(x_i \right) := \sum_{j \neq i} f\left(\left\| x_j - x_i \right\| \right) \frac{x_j - x_i}{\left\| x_j - x_i \right\|}. \tag{44}$$

2. The *frictional* term, as given by (34):

$$\epsilon_{\mu,i}\left(x_i, v_i \right) := -\mu\left(\rho_i \right) v_i. \tag{45}$$

The *overall* coercion term is the sum of the individual effects, $\epsilon_i = \epsilon_{f,i} + \epsilon_{\mu,i}$.

One last numerical simulation is presented in Fig. 16, demonstrating the interplay between the different components of the model. Two crowds traverse a corridor in opposite directions. Initially each crowd is sparse, and agents are able to move comfortably in straight paths. As the two groups approach, interactions occur at the interface, and collisions begin to be resolved. Simultaneously, as the crowds move through each other, the agent density becomes sufficiently high for the environmental constraints to manifest, leading to distance-keeping behaviour from pedestrians. Lane formation [36, 41] is observed, not as a consequence of the initial configuration of the agents but as a combined effect of the avoidance behaviours.

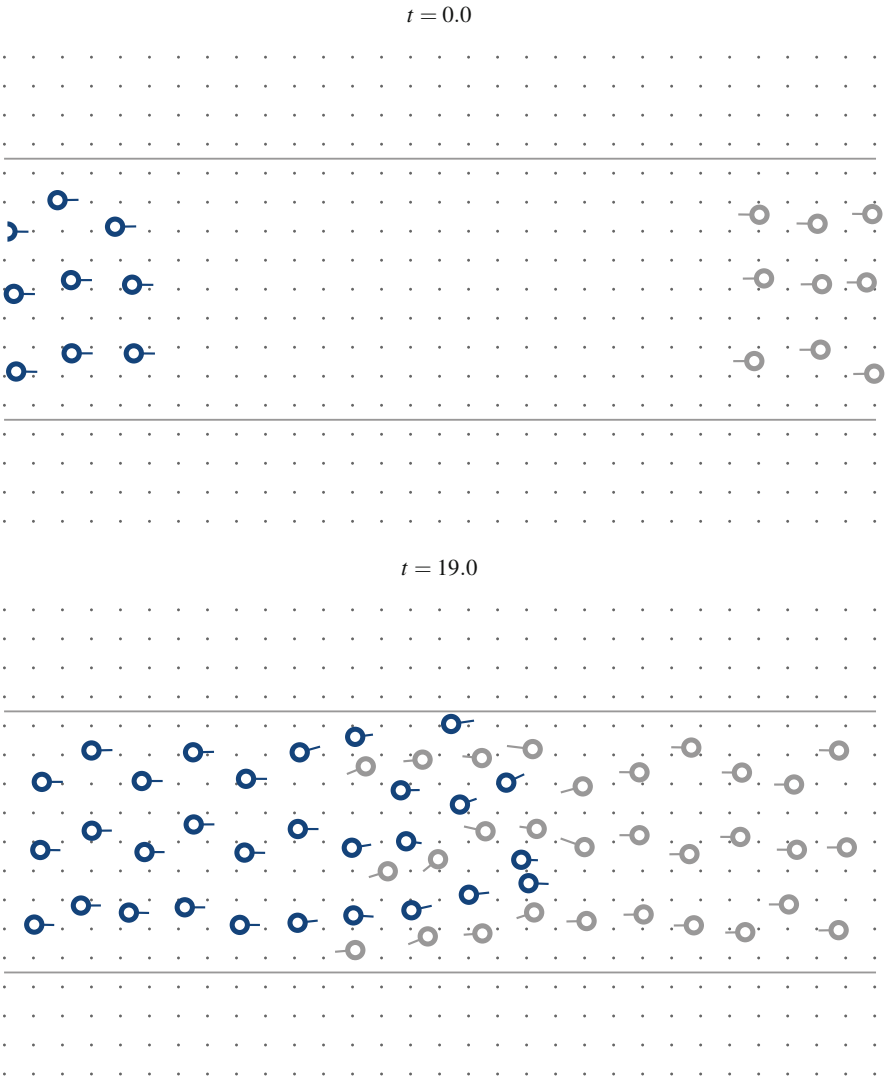

Fig. 16 Corridor—high-density setting. Simulation of two dense crowds traversing a corridor in opposite directions using the gradient formulation. Agents are able to enter the corridor unobstructed at first. The initial interactions are quickly resolved through the formation of lanes, which persist in time. Interactive simulations available online at rafaelbailo.com/rationalbehaviour/

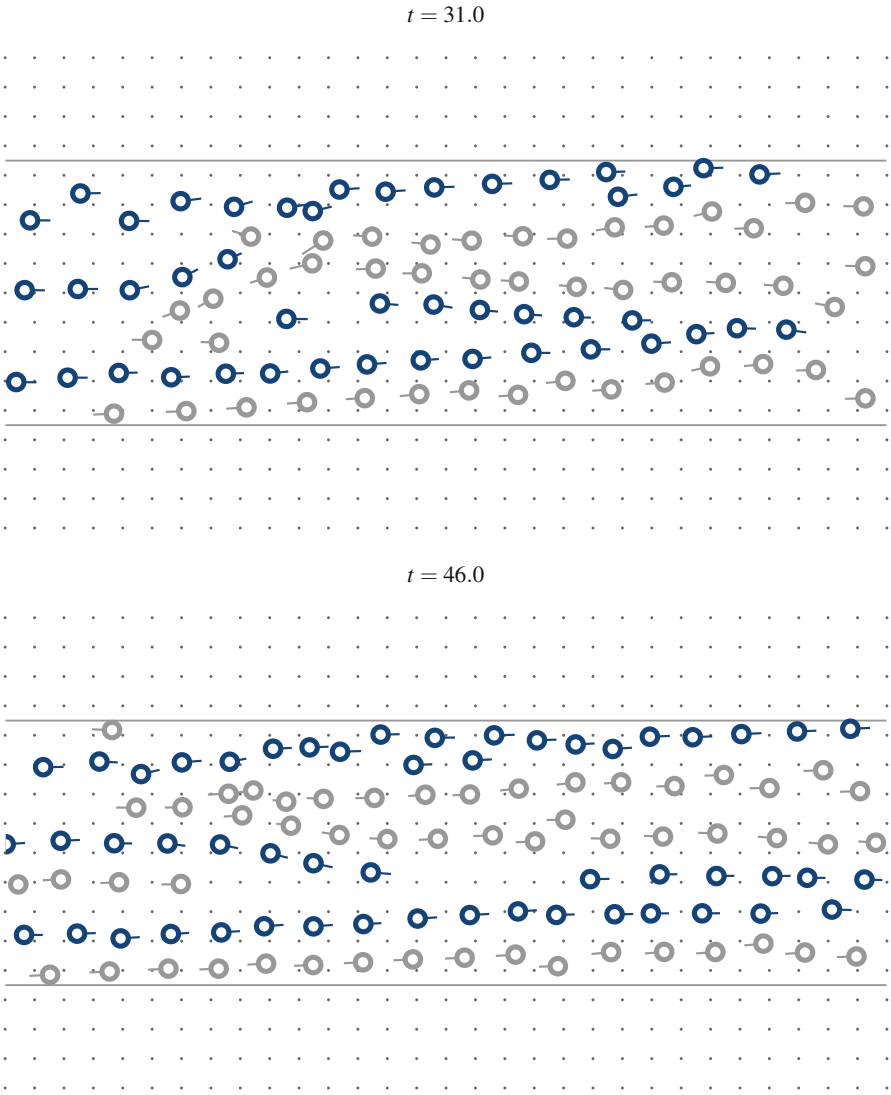

Fig. 16 (continued)

4 Conclusion and Outlook

This work has presented an individual-based model for pedestrians based on a game-theoretical principle that aims to accurately reproduce the rational behaviour of walking humans. We have explored the original formulation, which involves the use of heuristics in a decision process in order to avoid collisions. We have also

explored a series of modifications to extend the validity of the model to regimes of varying characteristics.

A majority of the pedestrian models found in the literature are purely force-based. Many of these models have been applied successfully in academic and industrial settings. While, through suitable calibration, they seem to reproduce the basic principles of the dynamics and allow for the computation of crowd statistics, we feel that they do not capture the finer detail of the dynamics. As discussed previously, pedestrian motion is particularly complex, and our model seems to improve on its predecessors by faithfully replicating the rational anticipation behaviour of humans. The immediate priority for future work will be the calibration of the parameters of the model. Each of the mechanisms described in this work involves a number of variables, many of which have a physical meaning. The currently known suitable parameters for these have been found heuristically, but a more systematic approach will be required. Different situations give rise to specific pedestrian profiles according to the context, for instance, humans move differently in a train station than they do in a retail and leisure area. Such diverse dynamics, in addition to different density regimes, will require a range of calibrations of the model in order to provide adaptability. Furthermore, these calibrations should be based on real-world data to ensure fidelity.

A related line of work will involve revisiting the fundamental diagram for pedestrian dynamics in order to include it in the model in a more suitable way. The current frictional effects are too pervasive, slowing down pedestrians even when the neighbouring densities are low. Furthermore, they are prescriptive, as the form of the friction is somewhat arbitrary and should be improved. A number of machine learning techniques are now available and will be used to extract a frictional term directly from pedestrian data, rather than imposing a preconceived model.

A well-calibrated model together with an efficient implementation of the gradient formulation of (12) will yield realistic live simulations. The capacity to simulate large crowds in real time will enable for the making of short-term predictions based on automated sensor data, as measurements of density and flowrates can be used to estimate an initial condition, and the model can be used to compute its evolution in time. The applications of such predictions are manyfold, allowing the anticipation and early response to undesired phenomena. Of particular interest is the optimal steering of crowds along different routes, which would be accomplished through automated signals able to adjust their information according to output from the model based on data from the crowd.

The last item of interest comprises the development of mesoscopic and macroscopic models corresponding to the dynamics of the model presented in this work. The first kinetic and hydrodynamic models derived from the original formulation appeared in [20]; the comparison between these and those developed from the modified models discussed above will be relevant in understanding the properties and scales of the different components of the dynamics. Furthermore, an understanding of the correspondence between the microscopic and macroscopic scales could allow for the development of a hybrid model. This would be achieved following a *level*

of detail principle, where the majority of a large number of pedestrians is simulated efficiently through the macroscopic model and only the areas of particular interest are resolved at the microscopic scale.

Acknowledgements JAC acknowledges support by the EPSRC grant no. EP/P031587/1. PD acknowledges support by the EPSRC grant no. EP/M006883/1, by the Royal Society and the Wolfson Foundation through a Royal Society Wolfson Research Merit Award no. WM130048. PD is on leave from CNRS, Institut de Mathmatiques de Toulouse, France. JAC and PD acknowledge support by the National Science Foundation (NSF) under Grant no. RNMS11-07444(KI-Net).

Supplementary Material

Interactive versions of the simulations presented on Figs. 7, 12, 15, and 16 are available online at rafaelbailo.com/rationalbehaviour/. Videos of the simulations can be found at the permanent repository figshare.com/projects/Pedestrian_Models_based_on_Rational_Behaviour/38357.

Data Statement

No new data was generated during the course of this research.

References

1. C. Appert-Rolland, A. Jelić, P. Degond, J. Fehrenbach, J. Hua, A. Cretual, R. Kulpa, A. Marin, A.-H. Olivier, S. Lemercier, and J. Pettré. Experimental Study of the Following Dynamics of Pedestrians. In *Pedestr. Evacuation Dyn. 2012*, pages 305–315. Springer International Publishing, Cham, 2014.
2. I. L. Bajec, M. Mraz, and N. Zimic. Boids with a fuzzy way of thinking. *Proc. ASC*, 25:58–62, 2003.
3. M. Batty. Predicting where we walk. *Nature*, 388(6637):19–20, jul 1997.
4. N. Bellomo and A. Bellouquid. On the modelling of vehicular traffic and crowds by kinetic theory of active particles. In *Math. Model. Collect. Behav. Socio-Economic Life Sci.*, pages 273–296. Birkhäuser Boston, Boston, 2010.
5. N. Bellomo and A. Bellouquid. On the modeling of crowd dynamics: Looking at the beautiful shapes of swarms. *Networks Heterog. Media*, 6(3):383–399, aug 2011.
6. N. Bellomo, C. Bianca, and V. Coscia. On the modeling of crowd dynamics: An overview and research perspectives. *SeMA J.*, 54(1):25–46, apr 2011.
7. N. Bellomo and C. Dogbe. On the Modeling of Traffic and Crowds: A Survey of Models, Speculations, and Perspectives. *SIAM Rev.*, 53(3):409–463, jan 2011.
8. A. Borzì and S. Wongkaew. Modeling and control through leadership of a refined flocking system. *Math. Model. Methods Appl. Sci.*, 25(02):255–282, feb 2015.

9. V. Braitenberg. *Vehicles: Experiments in Synthetic Psychology*. MIT Press, Cambridge, Massachusetts, 1984.
10. M. Caponigro, M. Fornasier, B. Piccoli, and E. Trélat. Sparse stabilization and optimal control of the Cucker-Smale model. *Math. Control Relat. Fields*, 3(4):447–466, sep 2013.
11. J. A. Carrillo, M. Fornasier, J. Rosado, and G. Toscani. Asymptotic Flocking Dynamics for the Kinetic CuckerSmale Model. *SIAM J. Math. Anal.*, 42(1):218–236, jan 2010.
12. J. A. Carrillo, M. Fornasier, G. Toscani, and F. Vecil. Particle, kinetic, and hydrodynamic models of swarming. In *Math. Model. Collect. Behav. Socio-Economic Life Sci.*, pages 297–336. Birkhäuser Boston, Boston, 2010.
13. J. A. Carrillo, S. Martin, and M.-T. Wolfram. An improved version of the Hughes model for pedestrian flow. *Math. Model. Methods Appl. Sci.*, 26(04):671–697, apr 2016.
14. E. Cristiani, B. Piccoli, and A. Tosin. Modeling self-organization in pedestrians and animal groups from macroscopic and microscopic viewpoints. In *Math. Model. Collect. Behav. Socio-Economic Life Sci.*, pages 337–364. Birkhäuser Boston, Boston, 2010.
15. F. Cucker and S. Smale. Emergent Behavior in Flocks. *IEEE Trans. Automat. Contr.*, 52(5):852–862, may 2007.
16. F. Cucker and S. Smale. On the mathematics of emergence. *Japanese J. Math.*, 2(1):197–227, 2007.
17. J. E. Cutting, P. M. Vishton, and P. A. Braren. How we avoid collisions with stationary and moving objects. *Psychol. Rev.*, 102(4):627–651, 1995.
18. W. Daamen and S. P. Hoogendoorn. Controlled Experiments to derive Walking Behaviour. *Eur. J. Transp. Infrastruct. Res.*, 3(1):39–59, 2003.
19. W. Daamen and S. P. Hoogendoorn. Experimental Research of Pedestrian Walking Behavior. *Transp. Res. Rec. J. Transp. Res. Board*, 1828(January):20–30, jan 2003.
20. P. Degond, C. Appert-Rolland, M. Moussaïd, J. Pettré, and G. Theraulaz. A Hierarchy of Heuristic-Based Models of Crowd Dynamics. *J. Stat. Phys.*, 152(6):1033–1068, sep 2013.
21. P. Degond, C. Appert-Rolland, J. Pettré, and G. Theraulaz. Vision-based macroscopic pedestrian models. *Kinet. Relat. Model.*, 6(4):809–839, nov 2013.
22. M. R. D'Orsogna, Y. L. Chuang, A. L. Bertozzi, and L. S. Chayes. Self-Propelled Particles with Soft-Core Interactions: Patterns, Stability, and Collapse. *Phys. Rev. Lett.*, 96(10):104302, mar 2006.
23. J. J. Fruin. *Pedestrian Planning and Design*. Metropolitan Association of Urban Designers and Environmental Planners, New York, 1971.
24. Q. Gibson. Social Forces. *J. Philos.*, 55(11):441, may 1958.
25. G. Gigerenzer. Why Heuristics Work. *Perspect. Psychol. Sci.*, 3(1):20–29, jan 2008.
26. J. R. Gill and K. Landi. Traumatic Asphyxial Deaths Due to an Uncontrolled Crowd. *Am. J. Forensic Med. Pathol.*, 25(4):358–361, dec 2004.
27. S.-Y. Ha, T. Ha, and J.-H. Kim. Emergent Behavior of a Cucker-Smale Type Particle Model With Nonlinear Velocity Couplings. *IEEE Trans. Automat. Contr.*, 55(7):1679–1683, jul 2010.
28. B. D. Hankin and R. A. Wright. Passenger Flow in Subways. *Oper. Res. Q.*, 9(2):81, jun 1958.
29. D. Helbing. A mathematical model for the behavior of pedestrians. *Behav. Sci.*, 36(4):298–310, oct 1991.
30. D. Helbing. A Fluid Dynamic Model for the Movement of Pedestrians. *Complex Syst.*, 6:391–415, may 1992.
31. D. Helbing. Self-organization in Pedestrian Crowds. In *Soc. Self-Organization*, pages 71–99. 2012.
32. D. Helbing, L. Buzna, A. Johansson, and T. Werner. Self-Organized Pedestrian Crowd Dynamics: Experiments, Simulations, and Design Solutions. *Transp. Sci.*, 39(1):1–24, feb 2005.
33. D. Helbing, I. J. Farkas, and T. Vicsek. Simulating dynamical features of escape panic. *Nature*, 407(6803):487–490, 2000.
34. D. Helbing, A. Johansson, and H. Z. Al-Abideen. Crowd turbulence: the physics of crowd disasters. *Fifth Int. Conf. Nonlinear Mech.*, (June):967–969, aug 2007.

35. D. Helbing, A. Johansson, and H. Z. Al-Abideen. Dynamics of crowd disasters: An empirical study. *Phys. Rev. E*, 75(4):046109, apr 2007.
36. D. Helbing and P. Molnár. Social force model for pedestrian dynamics. *Phys. Rev. E*, 51(5):4282–4286, may 1995.
37. D. Helbing, P. Molnár, I. J. Farkas, and K. Bolay. Self-organizing pedestrian movement. *Environ. Plan. B Plan. Des.*, 28(3):361–383, 2001.
38. D. Helbing and T. Vicsek. Optimal self-organization. *New J. Phys.*, 1:13.1–13.7=17, 1999.
39. L. F. Henderson. The Statistics of Crowd Fluids. *Nature*, 229(5284):381–383, feb 1971.
40. L. F. Henderson. On the fluid mechanics of human crowd motion. *Transp. Res.*, 8(6):509–515, dec 1974.
41. S. P. Hoogendoorn and W. Daamen. Pedestrian Behavior at Bottlenecks. *Transp. Sci.*, 39(2):147–159, may 2005.
42. B. Hopkins, A. Churchill, S. Vogt, and L. Rönnqvist. Braking Reaching Movements: A Test of the Constant Tau-Dot Strategy Under Different Viewing Conditions. *J. Mot. Behav.*, 36(1):3–12, may 2004.
43. R. L. Hughes. A continuum theory for the flow of pedestrians. *Transp. Res. Part B Methodol.*, 36(6):507–535, jul 2002.
44. R. L. Hughes. The Flow of Human Crowds. *Annu. Rev. Fluid Mech.*, 35(1):169–182, jan 2003.
45. A. Jelić, C. Appert-Rolland, S. Lemercier, and J. Pettré. Properties of pedestrians walking in line: Fundamental diagrams. *Phys. Rev. E*, 85(3):036111, mar 2012.
46. Y.-q. Jiang, P. Zhang, S. Wong, and R.-x. Liu. A higher-order macroscopic model for pedestrian flows. *Phys. A Stat. Mech. its Appl.*, 389(21):4623–4635, nov 2010.
47. A. Johansson and D. Helbing. Analysis of Empirical Trajectory Data of Pedestrians. In *Pedestr. Evacuation Dyn. 2008*, pages 203–214. Springer Berlin Heidelberg, Berlin, Heidelberg, 2010.
48. N. R. Johnson. Panic at the 'Who Concert Stampede': An Empirical Assessment. *Soc. Probl.*, 34(4):362–373, 1987.
49. T. Kretz, A. Grünebohm, M. Kaufman, F. Mazur, and M. Schreckenberg. Experimental study of pedestrian counterflow in a corridor. *J. Stat. Mech. Theory Exp.*, 2006(10):P10001–P10001, oct 2006.
50. T. Kretz, A. Grünebohm, and M. Schreckenberg. Experimental study of pedestrian flow through a bottleneck. *J. Stat. Mech. Theory Exp.*, (10), 2006.
51. S. Lemercier, A. Jelić, R. Kulpa, J. Hua, J. Fehrenbach, P. Degond, C. Appert-Rolland, S. Donikian, and J. Pettré. Realistic following behaviors for crowd simulation. *Comput. Graph. Forum*, 31(2pt2):489–498, may 2012.
52. K. Lewin. *Field Theory in Social Science*. Harper, 1951.
53. M. J. Lighthill and G. B. Whitham. On Kinematic Waves I - Flood Movement in Long Rivers. *Proc. R. Soc. A Math. Phys. Eng. Sci.*, 229(1178):281–316, may 1955.
54. M. J. Lighthill and G. B. Whitham. On Kinematic Waves II - A Theory of Traffic Flow on Long Crowded Roads. *Proc. R. Soc. A Math. Phys. Eng. Sci.*, 229(1178):317–345, may 1955.
55. L. Luo, Z. Fu, X. Zhou, K. Zhu, H. Yang, and L. Yang. Fatigue effect on phase transition of pedestrian movement: experiment and simulation study. *J. Stat. Mech. Theory Exp.*, 2016(10):103401, oct 2016.
56. M. Moussaïd, E. G. Guillot, M. Moreau, J. Fehrenbach, O. Chabiron, S. Lemercier, J. Pettré, C. Appert-Rolland, P. Degond, and G. Theraulaz. Traffic instabilities in self-organized pedestrian crowds. *PLoS Comput. Biol.*, 8(3), 2012.
57. M. Moussaïd, D. Helbing, S. Garnier, A. Johansson, M. Combe, and G. Theraulaz. Experimental study of the behavioural mechanisms underlying self-organization in human crowds. *Proc. R. Soc. B Biol. Sci.*, 276(1668):2755–2762, 2009.
58. M. Moussaïd, D. Helbing, and G. Theraulaz. How simple rules determine pedestrian behavior and crowd disasters. *Proc. Natl. Acad. Sci.*, 108(17):6884–6888, 2011.
59. M. Moussaïd, N. Perozo, S. Garnier, D. Helbing, and G. Theraulaz. The walking behaviour of pedestrian social groups and its impact on crowd dynamics. *PLoS One*, 5(4):1–7, 2010.
60. M. Mri and H. Tsukaguchi. A new method for evaluation of level of service in pedestrian facilities. *Transp. Res. Part A Gen.*, 21(3):223–234, may 1987.

61. K. M. Ngai, F. M. Burkle, A. Hsu, and E. B. Hsu. Human Stampedes: A Systematic Review of Historical and Peer-Reviewed Sources. *Disaster Med. Public Health Prep.*, 3(04):191–195, dec 2009.
62. S. J. Older. Movement of Pedestrians on Footways in Shopping Streets. *Traffic Eng. Control*, 10(4):160–163, 1968.
63. A. Polus, J. L. Schofer, and A. Ushpiz. Pedestrian Flow and Level of Service. *J. Transp. Eng.*, 109(1):46–56, jan 1983.
64. C. W. Reynolds. Flocks, herds and schools: A distributed behavioral model. *ACM SIGGRAPH Comput. Graph.*, 21(4):25–34, aug 1987.
65. C. W. Reynolds. Steering behaviors for autonomous characters. *Game Dev. Conf.*, pages 763–782, 1999.
66. P. R. Schrater, D. C. Knill, and E. P. Simoncelli. Mechanisms of visual motion detection. *Nat. Neurosci.*, 3(1):64–68, jan 2000.
67. A. Seyfried, B. Steffen, W. Klingsch, and M. Boltes. The fundamental diagram of pedestrian movement revisited. *J. Stat. Mech. Theory Exp.*, (10):41–53, 2005.
68. D. Strömbom. Collective motion from local attraction. *J. Theor. Biol.*, 283(1):145–151, 2011.
69. D. Strömbom, R. P. Mann, A. M. Wilson, S. Hailes, A. J. Morton, D. J. T. Sumpter, and A. J. King. Solving the shepherding problem: heuristics for herding autonomous, interacting agents. *J. R. Soc. Interface*, 11(100):20140719–20140719, aug 2014.
70. Transportation Research Board. *Highway Capacity Manual: Special Report 209*. U.S. Dept. of Transportation, Federal Highway Administration, Washington, D.C., 1985.
71. Transportation Research Board. *Highway Capacity Manual 2000*. U.S. Dept. of Transportation, Federal Highway Administration, Washington, D.C., 2000.
72. H. M. Traquair. *Clinical perimetry*. Kimpton, London, 1876.
73. T. Vicsek, A. Czirók, E. Ben-Jacob, I. Cohen, and O. Shochet. Novel Type of Phase Transition in a System of Self-Driven Particles. *Phys. Rev. Lett.*, 75(6):1226–1229, aug 1995.
74. W. H. Warren and B. R. Fajen. From Optic Flow to Laws of Control. In *Opt. Flow Beyond*, pages 307–337. Springer Netherlands, Dordrecht, 2004.
75. U. Weidmann. *Transporttechnik der Fussgänger, Transporttechnische Eigenschaften des Fussgängerverkehrs (Literturauswertung)*, volume 90. Institut für Verkehrsplanung, Transporttechnik, Strassen- und Eisenbahnbau (IVT), ETH Zürich, 1993.